

BIO-INSPIRED CRYSTALLIZATION OF OXIDE COMPOUNDS WITHIN  
INORGANIC MATRICES

A Dissertation

Presented to the Faculty of the Graduate School

of Cornell University

In Partial Fulfillment of the Requirements for the Degree of

Doctor of Philosophy

by

Emily Asenath Smith

May 2015

© 2015 Emily Asenath Smith

# BIO-INSPIRED CRYSTALLIZATION OF OXIDE COMPOUNDS WITHIN INORGANIC MATRICES

Emily Asenath Smith, Ph. D.

Cornell University 2015

The energy crisis facing our planet requires solutions that take an interdisciplinary approach to the improvement of existing energy systems as well as the development of new energy sources. Moreover, the composition of the materials is important: thermally- and chemically-stable materials based on abundant, non-toxic elements are needed to support the sustainability of both the technology and our environment. Biological organisms present multiple examples of hierarchical structures that are optimized for a given function. In particular, biomineralized materials: (i) display crystallographic control across length scales; (ii) are often organic-inorganic composites due to the occlusion of components from the associated organic growth matrix; (iii) and exhibit tailored mechanical properties that are unique to their function. Of great importance to the development of advanced energy materials is the observation that biomineral architectures are built from crystallographically-defined structural elements with interfaces that span multiple length scales.

Synthetically, the translation of biological mineralization strategies to oxide compounds is hindered by the low melting temperatures of biopolymer hydrogels that compose extracellular matrices. In order to successfully crystallize oxide compounds using a (bio-inspired) matrix-mediated approach, I had to identify and develop a hydrogel system with thermal stability and chemical compatibility to the growth conditions needed for the oxide. By moving to inorganic networks based on silica, I achieved a thermally-stable growth matrix. By forming these networks at low pH, I obtained a growth environment that was compatible with the crystallization of hematite. With these two features, hematite was crystallized under diffusion-limited conditions, which provided a means to to manipulate its structure and assembly from the atomic- to the microscale.

By combining inductively coupled plasma atomic emission spectroscopy with Rietveld refinements to x-ray diffraction data, expansion of the hematite lattice along the c-axis was found to be correlated to increasing silicon in the crystals and the preferential growth of the coherent domains along [110] (perpendicular to the strained c-axis). Using single particle manipulation in a focused ion beam system, electron-transparent thin sections were prepared from precisely-defined geometric locations within the hematite crystals for analysis by transmission electron microscopy. Quantitative analysis on selected area electron diffraction patterns was used to unravel the net orientation of the hematite lattice with respect to the quasi-spherical form and to calculate the misorientation (mosaicity) between the coherent domains. The combined results of these analyses showed that silicon from the growth environment had consistently modified the architecture of hematite, from the atomic to the microscale, leading to microscale structures with surfaces composed of nanoscale, high catalytic activity {110} facets. With hydrogel growth as a demonstrated route to tune the hierarchical structure of a transition metal oxide to preferentially express desired planes, the bandgap and photocatalytic activity of the samples was studied, to reveal that these micro-scale hierarchical architectures outperform their nano-sized counterparts, presenting a new approach to the design of materials for advanced energy applications.



## ACKNOWLEDGEMENTS

Few would argue that completing a PhD is a major undertaking that requires commitment and perseverance. I would argue that the PhD itself is not the biggest challenge; it is all those other ‘things’ that occur while completing the PhD that introduce most difficult complexities. As an example, consider having a middle school social studies project that is due the day of your qualifying exam. Then, imagine hosting a proper tea party for a girl’s birthday celebration (complete with authentic Genoise Petits Fours) when you are only home for 48 h in a 10 d period. Next try to visualize yourself working through the geometry of arcs and cords via Skype after a 12 h day running experiments in 3 different labs. Finally, visualize mentoring a special education student on an electrical engineering science fair project and report that is to be on display the day your thesis is due. How is a PhD candidate to handle such challenges with grace and patience?! It is only with a multi-dimensional support network (of course!) that I have been able to balance all of these ‘things’ while completing my PhD with a normal timeline –and somewhere along the way, I have still found time to take care of myself.

The foundation of my support network is held together by my husband –I must express my sincerest gratitude and appreciation to him for being my champion partner in this high-stakes high-rewards life we have together. I am so very grateful for my children, whose interests and understandings are my strongest motivators throughout my educational pursuits. Thank you to Tahquiy, for making me a better mathematician. Thank you to Jaleal for helping me to use electrical engineering skills I didn’t know I had! Thank you to Natiqia for always being excited to try new things; whether it is knitting or cooking, softball or growing crystals, you are always smiling. I appreciate my mother and my sister for supporting my decisions and understanding that physical distance is no measure of love. I honor my grandparents for the value that they put on education and the example that they set in developing their careers and growing their family simultaneously.

I want to acknowledge financial support from the National Science Foundation through the Graduate Research Fellowship and IGERT Programs. These sources of independent funding both helped

me to support my family during my graduate studies and enabled me to personally design my own thesis and those of multiple undergraduate researchers. It allowed me the flexibility that I needed to pursue new research directions and grow as a mentor. I want to specifically acknowledge Prof. Wei Chen, my research advisor at Mount Holyoke College, for encouraging me to pursue a PhD and fostering my ability to secure funding to support it.

In the academic realm, I am thankful to my advisor, Prof. Lara Estroff, for allowing me the independence to design my own thesis and those of many others. Thank you to Lara for prioritizing my initiative to international research experiences. Thank you for supporting my involvement in research collaborations. I am grateful to my committee members, Prof. Frank DiSalvo and Prof. Sol Gruner, for providing me with new perspectives on research and supporting my career development. I am also grateful to Prof. Lena Kourkoutis for bolstering my ability to communicate across disciplines.

I greatly appreciate friends and colleagues that have been my steadfast mentors in this long journey. Francie Viggiani and Linda Jones have consistently guided my professional development and given me the right balance of thoughtful guidance and firm direction. Thank you to Jim DeYoreo for mentorship in research and career development. Thank you to Jason Dorvee for a mutually beneficial mentoring relationship that will surely stand the test of time. Thank you to Sarah Sadowska for helping me to define and articulate my goals for my career.

My network of colleagues has grown immensely throughout my graduate studies. I want to specifically acknowledge the A-team –for a bit of humor and social engagement within the framework of top flight research. I am thankful for the members of the Estroff Research Group –what a diversity of interests and personalities we all have. I appreciate what a complimentary set we represent. I am grateful to members of the Wiesner, DiSalvo and Abruna groups for sharing their facilities and guidance as I carried out what often turned out to be unusual experiments. I am grateful to the Kourkoutis and Muller groups for their openness to guide my development as a microscopist and their willingness to collaborate.

During my PhD, I have been involved in numerous collaborations, domestic and international. Specifically, I want to acknowledge Derk Joester and his students, Lyle Gordon and Michael Cohen, for their tireless efforts working with me to bring atom probe tomography to any crystal that I can make. I am indebted to Prof. Fiona Meldrum and her research group for a lively collaboration on crystallization in confinement and for warmly welcoming my visits and those of my undergraduates to Leeds.

More than anything else, I chose to undertake my PhD at Cornell University because of the Shared Facilities and their highly-skilled managerial staff. John Grazul and Mick Thomas are the perfect dynamic duo to any challenge that I have faced both in electron microscopy and in my personal life. Thank you, Thank you for caring so much about your users and the equipment. I am also grateful to Maura Weathers for running a great x-ray facility and freely sharing ideas to get the information I sought.

No support network would be complete without the involvement of administrative assistants and department staff. Dolores Dewbury, Michele Conrad, Carol Armstrong and Karen Jordan are an amazing team and are truly the foundation of the Department!

Last and certainly not least, I have benefitted immensely from programming put on by Diversity Programs in Engineering, Cornell Center for Teaching Excellence and the Cornell University Center for the Integration of Teaching and Learning. Through these programs I have grown as a teacher, a mentor and a researcher and I am ready for the next phase of my career!

# TABLE OF CONTENTS

Biographical Sketch.....	iii
Acknowledgements.....	iv
List of Figures.....	xi
List of Tables.....	xv
<b>1 PRELIMINARY DISCUSSION.....</b>	<b>1</b>
<b>1.1 Research Background .....</b>	<b>1</b>
<b>1.2 Dissertation Introduction.....</b>	<b>2</b>
<b>1.3 Dissertation Overview .....</b>	<b>3</b>
<b>1.4 Preface .....</b>	<b>6</b>
<b>2 CRYSTAL GROWTH OF CALCIUM CARBONATE IN HYDROGELS AS A MODEL OF BIOMINERALIZATION.....</b>	<b>9</b>
<b>2.1 Abstract .....</b>	<b>9</b>
<b>2.2 Introduction .....</b>	<b>9</b>
<b>2.3 Background .....</b>	<b>11</b>
2.3.1 Common Hydrogels Used for Crystal Growth.....	12
2.3.2 Hydrogels with Physical Bonding.....	14
2.3.3 Hydrogels with Chemically-Bonded Networks .....	16
2.3.4 Mixed Bonding Character and Solvent Structure in Hydrogel Networks.....	17
<b>2.4 Crystal Morphology and Crystal Growth Mechanisms.....</b>	<b>18</b>
2.4.1 Crystal Nucleation and Growth in Gels .....	19
<b>2.5 Crystallization Techniques for Growth in Gels .....</b>	<b>21</b>
<b>2.6 Biogenic Calcium Carbonate Systems that Mineralize in Gel-like Media .....</b>	<b>22</b>
2.6.1 Nacre (Mother-of-Pearl).....	25
2.6.2 Coral.....	27
2.6.3 Otoconia .....	28
2.6.4 Otoliths.....	29
<b>2.7 In Vitro Studies of Biomineralization: Crystal Growth in Gels.....</b>	<b>31</b>
2.7.1 Protein-Based Hydrogel Models for Nacre Formation .....	33
2.7.2 Hydrogels as a Crystallization Matrix.....	36
2.7.3 Incorporation of the Gel-Matrix During Crystal Growth.....	49

<b>2.8</b>	<b>SUMMARY AND OUTLOOK.....</b>	<b>59</b>
<b>2.9</b>	<b>Materials and Methods .....</b>	<b>63</b>
2.9.1	Hydrogel Preparation for Imaging .....	63
2.9.2	Crystal Growth Experiments .....	64
2.9.3	Characterization of Calcite Crystals.....	64
<b>3</b>	<b>SECTIONING OF INDIVIDUAL HEMATITE PSEUDOCUBES WITH FODUCES ION BEAM ENABLES QUANTITATIVE STRCUTRAL CHARACTERIZATION AT NANOMETER LENGTH SCALES.....</b>	<b>77</b>
<b>3.1</b>	<b>Abstract .....</b>	<b>77</b>
<b>3.2</b>	<b>Introduction .....</b>	<b>77</b>
3.2.1	Hematite Crystallography and Synthesis .....	78
3.2.2	Hematite Internal Structure .....	79
<b>3.3</b>	<b>Results.....</b>	<b>80</b>
3.3.1	Phase and Morphology Characterization .....	80
3.3.2	Internal Structure of Solution-Grown Pseudocubes .....	84
3.3.3	Net Crystallographic Orientation of Hematite Lattice within Pseudocubes .....	88
3.3.4	Mosaicity within Pseudocubes .....	90
<b>3.4</b>	<b>Discussion .....</b>	<b>93</b>
3.4.1	Crystallographic Registry Between Adjacent Domains within Pseudocubes .....	94
3.4.2	Net Crystallographic Orientation of Hematite Lattice within Non-Idiomorphic Pseudocubes 94	
<b>3.5</b>	<b>Summary and Conclusions .....</b>	<b>95</b>
<b>3.6</b>	<b>Materials and Methods .....</b>	<b>97</b>
3.6.1	Phase and Microscale Characterization.....	97
3.6.2	Preparation for Transmission Electron Microscopy.....	97
3.6.3	Analysis of Selected-Area Electron Diffraction (SAED) Patterns.....	98
<b>4</b>	<b>HIERARCHICALLY-STRUCTURED HEMATITE (<math>\alpha</math>-<math>\text{Fe}_2\text{O}_3</math>) ARCHITECTURES ACHIEVED BY GROWTH IN A SILICA HDYROGEL .....</b>	<b>101</b>
<b>4.1</b>	<b>Abstract .....</b>	<b>101</b>
<b>4.2</b>	<b>Introduction .....</b>	<b>101</b>
<b>4.3</b>	<b>Results and Discussion .....</b>	<b>103</b>
4.3.1	Microstructural Assessment of Hydrogel and Hematite Crystals .....	105
4.3.2	Mesoscale Assembly within Hematite Crystals .....	108

4.3.3	Nanoscale Domain Structure.....	114
4.3.4	Atomic Scale Effect of Silicon on the Hematite Lattice .....	116
4.3.5	Propagation of Atomic Structure Through Multiple Length Scales.....	120
4.3.6	Hierarchical Structure Influence on Properties .....	122
<b>4.4</b>	<b>Summary and Conclusions .....</b>	<b>127</b>
<b>4.5</b>	<b>Materials and Methods .....</b>	<b>131</b>
4.5.1	Methods.....	131
4.5.2	Solution-Based Crystallization.....	131
4.5.3	Silica Hydrogel Formation .....	131
4.5.4	Hydrogel-Based Crystallization Experiments .....	132
4.5.5	Silica Matrix Removal and Acid Etching.....	132
4.5.6	Elemental Analysis.....	133
4.5.7	Phase Analysis .....	133
4.5.8	Hydrogel Sample Preparation for SEM imaging .....	133
4.5.9	Whole Particle Imaging.....	133
4.5.10	Sample Preparation for TEM Analysis .....	134
4.5.11	TEM Analysis .....	134
4.5.12	Mosaicity Quantification .....	135
4.5.13	Scanning Transmission Electron Microscopy.....	135
4.5.14	Surface Area Determination .....	136
4.5.15	Bandgap Determination .....	136
4.5.16	Photocatalytic degradation of Rhodamine B .....	136
<b>5</b>	<b>THE ROLE OF AKAGANEITE (<math>\beta</math>-FeOOH) IN THE GROWTH OF HEMATITE (<math>\alpha</math>-Fe<sub>2</sub>O<sub>3</sub>)</b>	
	<b>IN AN INORGANIC SILICA HYDROGEL.....</b>	<b>141</b>
<b>5.1</b>	<b>Abstract .....</b>	<b>141</b>
<b>5.2</b>	<b>Introduction .....</b>	<b>141</b>
5.2.1	Hematite Morphology and Synthesis .....	143
5.2.2	Akaganeite ( $\beta$ -FeOOH) Crystallography and Structure .....	143
5.2.3	Relationship of Akaganeite to Hematite .....	144
<b>5.3</b>	<b>Results.....</b>	<b>145</b>
5.3.1	Overgrowth on hydrogel-grown hematite quasi-spheres .....	145
5.3.2	Effect of Silica Hydrogel and [FeCl <sub>3</sub> ] on Hematite Morphology.....	147
36.1.1	Aqueous Equilibria of Metal Salts.....	151

36.1.2	Effect of Silica Hydrogel and [FeCl <sub>3</sub> ] on Akaganeite morphology .....	151
151.1.1	Effect of [HCl] on Akaganeite Crystallization from Solution .....	155
151.1.2	Distinguishing the Effect of [Cl <sup>-</sup> ] from [H <sup>+</sup> ] on Akaganeite Crystallization.....	160
151.1.3	Physical role of hydrogel .....	162
<b>151.2</b>	<b>Discussion.....</b>	<b>163</b>
151.2.1	Hematite Morphology .....	163
151.2.2	Size and Aspect Ratio of Akaganeite Crystals .....	164
151.2.3	Crystallographic Twinning, Branching and Splitting of Akaganeite Crystals.....	164
151.2.4	Akaganeite-Goethite-Hematite Pathway .....	166
151.2.5	Role of Silica in the Formation Mechanism of Hematite in Silica Hydrogel .....	167
<b>151.3</b>	<b>Summary and Conclusions.....</b>	<b>170</b>
<b>151.4</b>	<b>Experimental .....</b>	<b>172</b>
151.4.1	Materials .....	172
151.4.2	Methods .....	172
151.4.3	Characterization.....	174
<b>152</b>	<b>CONCLUSIONS .....</b>	<b>181</b>
<b>152.1</b>	<b>Summary .....</b>	<b>181</b>
<b>152.2</b>	<b>Future Directions .....</b>	<b>182</b>
<b>152.3</b>	<b>Outlook.....</b>	<b>183</b>
<b>152.4</b>	<b>Related works .....</b>	<b>184</b>
<b>152.5</b>	<b>Career Development .....</b>	<b>186</b>

## LIST OF FIGURES

Figure 2.1. An assortment of gel microstructures imaged by scanning electron microscopy that illustrate the wide range of microstructures available in hydrogels as well as the factors that further influence those microstructures. ....	13
Figure 2.2 Schematic representation of experimental approaches used in the growth of two component crystals hydrogels .....	24
Figure 2.3 Schematic of the demineralized organic matrix of <i>Atrina rigida</i> , a model matrix-mediated biomineralization system .....	26
Figure 2.4 The non-collagenous, fibrillar, porous gel-like network associated with soft coral.....	28
Figure 2.5 Different gel-like domains associated with calcite otoconia imaged by scanning electron microscopy with a schematic graphic showing the regional locations of each within the guinea pig vestibular system.....	30
Figure 2.6 Asteriscus otolith from <i>Chondrostoma nasus nasus</i> and occluded matrix after de-calcification, showing fibrous, porous organic network.....	31
Figure 2.7 SEM micrograph of calcium carbonate crystallization on $\beta$ -chitin with 2.5 wt% silk fibrion hydrogel and 10 $\mu$ M n16N, a nacre specific peptide.....	34
Figure 2.8 Optical images of calcium carbonate crystallization in uniaxially deformed (200%, elongation) gelatin films. ....	36
Figure 2.9 Scanning electron microscope images of 8-pointed calcite stars grown in 1 (w/w%) agarose hydrogel with no additives. Morphological evolution of calcite grown in 0.3 % agar in the presence of variable radii impurity cations imaged by scanning electron microscopy.....	39
Figure 2.10 Scanning electron microscopy images of calcite grown in silica gels under double diffusion. Morphology changes are linked to changes in magnesium content and supersaturation.....	42
Figure 2.11 Scanning electron microscopy images of calcite crystals grown in 10 wt% gelatin matrices under double diffusion. ....	44
Figure 2.12 Pseudo-octahedral aggregates of calcite formed under double diffusion in 10 wt% polyacrylamide hydrogel .....	46
Figure 2.13 Structural characterization of porous single crystal calcite agarose composites. ....	52
Figure 2.14 The weight loss above 150 °C calculated from TGA analyses for the calcite single crystals grown under systematically varied conditions.....	54
Figure 2.15 The proposed mechanism for agarose matrix incorporation during calcite crystal growth: A balance between the resistance of the gel fibers to crystallization pressure and the growth rate.. ....	57
Figure 2.16 A schematic representation of the proposed gel-incorporation mechanism with force competition and mass competition at the growth front nearby an agarose gel fiber.....	58
Figure 3.1 Optical microscopy images of hematite pseudocubes under transmitted light and during rotation under cross-polarized light. ....	82
Figure 3.2 Scanning electron micrographs of hematite pseudocubes .....	83

Figure 3.3 X-ray powder diffraction pattern of hematite pseudocubes.....	83
Figure 3.4 Sequence of particle manipulation for FIB thinning of the equatorial slice of a hematite pseudocube.....	85
Figure 3.5 Schematic representation of the location/orientation of equatorial and diagonal slices taken through hematite particles by thinning with a focused ion beam. ....	86
Figure 3.6 Graphical representations of the relationship between the pseudocubic-shaped hematite particles and the hexagonal hematite lattice .....	89
Figure 3.7 The analysis sequence that was used to calculate azimuthal broadening from SAED patterns leading to quantification of mosaicity from electron diffraction patterns.....	91
Figure 4.1 (a) Scanning electron microscope (SEM) image of a freeze-dried silica hydrogel showing the cellular porous microstructure of silica hydrogel networks used in this study. (b) Experimental schematic for the growth of hematite in a silica hydrogel by a single diffusion method. (c) SEM micrograph of a freeze-dried silica hydrogel in which hematite particles have grown. ....	105
Figure 4.2 Optical microscopy images of hematite particles grown in silica hydrogel, taken in transmission and during rotation under cross-polarized light.....	107
Figure 4.3 Scanning electron micrographs of hematite particles grown in three different environments, each with a different amount of dissolved silicate.....	108
Figure 4.4 SEM micrographs showing the sequence of single particle manipulations (equatorial thin section shown) used to form electron transparent thin sections of hematite crystals grown in a silica hydrogel using a dual-beam focused ion beam system.....	109
Figure 4.5 Graphical representation of the geometric location from which thin sections were made with FIB milling: equatorial slice and axial slice. Bright-field TEM, SAED patterns and electron energy loss spectroscopy of an equatorial thin section from a hydrogel-grown crystal.....	111
Figure 4.6 Analysis of the symmetry of crystalline regions that propagate radially within the equatorial thin section from the hydrogel-grown quasi-spheres demonstrating the six-fold symmetry of crystalline regions within the equatorial plane of the quasi-sphere.....	113
Figure 4.7 X-ray powder diffraction patterns of the crystals reported in this study, confirming the pure phase formation of hematite under all three growth conditions. Lattice parameters of the hematite crystals, found by Rietveld refinements, showing that the hematite lattice expands along the c-axis as silicon in the growth environment increases .....	115
Figure 4.8 Rietveld refinement results for hematite crystals .....	118
Figure 4.9 Ball and stick representation of the hematite lattice, viewed normal to the (210) plane, showing the larger size of the tetrahedral interstices along a,b directions of the unit cell as compared to c. ....	120
Figure 4.10 Schematic representation of the hierarchical structure contained within microscale hematite architectures .....	121
Figure 4.11 Diffuse reflectance spectra and Kubelka-Munk analysis used to extract bandgap of the hematite crystals. ....	124

Figure 4.12 SEM and TEM of commercial hematite used as a control for bandgap determination, and photocatalytic measurements. ....	123
Figure 4.13 Porous mosaic crystalline structures of the hydrogel-grown hematite accessed by acid etching.....	125
Figure 4.14 Transmittance spectrum of the cut-off filter used to remove UV radiation from photocatalysis experiments.....	126
Figure 4.15 Raw absorbance plots for the decomposition of rhodamine B used in the photocatalytic assessment of hierarchical hematite architectures. ....	128
Figure 4.16 The photocatalytic performance of hematite samples as measured via the degradation of Rhodamine B solution under illumination with visible light in the presence of peroxide.....	129
Figure 5.1 Overgrowth of hematite on 0.90 M hydrogel-grown hematite quasi-spheres .....	146
Figure 5.2 Phase analysis by pXRD of all 4 week crystallizations, showing the complete formation of the hematite phase in all cases except hydrogel-based crystallizations with $[\text{FeCl}_3] = 0.018 \text{ M}$ . ....	148
Figure 5.3 Post-crystallization (4 wk) of sphere-forming solution protocol ( $[\text{FeCl}_3]=0.018 \text{ M}$ ) mapped into the silica hydrogel showing that it did not completely transform to hematite.....	149
Figure 5.4 Hematite crystals grown within silica hydrogels and from aqueous solutions over a range of iron (III) chloride hexahydrate concentrations.....	150
Figure 5.5 Phase analysis by pXRD of the hydrogel-based akaganeite crystallizations conducted for 24 h at $100 \text{ }^\circ\text{C}$ showing the complete formation of akaganeite.....	153
Figure 5.6 Phase analysis by pXRD of the solution-based akaganeite crystallizations conducted for 2 h at $100 \text{ }^\circ\text{C}$ showing the complete formation of akaganeite. ....	154
Figure 5.7 A series of akaganeite ( $\beta\text{-FeOOH}$ ) crystallizations conducted with variable iron chloride concentrations.....	155
Figure 5.8 A series of akaganeite ( $\beta\text{-FeOOH}$ ) crystallizations performed in solution at a fixed $[\text{FeCl}_3]$ , with variable acid (HCl) concentrations, illustrating the effect of pH on the crystal morphology and twinning and branching .....	156
Figure 5.9 TEM tilt series confirming the planarity of sample SA-D.....	157
Figure 5.10 Phase analysis by pXRD on the iron oxyhydroxide crystals grown from solution with variable acid.....	158
Figure 5.11 Analysis by selected-area electron diffraction of sample SA-D, after 4 h crystallization, demonstrating that the goethite phase is predominantly located at the core of the highly-branched forms, and twinned across (210) planes.....	159
Figure 5.12 Phase analysis by pXRD of sample SA-D confirming that the sample contains a mixture of goethite ( $\alpha\text{-FeOOH}$ ) and hematite ( $\alpha\text{-Fe}_2\text{O}_3$ ).....	159
Figure 5.13 SEM images of the goethite products from sample SA-D.....	160
Figure 5.14 TEM micrographs of akaganeite crystals (sample SS-A) grown from solution with $[\text{FeCl}_3] = 0.18 \text{ M}$ and $[\text{Cl}^-] = 0.610 \text{ M}$ .....	161

Figure 5.15 An SEM micrograph of freeze-dried silica hydrogel after 24 h crystallization, showing the highly-branched assemblies of akaganeite rods embedded within the cellular walls of the hydrogel network. .... 163

Figure 5.16 Representation of the proposed crystallization microenvironment associated with hematite quasi-sphere formation in silica hydrogel, shown in relation to hematite pseudo-cube growth from solution..... 169

## LIST OF TABLES

Table 2.1 Biom mineralization systems with gel-like organic matrices .....	10
Table 2.2 Hydrogels and additives used in calcium carbonate crystallization.....	32
Table 3.1 Crystallite Size (Scherrer) Analysis from pXRD data (Figure 3.3).....	84
Table 3.2 Calculated and theoretical distances for interplanar spacings of the [010] zone used to index the SAED pattern (Figure 3.5e) from the equatorial slice of a hematite pseudocube (equivalent to a geometric (200) plane of the pseudocube).....	87
Table 3.3 Calculated and theoretical distances for interplanar spacings of [441] zone used to index the SAED pattern (Figure 3.5f) from the diagonal slice of a hematite pseudocube (equivalent to a geometric (110) plane of pseudocube).....	87
Table 3.4 Azimuthal broadening (crystallite misorientation) as derived from FWHM of $\phi$ vs. $I$ of SAED intensities from [010] zone of equatorial slice (Figure 3.5e).....	92
Table 3.5 Azimuthal broadening (crystallite misorientation) as derived from FWHM of $\phi$ vs. $I$ of SAED intensities from [441] Zone of diagonal slice (Figure 3.5f) .....	92
Table 4.1 Analytical Data on Hematite Crystals and Reference Materials.....	104
Table 4.2 Calculated and theoretical distances for interplanar distances from SAED patterns used in the identification of [001] zone from <i>Equatorial</i> slice. ....	110
Table 4.3 Calculated and theoretical distances for interplanar distances from SAED patterns used in the identification of [221] zone from <i>Axial</i> slice.....	110
Table 4.4 Mosaicity calculations for <i>Equatorial</i> slice of hydrogel-grown hematite, zone [001]. ....	116
Table 4.5 Mosaicity calculations for <i>Axial</i> slice of hydrogel-grown hematite, zone [221].....	116
Table 4.6 Refined Rietveld parameters and statistics. ....	119
Table 4.7 Summary of bandgap results for hematite crystals found from diffuse reflectance (Kebulka-Munk) analysis.....	123
Table 5.1 Series of iron (III) chloride concentrations used in this work and their related hematite morphologies. ....	147
Table 5.2 Experimental conditions and statistics on akaganeite ( $\beta$ -FeOOH) crystals reported in this work. ....	152

# 1 PRELIMINARY DISCUSSION

## 1.1 Research Background

My interdisciplinary approach to research is a direct consequence of my development as a lifelong investigator in the fields of materials chemistry and ceramic engineering. Beginning as an apprentice to a ceramic artist, I was introduced to the concepts of inorganic chemistry and mineralogy while formulating glazes and clays; while building and firing kilns I was introduced to the frameworks of ceramic engineering and thermodynamics. Driven by my desire for a more quantitative understanding of these processes, I chose to pursue my undergraduate degree in Chemistry at Mount Holyoke College because it would allow me to develop a foundation for scientific research and prepare me for further study in engineering.

The choice to pursue my PhD in Materials Science and Engineering at Cornell University came with dual impetus related to the synthesis and characterization of materials for sustainable energy technologies. Building on my Chemistry training in the synthesis of organic-inorganic hybrid materials,<sup>1</sup> and my Ceramic Engineering experience using crystal lattice complexity as a means to decouple thermal and electrical transport,<sup>2,3</sup> I set out to refine my synthesis skills in materials chemistry, specifically working on the crystallization of transition metal oxides. In characterization, I sought to become adept at analyzing nanostructured materials. I chose to target my growth in these two areas because I wanted to develop a deep understanding of how to control the properties (e.g., thermal and electrical) of semiconducting transition metal oxides by controlling the structures and compositions of these materials across length scales.

For me, joining the Estroff Research Group seemed like an odd match to my educational and research background: they were a biomineralization group that was focused on biomimetic crystallization for biological applications and I was interested in transition metal oxides for sustainable energy technologies and had never taken a biology class. However, from my first exposure to biominerals, I

observed that biologically-mineralized structures have hierarchical porosity and second phase occlusions that are on the dimensions of phonon and electron mean free paths. With this perspective and my self-directed nature, I was able to develop a whole new direction in the Estroff Research Group based on a set of projects that I designed with a focus on bio-inspired crystallization of transition metal oxide compounds for sustainable energy applications.

## **1.2 Dissertation Introduction**

Biological organisms present multiple examples of hierarchical structures that are optimized for a given function. In particular, biomineralized materials: (i) display crystallographic control across length scales; (ii) are often organic-inorganic composites due to the occlusion of components from the associated organic growth matrix; (iii) and exhibit tailored mechanical properties that are unique to their function.<sup>4</sup> Of great importance to the development of advanced energy materials is the observation that biomineral architectures are built from crystallographically-defined structural elements with interfaces that span multiple length scales. Notably, these structures contain elements that correspond to electron and phonon mean free paths, providing a model structure for optimizing materials properties.

Synthetically, many biomineral structures are formed in association with an extracellular matrix, which is a hydrated, porous network based on biopolymer constituents. The key feature of these growth matrices is that they establish diffusion-limited transport of reagents which is supported by the porosity of the matrix as well as pendant chemical functionality in these networks. The diffusion-limited growth environment provides a means to control the assembly of interfaces throughout the crystalline, hierarchical structures, both structurally and compositionally. With this level of control, long-range crystallographic registry can be maintained on length scales that exceed the nanoscale interfaces that result from dislocations and occluded precipitates.

The translation of such matrix-mediated growth strategies to the design of advanced energy materials is hindered the low stability of biopolymer matrices at the hydrothermal temperatures needed to

drive crystallization of the target inorganic phases. In an effort to mitigate this challenge, researchers have first crystallized the corresponding carbonate phase in the porous networks at ambient temperature and then accessed the oxide via thermally-induced topotactic transformation.<sup>5</sup> While this approach is able to achieve hierarchically-structured transition metal oxide materials, it requires energy-intensive heating post-crystallization, which affects the interfaces within the materials. At such high temperatures, occluded components from the growth environment can be destroyed, and the occurrence of sintering can change the crystallographic interfaces.

This dissertation was designed around my hypothesis that the use of inorganic hydrogels would support the design of thermally-stable growth matrices, which would allow me to crystallize transition metal oxide phases directly within the hydrogels. With the ability to hierarchically structure transition metal oxide materials via growth under diffusion-limited conditions and the opportunity to occlude the growth networks into the target crystal, I would achieve an unprecedented level of control over the structure of materials. With architectures that contain hierarchical-structuring from the atomic to the nano and microscales the ability to tailor materials properties would become possible.

### **1.3 Dissertation Overview**

This dissertation was designed to serve the broad goal of translating biological mineralization strategies from the structural carbonates and phosphates to the semiconducting transition metal oxides. The body of this dissertation contains 4 main chapters (2-5) and builds logically and sequentially from biological mineralization models to biomimetic crystallization strategies to develop an entirely new bio-inspired approach for the development and characterization of transition metal oxides. The key questions and hypotheses investigated in the 4 main chapters are summarized in the following paragraphs.

Chapter 2 is predominantly a review article that takes an exhaustive literature study of the biominerals themselves, and builds to cover biomimetic crystallization reports with a focus on calcium carbonate. The key outcomes of this study stemmed from the establishment of a general framework for

biological crystallization: that biological organisms exhibit control over both the physical and chemical aspects of the crystallization microenvironment when forming their hierarchically-structured, nano-composite products. The crystallization environment is largely controlled by the extracellular matrix, which can be synthetically modeled as a hydrogel. This use of a hydrogel, as both a physical and chemical aspect of the growth environment and a means to control the architectures of mineral products, formed the basis for the experiments in the three chapters that follow (3-5).

In Chapter 3, the work of translating bio-inspired, matrix-mediated crystallization to transition metal oxides was undertaken using hematite as a model transition metal oxide system. Before delving into the crystallization of hematite in a hydrogel, a thorough characterization of hematite grown from aqueous solution under mild hydrothermal was performed. While the chemistry for the crystallization of hematite from aqueous solution at mild hydrothermal temperatures is fairly straightforward, the crystals that form have complex, hierarchical structures with crystallographic registry that propagates far beyond the nano-sized coherent domains. Up until this point, the characterization of such forms was limited. In the characterization community, it was understood that forming electron transparent thin sections from micron-sized crystals came with a cost: loss of spatial information about the geometrical location from which the thin section originated. Such limitations left a huge disconnect between nano and microscale characterization. This gap posed a major challenge for me as I needed to quantitatively assign the net lattice orientations that propagate throughout hierarchically-structured forms. To overcome this limitation, I developed a new sample preparation technique and quantitative analysis methods to fully interrogate the crystallographic relationships within complex architectures. Using focused-ion beam milling I was able to form electron transparent thin sections from precisely identified locations within microscale forms. Using extensive transmission electron diffraction analysis, I was able to quantitatively identify the nanoscale mosaic structure (mosaicity) within these crystals and report information about the interfaces between the nano-scale domains. With a means to unravel the lattice relationships, nanoscale

domain structure, and microscale habit of hierarchical architectures, the growth of hematite in a hydrogel could be addressed.

Armed with a clear understanding of how hydrogels can serve as a model of the extracellular matrix established in Chapter 2, and the ability to unravel crystallographic relationships within hierarchically-structured forms in Chapter 3, the hydrogel-based growth of hematite could be pursued in Chapter 4. The key to this work was to identify a hydrogel matrix that was chemically-compatible and thermally-stable with hematite synthesis conditions. Moving to an inorganic silica hydrogel, I was able to achieve the crystallization of a transition metal oxide (hematite) directly within the hydrogel. This accomplishment is a landmark development in the synthesis of materials: previous reports had accessed the oxide phase via thermal treatment of carbonates that were grown in biopolymer hydrogels. Unravelling the structural modifications to hematite that were caused by growth in a hydrogel, required that we recalibrate our entire understanding of hydrogel growth. That a ‘chemically-inert’ matrix could play a chemical role in the crystallization microenvironment was not immediately obvious, but presented a new variable that is a result of hydrogel growth of oxides at elevated temperatures and non-neutral pH. By combining inductively coupled plasma atomic emission spectroscopy with Rietveld refinements to x-ray diffraction data, the chemical role of silica was identified as an atomic scale dopant within the hematite lattice. These findings came in stark contrast to previous works on crystallization in hydrogels in which the hydrogel was incorporated as a second phase.<sup>6</sup> The combined results of these analyses showed that silicon from the growth environment had consistently modified the architecture of hematite, leading to microscale structures with surfaces composed of nanoscale, high catalytic activity {110} facets. With hydrogel growth as a demonstrated route to tune the hierarchical structure of a transition metal oxide to preferentially express desired planes, the bandgap and photocatalytic activity of the samples was studied, to reveal that these micro-scale hierarchical architectures outperform their nano-sized counterparts, presenting a new approach to the design of materials for advanced energy applications.

Crystallization of target oxide phases from aqueous solutions is often complicated by the existence of intermediate oxyhydroxide phases. In the case of hematite, the intermediate oxyhydroxide phase ( $\beta$ -FeOOH) serves as a template for the nucleation of the oxide phase, thereby playing a role in defining the final structure. Chapter 5 is an investigation of the physical role of akaganeite ( $\beta$ -FeOOH) as a template to the crystallization of hematite. This research was designed to investigate the hypothesis that the structural form of hematite would carry with it a signature from the structure of the intermediate phase, akaganeite. By investigating the formation of akaganeite from aqueous solution and within silica hydrogel, an understanding of the physical effect of the hydrogel and the chemical effect of pH and reagent concentration on the structure of akaganeite and the resulting hematite was established. Largely, the role of akaganeite as a (physical) structure-directing template for hematite nucleation and growth is investigated. This body of work pulls together all the physical variables of crystallization of oxides within hydrogels and pairs them with the chemical variables to provide a clear map to the structural and compositional design of transition metal oxides using bio-inspired crystallization in hydrogels.

#### **1.4 Preface**

All of the work presented henceforth was conducted at Cornell University in the Department of Materials Science and Engineering, Department of Chemistry and Chemical Biology and the CCMR Shared Facilities (a Materials Research Science and Engineering Center of the NSF (DMR 1120296)). All projects were screened by the Cornell University *Institutional Review Board* and determined to not require review.

A version of Chapter 2 has been published in *Advanced Functional Materials* (Asenath-Smith, E.; Li, H.; Keene, E. C.; Seh, Z. W.; Estroff, L. A., *Adv. Funct. Mater.* **2012**, 22, 2891-2914.). In this work, I was the lead investigator for the exhaustive literature review section and I contributed experimental design and characterization of the hydrogels. HYL was the lead researcher who designed the

crystallization experiments that are reported in the article. Additional experimental contributions were made by ZWS and ECK.

A version of Chapter 3 has been published in *Microscopy and Microanalysis* (Asenath-Smith, E.; Estroff, L. A., *Microsc. Microanal.* **2014**, 20, 635.). For this report, I conducted all the experiments, electron microscopy and data analysis.

A version of Chapter 4 is published in the *Journal of the American Chemical Society* (Asenath-Smith, E.; Hovden, R.; Kourkoutis, L. F.; Estroff, L. A., *J. Amer. Chem. Soc.* **2015**, DOI: 10.1021/jacs.5b01697.). In this study, I performed all the crystallization experiments, and properties measurements, including the design of photocatalysis experiments. I also performed all the electron microscopy sample preparation and TEM characterization and analysis. RH contributed STEM imaging and EELS analysis. ICP analysis was performed by the Cornell Nutrient Analysis Laboratory. BET analysis was performed by the Wiesner Research Group in Materials Science and Engineering at Cornell University.

A version of Chapter 5 is in submission to *Crystal Growth and Design*. The experiments and characterization reported in this paper were entirely carried out by me, including all the crystallization experiments as well as the electron microscopy imaging and analysis.

## REFERENCES

- 1 Asenath-Smith, E. & Chen, W. How to prevent the loss of surface functionality derived from aminosilanes. *Langmuir* **24**, 12405-12409, (2008).
- 2 Asenath-Smith, E., Misture, S. T. & Edwards, D. D. Structural behavior and thermoelectric properties of the brownmillerite system  $\text{Ca}_2(\text{Zn}_x\text{Fe}_{2-x})\text{O}_5$ . *Journal of Solid State Chemistry* **184**, 2167-2177, (2011).
- 3 Asenath-Smith, E., Lokuhewa, I. N., Misture, S. T. & Edwards, D. D. P-type thermoelectric properties of the oxygen-deficient perovskite  $\text{Ca}_2\text{Fe}_2\text{O}_5$  in the brownmillerite structure. *Journal of Solid State Chemistry* **183**, 1670-1677, (2010).
- 4 Wegst, U. G. K., Bai, H., Saiz, E., Tomsia, A. P. & Ritchie, R. O. Bioinspired structural materials. *Nature Materials* **14**, 23-36, (2015).
- 5 Dang, F. *et al.* Synthesis of Li-Mn-O mesocrystals with controlled crystal phases through topotactic transformation of  $\text{MnCO}_3$ . *Nanoscale* **5**, 2352-2357, (2013).
- 6 Li, H. Y., Xin, H. L., Muller, D. A. & Estroff, L. A. Visualizing the 3d internal structure of calcite single crystals grown in agarose hydrogels. *Science* **326**, 1244-1247, (2009).

## 2 CRYSTAL GROWTH OF CALCIUM CARBONATE IN HYDROGELS AS A MODEL OF BIOMINERALIZATION<sup>♦</sup>

### 2.1 Abstract

In recent years, the prevalence of hydrogel-like organic matrices in biomineralization has gained attention as a route to synthesizing a diverse range of crystalline structures. In this article, we discuss examples of hydrogels in biological, as well as synthetic, bio-inspired systems. Particular attention is given to understanding the physical versus chemical effects of a broad range of hydrogel matrices and their role in directing polymorph selectivity and morphological control in the calcium carbonate system. Finally, recent data regarding hydrogel-matrix incorporation into the growing crystals is discussed and a mechanism for the formation of these single-crystal composite materials is presented.

### 2.2 Introduction

Historically, the use of gel matrices for single crystal growth has been employed as a means to control the purity, morphology, and optical quality of the resulting crystals.<sup>1,2</sup> More recently, crystal growth in gels has emerged as a popular platform for modeling biomineralization processes.<sup>3-9</sup> This interest is motivated by the increasing number of gel-like matrices identified in association with mineralization by biological organisms (Table 2.1).

In matrix-mediated biomineralization, the mineralization environment is characterized by the presence of an extracellular matrix, which is a three-dimensional macromolecular assembly of proteins, polysaccharides and/or glycoproteins that mediates mineral formation.<sup>10,11</sup> These matrices are often fibrous, porous, and hydrated networks that both provide the structural framework upon which inorganic minerals grow and serve as a source of chemical functionalities, to direct nucleation and growth of the

---

<sup>♦</sup>Portions reproduced with permission from E. Asenath-Smith, H. Li, E. C. Keene, Z. W. Seh, & L. A. Estroff, *Adv. Funct. Mater.* **2012**, 22, 2891-2914. Copyright © 2012 WILEY-VCH.

crystals.<sup>12-14</sup> Often these organic matrix constituents are intimately associated with the inorganic crystals, and are sometimes even incorporated into the single crystals, thereby forming composite materials with unique optical, mechanical, or structural properties.<sup>15-17</sup>

**Table 2.1** Biomineralization systems with gel-like organic matrices

<b>Biogenic system</b>	<b>Mineral</b>	<b>Gel-like matrix components</b>	<b>Water-soluble matrix components</b>	<b>References</b>
Nacre, Mollusk Shell	Aragonite	Silk fibroin-like hydrogel	Acidic proteins	18-20
Coral	Aragonite	Fibrillar, non-collagenous proteins	Acidic (sulfonated) glycoproteins	21-27
Otoconia	Calcite	Short-chain meshwork-forming collagens (e.g., Otolin-1)	glycoproteins Otoconins	28-32
Otoliths	Aragonite, Vaterite, Calcite	Short-chain meshwork-forming collagens (e.g., Otolin-1)	OMP-1	33-41
Barnacles	Calcite	$\alpha$ -chitin and other unidentified protein(s)	Acidic proteins	42
Enamel	Carbonated apatite	Amelogenin	Glycoproteins (e.g., enamelin)	43-46
Bone	Carbonated apatite	Fibrillar collagen	Acidic glycoproteins Gla proteins Proteoglycans	47-50
Chiton/limpet teeth	Hydrous and non-hydrous iron oxides	$\alpha$ -chitin and other unidentified protein(s)	Not yet well-defined	51-53

The repeated theme of biomineralization in gel-like organic matrices provides new opportunities for the classical approaches to crystal growth in gels. What was once seen as a means to obtain large

crystals of high purity is now being employed as a method to both answer questions from biology as well as to create new composite materials with “designer” properties. For example, gel-based systems may help elucidate the origins of biological control over polymorph selection,<sup>54,55</sup> crystal orientation,<sup>43</sup> morphology,<sup>29,56</sup> and matrix incorporation.<sup>29,57</sup> Synthetically, crystal growth in gels can provide routes to achieve the controlled introduction of nanoscale inclusions to single crystals,<sup>58</sup> to access non-classical mesocrystal structures,<sup>59,60</sup> and obtain diverse morphologies.<sup>61,62</sup>

This article highlights both the biological motivations for crystal growth in gels as well as recent innovations in the application of synthetic gel-based systems for controlling crystallization. The examples presented here showcase the insights gel-growth can provide regarding the structure and formation of biominerals, including the role of the water-insoluble matrix, the role of chemical modification of the matrix, and the mechanisms by which the organic-matrix can become incorporated into the crystals during growth. These bio-inspired, synthetic approaches hold the potential to yield whole new classes of composite materials such as polymer-reinforced single crystals and hierarchical architectures.

### **2.3 Background**

Crystal growth in gels is a modification of crystal growth in solution and has been used as a crystal growth technique for more than one century.<sup>1,2</sup> The unique aspects of crystal growth in gels derive from the compartmentalization of the solution into small cavities within the three-dimensional porous gel network. This solute confinement has implications for nucleation and growth mechanisms as well as the morphology of the resulting crystals. In the following sections, we introduce the chemical and structural features of several types of gels commonly used for crystal growth as well as provide a brief overview of classical crystal growth mechanisms. Subsequently, nucleation and growth considerations will be discussed in the context of gel systems, followed by an overview of experimental techniques for crystal growth in gels.

### 2.3.1 Common Hydrogels Used for Crystal Growth

A gel is defined as a two-component (solid and liquid), continuous, solid-like material with viscoelastic rheological properties.<sup>63,64</sup> Put more simply, a solution is considered to be a gel when it no longer flows and can support its own weight (e.g., the inverted test-tube test). From a broad perspective, gels can be classified according to the type of bonding within the network. Of the four gel types proposed by Flory,<sup>65</sup> only the two most relevant to biomineralization will be formally discussed: physical gels and chemical gels. In physical gels, the network is primarily formed through physical entanglement and non-covalent intermolecular forces. The network in chemical gels is formed via covalent bonds, which can be formed by reactions such as free-radical polymerization by UV light or chemical initiators. Gel networks are often classified as cellular or fibrous, or a mixture of both depending on the network characteristics (Figure 2.1).

Characterization of gel structures is inherently difficult because of the low polymer/organic content and high solvent content. Most sample preparations introduce drying artifacts, thereby producing an image that may not be a completely accurate representation of gel conditions present during crystal growth.<sup>66-70</sup> For example, drying techniques can cause the gel structure to collapse and freezing techniques can introduce ice crystals, which may cause structural distortion of the gel network.<sup>71</sup> Additionally, the recipe (especially the solution) to prepare gel samples for structure characterization is usually different from that used for crystal growth. As discussed below, this difference often results in structural changes to the gel network. Finally, gels are not equilibrium structures and most likely there is structural evolution that occurs over timescales similar to those used for crystallization experiments.<sup>72,73</sup> While entire books and reviews have been written about gels and gelators,<sup>64,74-78</sup> here we highlight the chemistry and structure of several gels that are commonly used to study biomineralization.

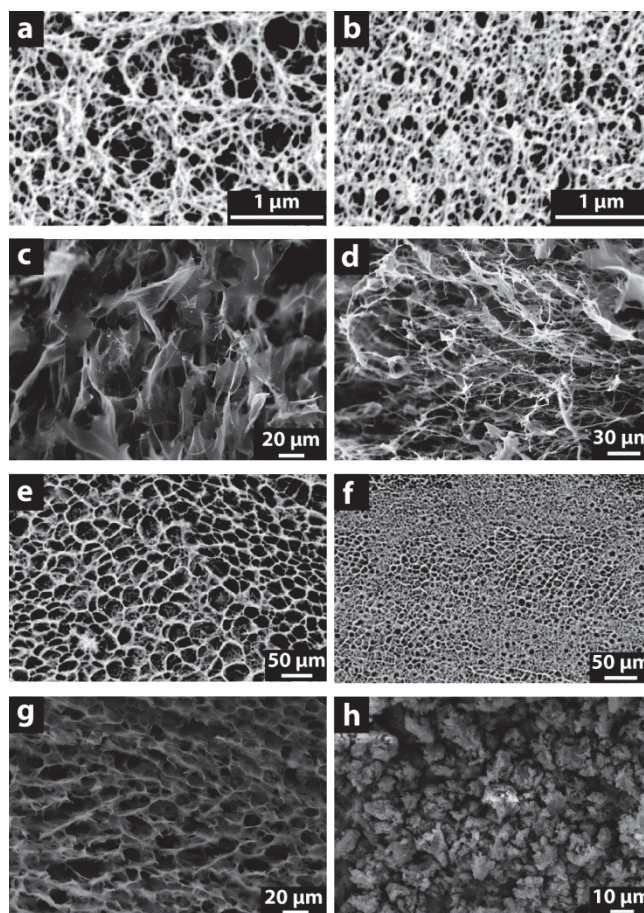


Figure 2.1. An assortment of gel microstructures imaged by scanning electron microscopy that illustrate the wide range of microstructures available in hydrogels as well as the factors that further influence those microstructures. Critical point dried agarose gels showing the dependence of microstructure on concentration: (a) 0.5 wt%; (b) 2 wt%.<sup>79</sup> Freeze-dried silk fibroin hydrogels showing the dependence of microstructure on purification method: (c) purified with Marseilles soap; (d) purified with sodium carbonate. Freeze-dried polyacrylamide hydrogel microstructure showing the effect of gel concentration on the microstructure: (e) 5 wt%, (f) 10 wt% polyacrylamide gel.<sup>80</sup> Freeze-dried silica hydrogels showing the dependence of microstructure pH: (g) pH ~9 cellular microstructure; (h) pH ~2 particulate microstructure. a, b, Adapted with permission from ref 51 copyright 2006 American Chemical Society. e, f adapted with permission from ref 64 copyright 2008 Elsevier

### 2.3.2 Hydrogels with Physical Bonding

Physical gels are the most commonly encountered class of hydrogels in biomineralization systems. They are often composed of biopolymers of polysaccharides such as agarose, pectin and cellulose, as well as proteins such as collagen, gelatin and silk fibroin.<sup>64</sup> The network in physical gels is formed through physical interactions, including, but not limited to, hydrogen-bonds, hydrophobic, or Coulombic forces, among biopolymer chains.<sup>81</sup> Secondary structural features of biopolymers can further influence the structure of the network formed in physical gels. Gelation of physical gels can be achieved by temperature as well as solvent or pH changes, with the potential for reversibility.<sup>65</sup> The physical nature of the bonding interactions in these gels can vary with temperature and time, imparting some dynamic character to the structure of these networks.

#### 2.3.2.1 Agarose

Agarose is a neutral polysaccharide that is derived from red algae.<sup>82</sup> The molecular structure of agarose is a neutral, linear polysaccharide consisting of alternating 1,3-linked  $\beta$ -D-galactopyranose and 1,4-linked 3,6-anhydro- $\alpha$ -L-galactopyranose units,<sup>83</sup> and consequently is regarded as a relatively inert medium for crystal growth. Agarose powder is soluble in hot water and the warm solution gels on cooling to  $\sim 40$  °C. Agarose gels melt at  $\sim 85$  °C, noticeably higher than the gelling temperature. During the process of gelation, polymer chains form helices (double or single helix) that subsequently aggregate into three-dimensional (3D) bundles, forming a porous network with fibrous characteristics (Figure 2.1a,b).<sup>84,85</sup> Both the gelling and melting temperatures can be tailored by chemical modification such as partial hydroxyethylation.<sup>86</sup> The mechanical behavior of agarose gels is sensitive to molecular weight and concentration<sup>87</sup> as well as chemical modification.

The pore sizes within agarose gels have been found to depend on a number of factors. First, pore sizes depend on the concentration of agarose used (Figure 1a,b). For example, when gel concentration increased from 0.5 wt% to 5 wt%, pore sizes were observed by SEM to decrease from 180 nm to 55 nm.<sup>71,79,88</sup> Secondly, the pore sizes within agarose networks depend on the solvent used. For example, gels

prepared with aqueous Tris-borate buffer have larger pore sizes than those gels made in deionized water.<sup>67</sup> Further, the diameter of agarose fibers can vary from 3-30 nm depending on experimental conditions.<sup>67,89,90</sup>

#### 2.3.2.2 Silk Fibroin

Silk fibroin is the structural component of silk fibers, and is composed of disulfide-linked polypeptides, which exist in anti-parallel  $\beta$ -sheets and are predominantly composed of the amino acids glycine, alanine, and serine.<sup>91</sup> In the formation of a hydrogel, silk fibroin undergoes gelation through hydrophobic and hydrogen-bonding interactions, forming a network with mixed fibrous and cellular character (Figure 2.1c,d). Gelation times are found to decrease with increasing silk fibroin concentration, increasing temperature, and decreasing pH.<sup>91,92</sup> Further, the secondary structure is found to vary from random coil to  $\beta$ -sheet with changes in pH and ionic concentration, thereby influencing the structure of the hydrogel network; the hydrophobic regions in random coil silk fibroin assemble in aqueous solutions via hydrophobic interactions and organize into  $\beta$ -sheets, physically cross-linking the hydrogels.<sup>93</sup> Pore sizes in silk fibroin hydrogels decrease with increasing silk fibroin concentration as well as temperature, showing  $\sim 1 \mu\text{m}$  pore sizes in a freeze-dried 4 wt% silk fibroin hydrogel.<sup>91</sup> Gelation rates and the mechanical properties of the resulting gels are also strongly dependent on the purification method used to obtain the silk fibroin (Figure 2.1c,d).<sup>94</sup>

#### 2.3.2.3 Gelatin

Gelatin is derived from the partial hydrolysis of collagen, which contains  $\sim 30\%$  glycine,  $\sim 15\%$  of each proline and hydroxyproline,  $\sim 4\%$  lysine and  $\sim 8\%$  arginine, and aspartic and glutamic acids each present at 7-10%.<sup>77,95,96</sup> More simply put, gelatin contains both acidic and basic amino acids, causing the isoelectric point of gelatin to depend on the preparation/extraction conditions. Acid-based protocols result in gelatins (Type A) with isoelectric points in the basic range (pH  $\sim 9$ ), while alkaline-based protocols result in gelatins (Type B) with acidic isoelectric points (pH  $\sim 5$ ).<sup>77</sup> Similar to other physical

hydrogel systems, gelation in gelatin proceeds thermally, occurring at ~30 °C. In addition, gelatin can be chemically crosslinked through carboxylic acid groups, to increase thermal stability and change the mechanical properties of the gel.<sup>76,97</sup> Gelatin forms cellular networks, with cavities on the order of tens of microns, which are defined by non-porous walls.<sup>72</sup>

### **2.3.3 Hydrogels with Chemically-Bonded Networks**

Chemical gels, also appropriately referred to as polymer or synthetic gels, are generally non-biological in origin. In this category of gels, the 3-D network structure is formed through covalent crosslinks between structural units of the polymer chains. These reactions proceed by UV-initiated copolymerization in the case of polyacrylamide and acid- or base-catalyzed condensation in the case of silica. Generally, gelation is not reversible in chemical gels.

#### **2.3.3.1 Polyacrylamide**

Formation of polyacrylamide (PAA) proceeds by radical copolymerization of acrylamide and N,N'-methylenebis(acrylamide), forming a covalently crosslinked hydrogel with potentially variable crosslink densities. Gelation times are affected by the crosslink density,<sup>98</sup> as are the cellular characteristics of the network.<sup>66,99</sup> The wall thicknesses of the cellular network in PAA hydrogels are found to increase with increasing PAA concentration in the gelling solution.<sup>70</sup> Pore sizes within the cellular network depend on the concentration of the gelating compound, showing a decrease from 150-30 nm with an increase in polymer concentration from 5-10 wt% (Figure 2.1e,f).<sup>80</sup> Further, the pore size distribution can be broad, causing a range in the polymer density within the gel medium.<sup>100</sup>

#### **2.3.3.2 Silica Gels**

Silica gels are traditionally the most widely used gels for crystal growth. While silica gels can be formed from the acidification of both alkoxyorthosilicates and sodium metasilicate, the latter will be emphasized in the following discussion. Silica hydrogel formation in sodium metasilicate systems

proceeds by three distinct steps: (i) dissolution of  $\text{Na}_2\text{SiO}_3$  in water to form silicic acid ( $\text{Si}(\text{OH})_4$ ) and sodium hydroxide (Equation 1);



(ii) acid-catalyzed polymerization of silicic acid by condensation to form 3-D clusters; and (iii) percolation to form a 3-D gel network. Through these processes, the network structure in silica hydrogels is established predominantly through covalent interactions<sup>2,64</sup> to form a basic hydrogel composed of cellular networks with porous walls (Figure 2.1g). The thickness and porosity of the cell walls depends on the concentration (density) of silicate species used in the gel.<sup>72</sup> The gelation time varies with silicate reactant concentration,<sup>101</sup> pH,<sup>102</sup> temperature,<sup>103</sup> and the identity of the acid catalyst<sup>104</sup> and affects the final structure of the hydrogel network. For example, acidification with stronger acid results in longer gelation times, forming acidic gels that are composed of networks with particulate character (Figure 2.1h).

### 2.3.4 Mixed Bonding Character and Solvent Structure in Hydrogel Networks

The broad categories of physical and chemical hydrogels discussed above do not always strictly apply. For example, gelatin networks can contain a combination of physical and chemical crosslinks depending on preparation conditions. Further, linking between silica clusters during percolation may be physical and/or covalent in nature, thereby imparting some physical characteristics to the structure.<sup>105,106</sup> Moreover, since gelation is a dynamic event, the network structure can continue to evolve even after the onset of the generally accepted “gel point”: when the gel resists pouring. For example, physical gels evolve with temperature and time as discussed above, and condensation in chemical gels, such as silica, is also temperature and time dependent.<sup>2</sup> As such, all of these factors require attention when preparing and characterizing hydrogels.

Lastly, for crystal growth in gels, it is important to consider the structure of solvent molecules, as they behave differently than their bulk counterparts when confined to the pores of a hydrogel network. In

gels, liquids are trapped within regions defined by the solid network. The interaction at the solid/liquid interface changes the structure of liquids nearby the interfaces.<sup>107,108</sup> For example, water in hydrogels has been studied<sup>109-114</sup> and found to exhibit three distinct structures: bound water, free water, and intermediate water.<sup>115-117</sup> The bound water interacts strongly with the solid network and has aggregation structures that are different from the bulk water. Free water behaves most similarly to bulk water. The intermediate water interacts weakly with the solid network and is in a state that is not bound or free, but structured.<sup>70</sup> Of importance for crystallization studies in gels, these differences in solvent structure will lead to changes in the activities of solutes thereby affecting both the relative supersaturation and the diffusion rates of solutes within the gel media.

## 2.4 Crystal Morphology and Crystal Growth Mechanisms

Before discussing crystal growth in hydrogel media, it is important to review, briefly, traditional crystal growth mechanisms and their role in defining crystal morphology. Over a century of study on crystal growth has identified several critical relationships among the thermodynamic and kinetic constraints on growth dynamics and the corresponding morphologies of the crystals.<sup>118-120</sup> In crystal growth from solution, as opposed to growth from a melt, the basic thermodynamic driving force is manifest in the supersaturation.<sup>118</sup> The supersaturation ( $\sigma$ ) is directly related to the solubility product ( $K_{sp}$ ) and the activity product (AP) of the ionic species (Equation 2).

$$\sigma = \ln \left( \frac{AP}{K_{sp}} \right) \quad \text{Equation 2}$$

As a function of the driving force and the crystallization kinetics, several key crystal growth regimes have been identified.<sup>12,121,122</sup> Near-equilibrium growth occurs at low supersaturation via addition to step edges formed by screw dislocations (spiral growth). Crystals formed in this regime have well-defined facets and smooth surface features, displaying equilibrium polyhedral morphologies. At slightly higher driving forces (supersaturation), layer-by-layer growth occurs via addition to step edges formed by

the nucleation of 2-D islands. Hopper or skeletal morphologies, can be observed in this regime, and are characterized by concavities on the faces resulting from the increased rate of nucleation at the corners of the growing crystal. As the supersaturation is increased further, growth proceeds by the nucleation of 3-D units on the surface, leading to fractal, dendritic morphologies. Finally, at the highest supersaturation, the critical nuclei radius can be smaller than a unit cell, and continuous, adhesive growth occurs, leading to aggregated, spherulitic morphologies with rough surfaces. Accordingly, crystal morphology can be used as an initial guide to unraveling the probable growth mechanisms that led to the final morphologies observed for crystals grown in different gels and under different conditions.

#### **2.4.1 Crystal Nucleation and Growth in Gels**

Crystal growth in gels has been widely used to prepare single-crystals of proteins for structural characterization,<sup>123-129</sup> to synthesize porous materials,<sup>79</sup> and to simulate crystallization in microgravity conditions.<sup>127</sup> Much of the early work on crystal growth in gels has been reviewed and collected in Henisch's book (1988)<sup>2</sup> and Lefauchaux and Robert's review (1994).<sup>1</sup> Herein, we focus on the development of crystal growth in gels as a model for biomineralization systems.

Similar to the organic matrices found in biomineralization systems, the local crystallization microenvironment in gel media is distinguished from that in solution by the confinement of solutes to within the pores of the gel network. Empirically, this microenvironment presents several advantages in crystal growth studies: Brownian motion, laminar flow and convective currents are suppressed, making diffusion the dominant mass transport mechanism available to solutes in gel media. Further, gel networks are capable of supporting the growing crystals, preventing sedimentation. Overall, these conditions present a means to obtain large, high quality crystals.

##### **2.4.1.1 Nucleation**

Detecting nucleation events within a gel is inherently difficult and complicates a quantification of the absolute supersaturation level present at nucleation. In addition, time-dependent gradients are formed

within the gel as reactants diffuse through the gel to the reaction front.<sup>130</sup> These additional (kinetic) complexities in the supersaturation are not addressed by classical nucleation theory.<sup>131,132</sup> Thus for nucleation in gels a *threshold supersaturation* is defined, which represents the supersaturation level present when nucleation can be visually observed in the gel.<sup>133</sup> Generally, within a diffusion-limited medium, there is a reduced probability that nuclei reach the critical size required for growth due to the diffusion-limited supply of reactants. Therefore, nucleation in gels takes place only when solutes accumulate to a fairly high threshold supersaturation and subsequently spontaneous nucleation is suppressed.<sup>133,134</sup> As a result, gels can be used to control the rate of nucleation to yield a smaller number of crystals with larger sizes than their solution-grown counterparts.<sup>135</sup>

To further complicate matters, the gel itself can affect the supersaturation threshold due to chemical functionality within the gel network, which can interact with solutes to suppress or enhance nucleation. If the gel fibers or “walls” themselves can act as heterogeneous nuclei, then the original picture changes and higher nucleation densities will be observed within the gels than in solution. For example, lead iodide and calcium tartrate have increased nucleation densities in gelatin, as compared to silica gels.<sup>72</sup> Other studies have demonstrated that nucleation rates of hen egg white lysozyme (HEWL) depend strongly on the type of gel used (e.g., silica versus agarose).<sup>105,136,137</sup> Further emphasizing the role of the gel, nucleation rates of other proteins in agarose gels have been found to depend on the agarose concentration.<sup>138</sup> Thus, the supersaturation threshold for a given species depends on more than just the type of gel in which the nucleation is taking place.

#### 2.4.1.2 Growth

The diffusion-limited conditions present in gels cause a modification to the crystal growth regimes and resulting morphologies discussed in Section 2.2. Whereas the morphology of solution-grown crystals is dictated by the driving force ( $\sigma$ ) alone, the morphology of gel-grown crystals represents a balance between the driving force and the diffusion rate(s) of ions to the reaction front.<sup>61,139</sup> Due to this

diffusive transport, concentration (and corresponding supersaturation) gradients are formed at the interface, introducing the potential for corners and edges of growing polyhedral crystals to experience higher supersaturation, and thus faster growth rates. This kinetic and thermodynamic balance is seen in crystals grown in gels under supersaturation conditions that favor 2-D growth mechanisms: hopper morphologies result from faster delivery of solutes to corners as opposed to faces.<sup>2,140</sup> Other experimental parameters such as temperature influence crystal growth in gels through the temperature dependence of diffusion coefficients and crystal solubilities. In general, diffusion coefficients increase by 2-3% per °C from a given value at 25 °C,<sup>141</sup> whereas the solubilities, and thus the supersaturation levels, may increase or decrease with temperature, depending on the system. Further, gel density can be an effective means to control growth rates in gel media, where increased gel concentration results in smaller pores and thus higher apparent supersaturation, increasing growth rates and affecting the observed morphologies.<sup>61</sup>

In addition to “generic” effects of gels on growth, specific (chemical) interactions between crystal-gel pairs have been suggested by many studies. For example, growth in agarose gels has been used to control the enantiomeric selectivity of sodium chlorate,<sup>142</sup> and the crystal morphology of multiple inorganic salts has also been shown to vary strongly as a function of gel type.<sup>4,143-146</sup> Finally, incorporation of the gel media into the growing crystals is known,<sup>58,123,147-149</sup> and may depend on both chemical and physical factors, as described further in Section 4.3. These studies and others demonstrate the wide range of crystal growth conditions that can be achieved in gel media and highlight that there is still much to be learned about crystal growth mechanisms in gels.

## **2.5 Crystallization Techniques for Growth in Gels**

Before describing the use of gels to model biomineralization, it is important to discuss some of the practical aspects of crystal growth in gels. As in solution crystallization, the key for gel growth is to trigger nucleation and then allow for slow, controlled growth of the crystal(s). For precipitation reactions involving two components (A and B), there are two typical methods for introducing A and B to the gel:

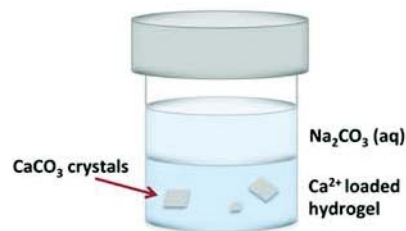
single and double diffusion geometries (Figure 2.2). In a single diffusion set-up, one component is embedded in the gel and the other one is introduced either via a solution layered on top of the gel (Figure 2.2a) or as a gas phase above the gel (Figure 2.2b). In this geometry, the crystals are usually found near the solution/gel or vapor/gel interface. Often a dense band of precipitate will be located at this interface, with larger, single crystals further down the gel column. When double diffusion is used, reservoirs containing solutions of the two reagents are physically separated on two sides of a gel column, in a U-tube or straight-tube configuration (Figure 2.2c), allowing diffusion of the two components into the gel from opposite ends. During the experiment, gradients of pH and concentration (supersaturation) that change with time develop along the length of the gel column, allowing access to a spectrum of conditions in one experimental set up. Generally, a band of crystals is observed to form near the center of the gel, but the exact location of crystallization depends on the gradients created along the length of the gel. Both single and double diffusion methods can be used to grow poorly soluble crystals, such as those of interest in modeling biomineralization, from two (or more) soluble reagents.<sup>2,150</sup> For all of these systems, it is essential to understand the underlying diffusion laws in order to predict when and where crystal growth will occur and how supersaturation gradients will evolve over the course of the reaction.<sup>151,152</sup>

For single-component crystals (e.g., proteins and small organics), or highly soluble salts, additional strategies are required to trigger the nucleation. For example, the single-diffusion geometry can be used to introduce a precipitant, such as a nonsolvent, either via solution or vapor phase.<sup>149,153</sup> Alternatively, crystallization can be induced by a change in a physical parameter, such as temperature.<sup>144</sup>

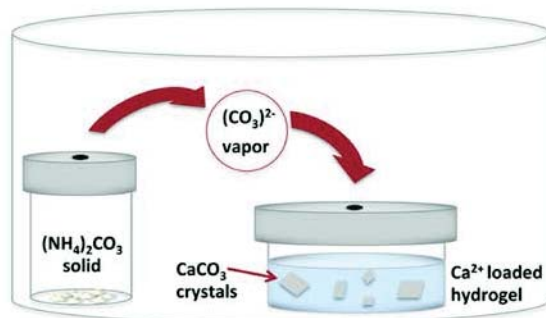
## **2.6 Biogenic Calcium Carbonate Systems that Mineralize in Gel-like Media**

Calcium carbonate, which exists as one of three polymorphs (calcite, aragonite, and vaterite), as well as an amorphous form, is the most common biomineral found in nature.<sup>48</sup> The matrix associated with calcium carbonate biominerals is often described as having a water-soluble and water-insoluble fraction. The water-insoluble components form the structural framework of the crystal growth environment, while

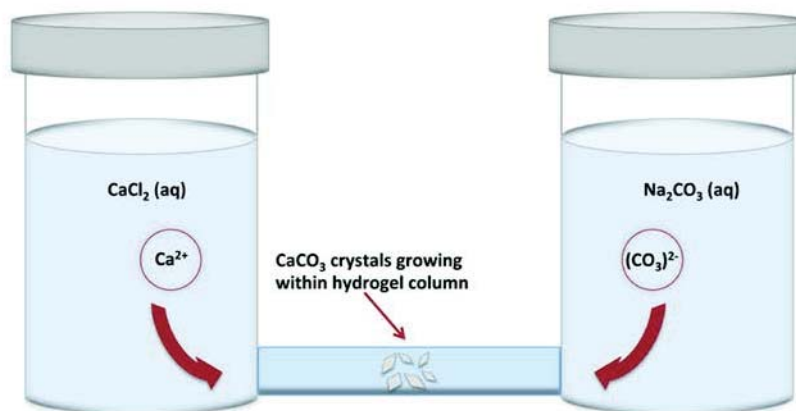
the water-soluble components impart chemical functionality, thereby affecting nucleation and growth.<sup>12</sup> The water-soluble components are predominantly acidic biomacromolecules, which may include carboxylated, sulfonated and/or phosphorylated glycoproteins and proteoglycans.<sup>14,154,155</sup> In the last 10 years, some of the protein- and polysaccharide-based components of the water-insoluble matrices have been identified as having a hydrogel-like character (Table 2.1). Here, we discuss several representative calcium carbonate systems that mineralize in gel-like matrices, however, mineralization in gel-like media has also been described for calcium phosphate systems. For example, enamel develops in a gel-like matrix of amelogenins,<sup>43</sup> and bone and dentin form in a fibrous, collagen-based matrix.<sup>47</sup>



**a. Single diffusion with solution phase reactant**



**b. Single diffusion with vapor phase reactant**



**c. Double diffusion with solution phase reactants**

Figure 2.2 Schematic representation of experimental approaches used in the growth of two component crystals hydrogels: (a) In the solution-based single diffusion set up, the solution phase reactant diffuses into the gel, where reaction and crystal growth takes place; (b) In the vapor phase single diffusion set up, the vapor phase reactant diffuses within the sealed atmosphere of a dessicator, and reaches the hydrogel through a small hole in the lid; (c) In the solution-based double diffusion system, aqueous solutions of either reactants diffuse into the gel, where they react and crystal growth takes place.

### 2.6.1 Nacre (Mother-of-Pearl)

Nacre, the inner layer of some mollusk shells, is a composite structure with ~500 nm thick single-crystal aragonite lamellae interspersed with ~30 nm thick layers of organic matrix.<sup>19</sup> The organic matrix amounts to 2-5 wt% of the dry shell. The aragonite tablets grow within a pre-formed organic matrix (Figure 2.3a) that is composed of water-soluble acidic proteins<sup>155</sup> and water-insoluble  $\beta$ -chitin fibers and a silk fibroin-like hydrogel.<sup>18,19,156</sup> Each of these matrix components has a role in controlling the crystal polymorph and orientation (nucleation), as well as morphology (growth), though none are thought to function in isolation and their assembly and interaction may be essential for correct regulation of crystal growth in vivo.<sup>19,157,158</sup> The crystallographic orientation of the aragonite platelets is related to the orientation of the  $\beta$ -chitin fibers and thus  $\beta$ -chitin is assigned a role in directing crystal orientation, while the acidic proteins decorate the chitin surface forming nucleation sites.<sup>19</sup> Additional acidic proteins are also occluded within the silk hydrogel, which are believed to control crystal polymorph and/or morphology. During mineral formation, acidic proteins are trapped within the aragonite crystals, while the hydrophobic hydrogel is pushed aside to regions between adjacent crystallites.<sup>19</sup>

In the organic matrix of *Atrina rigida*, a silk fibroin-like protein has been found to make up the largest weight fraction of the total protein content.<sup>19</sup> Based upon cryo-TEM and environmental SEM (ESEM) imaging of nacre, a gel-like phase has been identified.<sup>18,19,54</sup> In the ESEM images, as the pressure is reduced, a protein-based substance is seen "oozing" from between the aragonite tablets (Figure 2.3b). This proteinaceous gel-like material is hypothesized to be the silk-fibroin-like protein. Lending support to this hypothesis, silk fibroin proteins are known to form hydrogels in vitro (Figure 2.1c,d).<sup>91,92,94</sup> As a predominately hydrophobic constituent,<sup>96</sup> the silk fibroin-like gel in nacre has been suggested to inhibit calcite crystallization, thereby favoring growth of the less stable polymorph aragonite.<sup>19</sup> The gel could also serve as a "space-filler" that pre-fills the cavity into which the aragonite tablets grow. In this model, as the crystals grow, the gel itself is compressed and excluded to the crystal-crystal interfaces.<sup>54</sup>

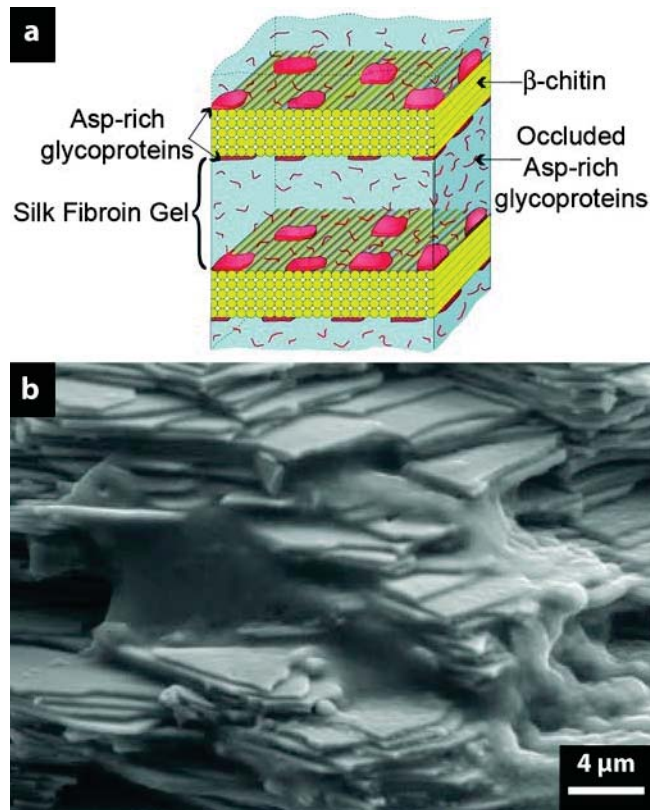


Figure 2.3 (a) Schematic of the demineralized organic matrix of *Atrina rigida*, a model matrix-mediated biomineralization system.<sup>18</sup> For further detail on the individual components see text. (b) Environmental scanning electron micrograph of nacre from *Atrina rigida* illustrating the gel-like organic matrix exuded from between aragonite tablets during drying.<sup>19</sup> a adapted with permission from ref 122 copyright 2001 Elsevier. b adapted with permission from ref 120 copyright 2006 Wiley.

Nacre serves as a classic biomineralization model, due to the demonstrated control over polymorph selectivity, crystal orientation, and mechanical properties. Further, the extensive chemical and structural characterization that has been reported in these systems has elucidated the role of matrix components in establishing the strict biological control seen during nacre formation. Many of the earliest in vitro studies on biomineralization were derived from nacre systems and it continues to serve as a model for in vitro studies, some of which are discussed in Section 2.7.1.

## 2.6.2 Coral

Both soft (octocorallia) and stony (scleractinia) corals have been found to mineralize in association with organic matrices.<sup>159</sup> From a structural perspective, coral architectures are composed of aragonite crystals embedded in an organic matrix, and additionally contain occluded organic material within the crystallites. While the aragonite crystallites are composed of nanocrystalline grains <100 nm, ordered aggregates >200 nm are found that appear as single crystals in diffraction studies<sup>160</sup> due to *c* axis alignment of the constituent crystallites.<sup>161</sup> Similar to other biomineralization systems, the organic matrices associated with corals can be distinguished in terms of water-soluble and water-insoluble components. The soluble portion contains as much as 30-50 mol% acidic proteins with a large fraction of sulfonated glycoproteins.<sup>22-24</sup> The insoluble components form a fibrous, porous network that is (in scleractinian, *Galaxea fascicularis*) composed of 26 nm fibrils.<sup>21</sup> In some species, the insoluble matrix components have collagenous character.<sup>162</sup> The characterization of these matrices as gel-like arises from observations of a fibrillar porous network associated with calcium in the scleractinian coral, *Galaxea fascicularis*,<sup>21</sup> as well as a visibly gelatinous mass that retains the shape of the soft coral *Isidella sp.* (bamboo coral) after decalcification (Figure 2.4a) and is seen to have a fibrillar porous network by TEM (Figure 2.4b).<sup>159</sup>

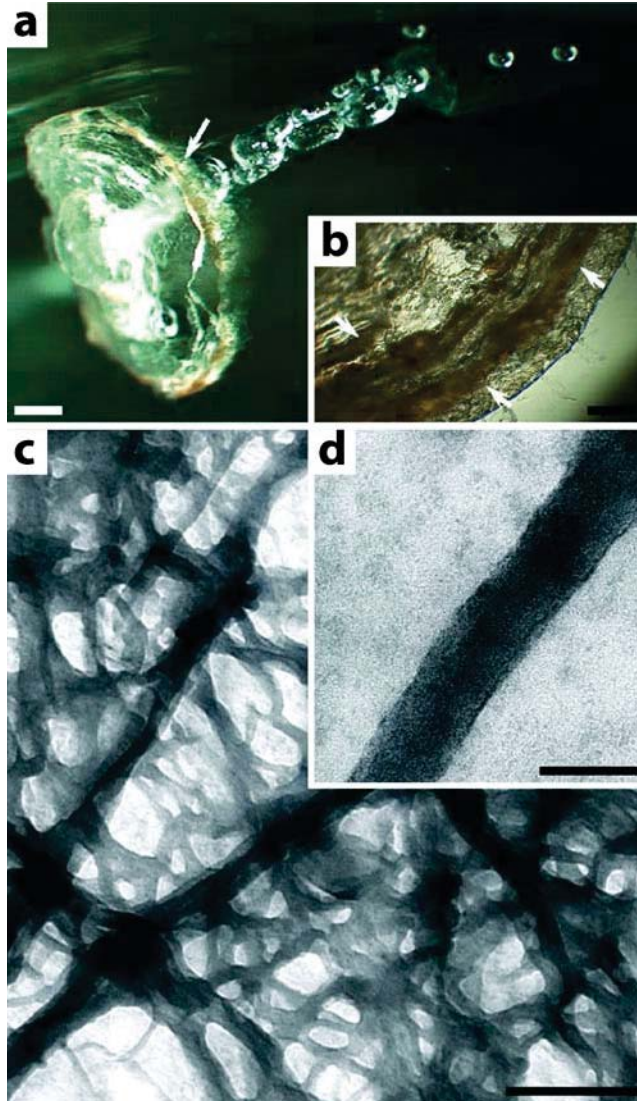


Figure 2.4 The non-collagenous, fibrillar, porous gel-like network associated with soft coral.<sup>25,159</sup> (a) optical image of demineralized matrix of *Isidella* sp., and (b) remaining gorgonin. (c) and (d) transmission electron microscopy image showing the fibrous network of the demineralized matrix show in (a). Adapted with Permission from ref 125 copyright 2009 Elsevier.

### 2.6.3 Otoconia

Crystals of calcium carbonate, located in the inner ear, form an integral component of the vestibular system of animals. In birds and mammals the calcite polymorph is found, while primarily aragonitic otoconia are found in amphibians and reptiles.<sup>35,39,163</sup> Across species, the glycoproteins

associated with calcite otoconia are similar to each other but different than those glycoproteins isolated from aragonite otoconia.<sup>30</sup> Calcitic otoconia are barrel-shaped with faceted tips, as seen in the central graphic in Figure 2.5 and are up to 30  $\mu\text{m}$  long in humans.<sup>28,164,165</sup> When these *single-crystals* are etched, the interior is seen to contain a dense network of fibers, suggesting occlusions of the organic matrix during crystal growth. Further, these small crystals are associated with distinct fibrous, organic networks (Figure 2.5a-d), wherein multiple otoconia are anchored to an organic matrix, known as the otoconial membrane, forming a viscoelastic mass that can transmit displacements resulting from linear acceleration.<sup>28,29</sup> The soluble matrix components are glycoproteins, known as otoconins, which comprise >90% of the total soluble organic content.<sup>30</sup> The characterization of the insoluble matrix components as gel-like stems from the fibrous, porous network structures (Figure 2.5a-d) as well as their viscoelastic properties. These insoluble components are found to be short chain, meshwork-forming collagens, known as otolins, which also comprise the insoluble components of otolith matrices (Section 0).<sup>166</sup>

#### 2.6.4 Otoliths

Similar to the otoconia discussed in Section 3.3, teleost fish detect linear acceleration and gravity as well as receive sound signals through *polycrystalline* aggregates of calcium carbonate, known as otoliths (Figure 2.6a). While multiple otoconia are assembled in a collective mass, only three single otolith pairs occur in fish, each in a separate region of the inner ear. Otoliths are composed of aragonite and vaterite polymorphs, each with different associated (soluble) acidic macromolecules.<sup>34</sup> In contrast to the fibrillar collagen found in bone (and associated with nanocrystals of hydroxyapatite), the insoluble components of the otolithic membrane include a short-chain meshwork-forming collagen, known as otolin-1.<sup>33,38,167</sup> Similar to otoconia, otoliths are anchored to this insoluble organic membrane, which has a gel-like layer that is present both during otolithic nuclei formation and within mature otoliths (Figure 2.6b).<sup>38</sup> Otolith growth proceeds by alternating deposition of mineral and matrix,<sup>40</sup> forming an organic-inorganic composite with a banded cross-section. The insoluble matrix components of otoliths have been

found to retain the shape of the original crystal after decalcification with EDTA, illustrating the hydrogel-like qualities of the incorporated collagenous matrix.<sup>33,38</sup>

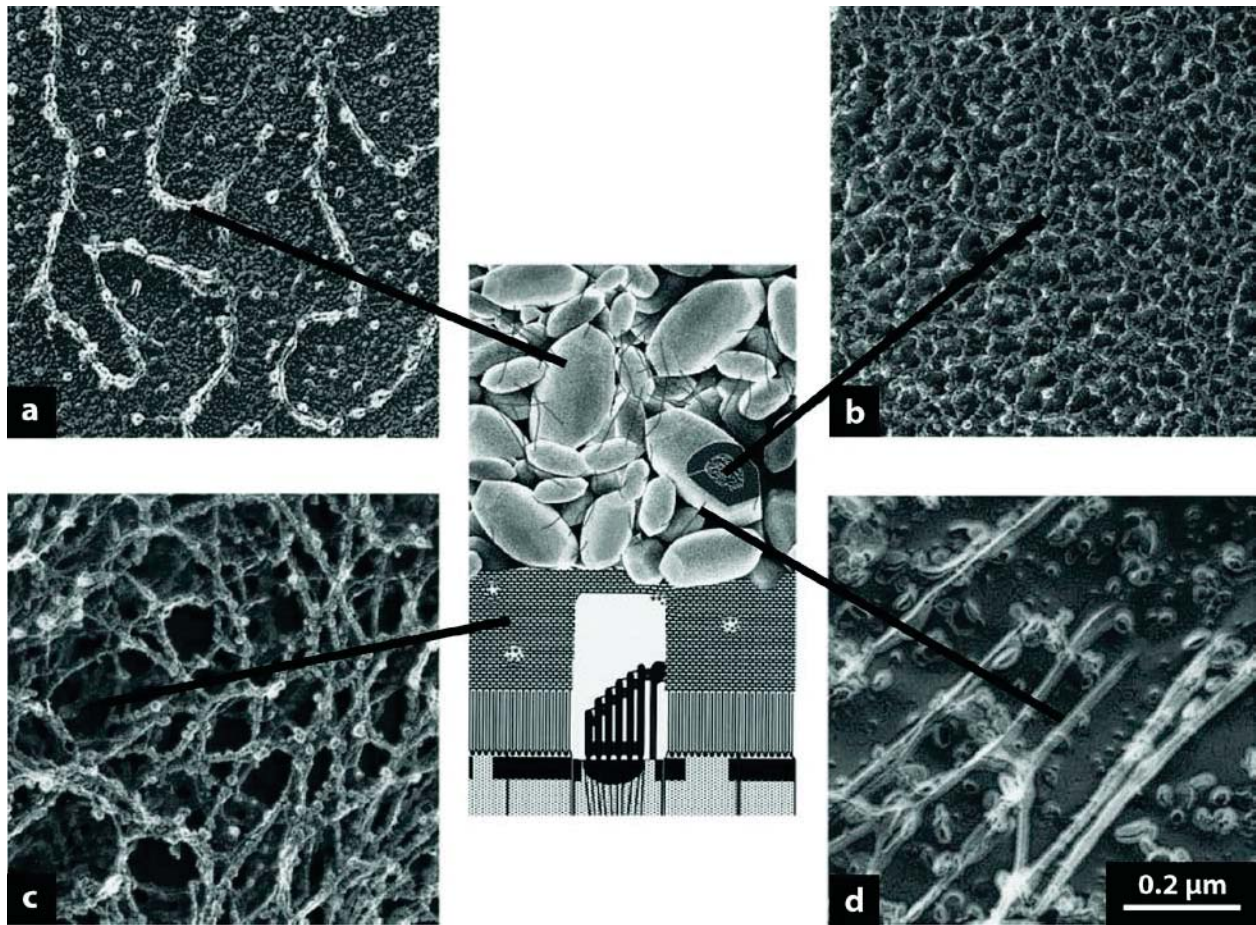


Figure 2.5 Different gel-like domains associated with calcite otoconia imaged by scanning electron microscopy with a schematic graphic showing the regional locations of each within the guinea pig vestibular system: (a) filaments adhered to the surface of octoconia (~20 nm diameter); (b) the inner core of otoconia contain an organic network; (c) supporting network (22 nm diameter filaments cross-linked by 11 nm filaments); and (d) inter-otoconial matrix filaments.<sup>29</sup> Adapted with permission from ref 21 copyright 2000 Elsevier.

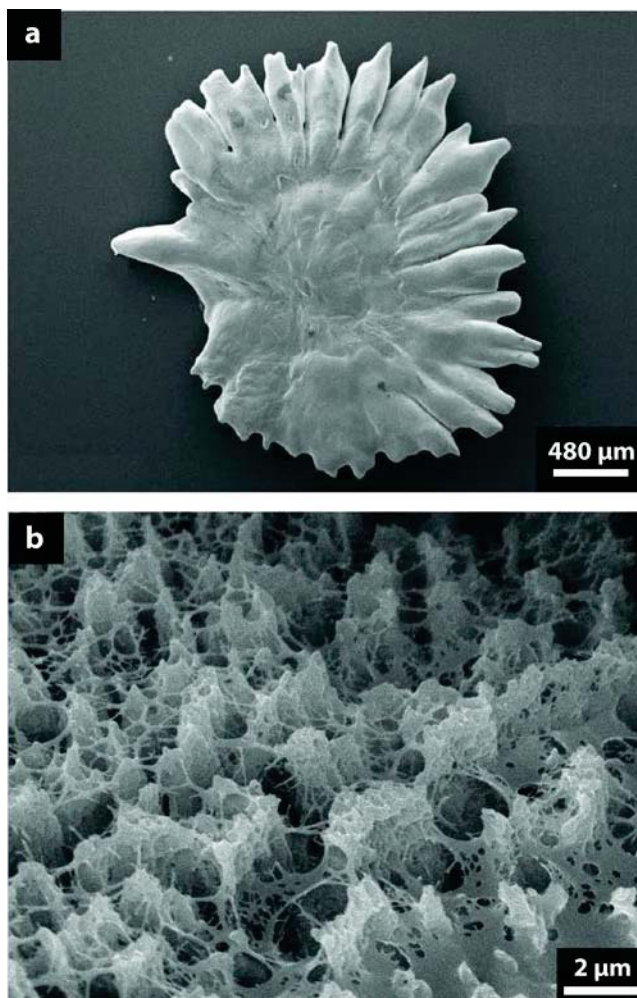


Figure 2.6 (a) Asteriscus otolith from *Chondrostoma nasus nasus* and (b) occluded matrix after decalcification, showing fibrous, porous organic network.<sup>34</sup> Adapted with permission from ref 140 copyright 2005 Wiley.

## 2.7 In Vitro Studies of Biomineralization: Crystal Growth in Gels

As discussed in the previous section, hydrogel-like matrices are associated with a diversity of biogenic systems and appear to play a role in controlling polymorph selectivity, influencing the final crystal morphology, and contributing to the materials properties of the biomineral composites. Armed with an understanding of the natural systems, hydrogel-based, bio-inspired systems have been designed to study biomineralization in vitro (Section 2.7.1) and to synthesize new materials.<sup>3,145,168-170</sup> These studies

**Table 2.2** Hydrogels and additives used in calcium carbonate crystallization

<b>Gel</b>	<b>Additives</b>	<b>References</b>
Agarose	none	3,62,149,173-177
	Cationic additives (e.g., $\text{Co}^{2+}$ , $\text{Fe}^{2+}$ , $\text{Ni}^{2+}$ , $\text{Zn}^{2+}$ , $\text{Cu}^{2+}$ , etc.)	178,179
	Carboxylic acids, polysaccharides	180-182 183
Charged polysaccharides (carrageenan, alginate, pectin, chitosan)	none	62,184-192
	Cationic additives	193
	Polyelectrolytes (e.g., poly (acrylic acid))	190,193
Gelatin	none	4,145,164
	polyelectrolytes (e.g., poly-aspartic acid)	6,168,194-196
	Cationic additives (e.g., $\text{Mg}^{2+}$ )	197,198
Polyacrylamide	none	27,60,80,145
	polyelectrolytes (e.g., poly-L-aspartate)	145
	Covalently-functionalized (e.g., carboxylic acid)	5,199
Silica	none	59,147,174,200-209
	Cationic additives (e.g., $\text{Mg}^{2+}$ , $\text{Cr}^{6+}$ , $\text{Mn}^{2+}$ , $\text{Co}^{2+}$ )	200,202,203,210,211
Silk	none	169
	peptides (e.g., n16N)	212
Synthetic Hydrogels	none	146,213,214

attempt to answer questions regarding the fundamental mechanism(s) that dictate polymorph selectivity, crystal orientation, organic-inorganic composite formation, and architectural assembly of complex structures. In particular, there has been a focus on the role of hydrogel matrices in defining the local crystal growth environment, both as a structural framework and as a source of chemical functionalities (Section 2.7.2). Finally, the factors that determine the incorporation or exclusion of the gel-like matrix into growing crystals must be clarified to enable successful composite formation in a wide variety of systems (Section 2.7.3). As we did in Section 3, we confine our discussion here to studies of calcium carbonate growth in gels (Table 2.2). Gel-based assays have also seen widespread use for growing calcium phosphate minerals and modeling biomineralization in bone and teeth. This work is reviewed elsewhere.<sup>8,152,171,172</sup>

### **2.7.1 Protein-Based Hydrogel Models for Nacre Formation**

Protein-based hydrogels serve as a logical starting point when designing in vitro models of nacre due to the identification of a silk-like hydrogel in the water-insoluble organic matrix of this biomineral (Section 2.6.1). The first in vitro models of nacre that demonstrated polymorph control were constructed using water-soluble organic matrix components that were extracted from biogenic nacre, in combination with insoluble matrix components derived from other sources.<sup>55,154,215-217</sup> More recent in vitro models have sought to incorporate the three distinct features found in the nacre system: a fibrous substrate (e.g.,  $\beta$ -chitin) for structural orientation; acidic macromolecules that are capable of serving as nucleation sites and controlling growth; and a hydrogel media (e.g., silk fibroin) to define the crystallization microenvironment.

#### **2.7.1.1 Silk Fibroin Hydrogels**

Silk fibroin hydrogels, as an analog to the silk-like proteins found in nacre, have been used to build in vitro models of nacre, due to the growing consensus that the aragonite tablets in nacre grow into a hydrated, gel-like phase.<sup>54</sup> Most assays to date, however, use a silk-fibroin solution or film,<sup>216,218-223</sup> rather

than a hydrogel. Recently, we have reported a study in which silk fibroin hydrogels were coupled with  $\beta$ -chitin substrates and acidic peptides.<sup>169</sup> In previous work, we had demonstrated that when n16N, a nacre-specific peptide, is bound to a  $\beta$ -chitin substrate, aggregates of needle-like aragonite crystals selectively form.<sup>212</sup> To further increase the complexity of this matrix, we added a silk fibroin hydrogel to the peptide-chitin construct. In contrast to the results in the absence of the gel, only flattened spherulites of vaterite and amorphous calcium carbonate were obtained when all three components were present (Figure 2.7).<sup>169</sup> These results suggest possible changes in the binding of n16N to  $\beta$ -chitin caused by the addition of silk fibroin hydrogel to the matrix. The morphological changes induced by the silk gel, as well as the stabilization of the amorphous phase, however, do suggest that perhaps there is a missing component in the model that could trigger the transformation to aragonite. Importantly, changing from solution-growth to gel-growth conditions profoundly changed the crystallization results. As the field moves forward, we anticipate the role of a hydrogel matrix to become increasingly important in the design of synthetic, nacre-like architectures.

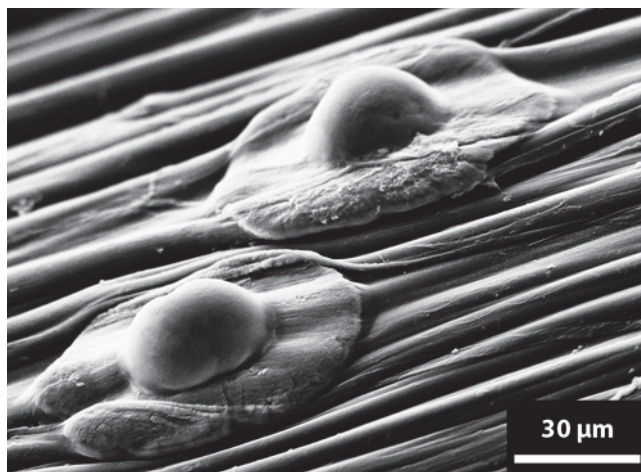


Figure 2.7 SEM micrograph of calcium carbonate crystallization on  $\beta$ -chitin with 2.5 wt% silk fibroin hydrogel and 10  $\mu$ M n16N, a nacre specific peptide. Analysis of crystal structures suggest they are a mixture of vaterite and amorphous calcium carbonate.<sup>169</sup> Adapted with permission from ref 146 copyright 2010 American Chemical Society.

### 2.7.1.2 Gelatin Xerogels

Cross-linked gelatin xerogels with incorporated acidic polypeptides have also been used as matrices for growing calcium carbonate. When uniaxially deformed, the collagen segments become aligned, providing an analogy to the oriented  $\beta$ -chitin fibrils in nacre. While this model initially presents as a substrate rather than a bulk hydrogel, upon deformation and exposure to the crystallization solution, crystals grow both on the surface of the film, as well as within the swelled xerogel matrix.<sup>168</sup> To add acidic functionality to the gelatin xerogels, Falini and co-workers incorporated polyelectrolytes such as poly(Aspartic acid) and poly(Glutamic acid). They also examined the effect of inorganic additives, in particular magnesium, a known promoter of aragonite.<sup>168,198</sup> Dependent on the deformation state and polymer content, they observed all three calcium carbonate polymorphs, calcite, vaterite, and aragonite, with variations in crystal orientation with respect to the matrix and crystal morphology (Figure 2.8).<sup>6,168,194-196</sup> For example, oriented calcite crystals grew on the surfaces of the uniaxially deformed xerogels, while in the interior of the swelled films, aragonite rods grew that were oriented in the direction of the deformation.<sup>168</sup> The formation of the aragonite polymorph was correlated to poly-Asp content and showed no dependence on magnesium concentration.<sup>168</sup> At higher poly-Asp content, a switch from aragonite to vaterite is observed, suggesting that the high concentrations of anionic polypeptides leads to high local supersaturations, which in turn trigger precipitation of the kinetic polymorph.<sup>6,194</sup> These results support the idea that calcium carbonate polymorph and crystal morphology are largely dictated by local structural and chemical characteristics of the crystallization environment.

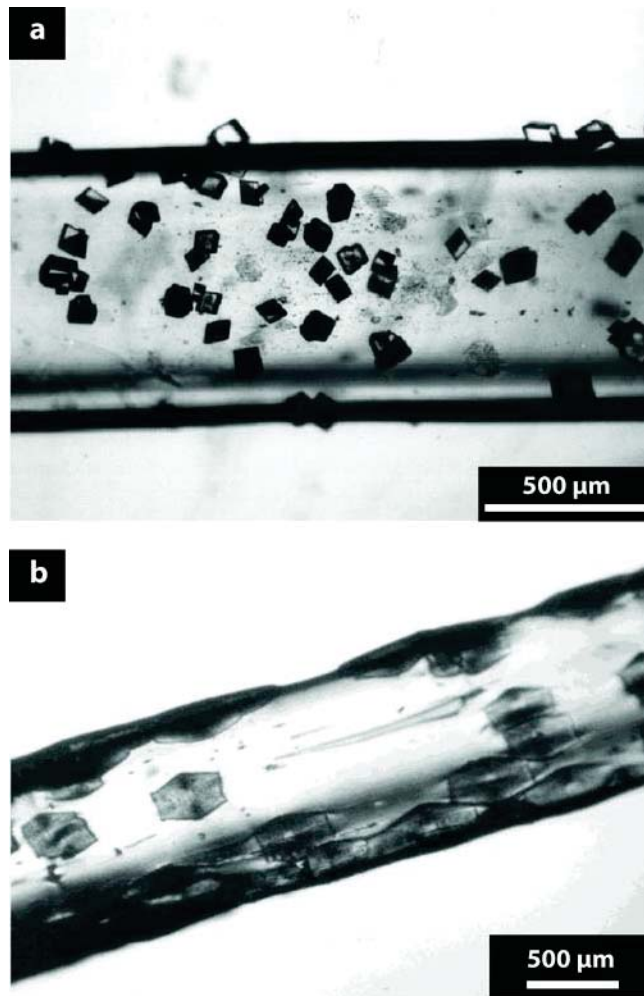


Figure 2.8 Optical images of calcium carbonate crystallization in uniaxially deformed (200%, elongation) gelatin films: (a) Rhombohedral calcite crystals formed on film without entrapped poly(Asp). (b) Aragonite aggregates formed inside the film with entrapped poly(Asp).<sup>168</sup> Adapted with permission from ref 145 copyright 1997 Wiley.

### 2.7.2 Hydrogels as a Crystallization Matrix

As a crystallization matrix, hydrogels can be used to expand both the kinetic and thermodynamic landscapes that are available to solution-based crystallization experiments. In addition to resembling the matrix environments in which biominerals are formed, hydrogel matrices have been used to model geologic crystallization in soils and sediments.<sup>200,203</sup> Regardless of perspective, the answers sought by crystallization studies in hydrogels are widely aimed at distinguishing the chemical versus physical

factors that determine the range of crystalline structures formed in these environments. Physically, the gel networks determine the diffusion rates of solutes, thus their local concentrations, and ultimately, the local supersaturation. In addition, gel networks have the potential to mechanically confine crystal growth (see Section 4.3). The chemistry within a hydrogel can be modulated either via the incorporation of soluble ionic species (e.g., cations) or by covalently attaching charged and/or polar functional groups (e.g., carboxylates, amines) to the hydrogel network. The presence of additional chemical functionality can influence crystallization in terms of the local supersaturation and/or by directly interacting with the growing crystal steps and facets. Carefully designed studies may be able to disentangle these chemical and physical effects and thus enable the design of synthetic crystal growth systems in gels that lead to the formation of complex crystalline structures for a wide variety of applications.

#### 2.7.2.1 Effect of Hydrogel Structure and Cationic Additives on Calcium Carbonate Crystallization in Hydrogels

In silica and agarose gels, the crystallization microenvironment is defined almost entirely by the porous structure of the hydrogel network (Section 2.3.1), due to the absence of strongly interacting chemical functionality within the matrix (e.g., charged groups). Thus, crystallization in these gels can be used to isolate the structural (physical) effects of the hydrogel matrix on calcium carbonate crystal growth without interference from strongly interacting chemical functionality. For example, the effects of variable pore sizes on supersaturation and crystal morphology can be examined without interference from changes in the local density of polar and/or charged functional groups in the matrix. Other physical effects, such as pH, temperature and time, can also be studied. Once the physical effects of these relatively inert gel matrices are elucidated, chemical functionality can be added back into the gels in a controlled manner, such as by the introduction of soluble ions or small molecules to distinguish the physical effects of crystallization in gels from the chemical.

### 2.7.2.2 Physical Effects on Morphology and Polymorph:

Historically, silica hydrogels have been used to grow large crystals of poorly soluble compounds using both single and double diffusion experimental configurations (Section 2.5).<sup>2</sup> As a growth system for calcium carbonate, double diffusion experiments allow access to a broad set of experimental conditions. The calcium and carbonate concentration gradients that form in these systems set up a continuous range of relative concentrations (and the corresponding supersaturation levels) along the gel column, allowing one to probe a number of experimental scenarios simultaneously.

Formation of the calcite polymorph in silica gels is possible over a wide range of pH and ion concentrations (supersaturation), with a diverse set of possible morphologies. At intermediate pH and low concentrations, single crystal equilibrium rhombohedra form.<sup>200</sup> Increasing pH or concentration can be used to shift the morphology towards hopper-like structures.<sup>200</sup> At high pH, polycrystalline aggregates form, including a distinct “sheaf-of-wheat” morphology, which consists of c-axis oriented aggregates of calcite rhombohedra.<sup>201,205</sup> Along these lines, spicule-like aggregates and hierarchically structured eight-pointed stars of calcite have also been reported at pH 10.5.<sup>59,200</sup>

In addition to calcite, aragonite and vaterite polymorphs can be grown in silica gels under conditions of high pH (8-10) and reactant concentration (supersaturation), using a double diffusion geometry.<sup>200</sup> Experimentally, the formation of vaterite spherulites was favored near the calcium reservoir, while spherulites of aragonite preferentially formed near the carbonate reservoir. Aragonite formation in silica gel at higher carbonate concentrations has also been achieved in silica gels that were formed at low pH (~5.5).<sup>202</sup> These examples of aragonite formation under ambient conditions in the absence of additives clearly demonstrate the kinetic control afforded by hydrogel environments.

Coral-like aggregates of aragonite have also been formed in silica gel at high pH using a single diffusion method.<sup>204</sup> These aggregates were composed of plate-like subunits of aragonite that were enveloped by silica, pointing toward the potential of silica to behave as a chemically interacting medium at high pH. The self-organization mechanisms that underlie the formation of hierarchical structures in

silica gel may stem from the experimental pH exceeding the pKa of the silanol groups in the hydrogel, thereby causing the gel to become an interacting medium. Further considerations regarding the observed morphologies include the possibility of (silica) gel incorporation during crystal growth, which was first observed in calcite even while the rhombohedral habit was preserved (see Section 2.7.3).<sup>147</sup>

Agarose hydrogels have also been used as a chemically inert matrix for the crystallization of calcium carbonate. Generally the calcite polymorph is obtained, although aragonite has been obtained by growth in agarose gels at elevated temperatures,<sup>175</sup> similar to results from solution-based experiments. Calcite crystals grown in agarose (1 w/v%) show a range of morphologies as a function of solute concentration (supersaturation), ranging from equilibrium rhombohedra to hopper-like 8-pointed stars (Figure 2.10).<sup>175</sup> In general, the hopper- or skeletal-like crystals are formed at higher driving forces obtained by changing the calcium concentration or carbonate reactant source.<sup>3,62,175</sup> In addition, under certain conditions, the calcite crystals are found to incorporate the gel medium during growth to form organic-inorganic composite single-crystals (see Section 2.7.3).<sup>173</sup> Hierarchically-structured calcite has also been grown in 2 wt% agar gels.<sup>62</sup> These crystals, which had a rhombohedral macroscopic morphology that was composed of rhombohedral subunits, represent a shift towards a self-organization mechanism facilitated by the higher supersaturation present in denser gel media.<sup>224</sup>

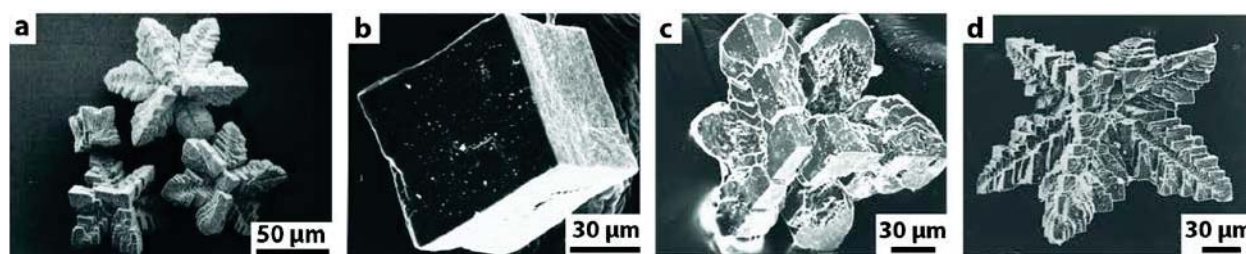


Figure 2.9 (a) Scanning electron microscope images of 8-pointed calcite stars grown in 1 (w/w%) agarose hydrogel with no additives.<sup>175</sup> (b)-(d) Morphological evolution of calcite grown in 0.3 % agar in the presence of variable radii impurity cations imaged by scanning electron microscopy: (b) Ag<sup>+</sup> (r = 115 pm), (c) Cr<sup>3+</sup> (r = 61.5 pm), (d) Al<sup>3+</sup> (r = 53.5 pm) (Note: ionic radius of Ca<sup>2+</sup> 100 pm).<sup>179</sup> a adapted with permission from ref 169 copyright 2003 Royal Society of Chemistry. b-d adapted with permission from ref 176 copyright 1998 Elsevier.

### 2.7.2.3 Introduction of Cationic Additives

As ‘chemically-inert’ crystal growth media, silica and agarose hydrogels present opportunities to the study of the chemical effects of soluble additives on calcium carbonate crystallization, in particular on polymorph selectivity and crystal morphology. The crystals formed in the presence of additives reflect changes to the growth mechanism(s) caused by impurity incorporations: modifying growth steps or changing solubility (and thus supersaturation).<sup>120</sup> While some studies have used carboxylic acid or polysaccharide additives in gels,<sup>180,181</sup> most have focused on cationic additives, due to the known correlation of  $Mg^{2+}$  with the aragonite polymorph and the anomalously high magnesium content found in some biological calcites.<sup>225</sup>

Introduction of cationic additives into double diffusion systems has been approached in different ways: loading of impurities into the gel itself, or by addition of the cationic impurity to the calcium reservoir. In most silica gel studies, impurities were added to the silicate solution before gelation to obtain an initially homogeneous distribution of impurity cations throughout the gel.<sup>200</sup> In the agar studies, the impurity cations were added to the calcium reservoir. The approach of loading impurity cations into only one region of the double diffusion system will result in impurity gradients. In addition, the two different loading procedures listed here will certainly have different effects on the solute diffusion gradients within the respective systems. These relatively unexplored considerations present opportunities for future studies on crystal growth in gels with additives.

In spite of the experimental complexities associated with crystallization studies in gels with additives some important relationships have been reported. At pH 5.5, calcite was precipitated under double diffusion in magnesium-loaded silica gels.<sup>202</sup> In this work, the concentrations of reactants along the gel column were determined at the time nucleation was first visible in the gel so that the supersaturation threshold could be monitored along the entire length of the gel column. The presence of magnesium in the gel media was found to increase the threshold supersaturation required to nucleate calcite, meaning that magnesium serves as an inhibitor to calcite formation. Calcite morphology evolved

along the length of the gel column during the reaction (Figure 2.10) consistent with the supersaturation gradient that was quantified along the column. Magnesium content in the final crystals was quantified by electron microprobe analysis showing greater  $\text{Mg}^{2+}$  incorporation under conditions of higher supersaturation. Individual crystals incorporated magnesium in zones, with the highest magnesium concentrations (up to 15 mol%) in the core. This zoning has also been observed with manganese substitution into calcite crystals grown in silica gels.<sup>206</sup> The morphologies of the magnesian calcites evolved from spherical aggregates (Figure 2.10a-d), formed at high supersaturation, to bundled sheafs at intermediate supersaturation (Figure 2.10e-g). Hopper-like morphologies formed in lower supersaturation regions were found to incorporate up to 7.5 mol% magnesium (Figure 2.10h).<sup>202</sup> These results illustrate a dependence of crystal morphology both on magnesium incorporation and on supersaturation, and may demonstrate that higher supersaturation can lead to greater impurity incorporation. While the individual connections from morphology to both supersaturation and magnesium content are well established, the relationship between impurity uptake (magnesium) and supersaturation is complicated. The relative contribution of each factor in determining the final morphology requires further investigation.

Other studies have expanded the range of cationic additives to include other alkaline earths as well as other metals, with both larger and smaller ionic radii than  $\text{Ca}^{2+}$  (Figure 2.9b-d).<sup>179,203</sup> Calcite crystals grown with substituted cations that have radii larger than calcium (e.g.,  $\text{Sr}^{2+}$ :  $r = 118$  pm) maintain a rhombohedral habit (Figure 2.10b), while those formed with cationic substituents with radii smaller than calcium (e.g.,  $\text{Co}^{2+}$ :  $r = 75$  pm) show a range of morphologies that depend on cationic additive concentration (Figure 2.10c,d). These results suggest a relationship between supersaturation and cation radius that is not yet well understood.

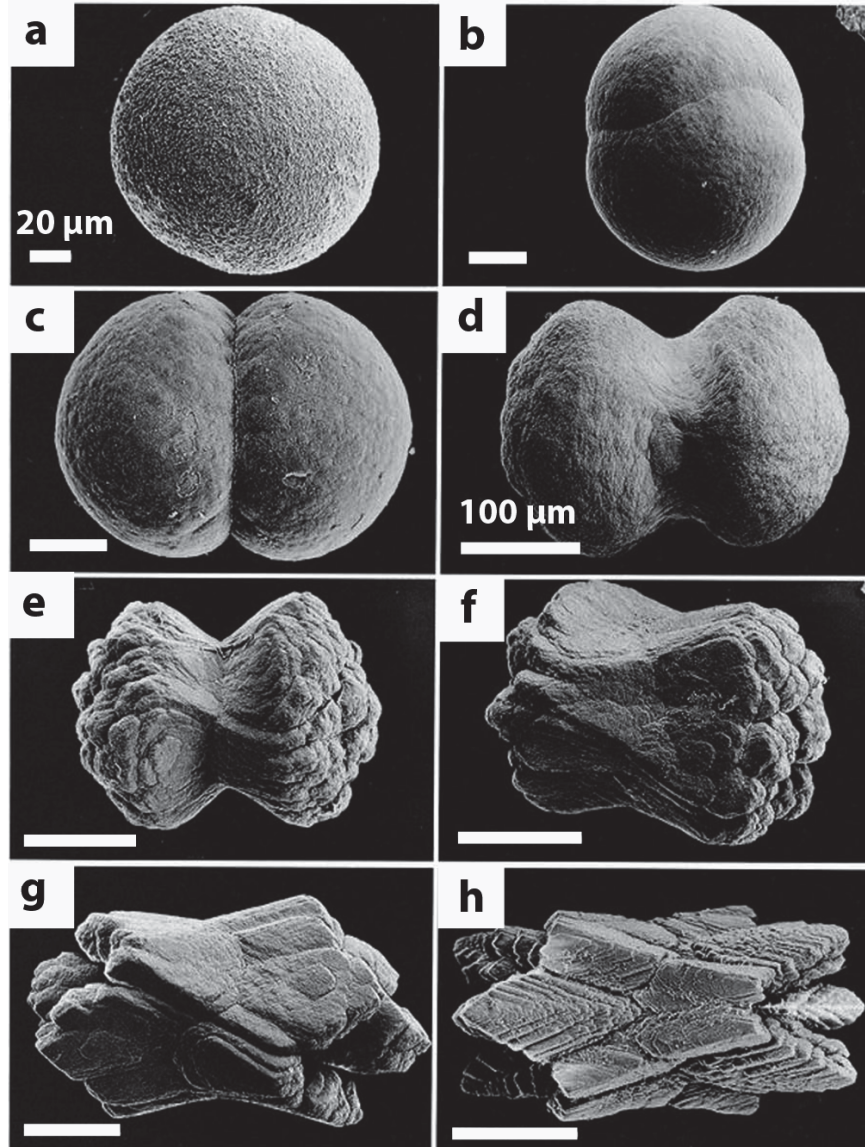


Figure 2.10 Scanning electron microscopy images of calcite grown in silica gels under double diffusion. Morphology changes are linked to changes in magnesium content and supersaturation. The spherical aggregates shown in (a) contain the highest  $Mg^{2+}$  content and formed at the highest supersaturation. The supersaturation as well as the magnesium content of the crystallites decreases alphabetically to (h) where hopper-like morphologies formed at the lowest supersaturation and contain the lowest magnesium content. Scale bars a-c all 20  $\mu m$ , d-h all 100  $\mu m$ .<sup>202</sup> Adapted with permission from ref 167 copyright 1996 Geoscience World.

Finally, similar to solution growth, cationic additives in calcium carbonate crystallization have been found to strongly influence polymorph selection.<sup>178,179,200,210</sup> In silica gel, vaterite formation has been associated with the addition of Ba<sup>2+</sup> and aragonite formation has been associated with the addition of Sr<sup>2+</sup> and Ni<sup>2+</sup>.<sup>200</sup> The formation of vaterite in agar gels has been observed with Ag<sup>+</sup>, Al<sup>3+</sup> and Cr<sup>3+</sup> impurities and displayed a dependence on concentration of the ionic additive.<sup>179</sup> In agar hydrogels, numerous divalent transition metal cationic additives have been shown to favor aragonite formation.<sup>178</sup> Aragonite can also be formed by additions of Ag<sup>+</sup>, Al<sup>3+</sup> and Cr<sup>3+</sup> impurities, with morphological variations that show a less clear dependence on the radius of the cations.<sup>179</sup>

#### 2.7.2.4 Chemistry of the Hydrogel Affects the Local Crystallization Microenvironment

Hydrogels that contain charged and/or polar functional groups present a number of additional control variables for the growth of calcium carbonate crystals. First, these functional groups can interact with diffusing solutes (e.g., Ca<sup>2+</sup>, CO<sub>3</sub><sup>2-</sup>) to change the local concentration of reactants (supersaturation). Secondly, they can serve as nucleation sites to direct the orientation of crystals within the hydrogel network. Finally, some functional groups can interact directly with the growth steps and facets of the crystals themselves. In all cases, the presence of interacting chemical functionality within hydrogel matrices presents a means to study the chemical (as opposed to physical) effects on crystallization in organic matrices. Two examples of such hydrogels are gelatin, which contains both acidic (carboxylic acid) and basic (amine) groups, and polyacrylamide, which contains pendant amide groups.

##### 2.7.2.4.1 *Gelatin*

When calcite is grown in 10 wt% gelatin hydrogels via double diffusion, spherulitic (polycrystalline) aggregates (100-400 μm diameter) of calcite form (Figure 2.11a)<sup>145</sup> In this work, the gelatin column was buffered to pH 8.35, the carbonate source was derived from sodium bicarbonate, and equimolar ratios of reactants were used. The appearance of the surfaces of the aggregates was found to vary as a function of position in the gel: particles formed closest to the Ca<sup>2+</sup> source showed rough surface

terraces, characteristic of formation under higher supersaturation, while those closest to the  $\text{CO}_3^{2-}$  source had smooth, faceted surface terraces, indicating formation at a lower supersaturation. The calcite aggregates were shown to incorporate  $\sim 4$  wt% of the gelatin matrix by thermogravimetric analysis (TGA). A radial internal microstructure was observed by optical cathodoluminescence that showed preferential incorporation of the gel into the core.<sup>145</sup> The spherical, aggregated morphology is generally indicative of formation under high supersaturation, and is quite similar to the spherulitic aggregates formed in silica gel with  $\text{Mg}^{2+}$  additives (Figure 2.10b,c).<sup>202</sup> Interestingly, Fernández-Díaz et al. quantified a higher supersaturation nearest the carbonate reservoir in their silica hydrogel system, while Grassmann et al. used surface morphology to infer that the higher supersaturation was present at the calcium side of their gelatin system.

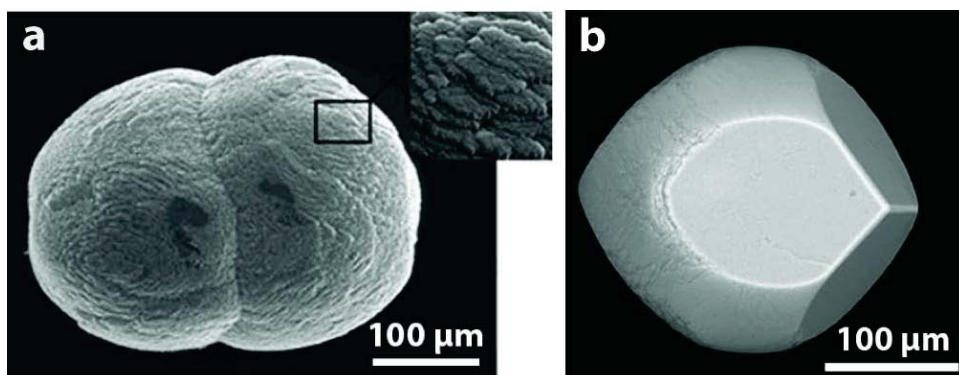


Figure 2.11 Scanning electron microscopy images of calcite crystals grown in 10 wt% gelatin matrices under double diffusion: (a) Spherulitic aggregate formed with equimolar ratio of reactants ( $\text{CaCl}_2$ ,  $\text{NaHCO}_3$ );<sup>145</sup> and (b) Single crystal formed with 1:3 molar ratio of reactants ( $\text{CaCl}_2$ : $\text{Na}_2\text{CO}_3$ ).<sup>4</sup> a adapted with permission from ref 107 copyright 2002 American Chemical Society. b adapted with permission from ref 4 copyright 2008 Wiley.

In a related study, *single-crystal* barrel-shaped calcite crystals ( $\sim 200$   $\mu\text{m}$  length) were formed closest to the calcium reservoir under double diffusion in 10 wt% gelatin gels (Figure 2.11b).<sup>4</sup> These crystals were also found to incorporate the gelatin fibers and to have a less-ordered and more porous central region by transmission electron microscopy (see Section 2.7.3).<sup>164</sup> In this work, the gelatin column

was buffered to pH 7.4, the carbonate source was a sodium carbonate solution, and 1:3 molar ratio of calcium to carbonate was used. A comparison of the different morphologies formed under double diffusion in gelatin (Figure 2.11) and the poly- versus single-crystalline nature indicates that their formation took place under very different supersaturation conditions. These different growth environments could be caused by the different pH, or the absolute and relative concentration of reactants, as well as the different carbonate sources. Further experimentation is necessary to determine which factor(s) dominate the formation mechanism.

#### 2.7.2.4.2 Polyacrylamide (PAA)

Pseudo-octahedral crystalline aggregates of calcite with  $\sim 150\text{-}250\ \mu\text{m}$  diameter were grown by double diffusion in a buffered (pH 8.35), 10 wt% PAA hydrogel using an equimolar ratio of reactants (100 mM) (Figure 2.12a).<sup>60</sup> These calcite composites were shown to consist of oriented rhombohedral crystallites  $\sim 5\ \mu\text{m}$  in diameter, interspersed with the PAA hydrogel matrix (Figure 2.12b). It is worth noting that the morphology of the aggregates did not vary with position along the PAA gel column. Individual aggregates diffracted electrons as single crystals (inset, Figure 2.12b). The morphology of the calcite aggregates was found to depend on the concentration of PAA in the hydrogel matrix, forming rhombohedral aggregates in lower concentration PAA hydrogel systems.<sup>27,80</sup> Further, incorporation of the hydrogel matrix into the aggregates was quantified by thermogravimetric analysis. In a gel with  $\sim 10\ \text{wt}\%$  polyacrylamide content, 0.7 mass% gel was incorporated within the composite products.<sup>60</sup> The assembly of rhombohedral subunits into pseudo-octahedral aggregates was speculated to result from a high heterogeneous nucleation rate in the PAA matrix caused by a high apparent supersaturation. In this scenario, the presence of numerous rhombohedral nuclei prevent classical ion-by-ion growth, and thus oriented assembly of these nuclei are driven by a reduction in surface energy, during which incorporation of the gel network occurs.<sup>60</sup>

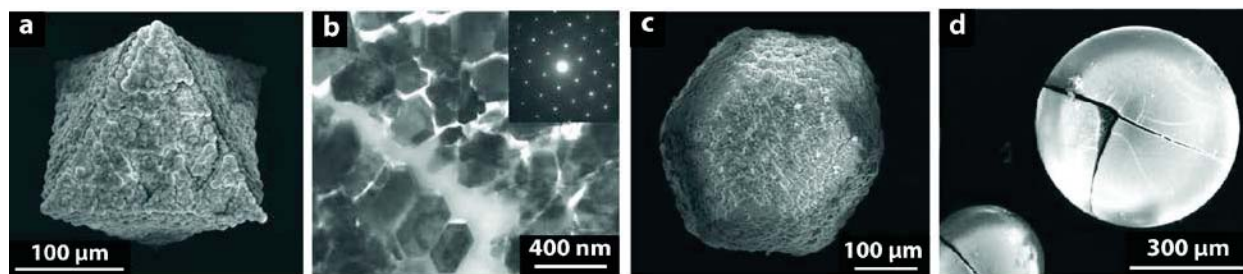


Figure 2.12 Pseudo-octahedral aggregates of calcite formed under double diffusion in 10 wt% polyacrylamide hydrogel: (a) scanning electron microscopy image of pseudo-octahedral morphology; (b) transmission electron microscopy of aligned subunits with selected area electron diffraction inset showing single crystal characteristics of individual crystallites,<sup>60</sup> and (c) cuboctahedral aggregates formed in 10 mol% sulfonated PAA hydrogel<sup>199</sup> (d) calcite spherulite formed in 10 wt% carboxylated PAA hydrogel.<sup>5</sup> a, b adapted with permission from ref 25 copyright 2003 Mineralogical Society of America. c adapted with permission from ref 182 copyright 2003 Wiley. d adapted with permission from ref 5 copyright 2004 Elsevier.

#### 2.7.2.5 Covalent Modification of Synthetic Hydrogels

In solution-based growth, the difference in function between soluble (free) and substrate-bound (immobile) additives is well-known. For example, small-molecule carboxylates in solution inhibit calcite growth,<sup>226</sup> whereas carboxylate functionalized surfaces can direct the oriented nucleation of calcite crystals.<sup>227</sup> Applying similar ideas to gel-growth becomes complicated: will a functional group covalently bound to the gel network behave more like a growth modifier (free in solution) or nucleation promoter (immobilized)? Based on the physical and chemical aspects of hydrogel matrices discussed above, covalent modification of synthetic hydrogel networks with acidic or basic species can be used to achieve refined control over the crystallization microenvironment.

##### 2.7.2.5.1 Sulfonated Polyacrylamide (sPAA)

Copolymerization of acrylamide with sulfonate-containing monomers<sup>199</sup> was used to introduce anionic functionality to a PAA hydrogel matrix, consistent with the sulfonated polysaccharides found in

some biomineralization systems.<sup>155</sup> The negatively charged sulfonate groups were chosen for their potential to interact with calcium cations to change the local chemical environment and thereby the growth rate. In addition, the sulfonate functionality has the potential to interact with growing crystal surfaces or act as nucleation sites.

Similar to the pseudo-octahedral calcite aggregates formed in pure PAA, calcium carbonate crystallization in sPAA with equimolar ratio of reactants forms aggregates of calcite with internal architectures composed of rhombohedral subunits.<sup>199</sup> While pseudo-octahedral aggregates were formed in native PAA, the external morphology of the aggregates formed in sPAA showed cuboctahedral symmetry (Figure 2.12c). The cuboctahedral morphology was observed along the entire length of the sPAA hydrogel column, but the size of these aggregates varied; from 100  $\mu\text{m}$  near the calcium reservoir to 500  $\mu\text{m}$  near the carbonate reservoir. The morphology of the aggregates was seen to change as a function of sulfonate content, proceeding from pseudo-octahedral aggregates (native PAA) to cuboctahedral aggregates at 10 mol% sulfonate via flattening of the pseudo-octahedral faces. While the aggregation-based growth model in PAA gels appeared to be maintained in the presence of sulfonate functionalities, the change in morphology suggests a role for the sulfonate groups in modifying the relative growth rates of the individual faces of the rhombohedral subunits.<sup>199</sup> While the similarity in proposed growth mechanism in sPAA as compared to native PAA suggests that matrix incorporation might occur, the incorporation of organic material was not monitored, so the effect of sulfonate functionality on matrix incorporation is yet to be determined.

#### 2.7.2.5.2 Carboxylated Polyacrylamide (cPAA)

Similar to the sPAA discussed above, copolymerization of polyacrylamide hydrogels with carboxylate groups (acrylic acid)<sup>5</sup> was used to model the Asp- and Glu-rich proteins found in many biogenic matrices.<sup>155</sup> In contrast to native PAA and sPAA gels, calcium carbonate crystallization in these cPAA gels proceeded much slower and formed polymorphs and morphologies that evolved with time. After seven days under double diffusion with equimolar ratio of reactants (100 mM), a mix of vaterite

spheres and calcite rhombohedra (less than 5  $\mu\text{m}$ ) were observed. These products exhibited no visible changes for an additional seven days. After twenty-eight days only spherical aggregates of calcite (300  $\mu\text{m}$ ) remained (Figure 2.12d). Thermogravimetric analysis was used to determine that these calcite aggregates contained 4.2 mass% (9 vol%) of the cPAA hydrogel network. Further analysis of the calcite aggregates showed a spherulitic microstructure, and conchoidal fracture, implying that they had formed rapidly from a central seed.

The significant differences in both the crystallization process and final morphology of crystals formed in cPAA as compared to native PAA and sPAA imply that a different growth mechanism governs their formation. The initially suppressed nucleation is consistent with the inhibitory effects of polyacrylic acid on calcium carbonate crystallization.<sup>182</sup> The formation of vaterite is consistent with kinetic stabilization of this less stable polymorph by the carboxylate groups.<sup>5</sup> The spherulitic character of the final aggregates as well as the delay in their formation indicates an induction period during which high supersaturations develop to facilitate the rapid growth mechanisms responsible for this morphology. Matrix incorporation may occur during this period of rapid growth or during ripening to the final morphology.

#### 2.7.2.6 “Designer” Hydrogels

More recently, small-molecule hydrogels have been designed to serve as biomimetic organic matrices for crystallization. For example, carboxylic acid functionalities have been introduced into a bis-urea hydrogel system to interact with calcium ions.<sup>146</sup> The morphology of calcite crystals grown in these gels evolved over time, initially growing as rhombohedral crystals that, with time, first developed etch pits and subsequently, irregular overgrowth structures. Etching studies performed on the initial, as-grown rhombohedral crystals resulted in non-regular and deep etch pits, suggesting the non-specific incorporation of gelator molecules into the crystals (Section 2.7.3). In other work, calcite was grown using a supramolecular gel composed of N,N',N''-tris(3-pyridyl)-trimesic amide.<sup>214</sup> In contrast to most

biomimetic approaches, this hydrogel was designed to interact with carbonate anions through the presence of amide and pyridyl functional groups. Similar utilization of positively charged additives to the calcium carbonate crystallization media is still relatively new in solution studies.<sup>228</sup> Calcite crystals grown in this fibrous gel were shown to grow around whole fibers (500-1000 nm in diameter).<sup>214</sup> These studies and others support the idea that synthetic matrices can be designed to interact specifically with either the ionic species during nucleation or with the growing crystals to direct growth and final morphology.

### **2.7.3 Incorporation of the Gel-Matrix During Crystal Growth.**

One of the outstanding questions in biomineralization is how large calcite single crystals can incorporate organic macromolecules while still diffracting X-rays and/or electron beams as single-crystals. Although the incorporation phenomenon in both biogenic<sup>57,149,229-232</sup> and synthetic<sup>58,233-243</sup> crystals has been widely addressed and studied, the incorporation mechanism(s) is still poorly understood.<sup>3,243</sup> Crystal growth in gels provides ideal platforms with which to study this phenomenon since several types of gel-grown crystals have been identified that incorporate the gel media and become gel/single-crystal composites.

Although the examples of gel-incorporated crystals are limited, as compared with the large number of gel-grown crystals, the types of gel-incorporated crystals are diverse, including crystals of inorganics and organics, small molecules and macromolecules. Initially, in 1969, Nickl and Henisch reported that calcite crystals grown from silica gels incorporated the silica matrix.<sup>147</sup> Subsequently, García-Ruiz et al. found that gel-grown protein (lysozyme, ferritin and thaumatin) crystals can incorporate the gel (silica and/or agarose) matrix.<sup>123,148</sup> We have demonstrated that calcite,  $\alpha$ -glycine, and calcium tartrate tetrahydrate crystals grown in agarose gels incorporate the polymer network, and that the crystals maintain their long-range order (single-crystal nature).<sup>3,58,173,244</sup>

In other work, Huang et al. showed that calcite crystals grown in gelatin gels also incorporate the gel material.<sup>4,164</sup> The barrel-shaped crystallites obtained by Huang et al. (Figure 2.11b) scattered x-rays as single crystals. These crystals were seen to have a less-ordered and more porous central region by

transmission electron microscopy, consistent with the different structural regions of *in vivo* otoconia (Figure 2.5). Matrix incorporation was attributed to high supersaturation conditions, which resulted from the interaction of ionic carboxylate groups on Asp and Glu residues in the gelatin with calcium ions thereby forming a specific microenvironment for crystal growth.<sup>145</sup> Huang et al. extended this work by modifying the gelatin media to more closely resemble an otoconia-like glycoprotein matrix by including agar as a polysaccharide source.<sup>4</sup> The morphology of crystals became more elongated with well-defined faceted ends, and more closely resembled human otoconia.

#### 2.7.3.1 Possible Incorporation Mechanisms

Before gel-incorporation was first reported by Nickl and Henisch, Khaimov-Mal'kov had proposed that a growing crystal exerts a crystallization pressure on the surrounding gel media.<sup>245</sup> His work suggested that whether or not the crystal incorporated the gel was determined by whether or not the gel was strong enough to resist the crystallization pressure. If the gel network were strong, then the crystal would grow around it, whereas if it were weak, it would be broken or pushed away. Indeed, “cusps” in gel are often observed at the corners and edges of the growing crystals where the gel has been disrupted.<sup>246,247</sup> Following Khaimov-Mal'kov's hypothesis, Gavira and García-Ruiz calculated the magnitude of the crystallization pressure from growing protein crystals on agarose gel networks and found that the pressure was much higher than the gel strengths, suggesting that the crystals would always break or push away the gel media.<sup>148</sup> In their experiments, however, the pressure did not disrupt the gel as expected and the authors only obtained crystals with gel-incorporation. The discrepancy between calculation and experimental results implies that the competition between gel strength and crystallization pressure at the growth front is not the only factor determining the incorporation of gel matrix.

The crystal growth rate is another possible variable that is important for determining incorporation of the gel matrix. It is well-known that at faster growth rates, crystals incorporate larger amounts of atomic or small molecule impurities.<sup>202</sup> A similar kinetic effect has also been observed for the incorporation of micrometer-sized particles into crystals: at slow growth rates, growing crystals do not

incorporate the particles, but once the growth rate increases beyond a critical value, incorporation of particles takes place.<sup>248-250</sup>

### 2.7.3.2 Experiments: Calcite Crystals Grown in Agarose Hydrogels

We have recently worked to understand the many factors leading to gel-incorporation during crystal growth, in particular, the interplay between crystal growth rate and gel strength on gel-incorporation. For this work, we have focused on the growth of calcite crystals in agarose hydrogels as a model system.<sup>3,173,244</sup> As discussed in Section 2.7.2.1, calcite growth in agarose can yield a range of morphologies from well-formed rhombohedra to hopper- or skeletal-like crystals. Results from our lab have revealed that calcite crystals grown in agarose hydrogels incorporate gel fibers uniformly without disrupting the rhombohedral morphology or crystallography of calcite crystals (Figure 2.13a). After gentle etching of the crystals in deionized (DI) water, the incorporated gel fibers emerge from the crystal (Figure 2.13b). To observe the incorporated fibers *in situ*, we have examined the internal structure of gel-grown calcite crystals by annular dark field scanning transmission electron microscopy (ADF-STEM) and electron tomography. These images reveal a network of gel fibers laced throughout the crystal (Figure 2.13c).<sup>58</sup> Higher magnification images reveal that the crystal uses both high- and low-energy facets to accommodate the gel's tortuous structure (Figure 2.13d,e). Selected area electron diffraction (SAED) demonstrates that despite the presence of the gel fibers, the single crystal nature of the calcite is not disrupted (Figure 2.13d inset).

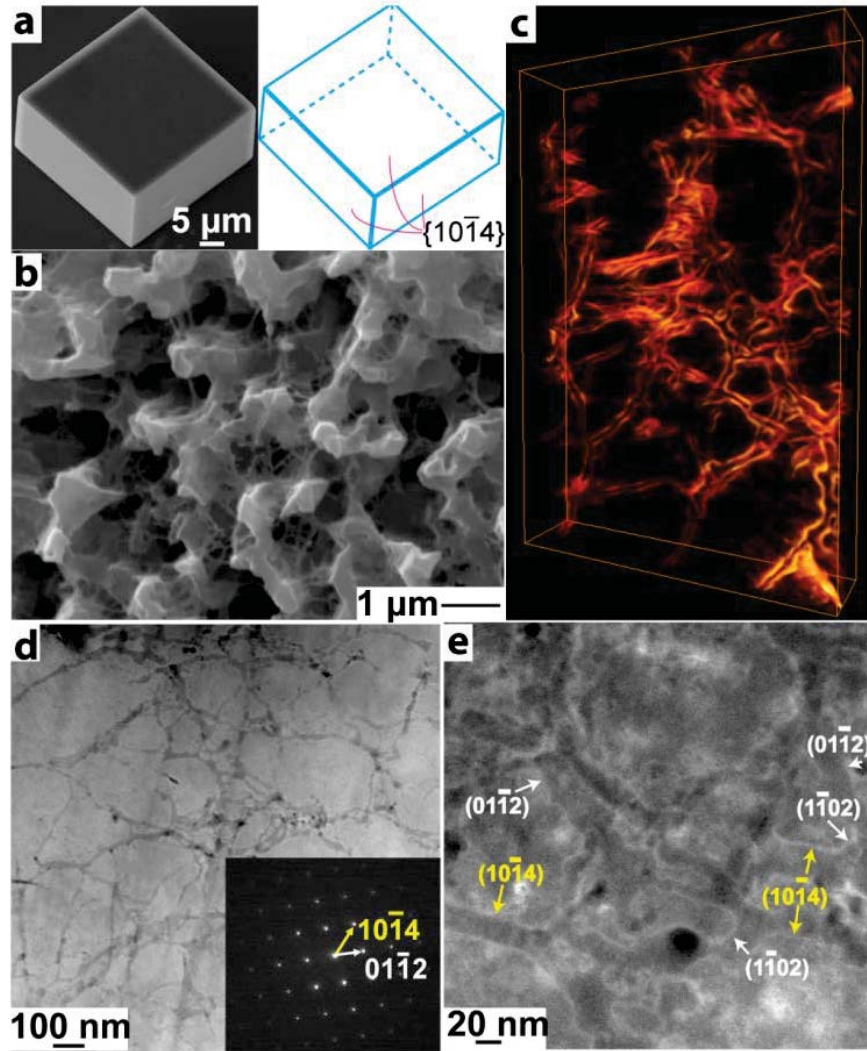


Figure 2.13 Structural characterization of porous single crystal calcite agarose composites: (a) a scanning electron microscopy image of single calcite rhombohedra and a model of a calcite crystal expressed by six  $\{10\bar{1}4\}$  faces, (b) a SEM image of a gel-grown calcite crystal after etching in DI water for 4 days, showing the exposed incorporated gel fibers, (c) tomographic reconstructions of randomly distributed agarose network inside a section of calcite single crystal, (d,e) porous internal structure shown by transmission electron microscopy. Interfaces between the crystal and fibers are partially indexed. For clarity, faces in the  $\{10\bar{1}4\}$  family are indicated in yellow, whereas faces in the  $\{01\bar{1}2\}$  family are highlighted in white. Inset in d: a SAED pattern.<sup>58,173</sup> a, c, d, e used with permission from ref 23 copyright 2009 American Association for the Advancement of Science. b used with permission from ref 170 copyright 2007 Royal Society of Chemistry.

More recently, we have investigated the factors relevant to gel-incorporation.<sup>3</sup> We predicted, based upon Khaimov-Mal'kov's work,<sup>245</sup> that for a given crystallization pressure (thermodynamic driving force) there should be a “threshold” gel strength at which gel-grown crystals should switch from no incorporation to complete incorporation. Similarly, for a given gel, there should be a critical growth rate at which incorporation begins to occur. Until now, this kind of transition, however, has not been demonstrated experimentally for a single gel-crystal pair. We designed a set of experiments to systematically examine the effects of gel strength and crystal growth rate on gel-incorporation. To change the growth rate, we varied  $\text{Ca}^{2+}$  concentration. Because we were using the gas diffusion (ammonium carbonate) method<sup>251</sup> to grow the crystals (Figure 2.2b), the carbonate concentration is continuously evolving throughout the experiment, and so we cannot define an absolute supersaturation in the gel. Qualitatively, increasing  $\text{Ca}^{2+}$  leads to an increase in growth rate, as suggested by the crystal morphology evolution (Figure 2.14a insets). To change the gel strength, we looked at growth in two different commercially available agaroses with different degrees of hydroxyethylation, agarose 1B (high strength) and agarose IX (low strength), both from Sigma-Aldrich. As the degree of hydroxyethylation increases, the gel strength decreases due to disruption of the hydrogen bonding network.<sup>3,84,86</sup> We then studied how agarose incorporation varied as a function of calcium and gel concentration in both of these gels. Increasing the agarose concentration in the gels is also a way of changing the gel strength since it leads to denser, cohesive interaction (e.g., hydrogen bonding) among agarose chains and, thus, higher gel strength.<sup>87</sup>

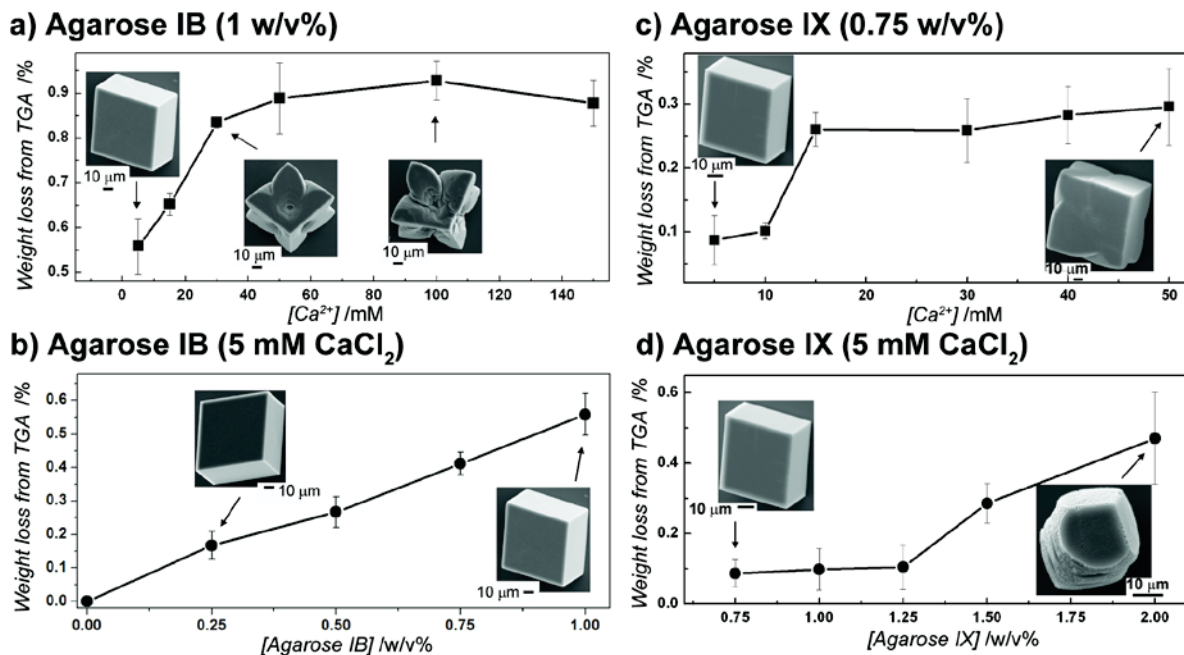


Figure 2.14 The weight loss above 150 oC calculated from TGA analyses for the calcite single crystals grown under systematically varied conditions: (a) different CaCl<sub>2</sub> concentrations in a gel (1 w/v% Agarose IB), (b) different CaCl<sub>2</sub> concentrations in a gel (0.75 w/v% Agarose IX), (c) different gel (Agarose IB) concentrations with a fixed CaCl<sub>2</sub> concentration (5 mM), (d) different gel (Agarose IX) concentrations with a fixed CaCl<sub>2</sub> concentration (5 mM). Insets: Representative SEM images of calcite crystals grown under the conditions indicated by the arrows.<sup>3</sup> a,b adapted with permission from ref 3 copyright 2009 Wiley.

### 2.7.3.2.1 Effects of Growth Rate ([Ca<sup>2+</sup>]) on Gel-Incorporation

Calcite crystals were grown in agarose hydrogels containing a range of concentrations of CaCl<sub>2</sub> ([CaCl<sub>2</sub>]). In both agarose 1B and agarose IX, at low [CaCl<sub>2</sub>], the crystals exhibit the characteristic rhombohedral morphology of calcite expressed by six {104} faces (Figure 2.14a,b, insets). With increasing [CaCl<sub>2</sub>] in both gel types, the crystal morphology gradually evolves into “hopper-like” shapes (Figure 2.14a,b insets), suggesting 2-D nucleation is taking place at the corners and edges of the crystals.<sup>2,119</sup> The observation of such crystal morphologies is consistent with diffusion-limited growth and faster growth rates, as would be expected at higher [CaCl<sub>2</sub>].

To quantify the amount of incorporated agarose, the gel-grown crystals were examined by thermogravimetric analysis (TGA).<sup>3</sup> In both gels, at higher  $[\text{CaCl}_2]$  (faster growth rates), the amount of incorporated material reaches a plateau, or saturation level (Figure 2.14a,b). The saturation values are close to the calculated value ( $\sim 0.3\%$ ) for crystals incorporating all of the agarose fibers they encounter, as well as some amount of water.<sup>3</sup> In agarose IX, at low  $[\text{CaCl}_2]$  (slow growth rates), TGA of the crystals shows no appreciable weight loss (Figure 2.14b). In contrast, in agarose 1B at low  $[\text{CaCl}_2]$ , incorporation is still observed, just at a lower level than the saturation amount. It is possible that for agarose 1B, we did not achieve slow enough growth rates to observe no incorporation in this stronger gel. Alternatively, differences in the gel chemistry may lead to different strength interactions between the gel and the growing crystals, which in turn lead to different amounts of incorporation.

#### 2.7.3.2.2 *Effects of Gel Strength on Gel-Incorporation*

Comparison of the above results for agarose 1B and agarose IX at the low  $[\text{CaCl}_2]$  already provides insight into a possible role for gel strength in determining incorporation. At the slow growth rates, there is no incorporation observed for the weaker of the two gels (agarose IX). This observation is consistent with Khaimov-Mal'kov's prediction,<sup>245</sup> however, since we are changing slightly the chemical structure of the gel, it is possible that changes in the gel-crystal interaction are responsible for the change in incorporation.

To further examine the role of gel strength, we examined calcite crystals grown in both types of agarose hydrogels with a fixed  $[\text{CaCl}_2]$  (5 mM), but different gel concentrations. The crystal morphology does not change significantly with increasing gel concentration in agarose 1B (Figure 2.14c).<sup>3</sup> In agarose IX, however, at higher gel concentrations the crystals develop curved surfaces at the corners (Figure 2.14d, insets). This change in morphology is possibly due to specific agarose-crystal interactions.

TGA was again used to determine the amount of incorporated organic material. For agarose 1B, the amount of gel incorporated increases approximately linearly with increasing gel concentration (Figure 2.14c).<sup>3</sup> In contrast, for agarose IX, the dependence of the amount of incorporated agarose on gel

concentration is nonlinear (Figure 2.14d). At lower gel concentrations (lower gel strength), TGA shows negligible weight loss. At higher gel concentrations, the amount of incorporation begins to increase as a function of gel concentration. In addition to changing gel strength, changing the gel concentration also will affect the gel structure (e.g., pore size) and possibly the supersaturation within the gel. Further experiments are required to fully deconvolute the contributions of all of these factors.

### 2.7.3.3 Proposed Mechanism for Gel Incorporation: Competition at the Growth Fronts

By examining a range of growth conditions and gels, we have gained further insight into the variables that determine the amount of gel incorporation observed in a given system. We have observed three main regimes: 1) no incorporation at slower growth rates in a weaker gel; 2) partial incorporation at slower growth rates in a stronger gel; and 3) complete incorporation at faster growth rates in both weaker and stronger gels (Figure 2.15). The transition of crystals between these three states suggests that competing factors favor and disfavor gel-incorporation and that these competing factors are dependent on crystal growth rate and gel strength. Increasing both growth rate and gel strength favors gel-incorporation. The effect of growth rate on gel-incorporation is consistent with the force competition model previously suggested by Chernov and Temkin<sup>248,252</sup> for crystallization in the presence of particles.<sup>248-250</sup> The effect of gel strength on gel-incorporation verifies the importance of gel resistance to the crystallization pressure proposed by Khaimov-Mal'kov.<sup>245</sup>

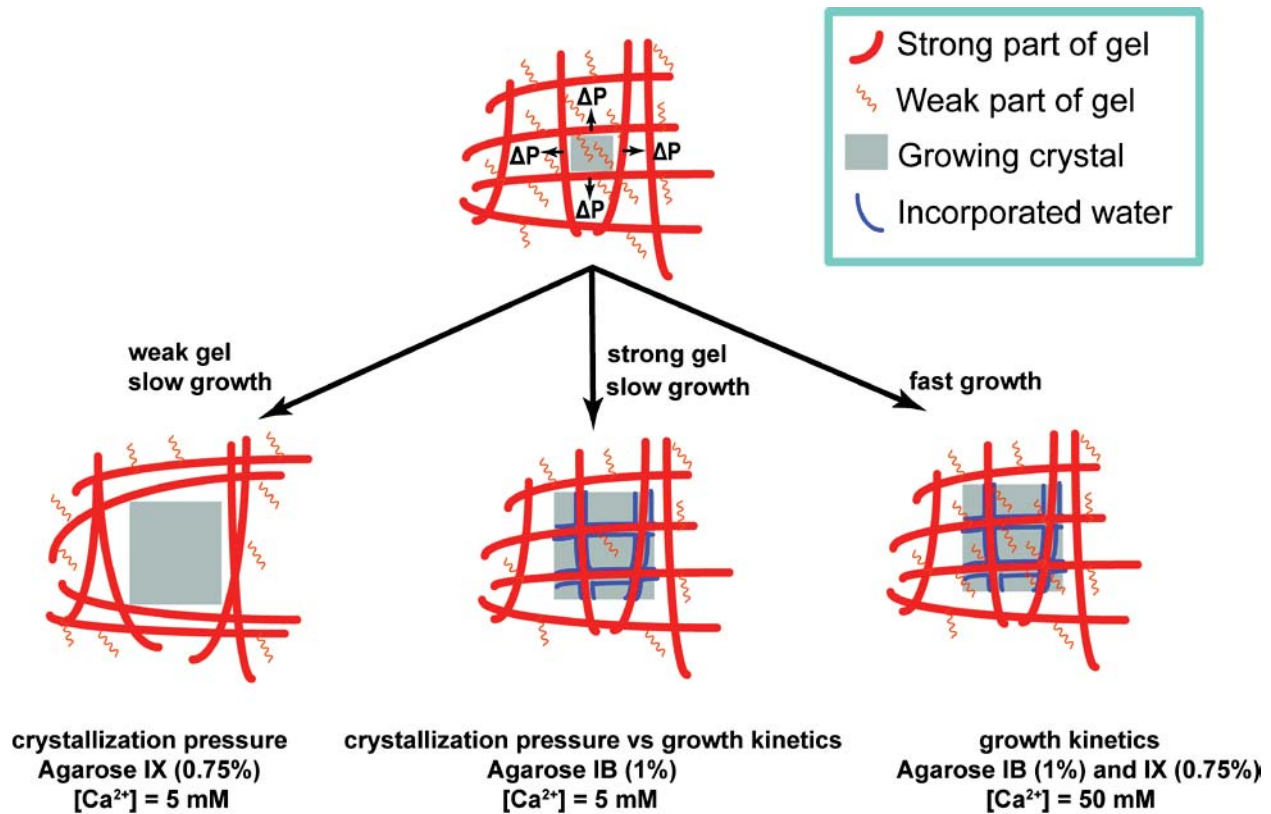


Figure 2.15 The proposed mechanism for agarose matrix incorporation during calcite crystal growth: A balance between the resistance of the gel fibers to crystallization pressure and the growth rate. Under a specific condition, crystallization pressure (or growth rate) dominates, and the resulting crystals become pure single-crystals (or single-crystals with completely incorporated gel fibers). In an intermediate case, crystals will partially incorporate the gel network.<sup>3</sup> For further details, see the text. Adapted with permission from ref 3 copyright 2009 Wiley.

As a growing crystal approaches a gel fiber with poor mutual wetting at the growth front, there is a force competition between a “disjoining force,” a hydrodynamic force, and the resistance of the gel network (Figure 2.16).<sup>245,248,252</sup> Chernov first described and defined the “disjoining force” as originating from repulsive van der Waals forces at the interface between a growing crystal and a foreign object.<sup>119</sup> In our case, the tendency of the disjoining force to push the fibers away from the crystal is equivalent to a reduction in the chemical potential of the liquid film between the crystal and the fiber as compared to that of the bulk liquid. For further discussion of the disjoining force, see references<sup>119, 239</sup> and<sup>245</sup>. The

disjoining force disfavors incorporation of the gel fiber by the growing crystal, while the hydrodynamic force and the resistance of the gel network favor it. The hydrodynamic force is proportional to the crystal growth rate and the resistance of the gel network increases with gel strength. When growth rate or gel strength is high enough, the cooperation of the hydrodynamic force and the resistance of gel network will withstand the disjoining force and the gel fibers will be incorporated. Otherwise, the disjoining force will overcome the combination of the other two and the gel fibers will be pushed away.

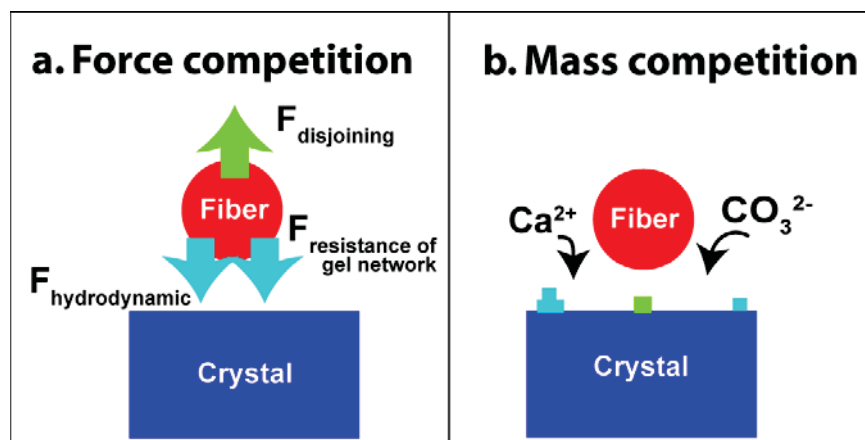


Figure 2.16 A schematic representation of the proposed gel-incorporation mechanism with a) a force competition and b) a mass competition at the growth front nearby an agarose gel fiber. For further details, see the text.

In addition to the force competition, we suggest that there is also a mass competition (Figure 2.16b).<sup>119</sup> As first suggested for particles by Chernov, the agarose fibers screen the growth fronts beneath them from mass transport so that these growth fronts have higher transport resistance than the nearby growth fronts that are free of screening. Both the screened (Figure 2.16b, green ‘brick’) and unscreened (Figure 2.16b, blue ‘brick’) growth fronts advance, competing for “nutrients”. Crystal growth at the screened growth fronts near the fiber disfavors gel-incorporation, while growth at the unscreened growth front favors it. The faster the growth rate, the higher the transport resistance for the screened growth

fronts because less time is allowed for ions to diffuse into the gap between the growth front and the fiber. Therefore, higher growth rates favor gel-incorporation because of this mass competition.

To summarize, for the calcite-agarose system, the two key variables for controlling gel incorporation are: 1) growth rate and 2) gel strength. While increased gel incorporation was found with increasing gel concentration, it is not clear if the changes to morphology were a result of the amount of incorporated gel or simply a result of changes to the growth rate caused by changes in the local chemical environment. The next step is to determine the generality of these “rules” for other gel-crystal pairs: first, for chemically “non-interacting” gels and then for gels that have the capability to strongly interact with the growing crystals. By understanding the interplay of physical and chemical effects on gel-incorporation, researchers will be able to determine design criteria for the pairing of host crystals with gels to achieve the desired degree of inclusion, and potentially thus tailor the mechanical properties of the resulting composite crystals.<sup>243</sup>

## **2.8 SUMMARY AND OUTLOOK**

The common theme of crystal growth in gels presented by matrix-mediated biomineralization systems provides a technique to investigate the mechanisms that govern composite formation in biogenic systems. As a medium for crystal growth, hydrogel networks maintain diffusion-limited growth conditions, which can be used to achieve a wide range of morphologies and architectural arrangements in the final crystalline products. The chemical functionality and microstructure of hydrogels varies amongst gel types and with gel concentration and provides a means to tune the kinetic variables of the growth rate and supersaturation in the crystallization microenvironment. A summary of calcium carbonate products obtained from growth in hydrogels is compiled in Table 2.

Crystallization of calcium carbonate in gels has elucidated some of the underlying effects that may govern the formation of complex mineral structures in biogenic systems. First, the observed morphology and polymorph appears largely to be a consequence of the growth mechanism as determined

by the supersaturation. The supersaturation in turn, is dictated by the local chemical environment, which depends on the chemical functional groups present in the matrix itself. Further, the local chemical environment in gels varies with the gel concentration due to changes in the pore sizes and microstructure of the gels. Moreover, organic matrix incorporation during crystal growth depends on the gel strength and concentration, and the growth rate.

At this point, it is an interesting exercise to look at the similarities and differences in products from among the gel types discussed. There are three main types of calcite structures that form: 1) Single crystals, with and without incorporated matrix, which have been reported to form in silica, agarose, and gelatin gels; 2) Pseudo-single crystal aggregates, which have been reported to form in native PAA, sPAA, and agar gels; 3) Polycrystalline, spherulitic aggregates, which have been reported in silica, gelatin, silk, and cPAA gels. Since all of these experiments have been performed over many years and by many different labs, there is significant variation in the reaction conditions (e.g., pH, reactant concentrations and ratios, gel length, gel diameter), making direct comparisons among gels nearly impossible. Several interesting trends, however, can still be identified. First, single crystals are most commonly reported in the two “non-interacting” gels, silica and agarose. This result strengthens the assignment of these gels as relatively, chemically-inert towards calcite. Second, the observation that multiple morphologies can be observed within the same gel-type (e.g., there are reports of both single crystals and polycrystalline spherulites in gelatin and silica gels) emphasizes the importance of growth conditions, and most likely supersaturation, on the final structure.

In those cases where care has been taken to maintain consistent conditions across gel types,<sup>5,60,145,199</sup> further conclusions can be drawn. For example, the striking differences observed by Grassmann and Lobmann between the pseudo-single crystal aggregates obtained in PAA and sPAA (Figure 2.11) and the spherulites from gelatin (Figure 2.11a) and cPAA (Figure 2.12d) imply that the chemistry and physical properties of the matrix do affect growth. It is difficult, however, even within this set of data to determine which characteristics of the matrix play the largest role in defining the product

morphology. For example, one possible interpretation is that the ionic groups within gelatin and cPAA lead to the polycrystalline spherulites by locally sequestering calcium and thus increasing the supersaturation. Spherulitic structures, however, are also observed in silica gel in the presence of  $Mg^{2+}$  or at a high pH. As is true for solution growth studies, therefore, it is important to remember that just because two crystals look like each other, does not mean that they formed via the same mechanism or as a result of the same types of interactions. Our hope for the future is that research will be aimed at merging these seemingly disparate works into a unified map for understanding the formation of complex, crystalline structures in gels.

In order to grow a variety of materials (i.e., beyond calcium carbonate) in hydrogels to obtain organic-inorganic composites for a range of applications, it is important to establish the relationship between growth conditions, hydrogel choice, and the amount of incorporated organic material and the final crystal morphology. As this area of research continues to grow, we anticipate that the use of “designer” gels with tailored chemical functionality, such as peptides derived from proteins involved in biomineralization, will become increasingly important. The presence of functionalized substrates coupled with hydrogel media<sup>169,244</sup> can also impart another level of control, particularly over nucleation. Ultimately, this field should strive to determine design criteria for the pairing of host crystals with hydrogels to achieve the desired structure for a given application. Regardless, as discussed in this article, crystal growth in gels has already established itself as a member of the ‘bio-inspired crystallization toolbox’ alongside small-molecule and polymeric additives.<sup>7,224,253,254</sup> As we move beyond the phenomenological treatment of growth in hydrogels to a fully developed understanding of the crystal growth mechanisms in such environments, we will enable the synthesis of complex, hierarchical, single-crystal composites with tunable physical properties.

## **ACKNOWLEDGEMENTS**

LAE acknowledges support from NSF (DMR 0845212), the Cornell Center for Materials Research (CCMR), a Materials Research Science and Engineering Center of the NSF (DMR 1120296), the J.D. Watson Investigator Program (NYSTAR contract no. C050017), and the Cornell Engineering Learning Initiatives (ELI). In addition, EAS acknowledges support from NSF Graduate Research Fellowship Program (DGE-0707428) and Integrative Graduate Education and Research Traineeship (DGE-0903653) Programs. Particular acknowledgement is made of the use of the shared facilities at CCMR (DMR 1120296). We thank Prof. Guiseppa Falini for kindly providing high-resolution images for Figures 6 and 8. Finally, we thank all of our lab members and colleagues who over the years have contributed to our understanding of crystal growth in gels.

## 2.9 Materials and Methods

### 2.9.1 Hydrogel Preparation for Imaging

*Silk.* Silk fibroin was obtained from *Bombyx mori* (silkworm) cocoons. The cocoon material was boiled in one of the following solutions: 1) 5 w/v % Marseilles soap solution (an olive oil based soap from Marseilles, France),<sup>218</sup> or 2) 0.02 M sodium carbonate ( $\text{Na}_2\text{CO}_3$ , J.T. Baker) for 2 hours,<sup>91</sup> changing the solution every 15 minutes to solubilize and remove the silk sericin. After boiling, the silk was rinsed with copious amounts of water to remove excess salts or surfactants. The resulting silk mass was dissolved overnight, at room temperature, in 9.3 M lithium bromide (LiBr, Reagent Plus  $\geq 99\%$ , Sigma-Aldrich). The solubilized silk was then filtered and dialyzed (Slide-a-Lyzer dialysis cassettes, Pierce, MWCO 3,500) for three days. Fresh aqueous silk solutions (3 mL), in capped glass test tubes and incubated in a hot water bath at 60° C. Hydrogels formed from Marseilles soap purified silk fibroin gelled in 2 days; those purified with sodium bicarbonate took 4 days to gel.

*Silica.* Aqueous solutions (0.5 M) of sodium metasilicate nonahydrate (Sigma Aldrich) were gelled by additions of equal volumes of diluted hydrochloric acid (Fisher Scientific). Basic gels (final pH ~9) were formed using 1 M hydrochloric acid, and acidic gels (final pH~2) were formed using 2 M hydrochloric acid. Solutions were allowed to gel in sealed scintillation vials in a water bath at 30 °C. Gel times varied depending on pH, with acidic gels taking 4 weeks to gel and basic gels taking less than 1 hour.

*Freeze-drying.* All hydrogel samples (~1 mL) were frozen in liquid nitrogen and placed on a lyophilizer for 18 h. Freeze-dried hydrogel samples were sputtered coated with carbon using a rotating, tilting stage. Subsequently, samples were sputtered coated with Au/Pd. Scanning

electron microscopy (STEREOSCAN 440 LEICA, 20 kV) was used to image the microstructures of the gel networks.

### 2.9.2 Crystal Growth Experiments

Experiments in Agarose IB were previously reported. For Agarose IX, agarose solutions (0.75-2 w/v %) were prepared by dissolving agarose powder (Type IX, Sigma, gel point: 8-17 °C) in a hot solution of 5-50 mM  $\text{CaCl}_2 \cdot 2\text{H}_2\text{O}$  (99+%, Sigma-Aldrich). The warm agarose solution (3 mL) was filtered (syringe filter; 0.2  $\mu\text{m}$ , Nylon, Millipore) into a Petri dish (35 mm x 10 mm) that was then cooled in a refrigerator (about 0 °C) for gelation (30 minutes) and equilibrated at ambient temperature for another 30 minutes. After gelation, the Petri dishes were covered with aluminum foil with one small hole.

The Petri dishes with the gels were placed in a closed desiccator containing one vial of ammonium carbonate (Sigma-Aldrich). After 48 hours in the desiccator, crystals grew in the bulk gels and were removed from the gels by dissolving the agarose in boiling deionized (DI) water (18.2 M $\Omega$ , Barnstead EASYpure<sup>®</sup> RoDI) for three times. The obtained crystals were then rinsed with DI water and ethanol.

### 2.9.3 Characterization of Calcite Crystals

The morphologies of the crystals were examined by scanning electron microscopy (STEREOSCAN 440, LEICA, 25 kV, 600 pA) after being sputter-coated with Au/Pd.

**Thermogravimetric analysis (TGA)** of the crystals was conducted with a **thermogravimetric analyzer (TA Instruments Q500) under a flowing air atmosphere and with a heating rate of 5°C per minute** from ambient temperature to 450°C. Ten to twenty milligrams of crystals were used for each run after drying overnight in oven (~80°C). Each TGA experiment was repeated 3 times. TGA of geological calcite (calcite Iceland spar, Carolina Biological) was used as a control.

## REFERENCES

- (1) Lefaucheur, F.; Robert, M. C. In *Handbook of Crystal Growth*; Hurle, D. T. J., Ed.; Elsevier Science: Amsterdam, 1994; Vol. 2, p 1271.
- (2) Henisch, H. K. *Crystal Growth in Gels and Liesegang Rings*; Cambridge University Press: Cambridge, 1988.
- (3) Li, H. Y.; Estroff, L. A. *Adv. Mater.* **2009**, *21*, 470.
- (4) Huang, Y. X.; Buder, J.; Cardoso-Gil, R.; Prots, Y.; Carrillo-Cabrera, W.; Simon, P.; Kniep, R. *Angew. Chem. Int. Ed.* **2008**, *47*, 8280.
- (5) Grassmann, O.; Lobmann, P. *Biomaterials* **2004**, *25*, 277.
- (6) Falini, G. *Int. J. Inorg. Mater.* **2000**, *2*, 455.
- (7) Meldrum, F. C.; Colfen, H. *Chem. Rev.* **2008**, *108*, 4332.
- (8) Silverman, L.; Boskey, A. L. *Calcif. Tissue Int.* **2004**, *75*, 494.
- (9) Shi, Y.; Geng, J. Q.; Yang, D. *Progress in Chemistry* **2010**, *22*, 2224.
- (10) Weiner, S.; Dove, P. M. In *Biomineralization*; Dove, P. M., DeYoreo, J. J., Weiner, S., Eds.; The Mineralogical Society of America: Washington, D.C., 2003; Vol. 54, p 1.
- (11) Veis, A. In *Biomineralization*; Dove, P. M., DeYoreo, J. J., Weiner, S., Eds.; The Mineralogical Society of America: Washington, D.C., 2003; Vol. 54.
- (12) Mann, S. *Biomineralization: Principles and Concepts in Bioinorganic Materials Chemistry*; Oxford University Press: New York, 2001.
- (13) Weiner, S.; Addadi, L. *J. Mater. Chem.* **1997**, *7*, 689.
- (14) Weiner, S. *Am. Zool.* **1984**, *24*, 945.
- (15) Jackson, A. P.; Vincent, J. F. V.; Turner, R. M. *Proc. R. Soc. London, Ser. B* **1988**, *234*, 415.
- (16) Aizenberg, J.; Tkachenko, A.; Weiner, S.; Addadi, L.; Hendler, G. *Nature* **2001**, *412*, 819.
- (17) Ma, Y.; Cohen, S. R.; Addadi, L.; Weiner, S. *Adv. Mater.* **2008**, *20*, 1555.
- (18) Levi-Kalishman, Y.; Falini, G.; Addadi, L.; Weiner, S. *J. Struct. Biol.* **2001**, *135*, 8.
- (19) Addadi, L.; Joester, D.; Nudelman, F.; Weiner, S. *Chem. A Eur. J.* **2006**, *12*, 981.
- (20) Evans, J. S. *Chem. Rev.* **2008**, *108*, 4455.

- (21) Clode, P. L.; Marshall, A. T. *Protoplasma* **2003**, 220, 153.
- (22) Constantz, B.; Weiner, S. J. *Exp. Zool.* **1988**, 248, 253.
- (23) Dauphin, Y. *Int. J. Biol. Macromol.* **2001**, 28, 293.
- (24) Sondi, I.; Salopek-Sondi, B.; Skapin, S. D.; Segota, S.; Jurina, I.; Vukelic, B. *J. Colloid Interf. Sci.* **2011**, 354, 181.
- (25) Ehrlich, H.; Etnoyer, P.; Litvinov, S. D.; Olenikova, M. M.; Domaschke, H.; Hanke, T.; Born, R.; Meissner, H.; Worch, H. *Materialwiss. Werkst.* **2006**, 37, 552.
- (26) Tambutté, S.; Tambutté, E.; Zoccola, D.; Allemand, D. In *Handbook of Biomineralization*; Bäuerlein, E., Ed.; Wiley-VCH Verlag GmbH & Co.: Weinheim, 2007.
- (27) Sethmann, I.; Helbig, U.; Worheide, G. *CrystEngComm* **2007**, 9, 1262.
- (28) Lim, D. J. *Ann. Oto. Rhinol. Laryn.* **1983**, 93, 17.
- (29) Lins, U.; Farina, M.; Kurc, M.; Riordan, G.; Thalmann, R.; Thalmann, I.; Kachar, B. *J. Struct. Biol.* **2000**, 131, 67.
- (30) Pote, K. G.; Ross, M. D. *Comp. Biochem. Physiol., B: Biochem. Molec. Biol.* **1991**, 98, 287.
- (31) Wang, Y. X.; Kowalski, P. E.; Thalmann, I.; Ornitz, D. M.; Mager, D. L.; Thalmann, R. *Proc. Natl. Acad. Sci. U. S. A.* **1998**, 95, 15345.
- (32) Xu, Y. F.; Zhang, H.; Yang, H.; Zhao, X.; Lovas, S.; Lundberg, Y. W. *Developmental Dynamics* **2010**, 239, 2659.
- (33) Davis, J. G.; Oberholtzer, J. C.; Burns, F. R.; Greene, M. I. *Science* **1995**, 267, 1031.
- (34) Falini, G.; Fermani, S.; Vanzo, S.; Miletic, M.; Zaffino, G. *Eur. J. Inorg. Chem.* **2005**, 162.
- (35) Gauldie, R. W. *J. Morphol.* **1993**, 218, 1.
- (36) Hughes, I.; Blasiolo, L.; Huss, D.; Warchol, M. E.; Rath, N. P.; Hurle, B.; Ignatova, E.; Dickman, J. D.; Thalmann, R.; Levenson, R.; Ornitz, D. M. *Dev. Biol.* **2004**, 276, 391.
- (37) Murayama, E.; Herbomel, P.; Kawakami, A.; Takeda, H.; Nagasawa, H. *Mech. Develop.* **2005**, 122, 791.
- (38) Murayama, E.; Takagi, Y.; Ohira, T.; Davis, J. G.; Greene, M. I.; Nagasawa, H. *Eur. J. Biochem.* **2002**, 269, 688.
- (39) Oliveira, A. M.; Farina, M.; Ludka, I. P.; Kachar, B. *Naturwissenschaften* **1996**, 83, 133.
- (40) Mugiya, Y. *Fish B-NOAA* **1987**, 85, 395.

- (41) Murayama, E.; Okuno, A.; Ohira, T.; Takagi, Y.; Nagasawa, H. *Comp. Biochem. Physiol., B: Biochem. Molec. Biol.* **2000**, *126*, 511.
- (42) Khalifa, G. M.; Weiner, S.; Addadi, L. *Cryst. Growth Des.* **2011**, *11*, 5122.
- (43) Moradian-Oldak, J. *Matrix Biol.* **2001**, *20*, 293.
- (44) Iijima, M.; Moradian-Oldak, J. *J. Mater. Chem.* **2004**, *14*, 2189.
- (45) Margolis, H. C.; Beniash, E.; Fowler, C. E. *J. Dent. Res.* **2006**, *85*, 775.
- (46) Fang, P. A.; Conway, J. F.; Margolis, H. C.; Simmer, J. P.; Beniash, E. *Proc. Natl. Acad. Sci. U. S. A.* **2011**, *108*, 14097.
- (47) Weiner, S.; Wagner, H. D. *Annu. Rev. Mater. Sci.* **1998**, *28*, 271.
- (48) Lowenstam, H.; Weiner, S. *On Biomineralization*; Oxford University Press: New York, 1989.
- (49) Boskey, A. L. *Bone Miner.* **1989**, *6*, 111.
- (50) George, A.; Veis, A. *Chem. Rev.* **2008**, *108*, 4670.
- (51) Towe, K. M.; Lowenstam, H. A. *J. Ultrastruct. Res.* **1967**, *17*, 1.
- (52) Gordon, L. M.; Joester, D. *Nature* **2011**, *469*, 194.
- (53) Sone, E. D.; Weiner, S.; Addadi, L. *J. Struct. Biol.* **2007**, *158*, 428.
- (54) Nudelman, F.; Shimoni, E.; Klein, E.; Rousseau, M.; Bourrat, X.; Lopez, E.; Addadi, L.; Weiner, S. *J. Struct. Biol.* **2008**, *162*, 290.
- (55) Falini, G.; Albeck, S.; Weiner, S.; Addadi, L. *Science* **1996**, *271*, 67.
- (56) Albeck, S.; Weiner, S.; Addadi, L. *Chem. A Eur. J.* **1996**, *2*, 278.
- (57) Nudelman, F.; Chen, H. H.; Goldberg, H. A.; Weiner, S.; Addadi, L. *Faraday Discuss.* **2007**, *136*, 9.
- (58) Li, H. Y.; Xin, H. L.; Muller, D. A.; Estroff, L. A. *Science* **2009**, *326*, 1244.
- (59) Imai, H.; Terada, T.; Yamabi, S. *Chem. Commun.* **2003**, 484.
- (60) Grassmann, O.; Neder, R. B.; Putnis, A.; Löbmann, P. *Am. Mineral.* **2003**, *88*, 647.
- (61) Oaki, Y.; Imai, H. *Crystal Growth & Design* **2003**, *3*, 711.
- (62) Oaki, Y.; Hayashi, S.; Imai, H. *Chem. Commun.* **2007**, 2841.

- (63) Almdal, K.; Dyre, J.; Hvidt, S.; Kramer, O. *Makromol. Chem., Macromol. Symp.* **1993**, 76, 49.
- (64) Kavanagh, G. M.; Ross-Murphy, S. B. *Prog. Polym. Sci.* **1998**, 23, 533.
- (65) Flory, P. J. *Faraday Discuss. Chem. Soc.* **1974**, 57, 7.
- (66) Ruchel, R.; Steere, R. L.; Erbe, E. F. *J. Chromatogr.* **1978**, 166, 563.
- (67) Waki, S.; Harvey, J. D.; Bellamy, A. R. *Biopolymers* **1982**, 21, 1909.
- (68) Favard, P.; Lechaire, J. P.; Maillard, M.; Favard, N.; Djabourov, M.; Leblond, J. *Biol. Cell* **1989**, 67, 201.
- (69) Trieu, H. H.; Qutubuddin, S. *Colloid Polym. Sci.* **1994**, 272, 301.
- (70) Blank, Z.; Reimschuessel, A. C. *J. Mater. Sci.* **1974**, 9, 1815.
- (71) Pernodet, N.; Maaloum, M.; Tinland, B. *Electrophoresis* **1997**, 18, 55.
- (72) Halberstadt, E. S.; Henisch, H. K.; Nickl, J.; White, E. W. *J. Colloid Interf. Sci.* **1969**, 29, 469.
- (73) Geiger, C.; Stanescu, M.; Chen, L. H.; Whitten, D. G. *Langmuir* **1999**, 15, 2241.
- (74) Estroff, L. A.; Hamilton, A. D. *Chem. Rev.* **2004**, 104, 1201.
- (75) Lee, K. Y.; Mooney, D. J. *Chem. Rev.* **2001**, 101, 1869.
- (76) Van Vlierberghe, S.; Dubruel, P.; Schacht, E. *Biomacromolecules* **2011**, 12, 1387.
- (77) Veis, A. *The Macromolecular Chemistry of Gelatin*; Academic Press: New York, 1964.
- (78) Weiss, R. G.; Terech, P. *Molecular Gels: Materials with Self-Assembled Fibrillar Networks*; Springer: Netherlands, 2006.
- (79) Zhou, J. F.; Zhou, M. F.; Caruso, R. A. *Langmuir* **2006**, 22, 3332.
- (80) Helbig, U. *J. Cryst. Growth* **2008**, 310, 2863.
- (81) Tsuchida, E.; Abe, K. *Adv. Polym. Sci.* **1982**, 45, 1.
- (82) Rinaudo, M. *Polym. Int.* **2008**, 57, 397.
- (83) Lahaye, M.; Rochas, C. *Hydrobiologia* **1991**, 221, 137.
- (84) Arnott, S.; Fulmer, A.; Scott, W. E.; Dea, I. C. M.; Moorhouse, R.; Rees, D. A. *J. Mol. Biol.* **1974**, 90, 269.
- (85) Guenet, J. M.; Rochas, C. *Macromol. Symp.* **2006**, 242, 65.

- (86) Guiseley, K. B., (Union, ME); MARINE COLLOIDS INC: US, 1976; Vol. 3956273.
- (87) Normand, V.; Lootens, D. L.; Amici, E.; Plucknett, K. P.; Aymard, P. *Biomacromolecules* **2000**, *1*, 730.
- (88) Maaloum, M.; Pernodet, N.; Tinland, B. *Electrophoresis* **1998**, *19*, 1606.
- (89) Whytock, S.; Finch, J. *Biopolymers* **1991**, *31*, 1025.
- (90) Griess, G. A.; Guiseley, K. B.; Serwer, P. *Biophys. J.* **1993**, *65*, 138.
- (91) Kim, U.-J.; Park, J.; Li, C.; Jin, H.-J.; Valluzzi, R.; Kaplan, D. L. *Biomacromolecules* **2004**, *5*, 786.
- (92) Vepari, C.; Kaplan, D. L. *Prog. Polym. Sci.* **2007**, *32*, 991.
- (93) Matsumoto, A.; Chen, J.; Collette, A. L.; Kim, U.-J.; Altman, G. H.; Cebe, P.; Kaplan, D. L. *J. Phys. Chem. B* **2006**, *110*, 21630.
- (94) Keene, E. C., Cornell University, 2010.
- (95) Eastoe, J. E. *Biochem. J.* **1955**, *61*, 589.
- (96) Voet, D.; Voet, J. G.; Pratt, C. W. In *Fundamentals of Biochemistry*; John Wiley & Sons: New York, 2002, p 132.
- (97) Kuijpers, A. J.; Engbers, G. H. M.; Feijen, J.; De Smedt, S. C.; Meyvis, T. K. L.; Demeester, J.; Krijgsveld, J.; Zaat, S. A. J.; Dankert, J. *Macromolecules* **1999**, *32*, 3325.
- (98) Naghash, H. J.; Okay, O. *J. Appl. Polym. Sci.* **1996**, *60*, 971.
- (99) Suzuki, A.; Yamazaki, M.; Kobiki, Y. *J. Chem. Phys.* **1996**, *104*, 1751.
- (100) Hsu, T. P.; Cohen, C. *Polymer* **1984**, *25*, 1419.
- (101) Iler, R. K. *The Chemistry of Silica: Solubility, Polymerization, Colloid and Surface Properties, and Biochemistry*; John Wiley & Sons: New York, 1979.
- (102) Plank, C. J. *J. Colloid Sci.* **1947**, *2*, 413.
- (103) Hurd, C. B. *J. Phys. Chem.* **1936**, *40*, 21.
- (104) Merrill, R. C.; Spencer, R. W. *J. Phys. Colloid Chem.* **1950**, *54*, 806.
- (105) Vidal, O.; Robert, M. C.; Boue, F. *J. Cryst. Growth* **1998**, *192*, 271.
- (106) Acker, E. G. *J. Colloid Interf. Sci.* **1970**, *32*, 41.
- (107) Drost-Hansen, W. *Ind. Eng. Chem.* **1969**, *61*, 10.

- (108) Mashl, R. J.; Joseph, S.; Aluru, N. R.; Jakobsson, E. *Nano Letters* **2003**, *3*, 589.
- (109) Ratajska-Gadomska, B.; Bialkowski, B.; Gadomski, W.; Radzewicz, C. *J. Chem. Phys.* **2007**, *126*, 184708.
- (110) Sekine, Y.; Ikeda-Fukazawa, T. *J. Chem. Phys.* **2009**, *130*.
- (111) Singh, T.; Meena, R.; Kumar, A. *J. Phys. Chem. B* **2009**, *113*, 2519.
- (112) Ratajska-Gadomska, B.; Gadomski, W. *J. Chem. Phys.* **2004**, *121*, 12583.
- (113) Goda, T.; Watanabe, J.; Takai, M.; Ishihara, K. *Polymer* **2006**, *47*, 1390.
- (114) Chavez, F. V.; Persson, E.; Halle, B. *J. Am. Chem. Soc.* **2006**, *128*, 4902.
- (115) Jhon, M. S.; Andrade, J. D. *J. Biomed. Mater. Res.* **1973**, *7*, 509.
- (116) Lee, H. B.; Jhon, M. S.; Andrade, J. D. *J. Colloid Interf. Sci.* **1975**, *51*, 225.
- (117) Aizawa, M.; Suzuki, S. *Bull. Chem. Soc. Jpn.* **1971**, *44*, 2967.
- (118) Garside, J.; Davey, R. *From Molecules to Crystallizers: An Introduction to Crystallization*; Oxford University Press: New York, 2000.
- (119) Chernov, A. A. *Modern Crystallography III: Crystal Growth*; Springer-Verlag: New York, 1984; Vol. 36.
- (120) De Yoreo, J. J.; Vekilov, P. In *Reviews in Mineralogy and Geochemistry: Biomineralization*; Dove, P. M., Yoreo, J. J. D., Weiner, S., Eds.; The Mineralogical Society of America: Washington, D. C., 2003; Vol. 54, p 57.
- (121) Sunagawa, I. *Growth, Morphology and Perfection*; Cambridge University Press: Cambridge, 2005.
- (122) Sunagawa, I. *Bulletin De Mineralogie* **1981**, *104*, 81.
- (123) Garcia-Ruiz, J. M.; Gavira, J. A.; Otalora, F.; Guasch, A.; Coll, M. *Mater. Res. Bull.* **1998**, *33*, 1593.
- (124) Sica, F.; Demasi, D.; Mazzarella, L.; Zagari, A.; Capasso, S.; Pearl, L. H.; Dauria, S.; Raia, C. A.; Rossi, M. *Acta Crystallogr. Sect. D-Biol. Crystallogr.* **1994**, *50*, 508.
- (125) Vidal, O.; Robert, M. C.; Arnoux, B.; Capelle, B. *J. Cryst. Growth* **1999**, *196*, 559.
- (126) Lorber, B.; Sauter, C.; Ng, J. D.; Zhu, D. W.; Giege, R.; Vidal, O.; Robert, M. C.; Capelle, B. *J. Cryst. Growth* **1999**, *204*, 357.
- (127) Miller, T. Y.; He, X.-m.; Carter, D. C. *J. Cryst. Growth* **1992**, *122*, 306.

- (128) Lorber, B.; Sauter, C.; Theobald-Dietrich, A.; Moreno, A.; Schellenberger, P.; Robert, M. C.; Capelle, B.; Sanglier, S.; Potier, N.; Giege, R. *Prog. Biophys. Mol. Biol.* **2009**, *101*, 13.
- (129) Pietras, Z.; Lin, H. T.; Surade, S.; Luisi, B.; Slattery, O.; Pos, K. M.; Moreno, A. *J. Appl. Crystallogr.* **2010**, *43*, 58.
- (130) Prieto, M.; Putnis, A.; Fernández-Díaz, L.; Lúpez-Andrés, S. *J. Cryst. Growth* **1994**, *142*, 225.
- (131) Srzic, D.; Pokric, B.; Pucar, Z. *Z. Phys. Chem.* **1976**, *103*, 157.
- (132) Pučar, Z.; Pokrić, B.; Graovac, A. *Anal. Chem.* **1974**, *46*, 403.
- (133) Putnis, A.; Prieto, M.; Fernández-Díaz, L. *Geol. Mag.* **1995**, *132*, 1.
- (134) Andreatza, P.; Lefauchaux, F.; Mutaftschiev, B. *J. Cryst. Growth* **1988**, *92*, 415.
- (135) Dennis, J.; Henisch, H. K. *J. Electrochem. Soc.* **1967**, *114*, 263.
- (136) Provost, K.; Robert, M. C. *J. Cryst. Growth* **1991**, *110*, 258.
- (137) Van Driessche, A. E. S.; Otalora, F.; Gavira, J. A.; Sazaki, G. *Cryst. Growth Des.* **2008**, *8*, 3623.
- (138) Tanabe, K.; Hirose, M.; Murai, R.; Sugiyama, S.; Shimizu, N.; Maruyama, M.; Takahashi, Y.; Adachi, H.; Takano, K.; Murakami, S.; Mori, Y.; Mizohata, E.; Inoue, T.; Matsumura, H. *Appl. Phys. Express* **2009**, *2*.
- (139) Imai, H.; Oaki, Y. *CrystEngComm* **2010**, *12*, 1679.
- (140) Garcia-Ruiz, J. M. *J. Cryst. Growth* **1986**, *75*, 441.
- (141) *CRC Handbook of Chemistry and Physics*; 87 ed., 2007.
- (142) Petrova, R. I.; Swift, J. A. *J. Am. Chem. Soc.* **2004**, *126*, 1168.
- (143) Petrova, R. I.; Patel, R.; Swift, J. A. *Cryst. Growth Des.* **2006**, *6*, 2709.
- (144) Petrova, R. I.; Swift, J. A. *Cryst. Growth Des.* **2002**, *2*, 573.
- (145) Grassmann, O.; Muller, G.; Lobmann, P. *Chem. Mater.* **2002**, *14*, 4530.
- (146) Estroff, L. A.; Addadi, L.; Weiner, S.; Hamilton, A. D. *Org. Biomol. Chem.* **2004**, *2*, 137.
- (147) Nickl, H. J.; Henisch, H. K. *J. Electrochem. Soc.* **1969**, *116*, 1258.
- (148) Gavira, J. A.; Garcia-Ruiz, J. M. *Acta Crystallogr. Sect. D-Biol. Crystallogr.* **2002**, *58*, 1653.
- (149) Li, H.; Fujiki, Y.; Sada, K.; Estroff, L. A. *CrystEngComm* **2011**, *13*, 1060.

- (150) Patel, A.; Venkateswara Rao, A. *Bull. Mater. Sci.* **1982**, *4*, 527.
- (151) Prieto, M.; Fernández-Díaz, L.; Lúpez-Andrès, L.; Lúpez-Andrès, S. *J. Cryst. Growth* **1989**, *98*, 447.
- (152) Dorvee, J. R.; Boskey, A. L.; Estroff, L. A. *CrystEngComm* **2012**, *submitted*.
- (153) Pina, C. M.; Fernández-Díaz, L.; Prieto, M. *J. Cryst. Growth* **1997**, *177*, 102.
- (154) Gotliv, B. A.; Addadi, L.; Weiner, S. *ChemBioChem* **2003**, *4*, 522.
- (155) Nudelman, F.; Gotliv, B. A.; Addadi, L.; Weiner, S. *J. Struct. Biol.* **2006**, *153*, 176.
- (156) Sudo, S.; Fujikawa, T.; Nagakura, T.; Ohkubo, T.; Sakaguchi, K.; Tanaka, M.; Nakashima, K.; Takahashi, T. *Nature* **1997**, *387*, 563.
- (157) Weiner, S.; Traub, W. *FEBS Lett.* **1980**, *111*, 311.
- (158) Weiner, S.; Talmon, Y.; Traub, W. *Int. J. Biol. Macromol.* **1983**, *5*, 325.
- (159) Ehrlich, H.; Koutsoukos, P. G.; Demadis, K. D.; Pokrovsky, O. S. *Micron* **2009**, *40*, 169.
- (160) Przenioslo, R.; Stolarski, J.; Mazur, M.; Brunelli, M. *J. Struct. Biol.* **2008**, *161*, 74.
- (161) Wainwright, S. A. *Exp. Cell Res.* **1964**, *34*, 213.
- (162) Kingsley, R. J.; Tsuzaki, M.; Watabe, N.; Mechanic, G. L. *Biol. Bull.* **1990**, *179*, 207.
- (163) Rosauer, E. A.; Redmond, J. R. *J. Laryngol. Otol.* **1985**, *99*, 21.
- (164) Simon, P.; Carrillo-Cabrera, W.; Huang, Y. X.; Buder, J.; Borrmann, H.; Cardoso-Gil, R.; Rosseeva, E.; Yarin, Y.; Zahnert, T.; Kniep, R. *Eur. J. Inorg. Chem.* **2011**, 5370.
- (165) Fermin, C. D. *Microscopy Research and Technique* **1993**, *25*, 297.
- (166) Zhao, X.; Yang, H.; Yamoah, E. N.; Lundberg, Y. W. *Dev. Biol.* **2007**, *304*, 508.
- (167) Davis, J. G.; Burns, F. R.; Navaratnam, D.; Lee, A. M.; Ichimiya, S.; Oberholtzer, J. C.; Greene, M. I. *Proc. Natl. Acad. Sci. U. S. A.* **1997**, *94*, 707.
- (168) Falini, G.; Fermani, S.; Gazzano, M.; Ripamonti, A. *Chem. A Eur. J.* **1997**, *3*, 1807.
- (169) Keene, E. C.; Evans, J. S.; Estroff, L. A. *Cryst. Growth Des.* **2010**, *10*, 5169.
- (170) Mata, A.; Geng, Y. B.; Henrikson, K. J.; Aparicio, C.; Stock, S. R.; Satcher, R. L.; Stupp, S. I. *Biomaterials* **2010**, *31*, 6004.
- (171) Busch, S.; Schwarz, U.; Kniep, R. *Chem. Mater.* **2001**, *13*, 3260.

- (172) Gkioni, K.; Leeuwenburgh, S. C. G.; Douglas, T. E. L.; Mikos, A. G.; Jansen, J. A. *Tissue Engineering Part B-Reviews* **2010**, *16*, 577.
- (173) Li, H. Y.; Estroff, L. A. *CrystEngComm* **2007**, *9*, 1153.
- (174) Pastero, L.; Costa, E.; Alessandria, B.; Rubbo, M.; Aquilano, D. *J. Cryst. Growth* **2003**, *247*, 472.
- (175) Yang, D.; Qi, L. M.; Ma, J. M. *Chem. Commun.* **2003**, 1180.
- (176) Watanabe, J.; Akashi, M. *Cryst. Growth Des.* **2008**, *8*, 478.
- (177) Borah, B. M.; Lakshmi, H.; Das, G. *Mater. Sci. Eng. C-Biomimetic Supramol. Syst.* **2008**, *28*, 1173.
- (178) Wada, N.; Yamashita, K.; Umegaki, T. *J. Cryst. Growth* **1995**, *148*, 297.
- (179) Wada, N.; Yamashita, K.; Umegaki, T. *J. Colloid Interf. Sci.* **1998**, *201*, 1.
- (180) Wada, N.; Okazaki, M.; Tachikawa, S. *J. Cryst. Growth* **1993**, *132*, 115.
- (181) Wada, N.; Yamashita, K.; Umegaki, T. *J. Colloid Interf. Sci.* **1999**, *212*, 357.
- (182) Boggavarapu, S.; Chang, J.; Calvert, P. *Mater. Sci. Eng. C* **2000**, *11*, 47.
- (183) Kayano, K.; Saruwatari, K.; Kogure, T.; Shiraiwa, Y. *Marine Biotechnology* **2011**, *13*, 83.
- (184) Butler, M. F.; Glaser, N.; Weaver, A. C.; Kirkland, M.; Heppenstall-Butler, M. *Cryst. Growth Des.* **2006**, *6*, 781.
- (185) Kosanović, C.; Falini, G.; Kralj, D. *Cryst. Growth Des.* **2011**, *11*, 269.
- (186) Ma, Y.; Feng, Q. *J. Solid State Chem.* **2011**, *184*, 1008.
- (187) Xie, M.; Olderoy, M. O.; Andreassen, J.-P.; Selbach, S. M.; Strand, B. L.; Sikorski, P. *Acta Biomaterialia* **2010**, *6*, 3665.
- (188) Olderoy, M. O.; Xie, M. L.; Strand, B. L.; Flaten, E. M.; Sikorski, P.; Andreassen, J. P. *Cryst. Growth Des.* **2009**, *9*, 5176.
- (189) Xiao, J. W.; Zhu, Y. C.; Liu, Y. Y.; Liu, H. J.; Zeng, Y.; Xu, F. F.; Wang, L. Z. *Cryst. Growth Des.* **2008**, *8*, 2887.
- (190) Munro, N. H.; Green, D. W.; Dangerfield, A.; McGrath, K. M. *Dalton T.* **2011**, *40*, 9259.
- (191) Xie, M. L.; Olderoy, M. O.; Andreassen, J. P.; Selbach, S. M.; Strand, B. L.; Sikorski, P. *Acta Biomaterialia* **2010**, *6*, 3665.

- (192) Li, X. P.; Shen, Q.; Su, Y. L.; Tian, F.; Zhao, Y.; Wang, D. J. *Cryst. Growth Des.* **2009**, *9*, 3470.
- (193) Munro, N. H.; McGrath, K. M. *Dalton T.* **2011**, *40*, 9269.
- (194) Falini, G.; Fermani, S.; Gazzano, M.; Ripamonti, A. *Chem. A Eur. J.* **1998**, *4*, 1048.
- (195) Falini, G.; Fermani, S.; Gazzano, M.; Ripamonti, A. *J. Chem. Soc., Dalton Trans.* **2000**, 3983.
- (196) Falini, G.; Gazzano, M.; Ripamonti, A. *Adv. Mater.* **1994**, *6*, 46.
- (197) Xiao, J. W.; Yang, S. H. *CrystEngComm* **2011**, *13*, 2472.
- (198) Falini, G.; Gazzano, M.; Ripamonti, A. *J. Cryst. Growth* **1994**, *137*, 577.
- (199) Grassmann, O.; Lobmann, P. *Chem. A Eur. J.* **2003**, *9*, 1310.
- (200) McCauley, J. W.; Roy, R. *Am. Mineral.* **1974**, *59*, 947.
- (201) Dominguez-Bella, S.; Garcia-Ruiz, J. M. *J. Cryst. Growth* **1986**, *79*, 236.
- (202) Fernández-Díaz, L.; Putnis, A.; Prieto, M.; Putnis, C. V. *J. Sediment. Res.* **1996**, *66*, 482.
- (203) Fernandez-Diaz, L.; Astilleros, J. M.; Pina, C. M. *Chem. Geol.* **2006**, *225*, 314.
- (204) Imai, H.; Terada, T.; Miura, T.; Yamabi, S. *J. Cryst. Growth* **2002**, *244*, 200.
- (205) Garcia-Ruiz, J. M. *J. Cryst. Growth* **1985**, *73*, 251.
- (206) Katsikopoulos, D.; Fernández-González, A.; Prieto, M. *Mineral. Mag.* **2009**, *73*, 269.
- (207) Katsikopoulos, D.; Fernández-González, A.; Prieto, A. C.; Prieto, M. *Chem. Geol.* **2008**, *254*, 87.
- (208) Barta, C.; Zemlicka, J.; Rene, V. *J. Cryst. Growth* **1971**, *10*, 158.
- (209) Prieto, M.; García-Ruiz, J. M.; Amoros, J. L. *J. Cryst. Growth* **1981**, *52*, 864.
- (210) Sánchez-Pastor, N.; Gigler, A. M.; Cruz, J. A.; Park, S.-H.; Jordan, G.; Fernández-Díaz, L. *Cryst. Growth Des.* **2011**, *11*, 3081.
- (211) Prieto, M.; Fernández-González, A.; Putnis, A.; Fernández-Díaz, L. *Geochim. Cosmochim. Acta* **1997**, *61*, 3383.
- (212) Keene, E. C.; Evans, J. S.; Estroff, L. A. *Cryst. Growth Des.* **2010**, *10*, 1383.
- (213) Kuang, M.; Wang, D. Y.; Gao, M. Y.; Hartmarm, J.; Mohwald, H. *Chem. Mater.* **2005**, *17*, 656.

- (214) Shi, N.; Yin, G.; Han, M.; Xu, Z. *Colloid Surface B* **2008**, *66*, 84.
- (215) Belcher, A. M.; Wu, X. H.; Christensen, R. J.; Hansma, P. K.; Stucky, G. D.; Morse, D. E. *Nature* **1996**, *381*, 56.
- (216) Levi, Y.; Albeck, S.; Brack, A.; Weiner, S.; Addadi, L. *Chem. A Eur. J.* **1998**, *4*, 389.
- (217) Falini, G.; Sartor, G.; Fabbri, D.; Vergni, P.; Fermani, S.; Belcher, A. M.; Stucky, G. D.; Morse, D. E. *J. Struct. Biol.* **2011**, *173*, 128.
- (218) Falini, G.; Weiner, S.; Addadi, L. *Calcif. Tissue Int.* **2003**, *72*, 548.
- (219) Cheng, C.; Shao, Z. Z.; Vollrath, F. *Adv. Funct. Mater.* **2008**, *18*, 2172.
- (220) An, X. Q.; Cao, C. B. *J. Phys. Chem. C* **2008**, *112*, 15844.
- (221) An, X. Q.; Cao, C. B. *J. Phys. Chem. C* **2008**, *112*, 6526.
- (222) Wang, T.; Che, R. C.; Li, W. T.; Mi, R. X.; Shao, Z. Z. *Cryst. Growth Des.* **2011**, *11*, 2164.
- (223) Wu, Y. D.; Cheng, C.; Yao, J. R.; Chen, X.; Shao, Z. Z. *Langmuir* **2011**, *27*, 2804.
- (224) Imai, H.; Oaki, Y.; Kotachi, A. *Bull. Chem. Soc. Jpn.* **2006**, *79*, 1834.
- (225) Raz, S.; Weiner, S.; Addadi, L. *Adv. Mater.* **2000**, *12*, 38.
- (226) Mann, S.; Didymus, J. M.; Sanderson, N. P.; Heywood, B. R.; Samper, E. J. A. *J. Chem. Soc., Faraday Trans.* **1990**, *86*, 1873.
- (227) Han, Y. J.; Aizenberg, J. *J. Am. Chem. Soc.* **2003**, *125*, 4032.
- (228) Cantaert, B.; Kim, Y.-Y.; Ludwig, H.; Nudelman, F.; Sommerdijk, N. A. J. M.; Meldrum, F. C. *Adv. Funct. Mater.* **2012**, *10.1002/adfm.201102385*.
- (229) Gries, K.; Kroger, R.; Kubel, C.; Fritz, M.; Rosenauer, A. *Acta Biomater.* **2009**, *5*, 3038.
- (230) Robach, J. S.; Stock, S. R.; Veis, A. *J. Struct. Biol.* **2005**, *151*, 18.
- (231) Aizenberg, J.; Hanson, J.; Koetzle, T. F.; Weiner, S.; Addadi, L. *J. Am. Chem. Soc.* **1997**, *119*, 881.
- (232) Berman, A.; Hanson, J.; Leiserowitz, L.; Koetzle, T. F.; Weiner, S.; Addadi, L. *Science* **1993**, *259*, 776.
- (233) Aizenberg, J.; Muller, D. A.; Grazul, J. L.; Hamann, D. R. *Science* **2003**, *299*, 1205.
- (234) Finnemore, A. S.; Scherer, M. R. J.; Langford, R.; Mahajan, S.; Ludwigs, S.; Meldrum, F. C.; Steiner, U. *Adv. Mater.* **2009**, *21*, 3928.

- (235) Li, C.; Qi, L. M. *Angew. Chem. Int. Ed.* **2008**, *47*, 2388.
- (236) Park, R. J.; Meldrum, F. C. *J. Mater. Chem.* **2004**, *14*, 2291.
- (237) Hetherington, N. B. J.; Kulak, A. N.; Sheard, K.; Meldrum, F. C. *Langmuir* **2006**, *22*, 1955.
- (238) Muñoz-Espí, R.; Chandra, A.; Wegner, G. *Cryst. Growth Des.* **2007**, *7*, 1584.
- (239) Lu, C. H.; Qi, L. M.; Cong, H. L.; Wang, X. Y.; Yang, J. H.; Yang, L. L.; Zhang, D. Y.; Ma, J. M.; Cao, W. X. *Chem. Mater.* **2005**, *17*, 5218.
- (240) Kim, Y. Y.; Ribeiro, L.; Maillot, F.; Ward, O.; Eichhorn, S. J.; Meldrum, F. C. *Adv. Mater.* **2010**, *22*, 2082.
- (241) Huang, Y. X.; Burder, J.; Cardoso-Gli, R.; Prots, Y.; Carrillo-Cabrera, W.; Simon, P.; Kniep, R. *Angewandte Chemie International Edition* **2008**, *47*, 8280.
- (242) Page, M. G.; Nassif, N.; Borner, H. G.; Antonietti, M.; Colfen, H. *Cryst. Growth Des.* **2008**, *8*, 1792.
- (243) Kim, Y. Y.; Ganesan, K.; Yang, P. C.; Kulak, A. N.; Borukhin, S.; Pechook, S.; Ribeiro, L.; Kroger, R.; Eichhorn, S. J.; Armes, S. P.; Pokroy, B.; Meldrum, F. C. *Nat. Mater.* **2011**, *10*, 890.
- (244) Li, H. Y.; Estroff, L. A. *J. Am. Chem. Soc.* **2007**, *129*, 5480.
- (245) Khaimov-Mal'kov, V. I. *Sov. Phys.: Crystallogr.* **1958**, *3*, 487.
- (246) Hanoka, J. I. *J. Appl. Phys.* **1969**, *40*, 2694.
- (247) Lefauchaux, F.; Robert, M. C.; Bernard, Y.; Gits, S. *Cryst. Res. Technol.* **1984**, *19*, 1541.
- (248) Chernov, A. A.; Temkin, D. E. In *Current Topics in Materials Science*; Kaldis, E., Ed.; North-Holland: New York, 1977; Vol. 2, p 3.
- (249) Kliya, M. O.; Sokolova, I. G. *Sov. Phys. Crystallogr.* **1958**, *3*, 217.
- (250) Uhlmann, D. R.; Chalmers, B.; Jackson, K. A. *J. Appl. Phys.* **1964**, *35*, 2986.
- (251) Aizenberg, J.; Black, A. J.; Whitesides, G. M. *Nature* **1999**, *398*, 495.
- (252) Chernov, A. A.; Temkin, D. E.; Melnikova, A. M. *Kristallografiya* **1976**, *21*, 652.
- (253) Meldrum, F. C. *Int. Mater. Rev.* **2003**, *48*, 187.
- (254) Sommerdijk, N.; de With, G. *Chem. Rev.* **2008**, *108*, 4499.

### 3 SECTIONING OF INDIVIDUAL HEMATITE PSEUDOCUBES WITH FODUCES ION BEAM ENABLES QUANTITATIVE STRCUTRAL CHARACTERIZATION AT NANOMETER LENGTH SCALES<sup>♦</sup>

#### 3.1 Abstract

A dual-beam focused ion beam (FIB) microscope equipped with a nanomanipulator was used to fabricate slices from within individual hematite ( $\alpha$ -Fe<sub>2</sub>O<sub>3</sub>) pseudocubes with selected orientations with respect to the original pseudocubes. Transmission electron microanalysis through selected area electron diffraction enabled assignment of each thin section to a particular zone of the hematite lattice. While the pseudocubes are composed of numerous crystallites, 25-50 nm in size, they are not simply polycrystalline particles. Electron diffraction of thin-sections showed that while the pseudocubic hematite particles are composed of numerous coherent domains, the individual thin sections display a net crystallographic orientation to the underlying hematite lattice. Quantitative analysis of the lattice misorientation between coherent domains was calculated from the azimuthal spread of electron diffraction peaks and is consistent with a structure that contains small-angle grain boundaries. Based upon this analysis, we conclude that the pseudocubic hematite particles are mosaic crystals, composed of highly oriented coherent domains.

#### 3.2 Introduction

Due to its abundance, stability, and low cost, as well as its inherent electronic properties, hematite ( $\alpha$ -Fe<sub>2</sub>O<sub>3</sub>) holds great promise as a photocatalytic material.<sup>1</sup> Hematite is amenable to formation in a wide array of particle shapes and film morphologies.<sup>2-6</sup> The many shapes in which hematite can be synthesized provide opportunities to control the crystallographic planes that are expressed and thereby control the

---

<sup>♦</sup>Portions reproduced with permission from E. Asenath-Smith & L. A. Estroff, *Microscopy and Microanalysis* **2014**, 20, 635. Copyright © 2014 Microscopy Society of America.

catalytic activity of the materials.<sup>7-9</sup> Hematite particles are often single crystal-like,<sup>10</sup> meaning that they exist as non-idiomorphic particles, which are themselves composed of crystallites. An understanding of the crystallography of the various forms of hematite will inform the study of this material in technological applications. In this report, the crystallography of the hexagonal hematite lattice within pseudocubic-shaped hematite particles is investigated.

### 3.2.1 Hematite Crystallography and Synthesis

While hematite has a hexagonal lattice, space group  $R\bar{3}c$ , it can be synthesized in many forms, which include pseudocubes, spindles, and spheres, with sizes that are commonly 100's of nanometers up to  $\sim 1 \mu\text{m}$ . The shape of these particles is a function of synthesis conditions including reagent concentration, pH, temperature, reaction time, and counter-anions,<sup>2</sup> while their classification as (real) single crystals or polycrystalline particles can vary with the shape. Pseudocubes of hematite can be prepared in aqueous solution by both acid- and base-catalyzed hydrolysis of iron chloride solutions.<sup>2,11,12</sup> Under acidic conditions, the hematite phase recrystallizes from the metastable akaganeite ( $\beta\text{-FeO(OH)}$ ) phase.<sup>13,14</sup> Generally, a dissolution-reprecipitation mechanism is rationalized in terms of the relative solubilities of akaganeite and hematite: the higher solubility of the akaganeite phase dictates its dissolution with subsequent precipitation of the less soluble hematite.<sup>2,15-18</sup> The presence of chloride ions within hematite pseudocubes has been documented, and is suggested to play a role in the formation of the pseudocubic particle shape.<sup>12,14</sup> Based on a cryo-TEM, time-resolved study, the hematite pseudocubic particle shape is influenced by the rod-like morphology of the initial  $\beta\text{-FeO(OH)}$  phase.<sup>17</sup> Specifically, pseudocubes form in higher concentration solutions from the aggregation of akaganeite rods into planar, raft-like structures, which template the growth of the hematite phase and facilitate the heterogeneous nucleation of hematite on akaganeite surfaces.<sup>17</sup>

### 3.2.2 Hematite Internal Structure

While the hematite pseudocube is known to be composed of crystallites, the lattice relationships between these coherent domains and the pseudocubic shape are not well characterized. This deficiency stems from the length scales associated with the hematite particles. For example, the crystallites that compose hematite pseudocubes have been estimated at 10's nm by Scherrer analysis: a feasible size range for electron microscopy.<sup>12</sup> However, the 1  $\mu\text{m}$  size of the particles themselves demands that they be formed into thin sections for electron microanalysis. The methods utilized to thin section samples often involve the embedding of particles within a polymer matrix: thereby introducing ambiguity into the precise location within the particle from which the thin sections originated. The length scales of the pseudocubes and the coherent domains that compose them disqualify them from characterization with x-rays: even synchrotron-generated x-rays have spot sizes that are up to an order of magnitude larger than an individual pseudocubic particle.<sup>19</sup> A full characterization of complex structures, such as those seen in hematite pseudocubes, requires the resolution of TEM but the particles must also be sectioned without loss of the geometric relationship of the thin section to original particle; a requirement that is not easily met by current sample preparation techniques.

Despite the challenging combination of length scales present in hematite pseudocubes, some work has been done to characterize their internal structure in an effort to identify the net orientation of the hematite (hexagonal) c-axis within pseudocubes. After observing the dominance of  $\{012\}$  planes at the surface of pseudocubes and recognizing that a pseudocube can be derived from a hexagonal lattice via the expression of  $\{012\}$  planes, the net location of the c-axis was initially assigned along the body diagonal of the pseudocube.<sup>11</sup> Subsequently, through a process of embedding and sectioning with a microtome, Park and Shindo et al. were able to form thin sections of hematite pseudocubes for characterization with high-resolution electron microscopy.<sup>20-22</sup> From these studies, hematite pseudocubes were initially deemed polycrystals with “subcrystals ... oriented in the same direction”<sup>11</sup> and later called, “single crystals with internal discontinuities.”<sup>22</sup> Both descriptions implicate the pseudocubes as structures that are composed

of crystallites, but the extent of misorientation between adjacent coherent domains was not quantified. Lastly, because the assignment of the c-axis of the hematite lattice within the pseudocubic shape relied on surface structure, the net orientation of the hematite lattice was not unambiguously determined.

Sample preparation techniques for individual particles of  $\leq 10 \mu\text{m}$  have been developed within the atom probe tomography (APT) community. These techniques access high levels of precision using focused ion beam (FIB) milling to prepare needle-shaped specimens, with 50-150 nm tip radii, from whole particles and fibers<sup>23</sup> as well as from rectangular blocks lifted out from specific sites in a larger sample.<sup>24,25 26</sup> While the manipulation of individual particles with a nanomanipulator in a FIB is routine for preparation of needle-shaped APT specimens, it has rarely (if ever) been applied to the formation of thin sections of whole particles, less than  $\leq 10 \mu\text{m}$ , for transmission electron microanalysis.

We sought to extend the APT milling techniques for small particles to the hematite pseudocubes to assign the net orientation of the hematite lattice within pseudocubic-shaped particles using electron microscopy techniques. In order to perform this analysis with no a priori assumptions on the orientation of the lattice, we had to develop a technique that would allow us to make thin sections from the whole particles without introducing ambiguity as to the geometric location from which the thin sections originated within the pseudocubes. We devised a method to manipulate and mount whole, individual particles to TEM grids using the nanomanipulator within a dual-beam FIB microscope. With a clear view of the orientation of the pseudocube on the TEM grid, we were able to mill thin sections from specific geometric locations within each particle, allowing us to relate the crystallographic zones of the hematite lattice indexed from each slice back to the shape of the pseudocubic particles.

### **3.3 Results**

#### **3.3.1 Phase and Morphology Characterization**

Under observation with transmitted light in an optical microscope,  $\sim 1.5 \mu\text{m}$  red squares with rounded corners were observed (Figure 3.1, central image). Upon visual examination under cross-

polarized light, each particle displayed a bright red core, with a maltese cross around its periphery (Figure 3.1). The presence of a maltese cross under CPOM is characteristic of spherulitic structures.<sup>27</sup> Upon rotation under cross-polarized light, the red cores were found to extinguish at regular intervals, reminiscent of a single crystal (Figure 3.1). These two seemingly disparate signatures are indicative that the pseudocubic particles are composed of crystallites that must contain crystallographic registry between adjacent coherent domains. The pseudocubic hematite particles were formed in highly monodispersed batches (Figure 3.2a,b). The surfaces of individual cubes were rough and seem to be composed of somewhat oriented crystallites on the order of 10's of nanometers in size (Figure 3.2b,c).

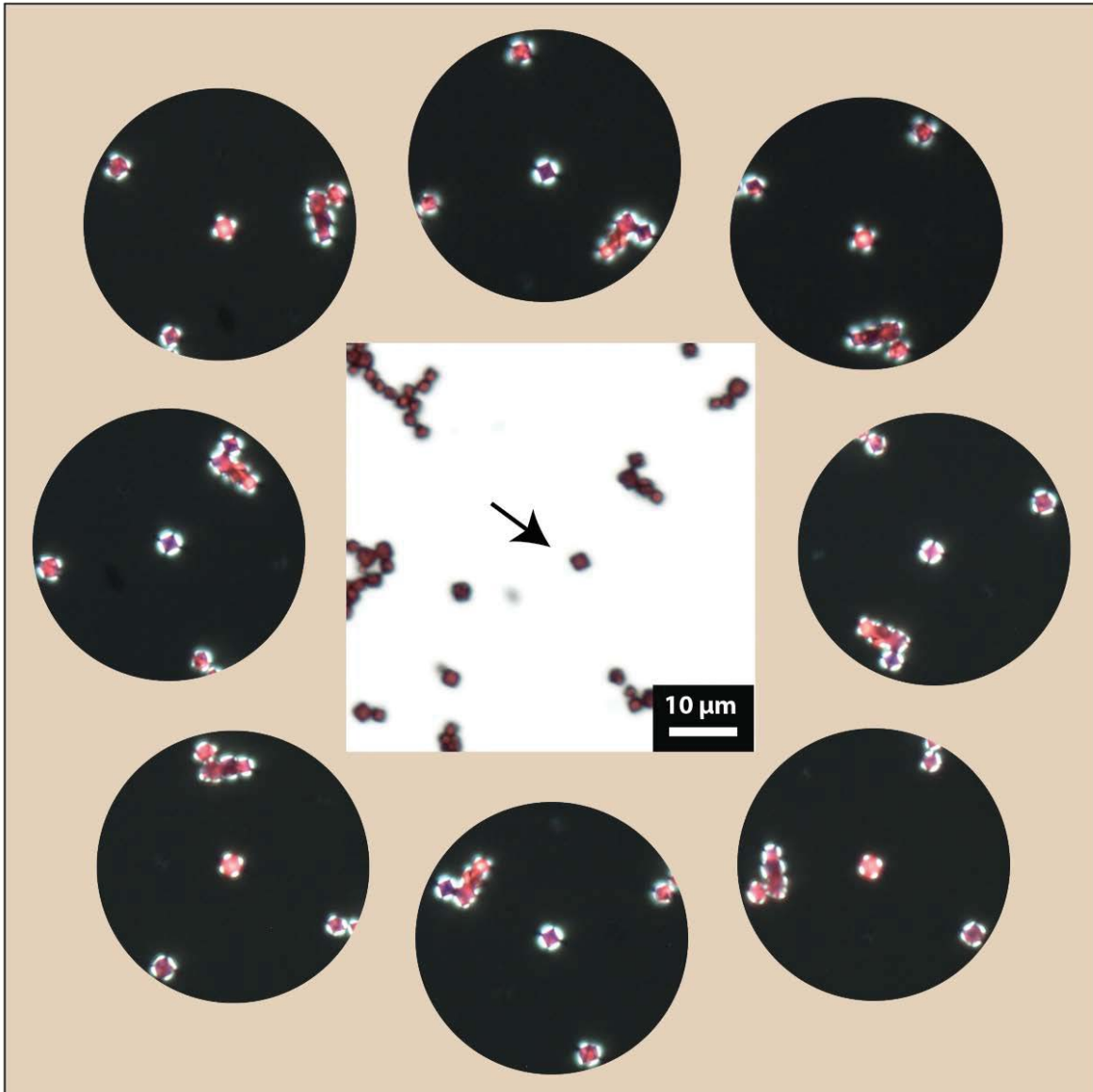


Figure 3.1 Optical microscopy images of hematite pseudocubes under transmitted light (central image) and during rotation under cross-polarized light (surrounding images). The red, pseudocubic-shaped particles are seen to exhibit a maltese cross when subject to cross polarized light, characteristic of a spherulitic particle. The particle denoted by an arrow in the central image is monitored during rotation under cross polarized light in the surrounding images and is seen to extinguish at regular intervals, a feature of a birefringent single crystals.

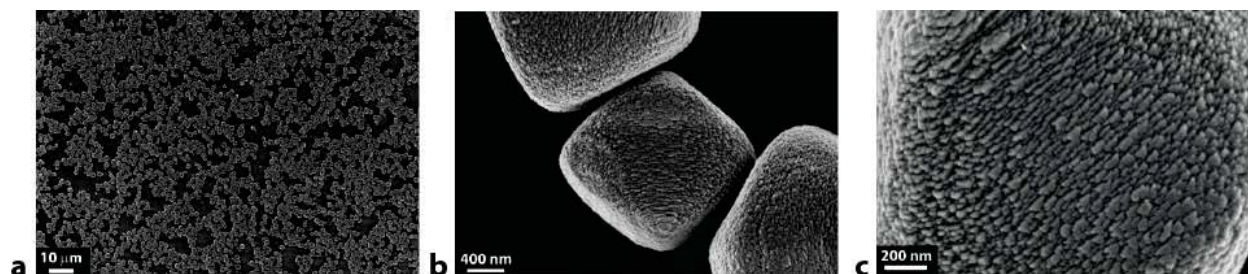


Figure 3.2 Scanning electron micrographs of hematite pseudocubes showing (a) monodispersed formation of (b) pseudocubic-shaped particles with rounded corners and (c) rough surface features.

Powder x-ray diffraction (pXRD) analysis confirmed complete formation of the hematite phase (Figure 3.3). Scherrer analysis of the pXRD data was used to estimate the crystallite size of the coherent domains that compose the hematite pseudocubes (Table S1). In all directions of the hematite lattice, it was found that the crystallites that compose the particles range from approximately 20-50 nm, consistent with the surface features seen under SEM (Figure 3.2c).

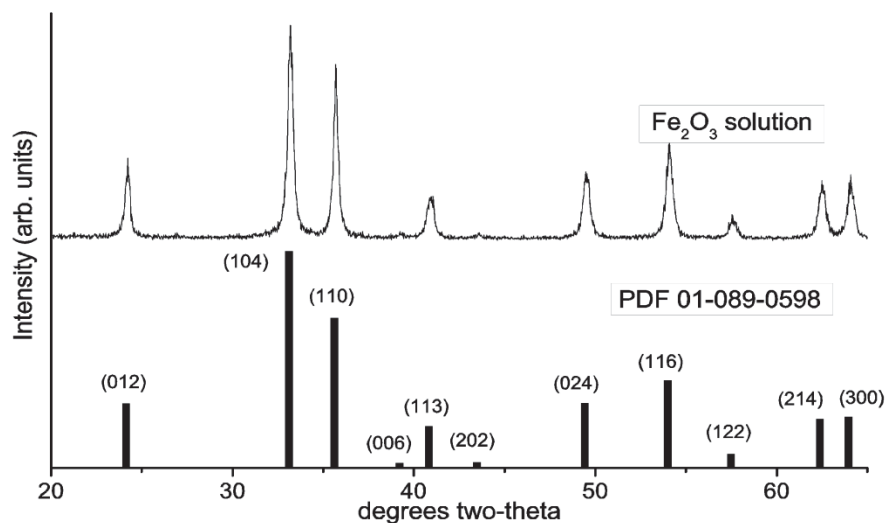


Figure 3.3 X-ray powder diffraction pattern of hematite pseudocubes and the associated reference pattern, confirming the phase pure formation of hematite.

Table 3.1 Crystallite Size (Scherrer) Analysis from pXRD data (Figure 3.3)

<b>Degrees Two-theta</b>	<b>(hkl)</b>	<b>Crystallite Size (Å)</b>
24.1	012	294(8)
33.1	104	243(4)
35.6	110	335(6)
39.5	006	479(81)
40.9	113	245(8)
43.4	202	347(54)
49.4	024	231(6)
53.9	116	241(4)

### 3.3.2 Internal Structure of Solution-Grown Pseudocubes

Given that hematite crystallizes in a hexagonal lattice, coupled with the simultaneous observation of single crystal and polycrystalline characteristics in the pseudocubic particle shapes, we sought to investigate the interior of these particles so that we could elucidate the crystallographic relationship between the pseudocubic shape and the underlying hematite lattice. Further, we sought to quantify the extent of crystallographic registry (lattice (mis)orientation) between the coherent domains that compose the particles. Noting the size of individual pseudocubes ( $\sim 1 \mu\text{m}$ ) and the length scales of the coherent domains that compose them (20 – 50 nm), it was necessary that we design a new sample preparation technique that would allow us to form thin sections from individual particles while retaining geometric correspondence to the pseudocubic shape.

We developed a technique to prepare slices through geometrically defined planes of the pseudocube using a focused ion beam system. In short, single particles were individually picked up

(Figure 3.4a) in specific orientations and transferred to copper TEM grids (Figure 3.4b) using the nanomanipulator needle. The individual particles were then thinned along specific planes of the pseudocube (Figure 3.4c). Thin sections were formed from two orientations within the pseudocubes: equatorial, which corresponds to the (200) plane of the pseudocube (Figure 3.5a); and diagonal, which corresponds to the (110) plane of the pseudocube (Figure 3.5b).

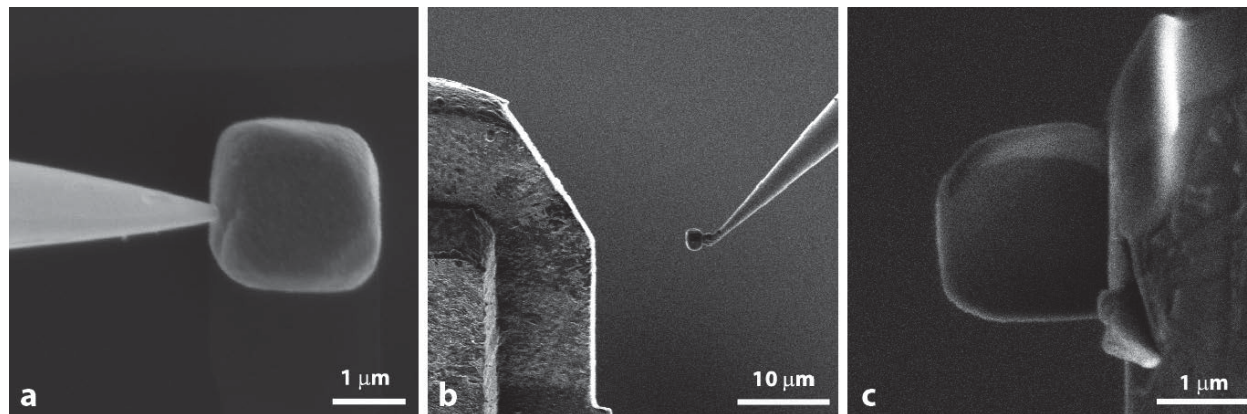


Figure 3.4 Sequence of particle manipulation for FIB thinning of the equatorial slice of a hematite pseudocube. (a) Individual particles were picked up (electron micrograph) and (b) mounted on pre-milled copper grids using the OmniProbe nanomanipulator (ion micrograph). (c) Particles were coated with a layer of Pt (lighter region capping pseudocube) before thinning with the ion beam to form sections from specific geometric planes within the pseudocubes (electron micrograph). The equatorial slice of a pseudocube is shown in (c).

Under bright field TEM, the thin sections showed radially-extending diffraction contrast (Figure 3.5c,d), consistent with a structure that is composed of crystallites with different crystallographic orientations. These data support the CPOM images, calculated crystallite sizes from pXRD, and SEM surface imaging, all of which indicate that the pseudocubes are composed of numerous coherent domains. Even with such evidences implicating the hematite pseudocubes as polycrystalline particles, all thin sections yielded distinct electron diffraction spots (Figure 3.5e,f), which are characteristic of a sample with minimal lattice misorientation between adjacent coherent domains (a real single crystal). The SAED

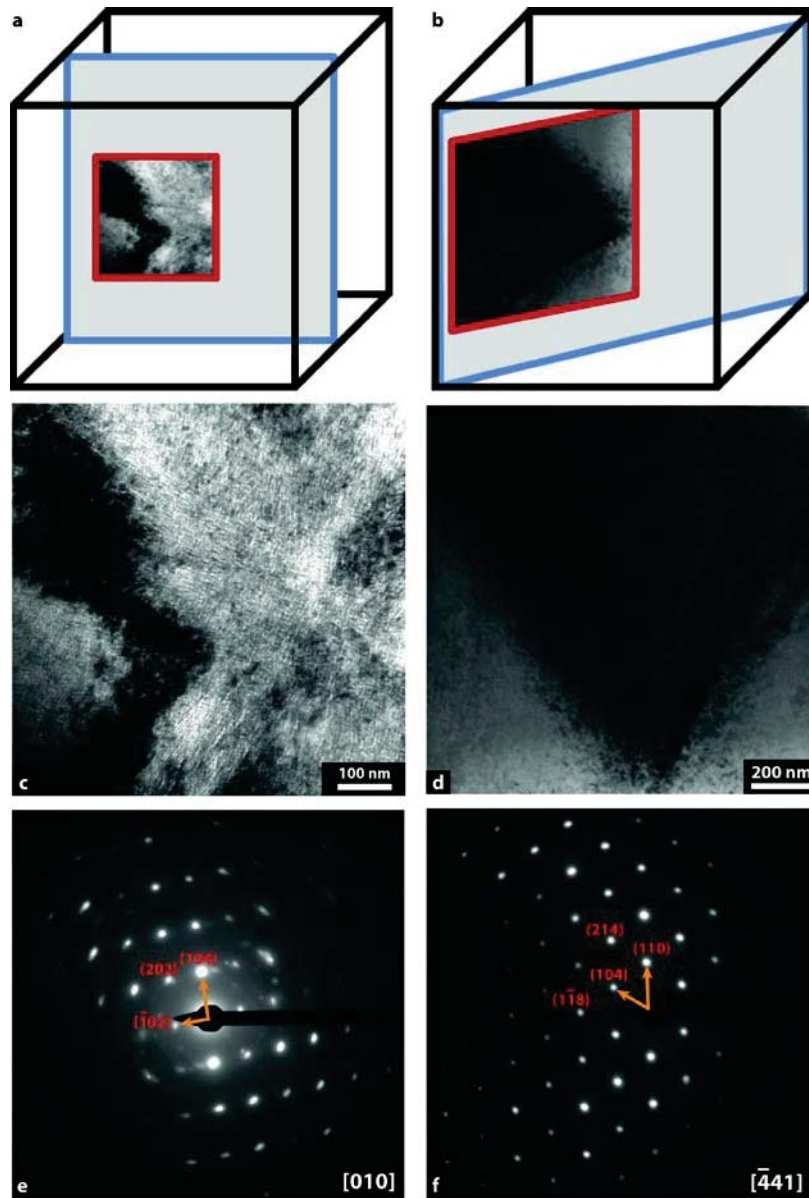


Figure 3.5 Schematic representation of the location/orientation of (a) equatorial and (b) diagonal slices taken through hematite particles by thinning with a focused ion beam. (c), (d) Bright field transmission electron micrographs of hematite particle sections shown in (a, b), respectively. (e) Selected area electron diffraction pattern taken from hematite samples shown in (c) and indexed to the [010] zone. (f) Selected area electron diffraction pattern taken from hematite sample shown in (d) and indexed to the  $[\bar{4}41]$  zone. The selected-area aperture used to obtain each diffraction pattern was roughly proportional to the area encompassed by the bright field image, as illustrated in the geometrical graphics.

pattern from the equatorial thin section (Figure 3.5e) was indexed to the [010] zone of the hematite lattice. The SAED pattern from the diagonal thin section (Figure 3.5f) was indexed to the  $[\bar{4}41]$  zone of the hematite lattice. Measured and theoretical distances are reported in Table 3.2 Table 3.3.

Table 3.2 Calculated and theoretical distances for interplanar spacings of the [010] zone used to index the SAED pattern (Figure 3.5e) from the equatorial slice of a hematite pseudocube (equivalent to a geometric (200) plane of the pseudocube).

<b>hkl</b>	<b>Theoretical <math>d_{hkl}</math> (nm)</b>	<b>Calculated <math>d_{hkl}</math> (nm)</b>
<b>10<math>\bar{2}</math></b>	0.3686	0.3706
<b>104</b>	0.2703	0.2715
<b>202</b>	0.2080	0.2282
<b>300</b>	0.1454	0.1472

Table 3.3 Calculated and theoretical distances for interplanar spacings of  $[\bar{4}41]$  zone used to index the SAED pattern (Figure 3.5f) from the diagonal slice of a hematite pseudocube (equivalent to a geometric (110) plane of pseudocube)

<b>hkl</b>	<b>Theoretical <math>d_{hkl}</math> (nm)</b>	<b>Calculated <math>d_{hkl}</math> (nm)</b>
<b>104</b>	0.2703	0.3089
<b>110</b>	0.2519	0.2719
<b>1<math>\bar{1}</math>8</b>	0.1421	0.1618
<b>214</b>	0.1340	0.1860

### 3.3.3 Net Crystallographic Orientation of Hematite Lattice within Pseudocubes

From a purely geometrical perspective, our analysis of hematite pseudocubes is based on the simplification that the pseudocubes are simply cubes; all sides were treated as equivalent. This simplification was used both in mounting/milling of particles and the subsequent zone/vector analysis that was used to identify the location of the hematite lattice within the pseudocubic shape. The geometrical analysis can then be simplified from 3D to 2D by considering only the x-y plane of the pseudocube representation. In 2D, the equatorial and diagonal thin sections of the hematite pseudocubes can be inscribed as lines over a square (Figure 3.6a red short dashed and blue dashed lines, respectively). This figure is meant to illustrate the angular relationship between the pseudocube slices made in the FIB: the equatorial and diagonal slices are geometrically positioned at  $45^\circ$  to one another within a cube. Subsequently, the crystallographically-indexed zone for each plane can be represented as a vector normal to that plane (Figure 3.6a, black solid line). Using vector analysis, the angle between the zones of the hematite lattice derived for each slice was found to be  $46^\circ$ . The physical correspondence between the geometrical slices and the angles between the crystallographic zones to which they were indexed provides both verification to the zone assignments and a link to identifying the net orientation of the hematite lattice within the pseudocubes.

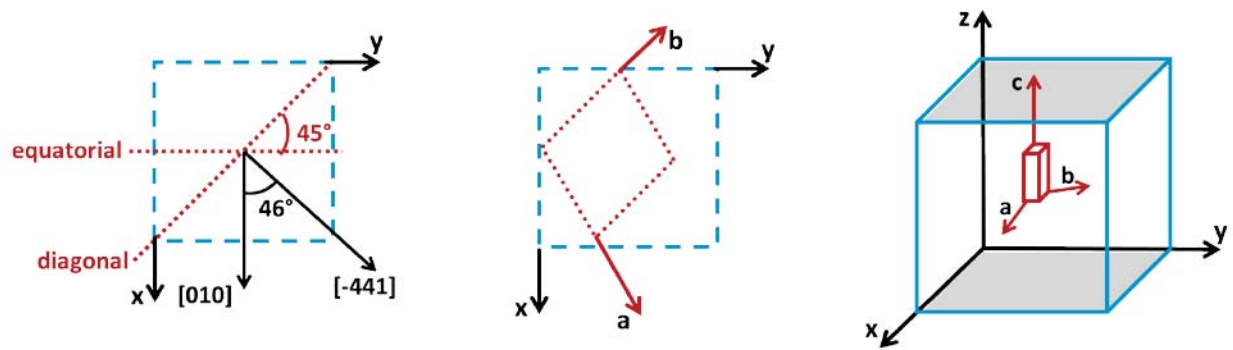


Figure 3.6 Graphical representations of the relationship between the pseudocubic-shaped hematite particles and the hexagonal hematite lattice.  $x, y, z$  axes are used to represent the geometric coordinate system of the pseudocubic particles.  $a, b, c$  axes are those of the hexagonal hematite lattice, where  $a=b$  in 3D hexagonal lattice. (a) A 2D representation of the thin sections prepared in the FIB; looking down the geometric  $z$ -axis. Blue dashed lines represent the boundary of a pseudocube, red short-dashed lines represent the FIB-prepared thin sections, and black solid lines represent the zones of the hematite lattice to which the thin sections were indexed. (b) By relationship to the  $c$ -axis of the hematite lattice, the 2D representation of the relative position of the hematite lattice within a pseudocubic shaped particle is shown. The  $c$ -axis of the hematite lattice aligns with the geometric  $z$ -axis of the pseudocube. (c) A full 3D representation of the position of the hematite lattice within a pseudocubic particle. The shaded faces of the pseudocube are meant to distinguish the two sets of equivalent faces derived for the pseudocube: 4 faces that are formed by the propagation of  $a, b$  lattice planes of hematite, and two faces that are defined by the propagation of  $c$  planes of the hematite lattice.

The 2D representation of the geometry and crystallography of the FIB slices to the hematite pseudocubes is still relevant for identification of the 3D lattice orientation through correlation of the indexed zones to the  $c$ -axis of the hematite lattice  $[001]$  within the pseudocubes. By inspection, the  $[010]$  zone is  $90^\circ$  from  $[001]$ . By calculation, the  $[\bar{4}41]$  zone is positioned at  $86^\circ$  from  $[001]$ ; approximately  $90^\circ$  also. Mathematically, if two vectors (the  $[010]$  and  $[\bar{4}41]$  zones in this case) are both oriented at approximately  $90^\circ$  to a third vector ( $[001]$ ), that third vector must be perpendicular to the plane that contains the two vectors. This result indicates that the  $[001]$  is out of the plane of the 2D representation (Figure 3.6a,b); along the geometric  $z$ -axis initially defined for the pseudocube. Thus, the 3D

representation of the hematite lattice position within the pseudocubic shape is relatively simple (Figure 3.6c). The implications of this analysis are that the hematite pseudocubes are not isotropic, but rather have two types of faces; a set of four faces that result from propagation of a,b lattice planes of hematite, and a set of 2 with character from basal planes of the hexagonal hematite lattice.

#### **3.3.4 Mosaicity within Pseudocubes**

The ability to assign a net orientation to the hematite lattice within the pseudocubic forms reveals that the pseudocubes are structures that are composed of coherent domains with minimal lattice misorientations between adjacent regions. Accordingly, we sought to quantify the extent of misorientation between adjacent crystalline domains to enable a classification of these crystals that are neither perfect single crystals nor random polycrystals. Consistent with the analyses typically applied to synchrotron x-ray diffraction experiments<sup>28</sup>, the broadening of diffraction intensities with respect to azimuthal angle is caused by a distribution of lattice orientations within the sample, where the extreme of this misorientation results in diffraction rings (a distribution of all orientations; a polycrystalline material). Mathematically, the angular distribution of lattice orientations can be derived from the FWHM of the intensity vs. azimuthal angle<sup>29</sup>. While such analyses are typically performed on the microstructural length scales accessible via x-ray diffraction experiments, we were able to translate these methods to the nanometer length scales that define the hematite pseudocubes. This analysis is the first quantitative demonstration of such nanostructural characterization of which we are aware.

Each SAED pattern was subject to polar transformation into a linear plot of azimuthal angle ( $\phi$ ) vs. radius (R) (Figure 3.7). Subsequently, line profiles were taken at constant R, to form plots of intensity (I) vs.  $\phi$ . Finally, these line profiles were fit with a Gaussian function to find FWHM of each intensity peak with respect to  $\phi$ . A single crystal of (100) oriented strontium titanate was used as a reference to estimate the instrumental contributions to azimuthal broadening; found to be  $\sim 3^\circ$ . Values of the azimuthal broadening for both the equatorial and diagonal slices are included in In the equatorial slice, the azimuthal broadening in intensity was as little as  $5^\circ$  in the [202] direction, and as much as  $13^\circ$  in the [104]

direction. Within the diagonal slice, the hematite pseudocubes were found to have angular spreads in intensity of  $\sim 5^\circ$  along the [104] and [110] directions. Noteworthy results for the diagonal slice were manifest in the azimuthal broadening of the  $[1\bar{1}8]$  reflection: the calculated value was the same as the STO single crystal reference, indicating a high degree of alignment along this direction between adjacent domains. The  $5\text{-}13^\circ$  degrees of azimuthal broadening calculated for the equatorial and diagonal slices are directly proportional to the angle of lattice mismatch between adjacent coherent domains and are consistent with the definition of small-angle grain boundaries,<sup>31</sup> supporting the classification of hematite pseudocubes as mosaic crystals (Tables 3.4 & 3.5).

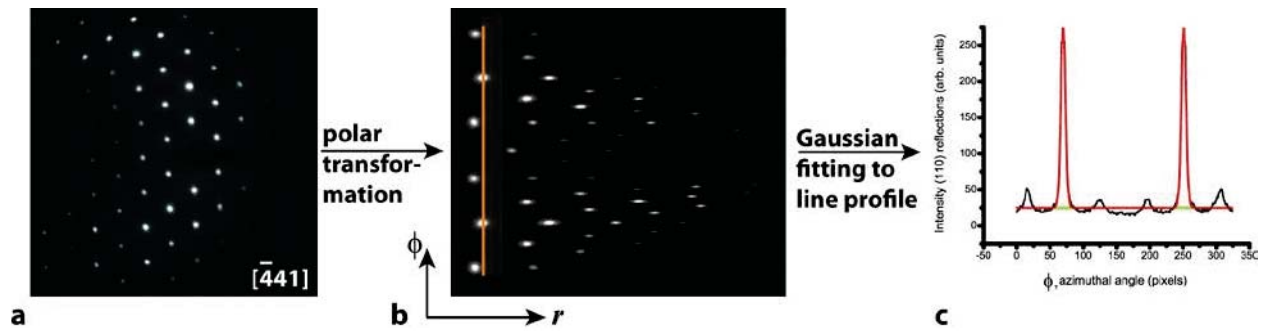


Figure 3.7 The analysis sequence that was used to calculate azimuthal broadening from SAED patterns. The SAED patterns (a) were subject to polar transformation to form linear plots of  $\phi$  vs.  $R$  (b). Subsequently linear profiles at constant  $R$  were taken to form intensity vs.  $\phi$  profiles (c) for each equivalent set of diffraction intensities. Gaussian fitting to the peaks was then used to find the  $\text{FWHM}_{\text{exp}}$  of the reflections, as it is related to the extent of misorientation between adjacent coherent domains (mosaicity) within the pseudocubes. The (110) reflections from the  $[\bar{4}41]$  zone of the diagonal slice are shown here as an example.

In the equatorial slice, the azimuthal broadening in intensity was as little as  $5^\circ$  in the [202] direction, and as much as  $13^\circ$  in the [104] direction. Within the diagonal slice, the hematite pseudocubes were found to have angular spreads in intensity of  $\sim 5^\circ$  along the [104] and [110] directions. Noteworthy results for the diagonal slice were manifest in the azimuthal broadening of the  $[1\bar{1}8]$  reflection: the calculated value was the same as the STO single crystal reference, indicating a high degree of alignment

Table 3.4 Azimuthal broadening (crystallite misorientation) as derived from FWHM of  $\phi$  vs.  $I$  of SAED intensities from [010] zone of equatorial slice (Figure 3.5e)

<b>reflection</b>	<b>FWHM<sub>exp</sub></b> <b>(pixels)</b>	<b>Azimuthal</b> <b>broadening</b> <b>(deg)</b>	<b>Mosaic</b> <b>Spread</b> <b>(deg)</b>	<b>R<sup>2</sup></b>
STO 110 <sup>a</sup>	3.879±0.117	2.895±0.087	n/a	0.97
10 $\bar{2}$	12.63±0.41	9.43±0.31	9.0	0.95
104	17.52±0.35	13.08±0.26	12.8	0.97
202	6.97±0.18	5.20±0.13	4.3	0.98

<sup>a</sup>Instrumental broadening was estimated from the (110) reflection of a 100-oriented SrTiO<sub>3</sub> single crystal (courtesy of Charles Brooks, fabricated as described in <sup>30</sup>)

Table 3.5 Azimuthal broadening (crystallite misorientation) as derived from FWHM of  $\phi$  vs.  $I$  of SAED intensities from [ $\bar{4}$ 41] Zone of diagonal slice (Figure 3.5f)

<b>reflection</b>	<b>FWHM<sub>exp</sub></b> <b>(pixels)</b>	<b>Azimuthal</b> <b>broadening</b> <b>(deg)</b>	<b>Mosaic</b> <b>Spread</b> <b>(deg)</b>	<b>R<sup>2</sup></b>
STO 110 <sup>a</sup>	3.879±0.117	2.895±0.087	n/a	0.97
104	6.47±0.21	4.83±0.15	3.9	0.95
110	7.26±0.15	5.42±0.11	5.4	0.96
1 $\bar{1}$ 8	3.88±0.08	2.89±0.06	~0	0.96

<sup>a</sup>Instrumental broadening was estimated from the (110) reflection of a 100-oriented SrTiO<sub>3</sub> single crystal (courtesy of Charles Brooks, fabricated as described in <sup>30</sup>)

along this direction between adjacent domains. The 5-13° degrees of azimuthal broadening calculated for the equatorial and diagonal slices are directly proportional to the angle of lattice mismatch between adjacent coherent domains and are consistent with the definition of small-angle grain boundaries,<sup>31</sup> supporting the classification of hematite pseudocubes as mosaic crystals.

### 3.4 Discussion

A discussion of the term ‘mosaic crystal’ must be premised with the earliest treatments of diffraction by authors such as W. L. Bragg and C. G. Darwin who introduced the idea of “mosaicity” to account for the deviation of experimental results from their theoretical predictions (which were based on the crystal as an ideal, completely perfect structure)<sup>32-34</sup>. Even real crystals that are easily perceived as single crystals can contain a mosaic structure with misorientations between adjacent domains that are up to 1°<sup>35</sup>. Once dislocations were understood (circa 1930s)<sup>36</sup>, the distribution of lattice orientations within a crystalline particle were understood to be caused by interfaces that are composed of regions with discrete dislocations within the crystalline sample<sup>35,37</sup>. Essentially, interfaces within a particle that are composed of discrete dislocations define what is known as a small-angle grain boundary, wherein the angle of misorientation between adjacent domains is <15°<sup>31</sup>. Above 15°, the dislocations that define the interface between adjacent coherent domains are no longer discrete; defining a high-angle grain boundary characteristic of polycrystalline structures<sup>31</sup>. Accordingly, we clarify that the term mosaic crystal refers to those materials that contain coherent domains, which are separated by small-angle grain boundaries. In this way, the term mosaic crystal represents a spectrum of misorientations that lie between real single crystals and polycrystals. Further, where the misorientation between adjacent crystallites is manifest in the azimuthal broadening of diffracted intensity, the mosaicity contained within a crystalline particle can be quantified.

### 3.4.1 Crystallographic Registry Between Adjacent Domains within Pseudocubes

From this perspective, we revisit the azimuthal broadening values that we calculated for the equatorial and diagonal slices of the hematite pseudocubes. The  $\{202\}$  planes along the  $[010]$  zone of the hematite lattice (within the equatorial slice) exhibit minimal lattice misorientations between adjacent coherent domains as evidenced by the calculated  $5^\circ$ . Conversely, the  $\{104\}$  planes along the same zone show misorientation values that are approaching the range of high-angle boundaries consistent with an interface composed of non-discrete dislocations. The lowest degrees of mismatch (mosaicities) between adjacent domains were calculated within the  $\{1\bar{1}8\}$  planes of the  $[\bar{4}41]$  zone (diagonal slice). The calculated values of  $\sim 3^\circ$  are on the order of the instrumental broadening indicating a high degree of coherence between the  $\{1\bar{1}8\}$  planes in adjacent domains; approaching the character of a (real) single crystal.

### 3.4.2 Net Crystallographic Orientation of Hematite Lattice within Non-Idiomorphic Pseudocubes

This work predicts that the c-axis of the hematite lattice should show a net orientation that is perpendicular to 2 faces of the pseudocube (Fig. 4c). This conclusion is in contrast to the work of Sugimoto and Muramatsu et al., who assigned the c-axis as along the body diagonal of the pseudocube<sup>11</sup>. The cause of this discrepancy could stem from two different sources. First, the hematite pseudocubes analyzed herein were formed under acidic conditions, which are known to precipitate from the akaganeite intermediate phase, with no precipitation before hydrothermal treatment. The previous works reported on pseudocubes that were formed under basic conditions, wherein hematite forms under hydrothermal conditions from a room temperature precipitated hydroxide phase. These different formation conditions may cause changes to the internal nanostructure of the resulting pseudocubes. Secondly, the previous efforts to identify the hematite lattice within pseudocubes have been largely based on observations of the surface structure. The dominant expression of  $\{012\}$  planes on the pseudocube faces lead to the derivation of the pseudocube as an  $\{012\}$  bound (single) crystal, wherein the c-axis naturally extends along the body diagonal. It is important to note that the observation of  $\{012\}$  planes on the exterior of the

pseudocubes does not imply a unique orientation of the hematite lattice within. The  $\{012\}$  family of planes are common to both  $[010]$  and  $[001]$  zones. The dominance of  $\{012\}$  planes at the surface of the pseudocubes is consistent with our assignment of the hematite lattice (Fig. 4c) as positioned with a net orientation that directs the  $[010]$  and  $[001]$  zones perpendicular to the pseudocube faces. Our ability to unambiguously track the geometric location from which our thin sections originated allowed us to assign the net orientation of the hematite lattice within hematite pseudocubes without any initial assumptions on the location of the lattice.

### **3.5 Summary and Conclusions**

A technique for single particle nanomanipulation and milling in a focused ion beam system was developed to access the nanometer-scale coherent domains contained within micron-sized pseudocubes of hematite for their crystallographic characterization. The power of this approach stems from the ability to section individual, micron-sized pseudocubes while maintaining geometric correspondence between the thin section and the parent pseudocube from which it originated. Armed with geometric knowledge on the individual thin sections, we were able to use TEM to unambiguously assign the net orientation of the hexagonal hematite lattice within the pseudocubic-shaped particles. Further, we were able to quantify the extent of misorientation between the coherent domains that compose the hematite pseudocubes, thereby introducing a quantitative description of these particles as mosaic crystals; those that are neither single crystals nor polycrystals. With the high level of interest recently directed at complex, hierarchical structures<sup>38</sup>, it is immediately apparent that the ability to quantitatively characterize these structures is a prerequisite to their successful application in developing technologies.

## **ACKNOWLEDGEMENTS**

We acknowledge support from the NSF (DMR 0845212 and DMR 1210304), and EAS acknowledges the NSF Graduate Research Fellowship (GRF, DGE-0707428), and Integrative Graduate Education and Research Traineeship (IGERT, DGE-0903653) Programs. The Cornell Center for Materials Research (CCMR) Shared Facilities, a Materials Research Science and Engineering Center of the NSF (DMR 1120296), were used extensively for this work, in particular the Electron Microscopy and X-Ray Diffraction facilities. Specific acknowledgment is made for the assistance of Malcolm G. Thomas and John Grazul during the use of the electron microscopy facilities. Special thanks are expressed to Lyle Gordon, Megan Holtz, Pinshane Huang and Hiroaki Sai for helpful discussions and experimental insight.

## 3.6 Materials and Methods

Iron (III) chloride hexahydrate (Sigma-Aldrich) and hydrochloric acid (Fisher Scientific) were used as received without further purification. Hematite pseudocubes were synthesized from a modified procedure from the literature<sup>2</sup>. Briefly, a solution of iron (III) chloride hexahydrate (1.8 M) was added to hydrochloric acid (13 mM) in a 1:3 ratio to a final volume of 80 mL in a 100 mL pyrex media bottles and stirred at room temperature for 60 mins. No precipitation was observed in the transparent yellow solution during this time. Subsequently, stirring was ceased; the pyrex bottles were sealed and heated to 100 °C in a furnace for 4 weeks. After cooling to room temperature, deep reddish hematite particles were isolated from the reaction mixture by centrifugation (3600 g, 5 min), rinsed with water (3x), and freeze-dried on a lyophilizer.

### 3.6.1 Phase and Microscale Characterization

Powders of hematite pseudocubes were dispersed in ethanol and observed with an optical microscope (OM) (Olympus BX51 with an Olympus Camedia C-7070 digital camera) using a 50x objective lens in transmission in the absence and presence of cross-polarizers (CPOM). Phase analysis was confirmed by powder x-ray diffraction (pXRD) using a Rigaku Ultima VI powder X-ray diffractometer with CuK $\alpha$  radiation (K $\alpha_1$ ,  $\lambda=1.5046$  Å and K $\alpha_2$ ,  $\lambda= 1.5444$  Å). Phase identification and crystallite size (Scherrer) analysis were performed using Jade (Materials Data, Inc.) software package. As synthesized hematite particles were imaged (uncoated) with a field-emission scanning electron microscope (FE-SEM) (Leo 1550, Zeiss) operating at 2 keV.

### 3.6.2 Preparation for Transmission Electron Microscopy

Thin sections of hematite pseudocubes were prepared using a dual-beam FIB microscope (Strata 400, FEI) equipped with a gallium liquid metal ion source and a nanomanipulator (OmniProbe AutoProbe 200, Oxford Instruments). The specific orientations of individual pseudocubic particles were accessed by manipulating them with the nanomanipulator needle. Each particle was then mounted whole onto the

needle with a Pt weld. The edge of a center post of a three-post copper lift-out grid was pre-milled to create a fresh, flat location for particle mounting (visible in Figure 3.7b). A rectangular section of Pt was deposited as a milling guide over the top of the particles (visible on top of particle shown in Figure 3.7c). Subsequently, particles were mounted (with Pt weld) directly on copper grids for milling. Milling was conducted at 30 and 10 keV, with 50% overlap. Final ion-polishing was conducted at 5 keV, with 85% overlap. The final thin sections were ~50 nm in thickness with lateral dimensions up to 1  $\mu$ m.

The thin sections from hematite pseudocubes were plasma-cleaned for 1 min immediately prior to characterization with TEM in an FEI Tecnai T12 transmission electron microscope, tungsten filament, operating at 120 kV. Camera calibration for selected area electron diffraction (SAED) was performed using a (100)-oriented single crystal of strontium titanate on silicon (courtesy of Charles Brooks, fabricated as described in <sup>30</sup>) using the relation  $Rd = L\lambda$ , where  $R$  is the radius of the diffraction spot,  $d$  is the interplanar spacing,  $L$  is the camera length, and  $\lambda$  is the wavelength of the incident beam.

### 3.6.3 Analysis of Selected-Area Electron Diffraction (SAED) Patterns

SAED patterns were analyzed using ImageJ. By use of the ‘polar transformer’ plugin, SAED plots were transformed into 2D linear plots of azimuthal angle ( $\phi$ ) vs.  $R$ . Subsequently, line profiles were taken from these plots at constant  $R$  to form profiles of intensity ( $I$ ) vs.  $\phi$ . The raw data from these profiles was exported into OriginPro<sup>®</sup> 8, and fit to a Gaussian function to find the full width half maximum ( $FWHM_{exp}$ ) of the peaks, which represents the azimuthal broadening of the diffracted intensity. The actual mosaicity (mosaic spread ( $MS$ )), the degree of lattice misorientation between adjacent coherent domains within the individual pseudocubic particles, can be estimated by taking into account the instrumental broadening. <sup>28,29</sup>

$$MS = \sqrt{FWHM_{exp}^2 - \sigma_{STO}^2}$$

Equation 3

## REFERENCES

- (1) Sivula, K.; Le Formal, F.; Graetzel, M. *Chemsuschem* **2011**, *4*, 432.
- (2) Matijevic, E.; Scheiner, P. *J. Colloid Interface Sci.* **1978**, *63*, 509.
- (3) Morales, M. P.; Gonzalezcarreno, T.; Serna, C. J. *J. Mater. Res.* **1992**, *7*, 2538.
- (4) Van, T. K.; Cha, H. G.; Nguyen, C. K.; Kim, S. W.; Jung, M. H.; Kang, Y. S. *Crystal Growth & Design* **2012**, *12*, 862.
- (5) Kay, A.; Cesar, I.; Gratzel, M. *J. Am. Chem. Soc.* **2006**, *128*, 15714.
- (6) Franking, R.; Li, L.; Lukowski, M. A.; Meng, F.; Tan, Y.; Hamers, R. J.; Jin, S. *Energy & Environmental Science* **2013**, *6*, 500.
- (7) Yin, J.; Yu, Z.; Gao, F.; Wang, J.; Pang, H.; Lu, Q. *Angewandte Chemie-International Edition* **2010**, *49*, 6328.
- (8) Liu, R.; Jiang, Y.; Fan, H.; Lu, Q.; Du, W.; Gao, F. *Chemistry-A European Journal* **2012**, *18*, 8957.
- (9) Liu, X. J.; Liu, J. F.; Chang, Z.; Sun, X. M.; Li, Y. D. *Catal. Commun.* **2011**, *12*, 530.
- (10) Fang, X.-L.; Chen, C.; Jin, M.-S.; Kuang, Q.; Xie, Z.-X.; Xie, S.-Y.; Huang, R.-B.; Zheng, L.-S. *J. Mater. Chem.* **2009**, *19*, 6154.
- (11) Sugimoto, T.; Muramatsu, A.; Sakata, K.; Shindo, D. *J. Colloid Interface Sci.* **1993**, *158*, 420.
- (12) Sugimoto, T.; Sakata, K.; Muramatsu, A. *J. Colloid Interface Sci.* **1993**, *159*, 372.
- (13) Blesa, M. A.; Matijevic, E. *Adv. Colloid Interface Sci.* **1989**, *29*, 173.
- (14) Kandori, K.; Kawashima, Y.; Ishikawa, T. *J. Chem. Soc., Faraday Trans.* **1991**, *87*, 2241.
- (15) Butler, G.; Ison, H. C. K. *Chem. Commun.* **1965**, 264.
- (16) Flynn, C. M. *Chem. Rev.* **1984**, *84*, 31.
- (17) Bailey, J. K.; Brinker, C. J.; Mecartney, M. L. *J. Colloid Interface Sci.* **1993**, *157*, 1.
- (18) Cornell, R. M.; Schwertmann, U. *The Iron Oxides*; Wiley-VCH, 2003.
- (19) Miller, M. P.; Suter, R. M.; Lienert, U.; Beaudoin, A. J.; Fontes, E.; Almer, J.; Schuren, J. *C. Synchrotron Radiation News* **2012**, *25*, 18.
- (20) Shindo, D.; Aita, S.; Park, G. S.; Sugimoto, T. *Materials Transactions Jim* **1993**, *34*, 1226.

- (21) Park, G. S.; Shindo, D.; Waseda, Y. *J. Electron Microsc.* **1994**, *43*, 208.
- (22) Park, G. S.; Shindo, D.; Waseda, Y.; Sugimoto, T. *J. Colloid Interface Sci.* **1996**, *177*, 198.
- (23) Miller, M. K.; Russell, K. F.; Thompson, K.; Alvis, R.; Larson, D. J. *Microscopy and Microanalysis* **2007**, *13*, 428.
- (24) Choi, P. P.; Al-Kassab, T.; Kwon, Y. S.; Kim, J. S.; Kirchheim, R. *Microscopy and Microanalysis* **2007**, *13*, 347.
- (25) Choi, P. P.; Kwon, Y. S.; Kim, J. S.; Al-Kassab, T. *J. Electron Microsc.* **2007**, *56*, 43.
- (26) Felfer, P.; Ringer, S. P.; Cairney, J. M. *Ultramicroscopy* **2011**, *111*, 435.
- (27) Shtukenberg, A. G.; Punin, Y. O.; Gunn, E.; Kahr, B. *Chem. Rev.* **2011**, *112*, 1805.
- (28) Ferrari, C.; Buffagni, E.; Marchini, L.; Zappettini, A. *Optical Engineering* **2012**, *51*.
- (29) Barabash, R. I.; Klimanek, P. *J. Appl. Crystallogr.* **1999**, *32*, 1050.
- (30) Warusawithana, M. P.; Cen, C.; Sleasman, C. R.; Woicik, J. C.; Li, Y. L.; Kourkoutis, L. F.; Klug, J. A.; Li, H.; Ryan, P.; Wang, L. P.; Bedzyk, M.; Muller, D. A.; Chen, L. Q.; Levy, J.; Schlom, D. G. *Science* **2009**, *324*, 367.
- (31) Baluffi, R. W.; Allen, S. M.; Carter, W. C. *Kinetics of Materials*; John Wiley & Sons, 2005.
- (32) Darwin, C. G. *Philos. Mag.* **1914**, 315.
- (33) Darwin, C. G. *Philos. Mag.* **1922**, *43*, 800.
- (34) Bragg, W. L.; Darwin, C. G.; James, R. W. *Philos. Mag.* **1926**, *1*, 897.
- (35) Guinier, A. *X-Ray Diffraction in Crystals, Imperfect Crystals and Amorphous Bodies*; Dover Publications: New York, 1956.
- (36) Hirth, J. P. *Metallurgical Transactions A* **1985**, *16A*, 2085.
- (37) Cullity, B. D.; Stock, S. R. *Elements of X-ray Diffraction*; 6 ed.; Prentice Hall: New Jersey, 2001.
- (38) Song, R.-Q.; Cölfen, H. *Adv. Mater.* **2010**, *22*, 1301.

## 4 HIERARCHICALLY-STRUCTURED HEMATITE ( $\alpha$ -Fe<sub>2</sub>O<sub>3</sub>) ARCHITECTURES ACHIEVED BY GROWTH IN A SILICA HDYROGEL<sup>♦</sup>

### 4.1 Abstract

Biom mineralization strategies include the use of hydrogels to direct the formation of composite, single-crystal-like structures with unique structure-property profiles. Application of similar synthetic approaches to transition metal oxides has the promise to yield low-temperature routes to hierarchically-structured crystals that are optimized for a range of applications. Here, growth of hematite ( $\alpha$ -Fe<sub>2</sub>O<sub>3</sub>) within a silica hydrogel resulted in hierarchical, mosaic crystals preferentially expressing catalytically active {110} facets, which are absent in solution-grown controls. Quantitative structural and compositional analysis reveals architectural changes that begin with the incorporation of silicon into the hematite lattice and propagate through to the nanoscale domain structure and assembly, leading to microscale morphologies that show improved photocatalytic performance. This work demonstrates the potential of applying bio-inspired crystallization techniques to design functional oxides with multi-scale architectural features.

### 4.2 Introduction

The control of structure across multiple-length scales remains an important challenge in the design of materials with improved functionality. Notably, transition metal oxides with nanostructured architectures have demonstrated increased performance across the map of sustainable energies: solar cells,<sup>1</sup> water splitting<sup>2</sup> and thermoelectric power generation.<sup>3</sup> Biological organisms present multiple

---

<sup>♦</sup>Portions reproduced with permission from E. Asenath-Smith, R. Hovden, L. F. Kourkoutis & L. A. Estroff, *Journal of the American Chemical Society* **2015**, DOI: 10.1021/jacs.5b01697. Copyright © 2015 American Chemical Society.

examples of hierarchical structures that are optimized for a given function.<sup>4</sup> In particular, biomineralized materials display crystallographic control across length scales and are often formed in association with an organic matrix. Taking cues from biology, researchers have developed synthetic crystallization strategies that yield morphological control in select model systems.<sup>5-7</sup> Characterizing the structural relationships across multiple levels of the hierarchy, for example, the interaction between the growth matrix and mineral, is key to understanding how structure dictates properties in these materials.<sup>8,9</sup> To date, most property studies have focused on improvements in mechanical performance.<sup>6,7</sup> To translate biological mineralization strategies to energy materials, we developed a hydrogel-based crystallization that allows us to harness the structure-directing power of matrix-mediated growth for metal oxides.

Hydrogels are versatile crystallization media that can be used to control the growth of both organic and inorganic materials.<sup>10-12</sup> In defining the crystallization microenvironment, hydrogels establish diffusion-limited conditions, which can lead to control over the local supersaturation levels in addition to influencing the morphology, polymorph, and internal structure of the resulting crystals.<sup>11,13</sup> Hydrogels have been used to model the organic matrix in biomineralization and, importantly provide a synthetic route to composite single crystals with incorporated polymeric aggregates (e.g., hydrogel fibers).<sup>9,14,15</sup> Translation of hydrogel-based crystallization methods to the formation of transition metal oxides has the potential to yield new materials with hierarchical structures and tunable compositions that can serve a wide variety of developing technologies. The growth of oxide phases directly within hydrogel matrices is largely hindered by the limited thermal stability of polysaccharide and protein hydrogels and the increased temperatures needed to drive oxide formation via the hydrolysis of metal salts.<sup>16,17</sup> Inorganic hydrogels such as those composed of silica, may be compatible with the hydrothermal growth of such materials,<sup>18</sup> broadly increasing the range of functional materials that can form by bio-inspired pathways. In this work, hematite was chosen as a first target oxide for growth in a hydrogel due to the broad range of pH conditions under which it can be formed<sup>19,20</sup> and the desirable photocatalytic properties it has shown due to nanostructure optimization.<sup>2,21,22</sup>

The growth of iron oxides in porous networks has largely focused on the use of *organic* matrices as stabilizers in the formation of superparamagnetic structures of  $\gamma\text{-Fe}_2\text{O}_3$  (maghemite) or  $\text{Fe}_3\text{O}_4$  (magnetite) phases.<sup>23-29</sup> Growth of iron oxides in *inorganic* matrices has primarily involved  $\gamma\text{-Fe}_2\text{O}_3$  growth in a silica matrix by drying and heating an iron-TEOS (tetraethoxy orthosilicate) sol-gel precursor to  $T > 500\text{ }^\circ\text{C}$ .<sup>30-32</sup> These examples demonstrate the potential of iron oxide formation in the presence of a matrix, and illustrate the need for further development of growth matrices to achieve a low-temperature, aqueous, matrix-mediated crystallization microenvironment, wherein the control over phase and morphology can be simultaneously achieved.

### 4.3 Results and Discussion

The key to developing synthetic approaches to the growth of oxides in hydrogels is to identify a hydrogel with both thermal stability and chemical compatibility to the hydrothermal growth conditions required by the oxide. Solution growth of hematite proceeds via acidic hydrolysis of iron (III) chloride solutions,<sup>19</sup> to yield mosaic, pseudo-cubic crystals that are composed of highly-oriented coherent domains separated by small-angle tilt boundaries.<sup>19,33</sup> Based upon this previous work, the premise for our experimental design was to translate the ‘pseudo-cube’ synthesis into a sodium metasilicate hydrogel matrix formed via acidification.<sup>10</sup>

The cellular, porous silica hydrogels (Figure 4.1a) were formed in single-diffusion geometry (Figure 4.1b). Since solution crystallizations of hematite are typically conducted in a borosilicate (Pyrex) vessel, we developed an additional solution-based control in which the pseudo-cube growth was carried out in a PTFE (Teflon) vessel, which served as a silica-free growth environment. The silicon content of the reaction supernatants was analyzed by ICP-AES (Table 4.1). The greatest amount of Si was found in the hydrogel growth media with intermediate amounts of Si in the supernatant from the reaction in a borosilicate vessel and undetectable amounts of Si from the PTFE control. With these carefully-designed

solution-based control experiments, we were able to critically evaluate the chemical effects of dissolved silica species in the growth environment, without significant modifications to the pH or ionic strength, on the formation of hematite across multiple length scales.

Table 4.1 Analytical Data on Hematite Crystals and Reference Materials

Sample Description	Si in growth environment (ppm) <sup>a</sup>	$I_{104/110}$ <sup>c</sup>	a-axis <sup>d</sup> (Å)	c-axis <sup>d</sup> (Å)	Surface Area <sup>e</sup> (m <sup>2</sup> /g)
<b>PDF #98-000-0240</b>	n/a	1.45	5.0355	13.7471	n/a
<b>Commercial Hematite</b>	n/a	n/a	n/a	n/a	10.38
<b>Solution-grown (PTFE)</b>	0.15 <sup>b</sup>	1.48	5.0357(2)	13.7649(5)	n/a
<b>Solution-grown (Borosilicate)</b>	32.57	1.02	5.0369(3)	13.7736(8)	13.38
<b>Hydrogel-grown quasi-sphere</b>	57.35	0.85	5.0343(7)	13.7864(21)	20.69
<b>Hydrogel-grown, acid-etched</b>	n/a	1.05	n/a	n/a	46.32

<sup>a</sup>ICP-AES analysis of supernatant growth solution

<sup>b</sup>Silicon amounts found by ICP in the silica-free growth condition (PTFE) were in the range of the blank solution and are thus negligible

<sup>c</sup>Ratio of the (104) and (110) reflected intensities from pXRD data (Fig. 4a)

<sup>d</sup>Values obtained from Rietveld refinements of pXRD patterns (Fig. 4a, Fig. S4, Table S5).

<sup>e</sup>Determined by BET analysis

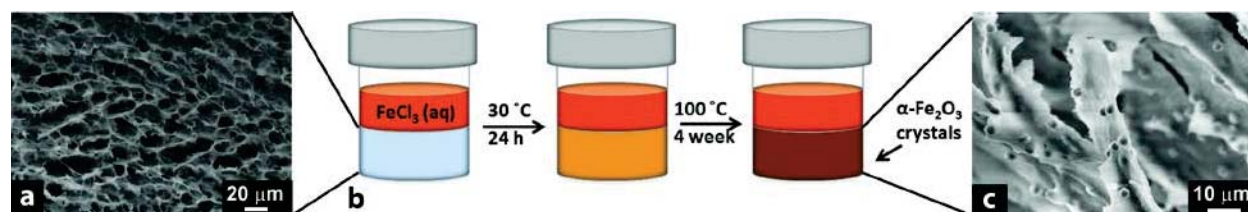


Figure 4.1 (a) Scanning electron microscope (SEM) image of a freeze-dried silica hydrogel showing the cellular porous microstructure of silica hydrogel networks used in this study. These silica hydrogels are formed by the acidification of sodium metasilicate solutions and can be considered to have undergone complete condensation, forming a fully percolated network of covalent siloxane (Si-O-Si) bonds. (b) Experimental schematic for the growth of hematite in a silica hydrogel by a single diffusion method. Iron (III) chloride solution is allowed to completely diffuse through the hydrogel at 30 °C before hydrothermal reaction (100 °C). By this approach, time-evolving concentration gradients were minimized in the growth environment and precipitation was not observed before hydrothermal treatment. In both solution- and hydrogel-based experiments, the color change throughout the course of reaction could be used to monitor the precipitation of the initial (yellow) akaganeite phase and its transformation into (reddish) hematite. (c) SEM micrograph of a freeze-dried silica hydrogel in which hematite particles have grown, illustrating the size relationship between the hydrogel microstructure and the crystals; namely that the hematite crystals are an order of magnitude *smaller* than the network features of the hydrogel.

#### 4.3.1 Microstructural Assessment of Hydrogel and Hematite Crystals

Upon imaging the freeze-dried silica hydrogel matrix post-crystallization, small quasi-spherical hematite crystals were observed along the cellular walls of the hydrogel (Figure 4.1c). The silica hydrogel pores are 10s of  $\mu\text{m}$  in diameter; an order of magnitude *larger* than the hematite crystals formed. With such size relationships, we find that the case of hematite grown in a silica hydrogel is different than many previous reports on the growth of crystals in hydrogels. For example, when calcite is grown in agarose at room temperature,<sup>9</sup> the hydrogel microstructure has features that are 2 orders of magnitude *smaller* than the crystals. Subsequently, the crystals grow through the hydrogel network and the supply of reagents is diffusion-limited. Those conditions favor the occlusion of the agarose fibers within the calcite crystals, forming single crystal composites. In the current study, considering the relative sizes between the hematite crystals and the silica hydrogel network, we hypothesize that physically, the silica

hydrogel walls provide heterogeneous nucleation sites for the hematite crystals while the adjacent pores serve as reagent reservoirs that contain iron species, as well as possibly dissolved silicate, due to the strongly acidic conditions imparted by iron (III) chloride.

Imaging the hematite crystals in transmitted light showed small, red, circular ( $d \sim 4 \mu\text{m}$ ) crystals (Figure 4.2, central image). Upon rotating under cross polarized light, the crystals both extinguish light at regular intervals and exhibit a Maltese cross (Figure 4.2, outer images).<sup>33</sup> These disparate signatures are consistent with the hydrogel-grown crystals being composed of highly-oriented coherent domains. Scanning electron microscopy (SEM) imaging confirmed highly monodisperse batches (Figure 4.3a) of the quasi-spherical hematite crystals. Pseudo-cubic hematite particles (Figure 4.3b,c) were formed in both solution experiments. Upon closer examination of the surface of the hematite particles (Figure 4.3d-f), all are seen to have rough surfaces, where the emergence of cube-like features is inversely correlated to the silicon content of the crystals.

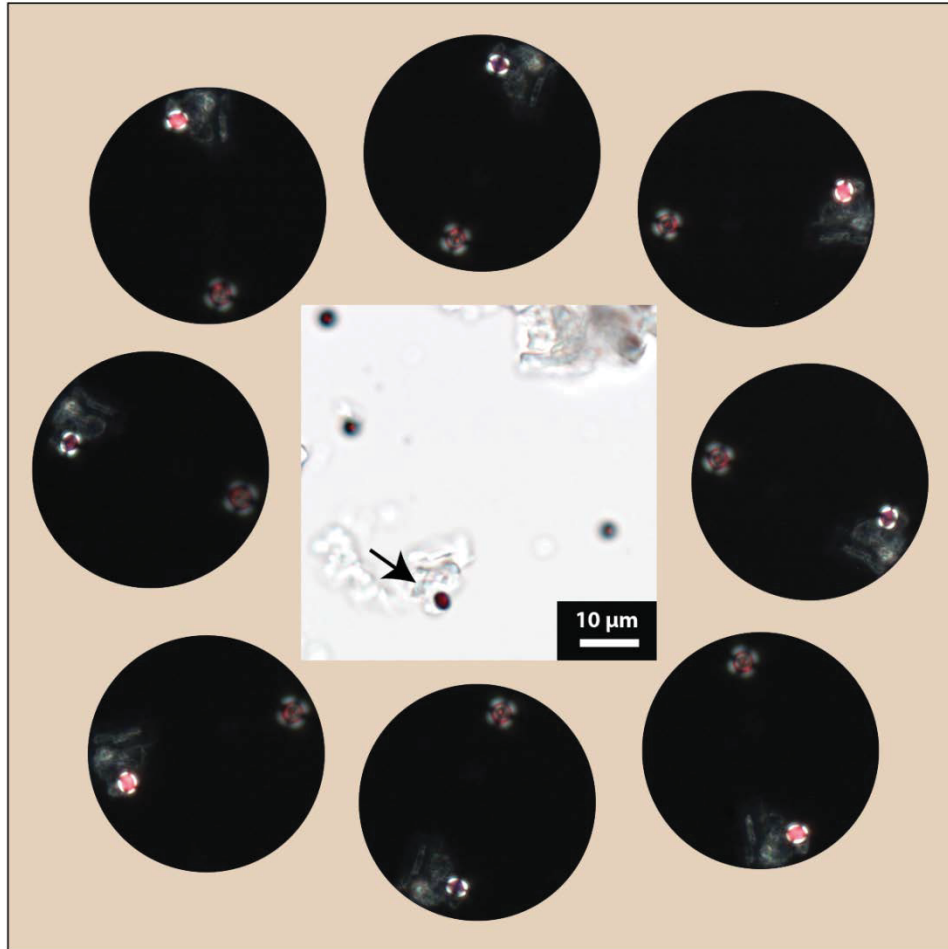


Figure 4.2 Optical microscopy images of hematite particles grown in silica hydrogel, taken in transmission (central image) and during rotation under cross-polarized light (peripheral series of images). The crystal denoted with the arrow is tracked during rotation under cross-polarized light. The tracked particle is seen to both extinguish the light at regular intervals, characteristic of a single crystal, and exhibit a Maltese cross at its edges, characteristic of a spherulitic crystal.

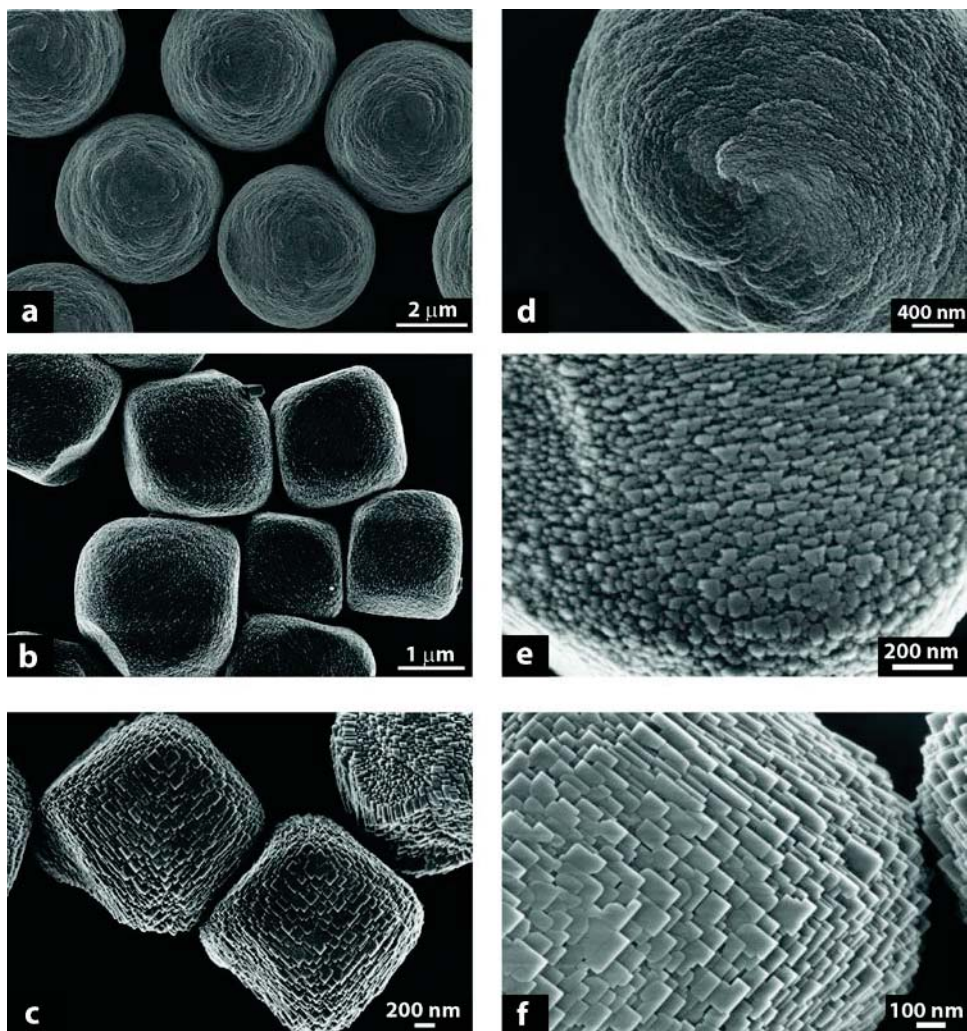


Figure 4.3 Scanning electron micrographs of hematite particles grown in three different environments, each with a different amount of dissolved silicate. (a), (d) Growth in a silica hydrogel supplied the greatest amount of dissolved silicate in the growth environment leading to the highest doping level of silicon in the hematite crystals. (b), (e) Solution growth of hematite in a borosilicate vessel allowed access to an intermediate level of dissolved silicate in the crystallization environment, leading to an intermediate level of doping in the hematite crystals. (c), (f) Solution growth of hematite in a silica-free (PTFE) vessel enabled the formation of un-doped hematite crystals (Table 4.1).

#### 4.3.2 Mesoscale Assembly within Hematite Crystals

Armed with microscale observations that implicate the hydrogel grown quasi-spheres as crystals that are composed of highly-oriented coherent domains, we set out to investigate the net orientation of the

hematite lattice. This task required the preparation of electron-transparent thin sections from at least two unique orientations within individual quasi-spheres.<sup>33</sup> Using single-particle manipulation and FIB milling (Figure 4.4), thin sections from the quasi-spheres could be formed from unique planes with respect to their parallel flattened sides; the *equatorial* slice (Figure 4.5a), and the *axial* slice (Figure 4.5d).

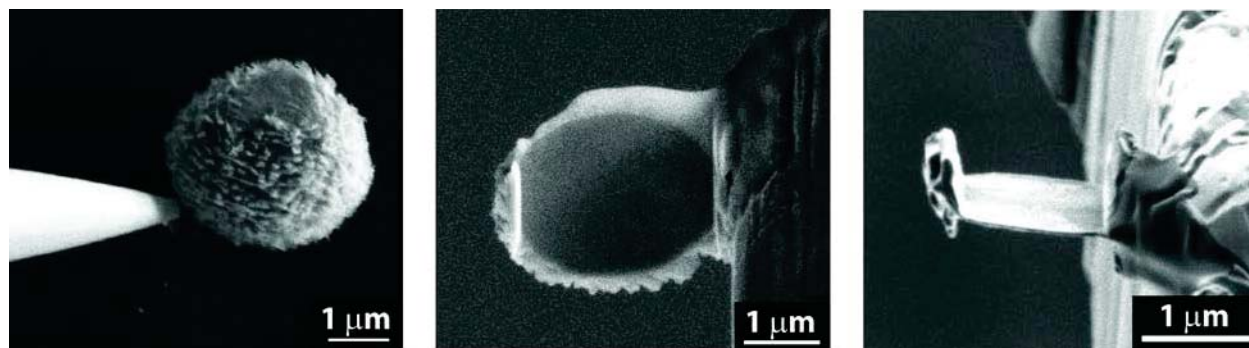


Figure 4.4 SEM micrographs showing the sequence of single particle manipulations (equatorial thin section shown) used to form electron transparent thin sections of hematite crystals grown in a silica hydrogel using a dual-beam focused ion beam system: (a) treatment in base allowed the unambiguous identification of two parallel flat sides to the spheres so that they could be individually picked up and (b,c) mounted on lift-out grids for ion beam thinning. Thin sections were  $\sim 50$  nm in thickness and extended up to 1  $\mu\text{m}$  in lateral dimensions. See ref. 33 for more details.

While both slices showed diffraction contrast stemming from domains with multiple crystallographic orientations (Figure 4.5b,e), the SAED patterns of both thin sections contained distinct spots (Figure 4.5c,f), indicating a high degree of registry between the domains leading to a net orientation of the hematite lattice within the quasi-spherical crystals. The equatorial slice indexed to the  $[001]$  zone of the hematite lattice and the axial slice to the  $[\bar{2}2\bar{1}]$  zone (Table 4.2 Table 4.3). These results identify the net orientation of the hematite *c*-axis as positioned normal to the equatorial plane of the quasi-spheres; perpendicular to the shortest diameter of the quasi-sphere. This collective alignment of the domains suggests that the quasi-spherical shape is a consequence of preferential growth in the hexagonal *a-b* plane.

Table 4.2 Calculated and theoretical distances for interplanar distances from SAED patterns used in the identification of  $[001]$  zone from *Equatorial* slice.

<b>hkl</b>	<b>Theoretical <math>d_{hkl}</math> (nm)</b>	<b>Calculated <math>d_{hkl}</math> (nm)</b>
<b>(104)</b>	0.2703	0.2812
<b>(110)</b>	0.2519	0.2625
<b>(116)</b>	0.1697	0.1779

Table 4.3 Calculated and theoretical distances for interplanar distances from SAED patterns used in the identification of  $[\bar{2}2\bar{1}]$  zone from *Axial* slice.

<b>hkl</b>	<b>Theoretical <math>d_{hkl}</math> (nm)</b>	<b>Calculated <math>d_{hkl}</math> (nm)</b>
<b>(012)</b>	0.3686	0.3888
<b>(<math>\bar{1}\bar{1}\bar{4}</math>)</b>	0.2033	0.2863
<b>(110)</b>	0.2519	0.2669
<b>(<math>\bar{1}\bar{2}\bar{6}</math>)</b>	0.1229	0.1800

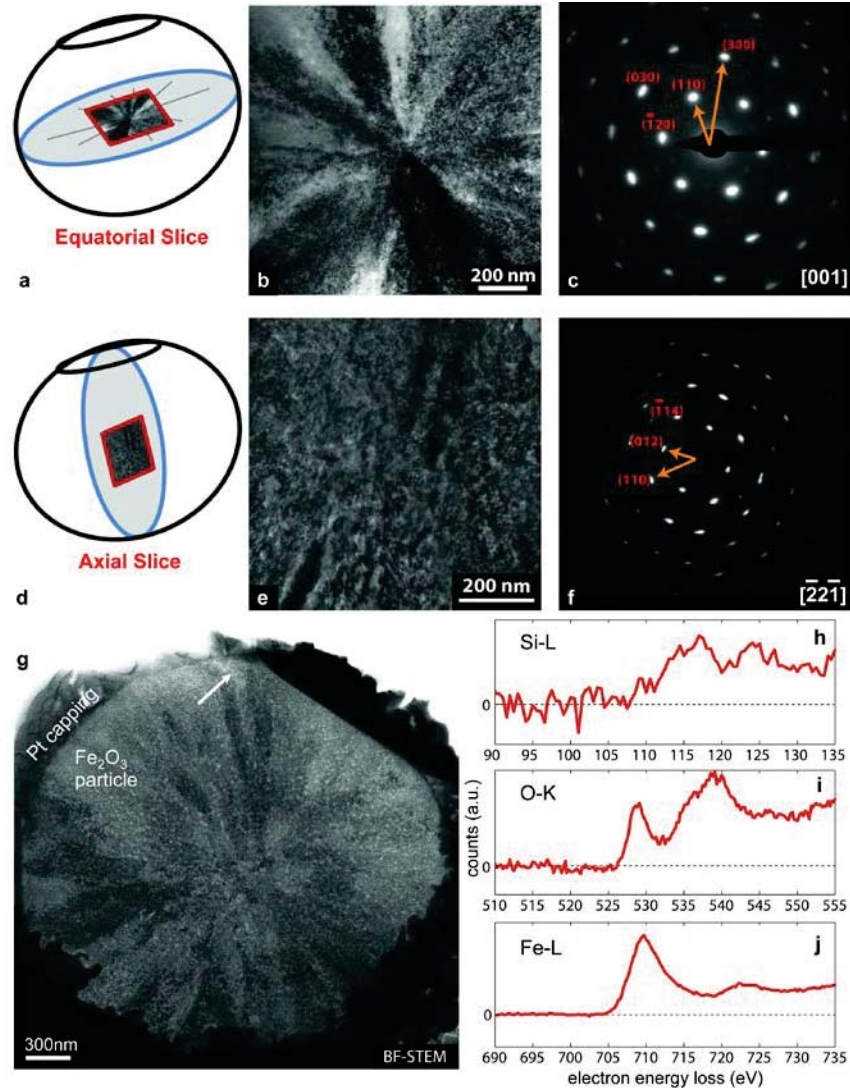


Figure 4.5 Graphical representation of the geometric location from which thin sections were made with FIB milling: equatorial slice (a) and axial slice (d). The equatorial slice: (b) bright-field TEM showing radially extending diffraction contrast, and (c) a single-crystal-like SAED pattern indexed to the [001] zone of hematite. The axial slice: (e) bright-field TEM showing randomly-oriented diffraction contrast, and (f) a single-crystal-like SAED pattern indexed to the  $[\bar{2}2\bar{1}]$  zone of hematite. The area selected for electron diffraction (in (c, f)) was approximately equivalent to the areas shown in the bright field images ((f) and (e), respectively). (g)-(j) Electron energy loss spectroscopy of an equatorial thin section from a hydrogel-grown crystal. (g) Bright field STEM (scanning transmission electron microscopy) image shows the entire thinned cross section of the crystal. The interior region investigated by EELS ( $\sim 50 \times 100$  nm) is marked by an arrow: (h) silicon-L; (i) oxygen-K; and (j) iron-L edge EELS spectra. The oxygen-K and iron-L edges (i,j) are consistent with hematite.

Closer observation of the thin sections under bright-field TEM imaging reveals differences in the crystalline domain assembly in each of the slices. In particular, elongated regions of radially-extending diffraction contrast are apparent in the equatorial slice (Figure 4.5b). This architecture is consistent with a spherulitic structure that propagates two-dimensionally in the equatorial plane of the quasi-sphere. In general, spherulites contain crystallographically-defined regions with radial branching from a central nucleus, where the branching within regions occurs across small-angle tilt boundaries and the branching between regions is subject to the constraints of orientation-dependent grain boundary energies as well as the geometrical limitations on space filling from a central point.<sup>34,35</sup> These constraints can cause the symmetry between the regions to match the symmetry of the underlying lattice. In the hydrogel-grown crystals, six single-crystal-like regions form a radial array that matches the six-fold symmetry of the hematite [001] zone resulting in a single-crystal-like diffraction pattern with modulated intensities. To further complicate matters, out-of-plane tilting within each region can cause further variations in the intensity of diffraction spots. Dark field imaging around the first set of diffraction spots of the [001] zone (*equatorial* slice) was used to illustrate these structural features (Figure 4.6). The results indicate that the interior of a quasi-sphere is composed of spherulitic structures that propagate two-dimensionally within the equatorial planes with out-of-plane lattice tilting.

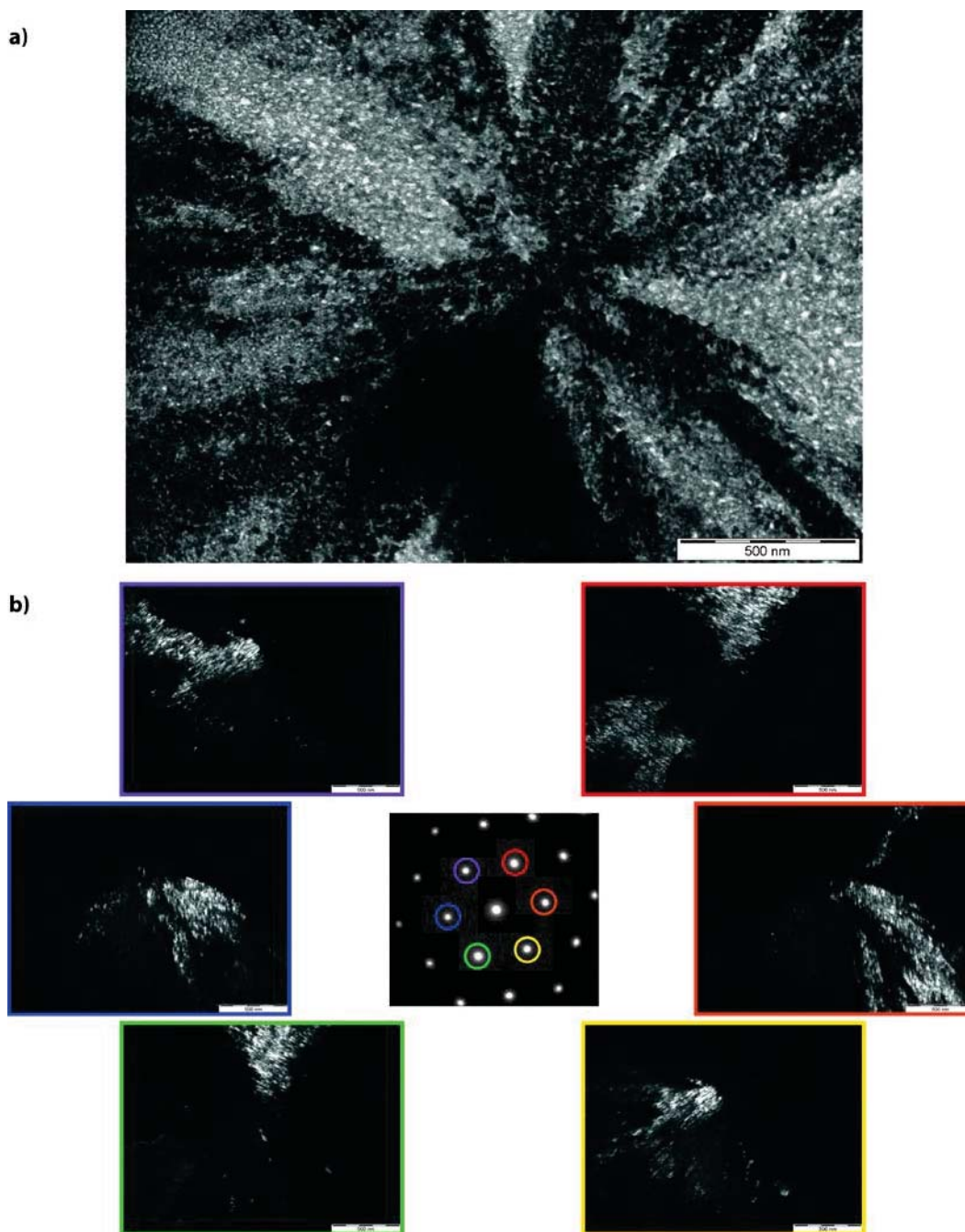


Figure 4.6 Analysis of the symmetry of crystalline regions that propagate radially within the equatorial thin section from the hydrogel-grown quasi-spheres: (a) bright field TEM of equatorial thin section analyzed in (b); (b) dark field imaging around the first set of reflections from the [001] zone of the equatorial slice demonstrating the six-fold symmetry of crystalline regions within the equatorial plane of the quasi-sphere. Regions that do not illuminate in dark field images do so because of out of plane lattice tilting within those regions.

### 4.3.3 Nanoscale Domain Structure

The aspect ratio of the nanoscale domains is apparent in the relative intensity of the  $\{104\}$  and  $\{110\}$  reflections in the pXRD patterns (Table 1, Figure 4.7a).<sup>36</sup> The  $I_{104}/I_{110}$  of less than 1 in the hydrogel grown crystals is consistent with domains that are elongated along  $[110]$  as compared to the more isotropic domains in the solution grown crystals. These results pair directly with the mesoscale analysis, which shows that the radial internal structure is collinear to the  $[110]$  position of the hematite lattice.

Information about the arrangement of the nanoscale domains is manifest in the azimuthal broadening of the spots in the SAED patterns (Figure 4.5c,f). Traditionally, such mosaicity is interrogated via XRD rocking curves, however, for these small particles, the mosaicity was extracted from the angular spread in SAED patterns.<sup>33</sup> The angular mismatch between domains within the  $[001]$  zone of the equatorial slice is as little as  $2^\circ$  along the  $[300]$  direction and as much as  $7^\circ$  along the  $[\bar{1}20]$  direction (Table 4.4). Within the axial slice, the  $[\bar{2}2\bar{1}]$  zone, mosaicity is approximately  $5^\circ$  along the  $[012]$ ,  $[110]$  and  $[\bar{1}14]$  directions (Table 4.5). The observation of a mosaic spread of  $\leq 7^\circ$  along all directions of both zones examined in the hydrogel-grown crystals, is consistent with both a spherulitic growth mechanism as suggested by the TEM analysis, as well as recent literature reports of oriented attachment growth for related hematite spindles.<sup>37</sup>

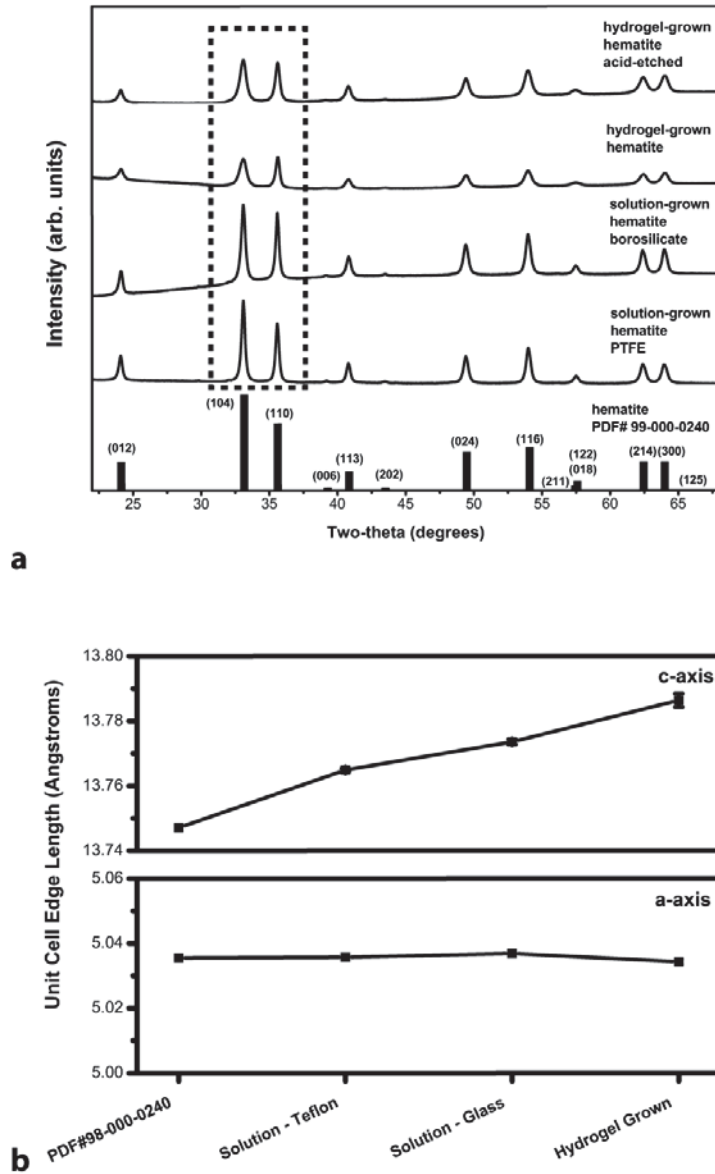


Figure 4.7 (a) X-ray powder diffraction patterns of the crystals reported in this study, confirming the pure phase formation of hematite under all three growth conditions. The relative intensity of the (104) and (110) reflections are emphasized to draw attention to the shift in their relative intensity with increasing dissolved silica in the growth environment, consistent with nanoscale domain elongation along [110]. (b) Lattice parameters of the hematite crystals, found by Rietveld refinements, showing that the hematite lattice expands along the c-axis (upper panel) as silicon in the growth environment increases. The c-axis expansion, while the a-axis is unaffected by silicon incorporation, is consistent with silicon as an interstitial dopant in the hematite lattice. Error bars that are not visible are smaller than data points.

Table 4.4 Mosaicity calculations for *Equatorial* slice of hydrogel-grown hematite, zone [001].

<b>Reflection (hkl)</b>	<b>FWHM<sub>exp</sub> (pixels)</b>	<b>Azimuthal Broadening (degrees)</b>	<b>Mosaic Spread (degrees)</b>	<b>R<sup>2</sup></b>
<b>STO 110a</b>	3.879±0.117	2.895±0.087	n/a	0.97
<b>(-120)</b>	9.61±0.27	7.17±0.20	6.6	0.97
<b>(110)</b>	11.79±0.39	8.80±0.29	4.7	0.96
<b>(300)</b>	4.60±0.10	3.44±0.08	1.9	0.98

Table 4.5 Mosaicity calculations for *Axial* slice of hydrogel-grown hematite, zone [ $\bar{2}2\bar{1}$ ].

<b>Reflection (hkl)</b>	<b>FWHM<sub>exp</sub> (pixels)</b>	<b>Azimuthal Broadening (degrees)</b>	<b>Mosaic Spread (degrees)</b>	<b>R<sup>2</sup></b>
<b>STO 110a</b>	3.879±0.117	2.895±0.087	n/a	0.97
<b>(012)</b>	7.83±0.18	5.84±0.13	5.1	0.98
<b>(110)</b>	7.45±0.16	5.56±0.12	4.7	0.97
<b>(<math>\bar{1}14</math>)</b>	6.70±0.16	5.00±0.12	4.1	0.96

#### 4.3.4 Atomic Scale Effect of Silicon on the Hematite Lattice

To understand the origins of the structural changes observed in the hydrogel-grown hematite, such as the increased aspect ratio of the coherent domains, we used EELS analysis to look for the presence of silicon within the bulk region of the interior of a hydrogel-grown crystal (Figure 4.5g-j). In addition to strong iron-L and oxygen-K edge spectra consistent with hematite, a present but weak silicon-L edge was uniformly detected from the  $\sim 50 \times 100$  nm field of view examined within the interior. To investigate a correlation between the silicon contained in the crystals and the atomic structure, we performed Rietveld refinements on pXRD patterns to quantify the lattice parameters from all three growth conditions (Figure 4.8, Table 4.6). Starting from  $c = 13.7471$  Å and  $a = b = 5.0355$  Å (PDF#99-000-

0240), the  $a$  lattice parameter remained relatively constant with changes to the amount of dissolved silica in the growth environment while the  $c$ -axis increased (Figure 4.7b), consistent with the reported decrease in the  $a/c$  ratio with increasing silicon in hematite crystals grown from a silicon-doped ferrihydrite precursor.<sup>38</sup>

To understand how silicon could cause an increase in  $c$  and little change in  $a$ , with no significant change to iron or oxygen site occupancy (Table 4.1 Table 4.6), we examined the hematite structure. The hexagonally-closest packed array of oxygen anions in the hematite lattice has 2/3 octahedral sites filled by ferric iron cations, leaving all tetrahedral sites vacant. Based upon this structure, silicon can reside in the hematite lattice as a substitutional ( $\text{Si}^{4+}$  for  $\text{Fe}^{3+}$  in an octahedral site) or an interstitial dopant ( $\text{Si}^{4+}$  in a vacant tetrahedral site).<sup>39</sup> As a substitutional dopant, silicon would be expected to cause a contraction of the hematite lattice on the basis of the smaller  $\text{Si}^{4+}$  radius. As an occupant of a tetrahedral interstice, silicon might be expected to cause an expansion of the hematite lattice along  $c$  based on the dimensions of the distorted tetrahedral sites and the O-Si-O distance. While the O-O distance across a tetrahedral site within the  $a$ - $b$  plane in the hematite lattice is 3.0 Å, it is only 2.7 Å along the  $c$ -axis (Figure 4.9).<sup>40</sup> Considering the equilibrium O-O distance in a tetrahedral silicate anionic cluster ( $\text{SiO}_4^{4-}$ ) is 2.70 Å,<sup>41</sup> we hypothesize that a silicon cation in a tetrahedral site of hematite may cause an expansion of the lattice along  $c$ , but not necessarily within the  $a$ - $b$  plane. With our results showing an increase in the  $c$ -axis of the hematite lattice with increasing silicon, and no change in the  $a$ -axis, we find strong evidence for silicon as an interstitial dopant into our hydrogel-grown hematite. While tetrahedral occupancy by silicon appears to be the most likely cause of  $c$ -axis expansion, other possibilities for this expansion may include an increase in hydroxyl content.<sup>42</sup>

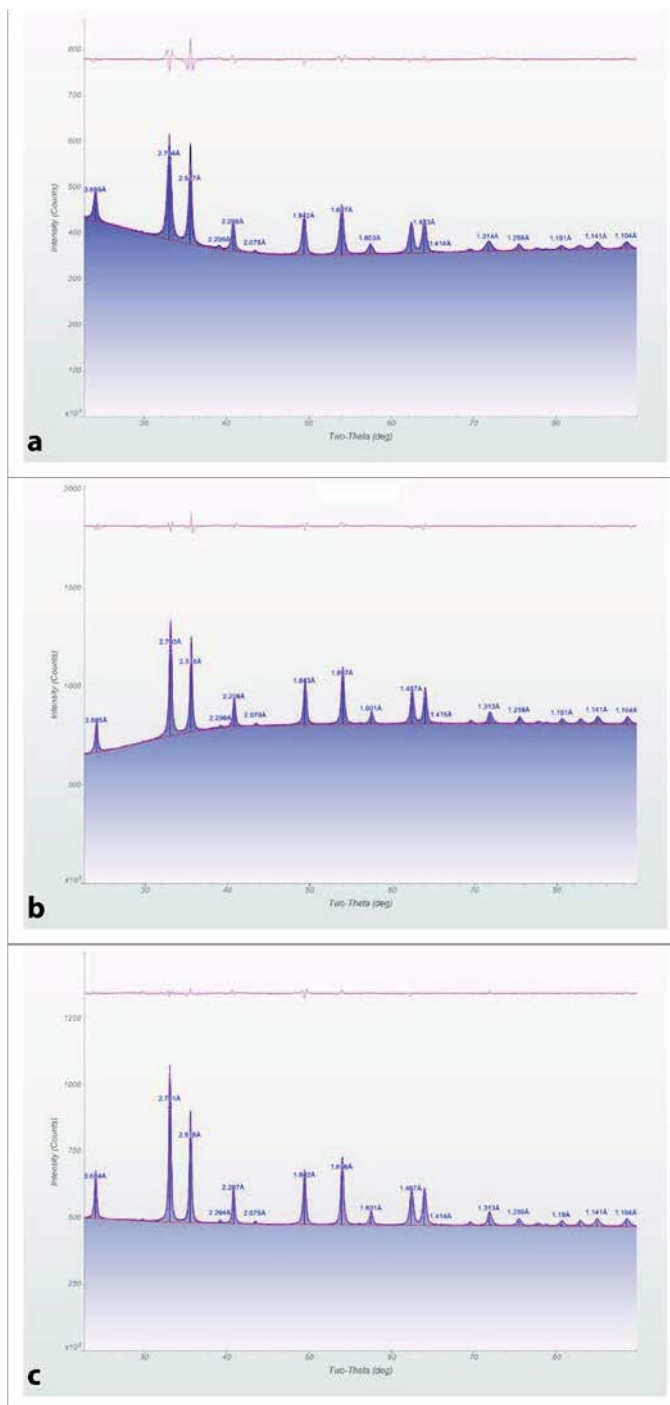


Figure 4.8 Rietveld refinement results for hematite crystals. The pXRD patterns are shown in black with overlaid Rietveld fits (red). Difference plots are shown above in beige. (a) hydrogel-grown hematite; (b) solution-grown (glass) hematite; (c) solution-grown, silica-free (Teflon) hematite.

Table 4.6 Refined Rietveld parameters and statistics.

Sample Growth Condition	R %	E %	R/E	a	c	Zero Offset	Intensity Scale Factor	Preferred Orientation	Temp. Factor	Fe Occ.	O Occ.
<b>Hydrogel</b>	0.79	0.16	4.88	5.03430 (0.00073)	13.78638 (0.00212)	-0.02314 (0.00607)	24111.5 (3394.79)	1.08336 (0.01993)	-0.54574 (0.33823)	0.99487 (0.04757)	1.05132 (0.06875)
<b>Solution-Borosilicate</b>	0.41	0.11	3.66	5.03685 (0.00026)	13.77355 (0.00077)	-0.03717 (0.00217)	39407.0 (2475.81)	1.03705 (0.00276)	-0.82489 (0.15741)	0.9970 (0.02121)	1.03471 (0.02993)
<b>Solution-PTFE</b>	0.36	0.14	2.56	5.03571 (0.00018)	13.76491 (0.00052)	-0.0563 (0.00145)	33542.3 (1412.69)	1.00176 (0.00165)	-0.79647 (0.10535)	0.99716 (0.01422)	1.03868 (0.02018)

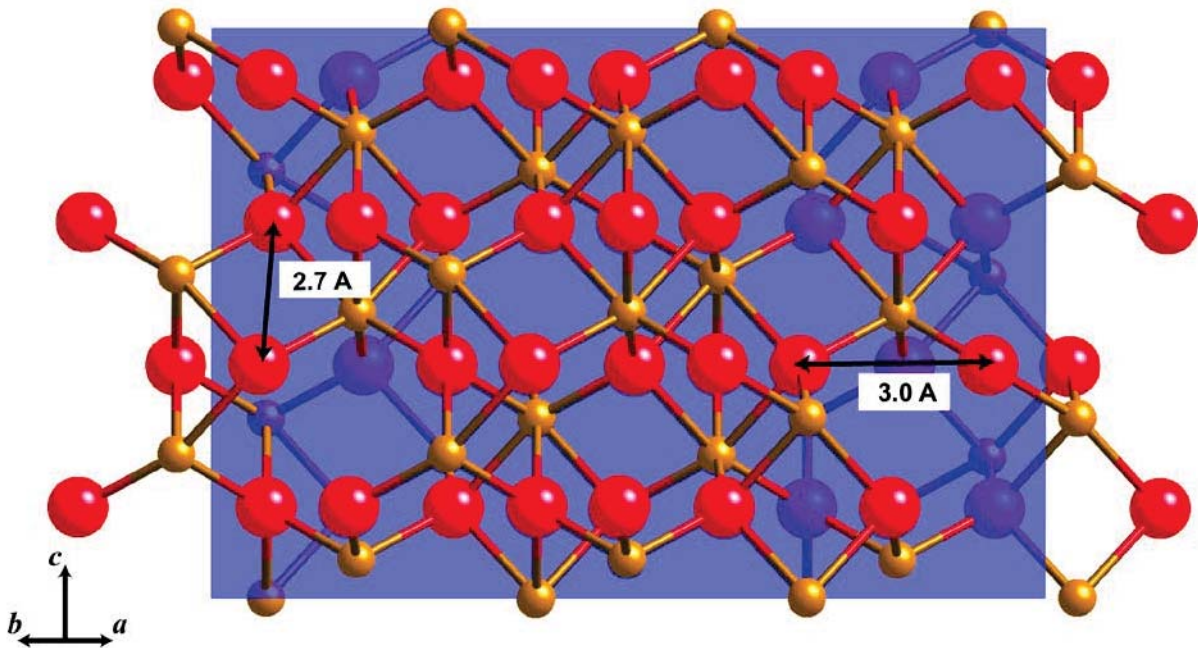


Figure 4.9 Ball and stick representation of the hematite lattice, viewed normal to the (210) plane (purple plane), showing the larger size of the tetrahedral interstices along a,b directions of the unit cell as compared to c. Gold spheres represent iron cations; red spheres represent oxygen anions. Model generated using CrystalMaker.

#### 4.3.5 Propagation of Atomic Structure Through Multiple Length Scales

We find that the *atomic* scale changes to the hematite lattice caused by silicon incorporation are the foundation for the *nano-, meso-, and microscale* architecture of the hydrogel grown crystals (Figure 4.10). The lattice expansion along *c* caused by silicon incorporation is reflected in the domain structure, namely that growth is hindered along [001], favoring the elongation of domains along [110]. In contrast, oxyanionic additives smaller than silicate, phosphate and sulfate, are known to favor growth along [001], leading to peanut- and spindle-shaped hematite crystals.<sup>37,40,43-45</sup> The nanoscale domain structure shows a signature in the mesoscale assembly, wherein the 2D spherulitic planes propagate radially along [110]. At the microscale, whole crystal level, we find that the net orientation of the hematite lattice is consistent

with the  $[110]$ -elongated domain structure: the  $c$ -axis of hematite is aligned with the shortest diameter of the quasi-spherical, mosaic crystals, leaving  $[110]$  aligned with the widest diameter. The net result of this multi-level structural analysis is that growth in a silica hydrogel allowed access to microscale architectures with a dominance of nanoscale  $\{110\}$  planes at their surfaces.

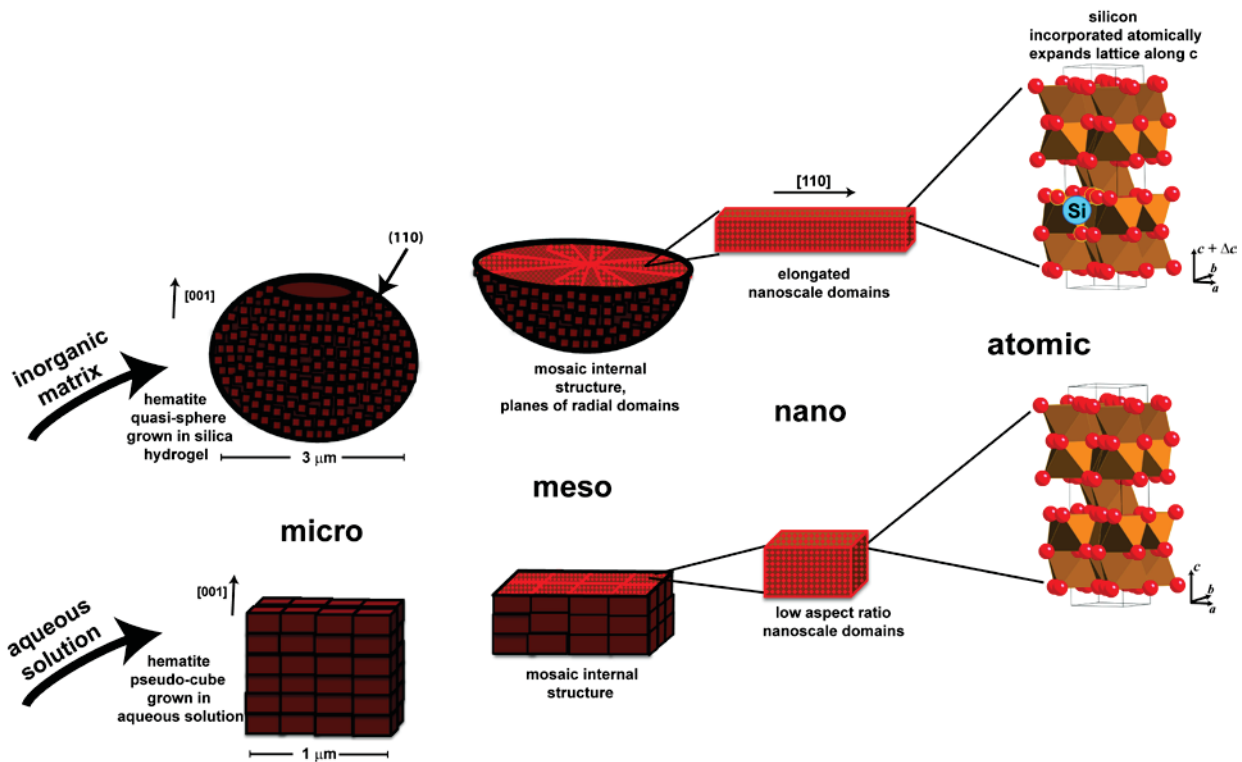


Figure 4.10 Schematic representation of the hierarchical structure contained within microscale hematite architectures. By crystallizing hematite in an inorganic silica hydrogel, the hierarchical structure is modified across length scales. The microscale, quasi-spherical forms are composed of mesoscale, spherulitic planes that stack along  $[001]$ . The planes are composed of nanoscale domains that are elongated along  $[110]$ , consistent with the  $c$ -axis expansion ( $c + \Delta c$ ) that is caused by silicon incorporation as an interstitial dopant at the atomic level. In contrast, the hematite pseudo-cubes crystallized from aqueous solution do not have a dominant anisotropic lattice expansion, leading to low aspect ratio domains.

#### 4.3.6 Hierarchical Structure Influence on Properties

Armed with results that indicate that the surfaces of the quasi-spheres contain high-catalytic activity {110} planes, we sought to evaluate the photocatalytic properties of these structures.<sup>21,22</sup> In particular, photocatalytic activity depends on multiple variables, including band gap, surface area, and the specific crystallographic planes that are expressed. Bandgap values were extracted from diffuse reflectance spectra (Figure 4.12).

Table 4.7). Regardless of the growth condition, all hematite crystals analyzed were found to have the same bandgap of 2.1 eV, indicating that silicon interstitials are not electron donating.<sup>46</sup> To control for and evaluate the effect of surface area, we also assessed commercial hematite (Figure 4.11 & Table 4.1) and acid-etched quasi-spheres (Figure 4.13). The acid etching allowed us to form porous structures from the hematite quasi-spheres with double the surface area, while retaining the mosaic crystal structure.<sup>47</sup> The solution-grown (borosilicate) pseudo-cubes were used as an additional control. The photocatalytic performance of hematite was probed through the ability of hematite to catalyze the degradation of an organic dye (rhodamine B) under illumination with visible light in the presence of peroxide. Judicious experimental design was undertaken to prevent the photobleaching of the dye to ensure that the degradation of the dye was solely due to processes catalyzed by the hematite crystals.<sup>48</sup> A UV cut-off filter ( $\lambda < 400$  nm, Figure 4.14) was used to remove high energy radiation, and the incident illumination was set to 100 mW/cm<sup>2</sup>.

Table 4.7 Summary of bandgap results for hematite crystals found from diffuse reflectance (Kebulka-Munk) analysis

Sample	$dF/d\lambda_{\min}$ (nm)	$E_g$ (eV)
Commercial hematite	588	2.11
Solution-grown pseudo-cube (Borosilicate)	600	2.07
Hydrogel-grown quasi-sphere	592	2.09
Hydrogel-grown quasi-sphere, acid-etched	600	2.07

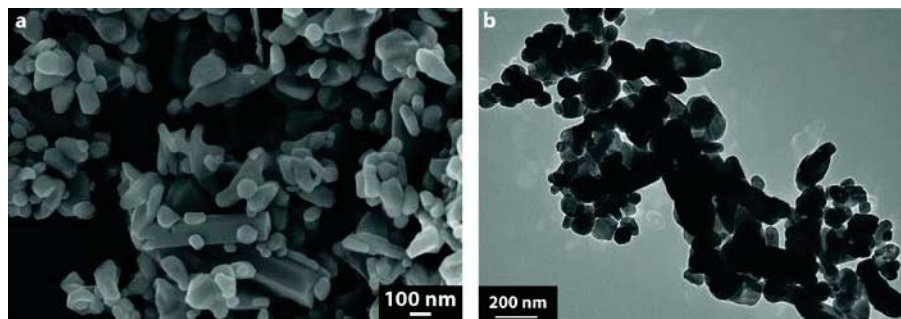


Figure 4.11 (a) SEM and (b) TEM of commercial hematite used as a control for bandgap determination, and photocatalytic measurements.

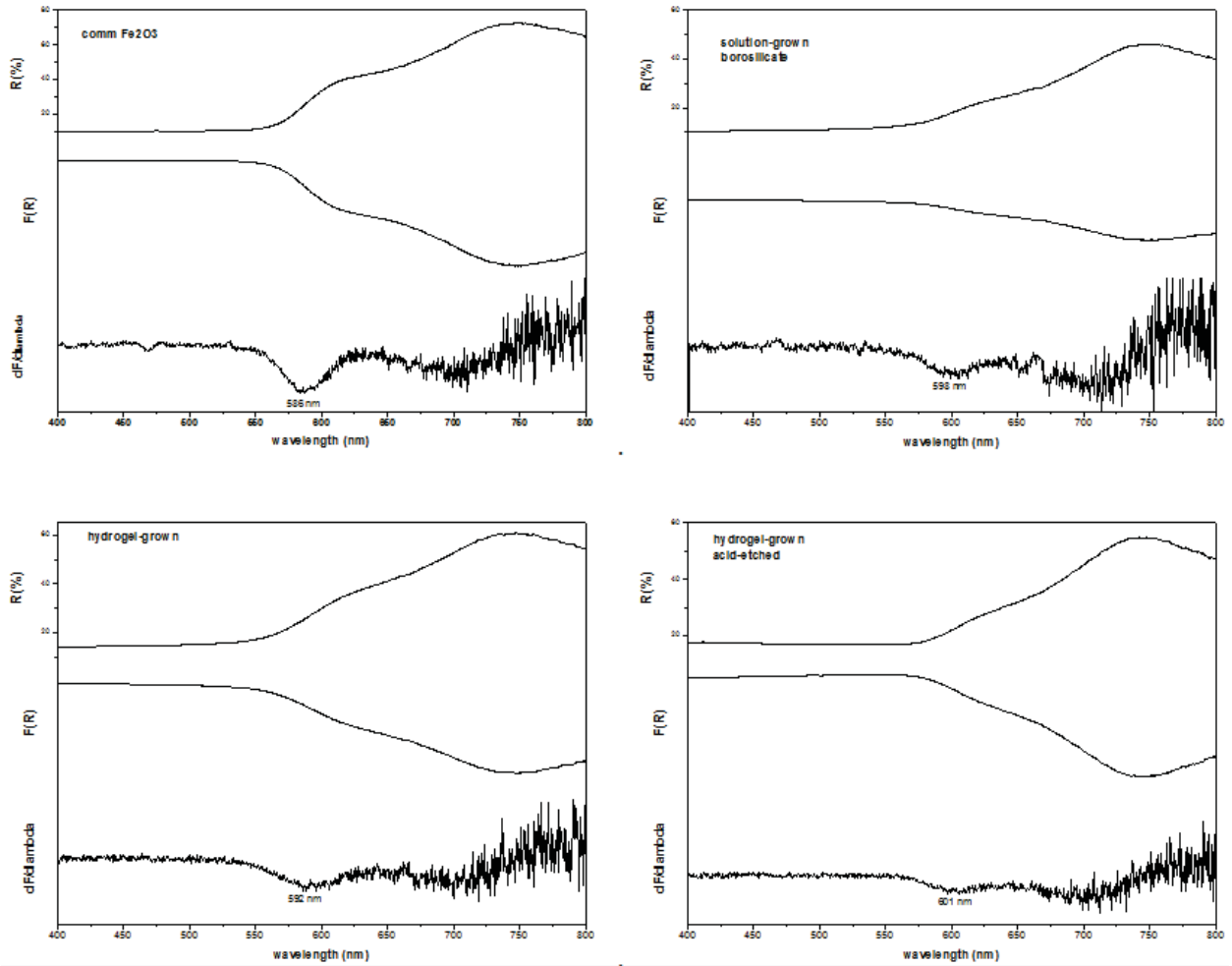


Figure 4.12 Diffuse reflectance spectra and Kubelka-Munk analysis used to extract bandgap of the hematite crystals.

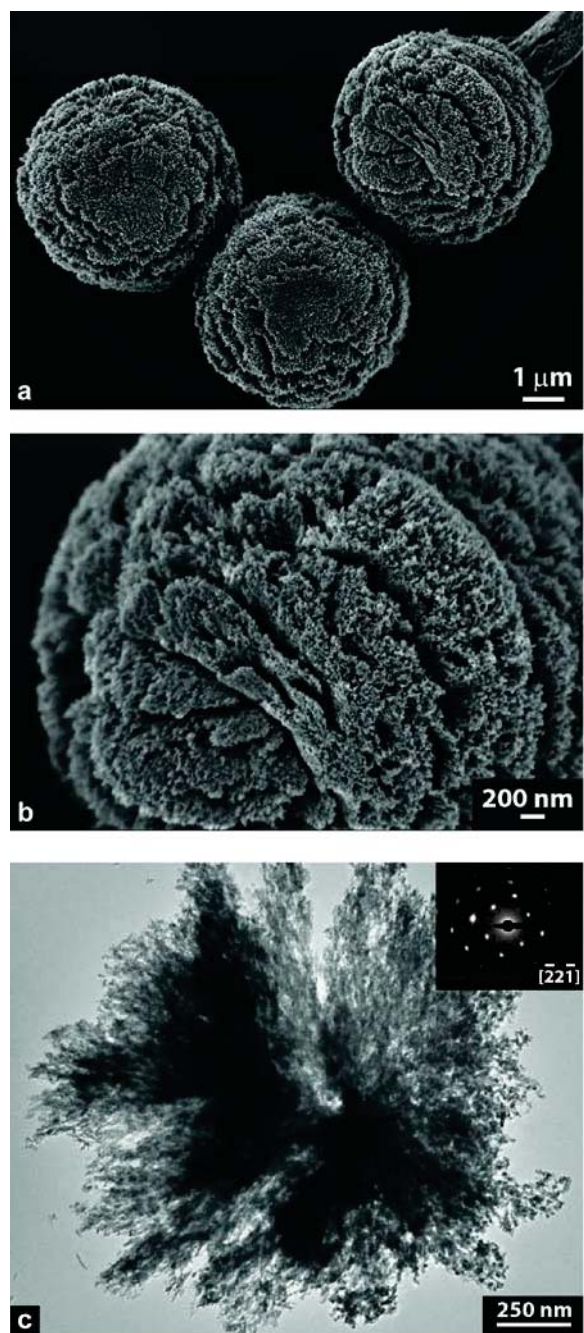


Figure 4.13 Porous mosaic crystalline structures of the hydrogel-grown hematite accessed by acid etching. These structures have increased surface area with respect to the un-etched crystals (Fig. 2a,d) and were used as an increased surface area reference material in photocatalysis measurements: (a) SEM image; (b) higher magnification of region from a; (c) bright field TEM image with SAED inset displaying single-crystal-like diffraction.

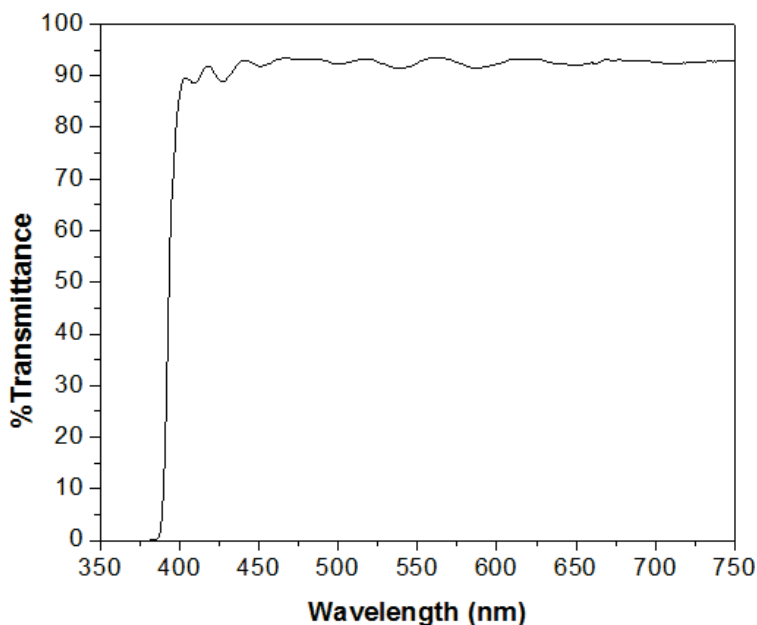


Figure 4.14 Transmittance spectrum of the cut-off filter used to remove UV radiation from photocatalysis experiments.

All hematite crystals studied were effective at catalyzing the degradation of rhodamine B (Figure 4.15Figure 4.16). In order to fully assess the photocatalytic performance of the micro-scale mosaic hematite crystals, we performed repeat experiments (minimum 3) and normalized the average  $A/A_0$  to the surface area (Figure 4.16b). With this closer look at the photocatalysis results, it can be seen that the un-etched quasi-spheres are the most effective at degrading the organic dye, as evidenced by their lower average and smaller standard deviation between experiments. While the commercial nano-scale hematite crystals were not able to degrade the dye to <50% after 12 h, all three micro-scale hematite crystals effectively quenched the dye, with the hydrogel-grown crystals completely removing the organic contaminant from the solution after 12 h. These results come in contrast to previous reports on the photocatalysis with hematite, wherein nano-sized crystals have been the target for improved performance.<sup>49</sup> The failure of the higher-surface-area, acid-etched quasi-spheres toward increased performance is consistent with the crystallographic features of the hydrogel-grown crystals: the higher

catalytic activity {110} planes are preferentially lost due to their higher reactivity toward acid dissolution.<sup>50</sup> The change in  $I_{104}/I_{110}$  when comparing the as-grown to acid-etched quasi-spheres further confirms that acid etching has preferentially removed {110} planes (Table 4.1 & Figure 4.7). The performance enhancement achieved by gel-growth highlights the potential for this matrix-mediated crystallization approach to tune the structure/property relationships in metal oxides.

#### 4.4 Summary and Conclusions

The growth of hematite in a silica hydrogel is demonstrated as a means to modulate the architecture of hematite crystals from the *atomic* to the *nano*, *meso* and *microscale* levels of the hierarchical structure. Careful analysis of the resulting hematite structures across multiple length scales was the key to elucidating the role of the hydrogel to modulate the architecture of the (iron) oxide crystals. At the atomic level, dissolved silica in the growth environment serves as a chemical additive, facilitating silicon incorporation into the hematite lattice. As a tetrahedral dopant, silicon causes expansion along the *c*-axis, favoring the growth of the nanoscale domains along [110]. These [110]-elongated nanoscale domains propagate within 2D spherulitic planes, leading to a net orientation of the hematite lattice that has the *c*-axis aligned perpendicular to these planes, collinear to the shortest diameter of the quasi-sphere. These micron-sized mosaic hematite crystals, which are decorated with nanoscale (110) planes, outperform their nano-scale counterparts in photocatalytic activity, presenting a new approach to the design of materials for advanced energy technologies. These results open the possibility to grow other functional oxide materials in hydrogels and exhibit predictive control over their structures and properties by judicious choice of hydrogel.

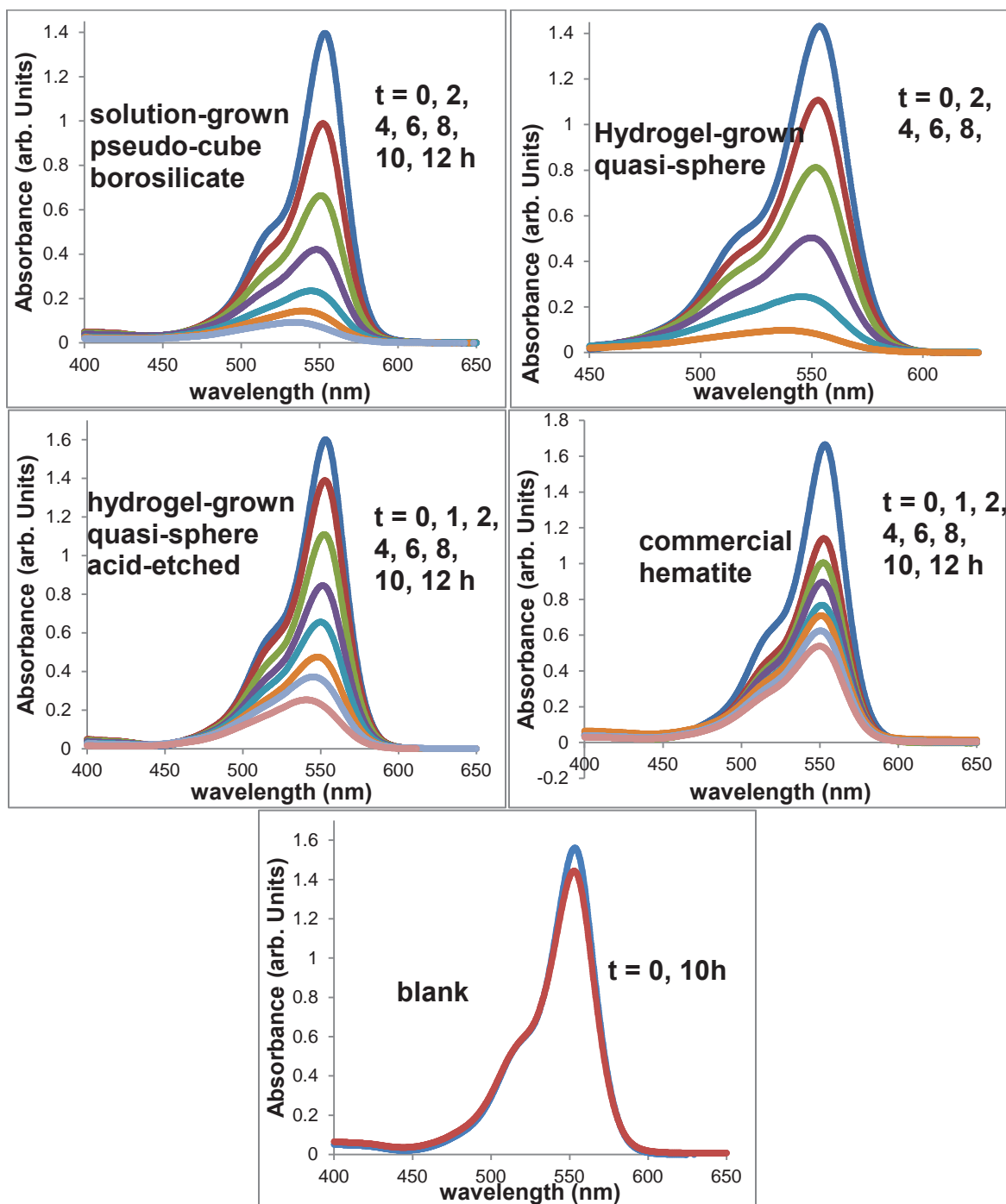


Figure 4.15 Raw absorbance plots for the decomposition of rhodamine B used in the photocatalytic assessment of hierarchical hematite architectures.

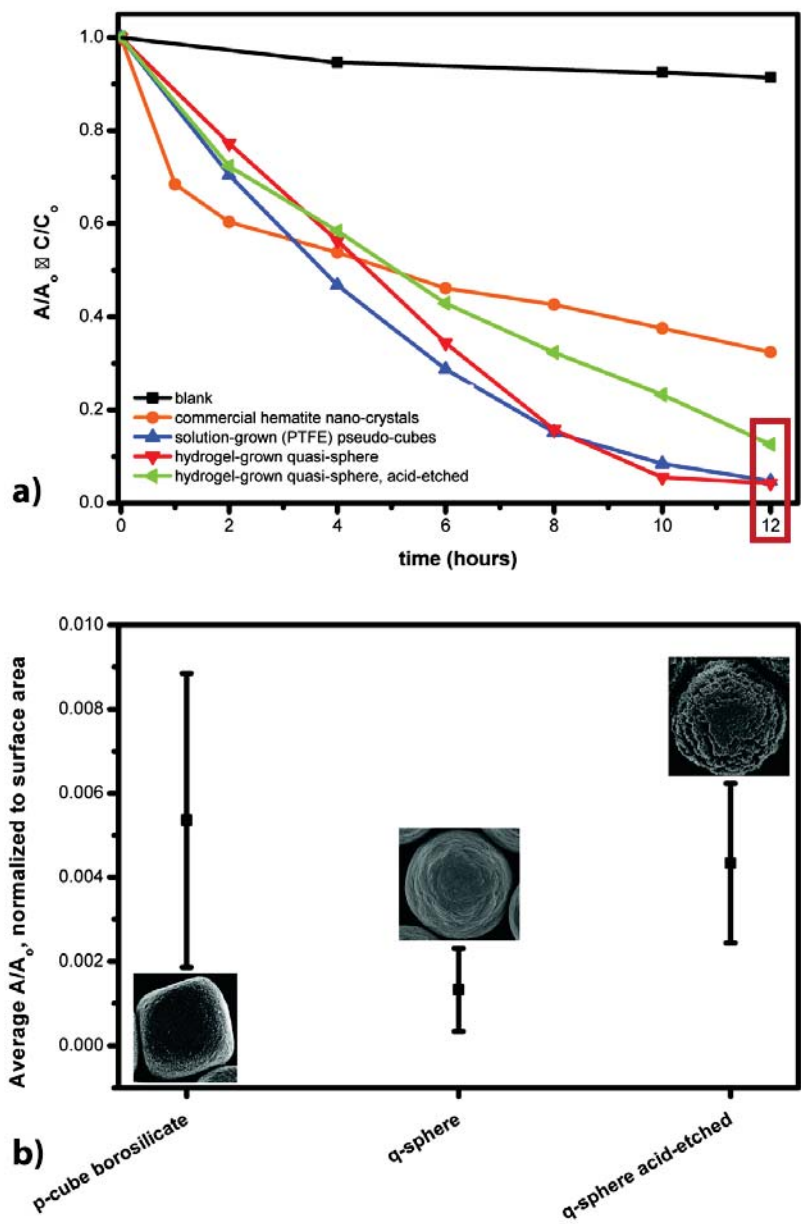


Figure 4.16 The photocatalytic performance of hematite samples as measured via the degradation of Rhodamine B solution under illumination with visible light in the presence of hematite. (a) Fractional amount of rhodamine B remaining in solution as a function of time under illumination with visible light. Blank experiment consisted of rhodamine B solution and peroxide only. (b) Focused analysis on the 12h time points denoted with red box in (a): The average of a minimum of three experiments, normalized by surface area is displayed for the three mosaic hematite architectures. Error bars represent the standard deviation between the experiments.

## ACKNOWLEDGEMENTS

We acknowledge support from the NSF (DMR 0845212 and DMR 1210304) and EAS acknowledges the NSF Graduate Research Fellowship (GRF, DGE-0707428), and Integrative Graduate Education and Research Traineeship (IGERT, DGE-0903653) Programs. This work was also supported in part by The Cornell Center for Materials Research (CCMR) and made use of the CCMR Shared Facilities, both funded by NSF MRSEC program (DMR 1120296). Specific acknowledgment is made for the assistance of Malcolm G. Thomas and John L. Grazul during the use of the electron microscopy facilities. Special thanks are expressed Megan E. Holtz and Pinshane Y. Huang for assistance with electron microscopy. Additional gratitude is expressed to Professor Frank DiSalvo and his Research Group for pXRD, Professor Hector Abruna and his Research Group for photocatalysis equipment, and Professor Ulrich Wiesner and his Research Group for assistance with BET analysis. Special thanks are expressed to Dr. Mike Rutzke and Tatyana Dokuchayeva of the Cornell Nutrient Analysis Laboratories for ICP-AES analysis.

## 4.5 Materials and Methods

### 4.5.1 Methods

*Reagents:* All reagents were used as received without further purification.

Iron (III) chloride hexahydrate ( $\geq 99\%$ ; Sigma-Aldrich)

Hydrochloric acid (Certified ACS Plus Reagent; Fisher Scientific)

Sodium metasilicate nonahydrate ( $\geq 98\%$ ; Sigma-Aldrich)

Sodium Hydroxide ( $\geq 97\%$ ; Fisher Scientific)

Rhodamine B

Hydrogen peroxide

### 4.5.2 Solution-Based Crystallization

Crystallization of hematite pseudocubes was performed by acid-catalyzed hydrolysis of iron (III) chloride as previously reported in the literature.<sup>19</sup> Specifically, solutions of iron (III) chloride hexahydrate (1.8 M) and hydrochloric acid (13 mM) were mixed in a 1:3 ratio to a final volume of 80 mL in Teflon-lined pressure vessels (Silica-free, solution condition) and Pyrex media bottles (regular solution condition). After stirring for 60 mins at room temperature, the vessels were sealed and subject to hydrothermal treatment in a mechanical convection oven at 100 °C for 4 weeks. The deep yellow solution remained free of precipitates for all times prior to hydrothermal heating. After 4 weeks, the reddish hematite precipitates were isolated by centrifugation (3600 g, 5 min) and rinsed with water (3x), followed by drying on a lyophilizer.

### 4.5.3 Silica Hydrogel Formation

When dissolved in water, sodium metasilicate forms a highly basic solution (0.5 M, pH~13) due to the following equilibrium:



Cellular, porous silica hydrogels are formed by neutralizing sodium metasilicate solutions as shown in Equation 2.



In this work, aqueous solutions of sodium metasilicate nonahydrate (0.5 M, 15 mL) were gelled in Teflon-lined pressure vessels and Pyrex media bottles by adding equal volumes of diluted (1.0 M) hydrochloric acid with stirring for 1 minute. The onset of gelation occurred within 5 minutes, and hydrogel-containing vessels were sealed and allowed to set for 24 h at 30 °C in a water bath to reach full gelation. After 24 h, sodium metasilicate hydrogels formed by stoichiometric acid addition have a roughly neutral pH (pH 6-7).

#### 4.5.4 Hydrogel-Based Crystallization Experiments

30 mL of iron (III) chloride hexahydrate solution (1.8 M) was added to the top of pre-formed silica hydrogels (30 mL) and allowed to diffuse into the hydrogel for 24 h at 30 °C in a water bath (Figure 4.1b). The sealed bottles were then heated to 100 °C in a mechanical convection oven for 4 weeks, during which time, hematite crystals formed within the hydrogel (Fig. 1c). Subsequently, the hydrogel/hematite samples were soaked in and rinsed with deionized water (3x) and dried on a lyophilizer for 24 h.

#### 4.5.5 Silica Matrix Removal and Acid Etching

Dissolution of the remnant silica matrix was performed by soaking hematite crystals in 1 M NaOH with gentle agitation for 3 d. Subsequently, the crystals were rinsed with deionized water (3x) and dried on a lyophilizer for 24 h. Acid etching was performed on dried hematite crystals that had been subject to silica matrix removal by soaking in 1 M HCl with gentle agitation for 14 d. After this time, crystals were rinsed with deionized water (3x) and dried on a lyophilizer for 24 h.

#### **4.5.6 Elemental Analysis**

Hematite crystals were analyzed by inductively coupled plasma atomic emission spectroscopy (ICP-AES) by the Cornell Nutrient Analysis Laboratory (Ithaca, NY) for the presence of elemental silicon. The samples were prepared by dissolving ~6 mg of crystals in 5 mL of HCl, followed by dilution with de-ionized water (18.2 M $\Omega$ ) to a final volume of 45 mL.

#### **4.5.7 Phase Analysis**

X-ray powder diffraction (pXRD) was performed using a Rigaku Ultima VI (Rigaku Americas, USA) diffractometer with CuK $\alpha$  radiation (K $_{\alpha 1}$ ,  $\lambda = 1.5046 \text{ \AA}$  and K $_{\alpha 2}$ ,  $\lambda = 1.5444 \text{ \AA}$ ) operating at 40 kV, 40 mA. Rietveld refinements were performed using Jade 10 Software. Patterns were fit over the range of 23°-90° two-theta using a pseudo-Voigt model with a polynomial (5<sup>th</sup> degree) background using starting parameters from PDF#98-000-0240. Peak intensities were found using OriginPro 9 by integrating the peak areas from  $y=0$  using a Gaussian fit with a spline background function.

#### **4.5.8 Hydrogel Sample Preparation for SEM imaging**

Fresh hydrogel samples before and after crystallization with hematite were sliced into thin sections (~1x1x0.2 cm) and frozen in liquid nitrogen. The samples were subsequently freeze-dried on a lyophilizer for 18-24 h. Freeze-dried samples were mounted with conductive carbon paste to silicon wafers and coated with carbon while on a rotating/tilting stage. Subsequently, samples were sputter-coated with Au/Pd. Hydrogel microstructures were imaged with a scanning electron microscope (Leica 440 Stereoscan) operating at 20 kV.

#### **4.5.9 Whole Particle Imaging**

Both solution- and hydrogel-grown hematite crystals were imaged (uncoated) with a Leo 1550 field-emission scanning electron microscope (Zeiss Microscopy, USA) operating at 2-5 keV. Prior to imaging, remnant hydrogel was removed from the hydrogel-grown particles with NaOH (1 M) base treatment. Powders of hematite pseudocubes were dispersed in ethanol and observed with an optical

microscope (OM) (Olympus BX51 with an Olympus Camedia C-7070 digital camera) using a 50x objective lens in transmission in the absence and presence of cross-polarizers (CPOM).

#### **4.5.10 Sample Preparation for TEM Analysis**

Electron transparent thin sections of hematite crystals were prepared using a dual-beam FIB microscope (Strata 400S, FEI) equipped with a liquid gallium ion source and a nanomanipulator (OmniProbe AutoProbe 200, Oxford Instruments), as previously described.<sup>33</sup> The non-spherical features of the hydrogel-grown hematite crystals were distinguished by treatment in base to allow us to form thin sections from two distinct locations within the gel grown spheres. The specific orientations of individual hematite particles were accessed by manipulating them with the nanomanipulator needle (Figure 4.4a). Each particle was then mounted whole onto the needle with a Pt weld. The edge of a center post of a three-post copper lift-out grid was pre-milled to create a fresh, flat location for particle mounting. The individual hematite crystals were mounted (with Pt weld) directly on copper grids for milling. A rectangular section of Pt was deposited as a milling guide over the top of the particles (visible on top of particle shown in Figure 4.4b). Milling was conducted at 30 and 10 keV, with 50% overlap. Final ion-polishing was conducted at 5 keV, with 85% overlap. The final thin sections were ~50 nm in thickness with lateral dimensions up to 1  $\mu\text{m}$  (Figure 4.4c).

#### **4.5.11 TEM Analysis**

The hematite thin sections were plasma-cleaned for 1 min immediately prior to bright-field TEM and selected-area electron diffraction (SAED) on an FEI Tecnai T12 electron microscope, LaB6 filament, operating at 120 kV, with spot size of 3. Images were taken with an SIS Megaview III CCD camera. Camera calibration for selected area electron diffraction (SAED) and mosaicity calculations was performed using a (100)-oriented single crystal of strontium titanate on silicon (courtesy of Charles Brooks, fabricated as described in ref.<sup>51</sup> using the relation  $Rd = L\lambda$ , where  $R$  is the radial distance of the

diffraction spot from the center,  $d$  is the interplanar spacing,  $L$  is the camera length, and  $\lambda$  is the wavelength of the incident beam.

#### 4.5.12 Mosaicity Quantification

SAED patterns were analyzed using the ‘polar transformer’ plugin in ImageJ as previously reported.<sup>33</sup> Briefly, SAED patterns were transformed into 2D linear plots of azimuthal angle ( $\phi$ ) vs.  $R$  and line profiles were taken from these plots at constant  $R$  to form profiles of intensity ( $I$ ) vs.  $\phi$ . These profiles were fit to a Gaussian function using OriginPro<sup>®</sup> 8, to find the full width half maximum ( $FWHM_{exp}$ ) of the peaks, which represents the azimuthal broadening of the diffracted intensity. The mosaicity (mosaic spread ( $MS$ )), is then estimated according to (Equation 6), where ( $\sigma_{STO}$ ) is the instrumental broadening<sup>52,53</sup> found by performing this analysis on a single crystal of strontium titanate.

$$MS = \sqrt{FWHM_{exp}^2 - \sigma_{STO}^2} \quad \text{Equation 6}$$

#### 4.5.13 Scanning Transmission Electron Microscopy

Electron energy loss spectroscopic (EELS) data were acquired on a 5th-order aberration-corrected scanning transmission electron microscope (Nion UltraSTEM) operated at 100 kV, with roughly ~90 pA of beam current, a probe forming semi-angle of roughly 30 mrad, and a collection semi-angle around 0-60 mrad for EELS.

The spectra in Figure 4.5 were taken over a 30nm field of view from the average of 600 spectra with 0.03 s acquisition time for the low loss Si-L edge and 0.7 s acquisition time for the higher-loss O-K and Fe-L edges. The background EELS spectra was modeled using a linear combination of power laws with an energy-offset to best model the background of the relatively thick specimen. This was implemented using the open-source Cornell Spectrum Imager software and are described in more detail by P. Cueva et al.<sup>54</sup>

#### 4.5.14 Surface Area Determination

The BET specific surface area was measured by N<sub>2</sub> adsorption at 77 K using a Micrometrics ASAP 2020 surface area and porosity analyzer. Prior to measurement, samples were degassed under vacuum at 120 °C overnight.

#### 4.5.15 Bandgap Determination

Diffuse reflectance spectra were recorded using a Shimadzu UV 3600 UV/Vis/NIR Spectrophotometer with integrating sphere referenced to BaSO<sub>4</sub>. Reflectance spectra were analyzed using a Kubelka-Munk remission function to extract bandgap.<sup>55</sup> In short, the reflectance spectra (R) was transformed according to  $F(R)=(1-R)^2/2R$ , and subsequently the band gap was extracted from the minimum of  $dF/d\lambda$  ( $d^2F/d\lambda^2=0$ ).

#### 4.5.16 Photocatalytic degradation of Rhodamine B

The photocatalytic performance of hematite was assessed via its ability to catalyze the photodegradation of an organic dye rhodamine B. Great care was taken to optimize the illumination conditions to prevent photobleaching of the dye so that the performance of hematite as a photocatalyst could be accurately measured. Briefly, hematite catalyzes the photodegradation of rhodamine B under illumination with visible light in the presence of peroxide. The reaction can be described by the following general pathway: (i) under illumination electron-hole pairs are formed on hematite surfaces; (ii) the electrons facilitate the formation of peroxide radicals; and (iii) peroxide radicals attack the conjugated system of the dye. By monitoring the absorbance of rhodamine B (553 nm) at regular time intervals during illumination, the photocatalytic performance of hematite can be assessed.

Specifically, 12 mg of hematite crystals were dispersed in 60 mL of freshly prepared Rhodamine B solution ( $2.0 \times 10^{-5}$  M) by sonicating and stirring for 15 min. Immediately following this mixing step, 300  $\mu$ L of H<sub>2</sub>O<sub>2</sub> (30%) was added under stirring. After 1 min of stirring, the  $t_0$  aliquot (3 mL) was extracted and the solution was subject to illumination while stirring continued. Aliquots were

immediately filtered (0.2  $\mu\text{m}$ ) and the absorbance measured within 5 minutes. During the experiment, 3 mL aliquots were extracted at regular time intervals. A minimum of 3 similar experiments were conducted to verify reproducibility and statistical significance.

Illumination was performed with a 200 W Hg/Xe lamp (Oriel Model 66902), equipped with a UV cut-off filter (transmittance spectrum shown in Fig. S9). Distance was set so that a power density of  $100\text{mW}/\text{cm}^2$  was achieved (as measured with a radiometer photometer (EG&G Electrooptics Model 450-1)). Absorbance was measured using a Shimadzu UV 3600 UV/Vis/NIR Spectrophotometer in a quartz cuvette.

## REFERENCES

- (1) Crossland, E. J. W.; Noel, N.; Sivaram, V.; Leijtens, T.; Alexander-Webber, J. A.; Snaith, H. J. *Nature* **2013**, *495*, 215.
- (2) Warren, S. C.; Voitchovsky, K.; Dotan, H.; Leroy, C. M.; Cornuz, M.; Stellacci, F.; Hebert, C.; Rothschild, A.; Gratzel, M. *Nat. Mater.* **2013**, *12*, 842.
- (3) Ohtaki, M. *Journal of the Ceramic Society of Japan* **2011**, *119*, 770.
- (4) Dunlop, J. W. C.; Fratzl, P. *Scripta Materialia* **2013**, *68*, 8.
- (5) Nudelman, F.; Pieterse, K.; George, A.; Bomans, P. H. H.; Friedrich, H.; Brylka, L. J.; Hilbers, P. A. J.; de With, G.; Sommerdijk, N. *Nat. Mater.* **2010**, *9*, 1004.
- (6) Kim, Y. Y.; Ganesan, K.; Yang, P. C.; Kulak, A. N.; Borukhin, S.; Pechook, S.; Ribeiro, L.; Kroger, R.; Eichhorn, S. J.; Armes, S. P.; Pokroy, B.; Meldrum, F. C. *Nat. Mater.* **2011**, *10*, 890.
- (7) Meza, L. R.; Das, S.; Greer, J. R. *Science* **2014**, *345*, 1322.
- (8) Gordon, L. M.; Joester, D. *Nature* **2011**, *469*, 194.
- (9) Li, H.; Xin, H. L.; Muller, D. A.; Estroff, L. A. *Science* **2009**, *326*, 1244.
- (10) Henisch, H. K. *Crystal Growth in Gels and Liesegang Rings*; Cambridge University Press: Cambridge, 1988.
- (11) Asenath-Smith, E.; Li, H.; Keene, E. C.; Seh, Z. W.; Estroff, L. A. *Adv. Funct. Mater.* **2012**, *22*, 2891.
- (12) Prieto, M.; García-Ruiz, J. M.; Amoros, J. L. *J. Cryst. Growth* **1981**, *52*, 864.
- (13) Iafisco, M.; Marchetti, M.; Morales, J. G.; Hernandez-Hernandez, M. A.; Ruiz, J. M. G.; Roveri, N. *Crystal Growth & Design* **2009**, *9*, 4912.
- (14) Gavira, J. A.; Garcia-Ruiz, J. M. *Acta Crystallogr. Sect. D-Biol. Crystallogr.* **2002**, *58*, 1653.
- (15) Gavira, J. A.; Van Driessche, A. E. S.; Garcia-Ruiz, J. M. *Crystal Growth & Design* **2013**, *13*, 2522.
- (16) Dang, F.; Oaki, Y.; Kokubu, T.; Hosono, E.; Zhou, H. S.; Imai, H. *Chem. Asian J.* **2013**, *8*, 760.
- (17) Kokubu, T.; Oaki, Y.; Hosono, E.; Zhou, H. S.; Imai, H. *Adv. Funct. Mater.* **2011**, *21*, 3673.
- (18) Franke, W. A. *J. Cryst. Growth* **1996**, *166*, 996.

- (19) Matijevic, E.; Scheiner, P. *J. Colloid Interface Sci.* **1978**, *63*, 509.
- (20) Sugimoto, T.; Sakata, K.; Muramatsu, A. *J. Colloid Interface Sci.* **1993**, *159*, 372.
- (21) Kay, A.; Cesar, I.; Gratzel, M. *J. Am. Chem. Soc.* **2006**, *128*, 15714.
- (22) Liu, X. J.; Liu, J. F.; Chang, Z.; Sun, X. M.; Li, Y. D. *Catal. Commun.* **2011**, *12*, 530.
- (23) Ziolo, R. F.; Giannelis, E. P.; Weinstein, B. A.; Ohoro, M. P.; Ganguly, B. N.; Mehrotra, V.; Russell, M. W.; Huffman, D. R. *Science* **1992**, *257*, 219.
- (24) Kroll, E.; Winnik, F. M.; Ziolo, R. F. *Chem. Mater.* **1996**, *8*, 1594.
- (25) Raymond, L.; Revol, J. F.; Ryan, D. H.; Marchessault, R. H. *Chem. Mater.* **1994**, *6*, 249.
- (26) Borah, B. M.; Saha, B.; Dey, S. K.; Das, G. *J. Colloid Interface Sci.* **2010**, *349*, 114.
- (27) Tannenbaum, R.; Zubris, M.; Goldberg, E. P.; Reich, S.; Dan, N. *Macromolecules* **2005**, *38*, 4254.
- (28) Sinha, A.; Nayar, S.; Murthy, G. V. S.; Joy, P. A.; Rao, V.; Ramachandrarao, P. *J. Mater. Res.* **2003**, *18*, 1309.
- (29) Helminger, M.; Wu, B. H.; Kollmann, T.; Benke, D.; Schwahn, D.; Pipich, V.; Faivre, D.; Zahn, D.; Colfen, H. *Adv. Funct. Mater.* **2014**, *24*, 3187.
- (30) Ennas, G.; Musinu, A.; Piccaluga, G.; Zedda, D.; Gatteschi, D.; Sangregorio, C.; Stanger, J. L.; Concas, G.; Spano, G. *Chem. Mater.* **1998**, *10*, 495.
- (31) delMonte, F.; Morales, M. P.; Levy, D.; Fernandez, A.; Ocana, M.; Roig, A.; Molins, E.; Ogrady, K.; Serna, C. J. *Langmuir* **1997**, *13*, 3627.
- (32) Niznansky, D.; Viart, N.; Rehspringer, J. L. *Journal of Sol-Gel Science and Technology* **1997**, *8*, 615.
- (33) Asenath-Smith, E.; Estroff, L. A. *Microscopy and Microanalysis* **2014**, *20*, 635.
- (34) Shtukenberg, A. G.; Punin, Y. O.; Gunn, E.; Kahr, B. *Chem. Rev.* **2011**, *112*, 1805.
- (35) Granasy, L.; Pusztai, T.; Tegze, G.; Warren, J. A.; Douglas, J. F. *Physical Review E* **2005**, *72*, 011605.
- (36) Sugimoto, T.; Muramatsu, A.; Sakata, K.; Shindo, D. *J. Colloid Interface Sci.* **1993**, *158*, 420.
- (37) Frandsen, C.; Legg, B. A.; Comolli, L. R.; Zhang, H. Z.; Gilbert, B.; Johnson, E.; Banfield, J. F. *CrystEngComm* **2014**, *16*, 1451.
- (38) Campbell, A. S.; Schwertmann, U.; Stanjek, H.; Friedl, J.; Kyek, A.; Campbell, P. A. *Langmuir* **2002**, *18*, 7804.

- (39) Cornell, R. M.; Schwertmann, U. *The Iron Oxides*; Wiley-VCH, 2003.
- (40) Reeves, N. J.; Mann, S. *J. Chem. Soc., Faraday Trans.* **1991**, *87*, 3875.
- (41) Sharma, R. K. *The Chemistry of Hydrides and Carbides*; Discovery Publishing: Delhi, 2007.
- (42) Stanjek, H.; Schwertmann, U. *Clays Clay Miner.* **1992**, *40*, 347.
- (43) Ozaki, M.; Kratochvil, S.; Matijevic, E. *J. Colloid Interface Sci.* **1984**, *102*, 146.
- (44) Galvez, N.; Barron, V.; Torrent, J. *Clays Clay Miner.* **1999**, *47*, 375.
- (45) Sugimoto, T.; Wang, Y. S.; Itoh, H.; Muramatsu, A. *Colloids and Surfaces a-Physicochemical and Engineering Aspects* **1998**, *134*, 265.
- (46) Cesar, I.; Sivula, K.; Kay, A.; Zboril, R.; Graetzel, M. *J. Phys. Chem. C* **2009**, *113*, 772.
- (47) Cornell, R. M.; Giovanoli, R. *Clay Minerals* **1993**, *28*, 23.
- (48) Wilhelm, P.; Stephan, D. *Journal of Photochemistry and Photobiology A: Chemistry* **2007**, *185*, 19.
- (49) Zhou, X. M.; Yang, H. C.; Wang, C. X.; Mao, X. B.; Wang, Y. S.; Yang, Y. L.; Liu, G. *J. Phys. Chem. C* **2010**, *114*, 17051.
- (50) Maurice, P. A.; Hochella, M. F.; Parks, G. A.; Sposito, G.; Schwertmann, U. *Clays Clay Miner.* **1995**, *43*, 29.
- (51) Warusawithana, M. P.; Cen, C.; Sleasman, C. R.; Woicik, J. C.; Li, Y. L.; Kourkoutis, L. F.; Klug, J. A.; Li, H.; Ryan, P.; Wang, L. P.; Bedzyk, M.; Muller, D. A.; Chen, L. Q.; Levy, J.; Schlom, D. G. *Science* **2009**, *324*, 367.
- (52) Barabash, R. I.; Klimanek, P. *J. Appl. Crystallogr.* **1999**, *32*, 1050.
- (53) Ferrari, C.; Buffagni, E.; Marchini, L.; Zappettini, A. *Optical Engineering* **2012**, *51*, 056501.
- (54) Cueva, P.; Hovden, R.; Mundy, J. A.; Xin, H. L.; Muller, D. A. *Microscopy & Microanalysis* **2012**, *18*, 667.
- (55) Gilbert, B.; Frandsen, C.; Maxey, E. R.; Sherman, D. M. *Physical Review B* **2009**, *79*, 035108.

## 5 THE ROLE OF AKAGANEITE ( $\beta$ -FeOOH) IN THE GROWTH OF HEMATITE ( $\alpha$ -Fe<sub>2</sub>O<sub>3</sub>) IN AN INORGANIC SILICA HYDROGEL <sup>♦</sup>

### 5.1 Abstract

The use of an inorganic hydrogel as a means to modulate the hierarchical architectures of oxide compounds requires an understanding of the effect of the matrix on intermediate phases. In this work, we report on the crystallization of akaganeite ( $\beta$ -FeOOH), both within a silica hydrogel and from aqueous solution, with a focus on understanding the chemical effects of pH, [Fe<sup>3+</sup>], and [Cl<sup>-</sup>], in concert with the physical effects of the silica hydrogel, on the ultimate formation of hematite ( $\alpha$ -Fe<sub>2</sub>O<sub>3</sub>). A distinct physical consequence of the hydrogel crystallization microenvironment is the stabilization of akaganeite as 3D assemblies; a contrast to the discrete rods which form in solution. Chemically, we find that [Fe<sup>3+</sup>] affects the size of akaganeite crystals while [H<sup>+</sup>] determines the aspect ratio. We also identify that crystal splitting is correlated to high [Cl<sup>-</sup>]. In addition, we demonstrate that branched aggregates of akaganeite rods are favored at high [H<sup>+</sup>] and associated with a pathway to hematite that proceeds through the goethite polymorph. With these results, we highlight the physical and chemical variables of the crystallization microenvironment that dictate the structural features of akaganeite crystals and their corresponding hematite forms.

### 5.2 Introduction

The growth of inorganic crystals within hydrogels has shown potential to control the architectures of functional oxide materials;<sup>1-3</sup> however, the role of intermediate oxyhydroxide phases in defining the final oxide morphology are less clearly understood. Research on the growth of ionic crystals within

---

<sup>♦</sup>Portions reproduced with permission from E. Asenath-Smith & L. A. Estroff, *Crystal Growth and Design* **2015**. Copyright © 2015 American Chemical Society.

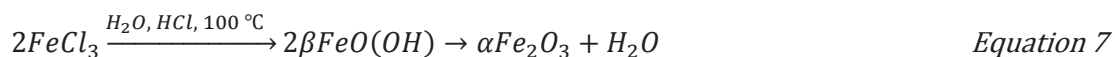
organic hydrogels has identified both chemical and physical characteristics of the gel as key variables for influencing the structure and composition of the crystals.<sup>4,5</sup> While such aspects of organic matrix-mediated crystallization are well understood at ambient conditions, the variables associated with the growth of oxide compounds within inorganic hydrogels under hydrothermal conditions requires further investigation. In addition to the obvious complexity introduced by elevated temperatures, crystallization of the target oxide phase is often complicated by the existence of intermediate oxyhydroxide phases.<sup>6,7</sup> In some cases, the intermediate phases serve as templates for the nucleation of the oxide phase, thereby playing a role in defining the final structure.<sup>8</sup> An understanding of the physical and chemical effects of an inorganic hydrogel under hydrothermal conditions on initial oxyhydroxide phases will inform the development of this method for the design of new oxide materials with tightly regulated structural features.

Using hematite ( $\alpha\text{-Fe}_2\text{O}_3$ ) as a model oxide system, we have previously reported the ability to modulate the hierarchical structure of hematite by growth in an inorganic silica hydrogel.<sup>1,9</sup> Specifically, quasi-spheres of hematite formed in the hydrogel, as compared to pseudocubes formed under equivalent conditions in solution. The previous work focused on understanding the chemical effects of dissolved silica in the crystallization microenvironment in modulating the hematite structure across length scales. The chemical role of silica was able to explain the net lattice orientation of hematite within the non-idiomorphic quasi-spheres, however, the radial internal mesoscale structure could not be fully attributed to chemically dissolved silica alone. The iron oxyhydroxide phase akaganeite ( $\beta\text{-FeOOH}$ ) was present as an intermediate in this work, and has been implicated with a role as a structural template to hematite growth from aqueous solution.<sup>8</sup> With this background, we designed an investigation of the akaganeite phase to elucidate the chemical and physical role played by the silica hydrogel environment in modulating the growth and assembly of this intermediate iron oxyhydroxide phase.

### 5.2.1 Hematite Morphology and Synthesis

Hematite, with the hexagonal space group  $R\bar{3}c$ , can be formed in a range of non-idiomorphic forms with mosaic internal structures that preserve the net orientation of the hematite lattice on the micro-scale. For example, pseudo-cubes of hematite, formed by acidic hydrolysis of iron salts,<sup>10</sup> show a [001] orientation of the hematite lattice that is normal to two parallel faces.<sup>9</sup> Hematite spindles, which exhibit a [001] orientation along their long axis, form in aqueous solution with phosphate additives.<sup>11</sup> In contrast, quasi-spheres of hematite formed in a silica hydrogel show a [001] orientation along their shortest axis.<sup>1</sup>

When grown from aqueous solutions, hematite forms through re-precipitation processes that proceed via the dissolution of oxyhydroxide phases of iron.<sup>12-15</sup> For example, under acidic conditions and in the presence of chlorine counter anions, hematite crystallization is preceded by the precipitation of akaganeite ( $\beta$ -FeOOH), as illustrated in Equation 7.



Ultimately, the growth of hematite subsequent to akaganeite precipitation can be rationalized based on their relative solubilities.<sup>12</sup> Under higher pH conditions, the formation pathway can proceed through the goethite ( $\alpha$ -FeOOH) polymorph.<sup>15</sup>

### 5.2.2 Akaganeite ( $\beta$ -FeOOH) Crystallography and Structure

Crystallographically, akaganeite has a hollandite-like structure with monoclinic symmetry.<sup>16</sup> Within the iron (oxy, hydr-)oxide family, the akaganeite crystal structure is distinguished by the *bcc* packing of the anion lattice as compared to the more common *hcp* packing found in goethite and hematite.<sup>13</sup> Double chains of  $(FeO_6)^{6-}$  face-shared octahedra propagate along *b*, forming an open tunnel structure within the lattice,<sup>13</sup> which can accommodate anionic species. As compared to the alpha polymorph (goethite), which is stabilized by incorporated OH, akaganeite is stabilized by 2-6 % chloride

or fluoride within its tunnels.<sup>16</sup> These structural qualities illustrate why akaganeite formation is favored at low pH in the presence of chloride.

The habit of akaganeite itself presents unusual characteristics; irregularly-shaped, ellipsoidal colloids with regular, crystalline internal structure.<sup>17</sup> Such *somatoid* forms of akaganeite are facilitated by the porous, tubular substructure, which is composed of bundles of parallel rods that are elongated along the b-axis of the unit cell.<sup>18</sup> In addition to this unique substructure, akaganeite exists in six-arm, pseudo-octahedral, star-like twinned forms, owing to its (332) twin plane, wherein each arm of the stars is elongated along [010] and forms an angle of 63° to the central rod.<sup>19</sup> A limited number of reports exist on the precipitation of akaganeite in the presence of cationic additives, however, a consistent trend among additives, counter ions, and morphology has not yet been established.<sup>20-23</sup> Further, how additives affect hematite morphology via the akaganeite polymorph is not well understood.

### 5.2.3 Relationship of Akaganeite to Hematite

The pathways available for hematite nucleation, subsequent to akaganeite formation, depend on reagent concentration and pH.<sup>8</sup> At low iron concentration, hematite nucleation occurs by a discrete dissolution-reprecipitation mechanism. At high iron concentration, hematite nucleation occurs heterogeneously on akaganeite surfaces. In this latter case, the akaganeite phase serves as a template for hematite nucleation, causing the final morphology of the hematite to reflect that of the initial akaganeite phase. The hematite pseudo-cube is an illustration of this latter case, wherein hematite nucleation takes place on square rafts composed of assembled akaganeite rods. The assigned role of akaganeite-akaganeite interfaces as promoters of hematite nucleation,<sup>11</sup> coupled with the amenability of akaganeite colloids to assembly into structures with long range orientational order in solution,<sup>17,24</sup> provides a key to understanding how micron-sized single-crystal-like particles of hematite can form in a variety of shapes.

In this report, we focus on the precipitation of akaganeite in aqueous solution and in a silica hydrogel in an effort to understand the effect of the hydrated, silica matrix on the formation of hematite.

By pairing a series of hydrogel-grown akaganeite crystals with a series of solution-based crystallization studies, we were able to separate the physical effects of the confining matrix from the chemical effects of concentration (of both  $\text{Fe}^{3+}$  and  $\text{Cl}^-$ ) and pH on the structure of akaganeite. In this work, we investigate the hypothesis that structural changes in the akaganeite precursor phase are manifested in the final morphology of the hematite crystals. By elucidating the chemical and physical effects of the crystallization microenvironment, we are able to understand how an inorganic hydrogel affects the crystallization and hierarchical structure of hematite.

### **5.3 Results**

The motivation for this work was derived from the observation that solution-based crystallization of hematite yielded the well-known mosaic pseudo-cubes of hematite, while hydrogel-based crystallizations yielded quasi-spheres, with hierarchically-structured architectures that are modulated by incorporated silicon across multiple length scales.<sup>1</sup> While the anisotropic nature of the quasi-spheres was correlated to the incorporation of silicon, the radial internal structure composed of stacked, spherulitic planes displaying six-fold symmetric regions was not completely explained by the chemical role of silicon in the growth environment, or by simply the high growth rate tied to the  $[\text{FeCl}_3]$  concentration.

#### **5.3.1 Overgrowth on hydrogel-grown hematite quasi-spheres**

Our previous work has revealed the internal structure of the hydrogel-grown hematite quasi-spheres to be composed of spherulitic regions with 6-fold symmetry.<sup>1</sup> For the purposes of this current report, we conducted over-growth experiments on quasi-spheres to provide a complimentary visualization of the underlying structure, which this current report seeks to explain. SEM imaging (Figure 5.1a) reveals an overgrowth of layers of rod-like crystals that extend from the quasi-spherical core with 6-fold symmetry (Figure 5.1b). HR-TEM imaging of the overgrown rods under bright field (Figure 5.1c) confirmed that they grow perpendicular to  $[001]$ , within the a-b plane. Overall, the habit of the overgrown hematite is consistent with internal structure characterizations of the hydrogel-grown quasi-

spheres which identified spherulitic planes that are stacked along the shortest diameter of the quasi-sphere, leading to a net orientation of [001] at the whole particle level.

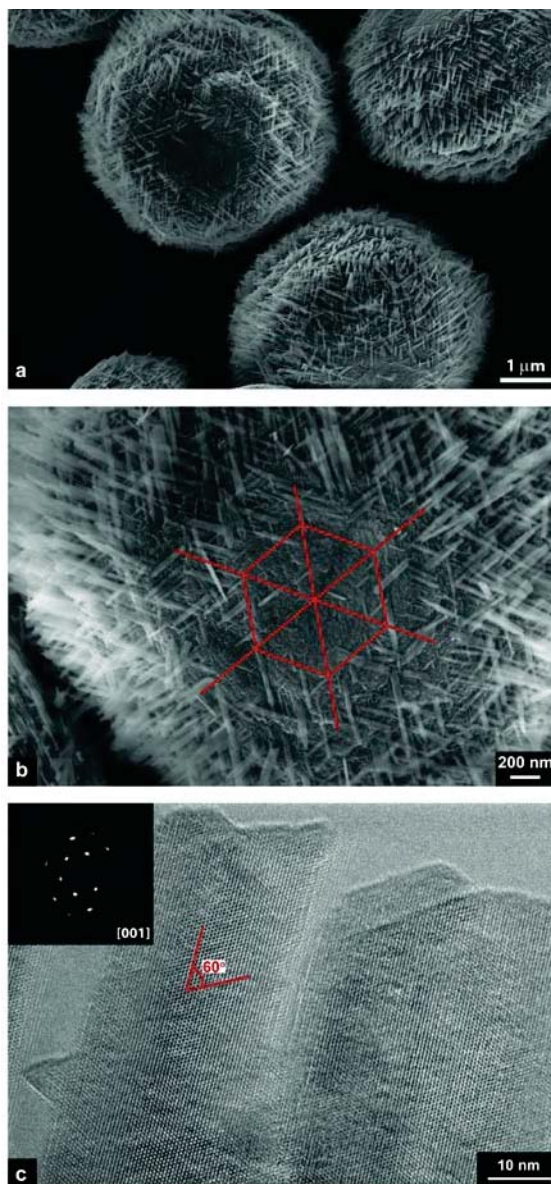


Figure 5.1 Overgrowth of hematite on 0.90 M hydrogel-grown hematite quasi-spheres. (a) SEM showing the layers of high aspect ratio domains contained within the hydrogel-grown quasi-spheres. (b) Higher magnification of a crystal similar to those shown in (a), highlighting (in red) the 6-fold symmetry of the overgrown, rod-like domains. (c) High-resolution-TEM and SAED (inset) showing the preferential growth direction of the overgrowth crystallites to be perpendicular to [001], along [110]. The 60° hematite lattice angle is highlighted in red.

### 5.3.2 Effect of Silica Hydrogel and [FeCl<sub>3</sub>] on Hematite Morphology

Being that the diversity of hematite morphologies<sup>8,10</sup> served as a starting point for this work (Table 5.1), the effect of [FeCl<sub>3</sub>] on the morphology of hematite crystals was first probed under both solution and hydrogel-based conditions. All conditions lead exclusively to the hematite phase after a 4 wk hydrothermal treatment, with exception of the 0.018 M hydrogel conditions, which yielded discrete bands of akaganeite and hematite within the hydrogel (Figure 5.2aFigure 5.3). All hematite crystals grown from solution-based conditions (Figure 5.4d-f) formed as crystals with relatively isometric structures; progressing from nanoscale, single crystal spheres at the lowest concentration to microscale, mosaic pseudo-cubes<sup>9</sup> at the highest concentration. Notably the ‘pseudocubic’ crystals of hematite formed in solution exhibit rounding at their corners that increases with iron reagent concentration.

Table 5.1 Series of iron (III) chloride concentrations used in this work and their related hematite morphologies.

[FeCl <sub>3</sub> ] (mol/L)	[HCl] (mol/L)	Notes on Hematite Morphology		References
		Solution Growth	Hydrogel Growth	
0.018	0.001	Nanoscale spheres	Nanoscale discs	Matijevic 1978 Bailey 1992
0.180	0, 0.004, <sup>a</sup> 0.017, 0.067	Pseudo-cubes	Microscale discs	n/a  Matijevic 1979 Bailey 1992
0.900	0.020	Rounded pseudo-cubes	Quasi-spheres	DeBlanco 1986 Asenath-Smith 2014 Asenath-Smith 2015

<sup>a</sup>The acid concentration used in hematite solution-based crystallization (Figure 5.1e).

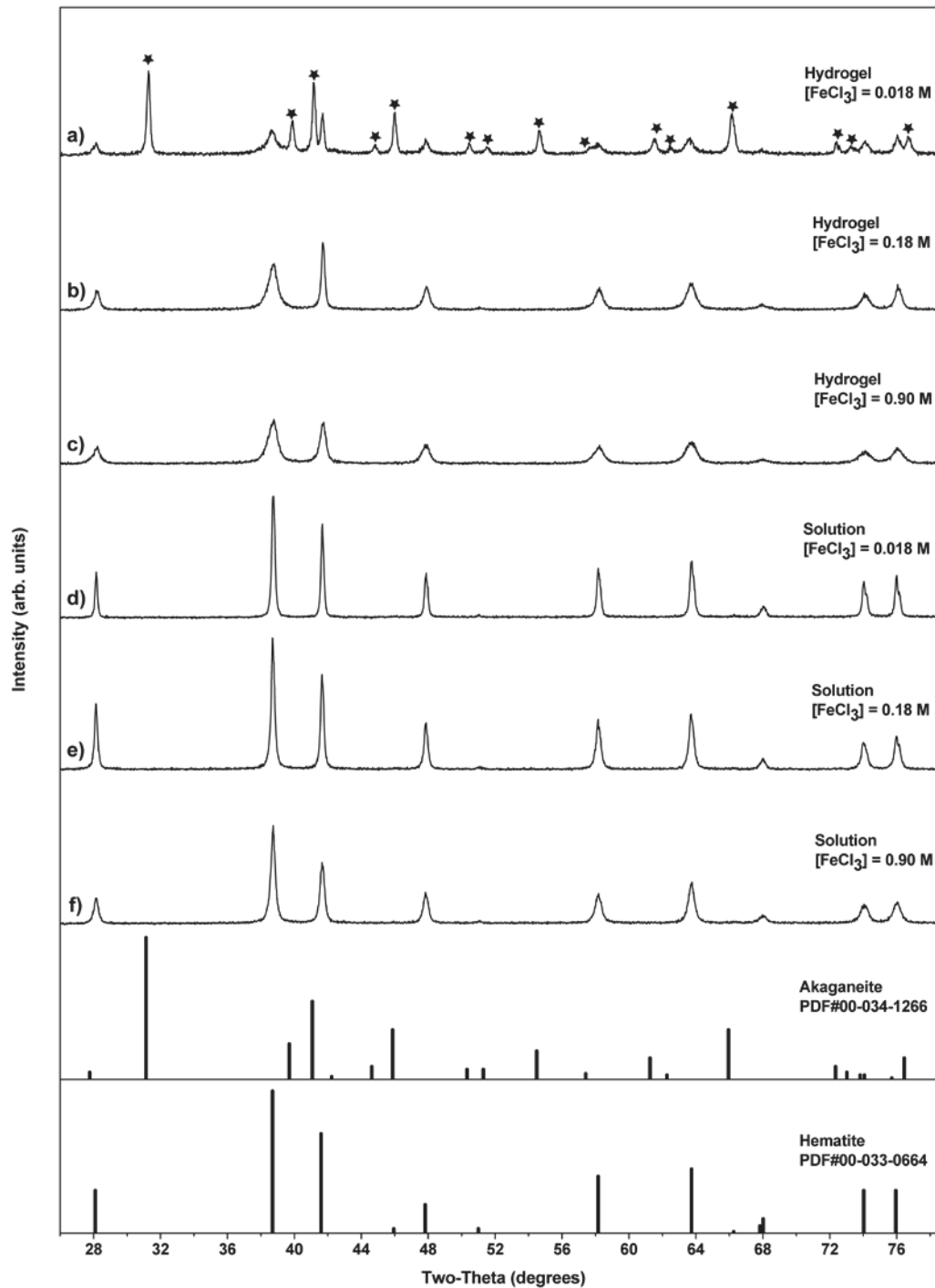


Figure 5.2 Phase analysis by pXRD of all 4 week crystallizations, showing the complete formation of the hematite phase in all cases except hydrogel-based crystallizations with  $[\text{FeCl}_3] = 0.018 \text{ M}$  (a), wherein the peaks corresponding to the akaganeite phase are labeled with a star. pXRD pattern acquired using  $\text{CoK}\alpha$  radiation.

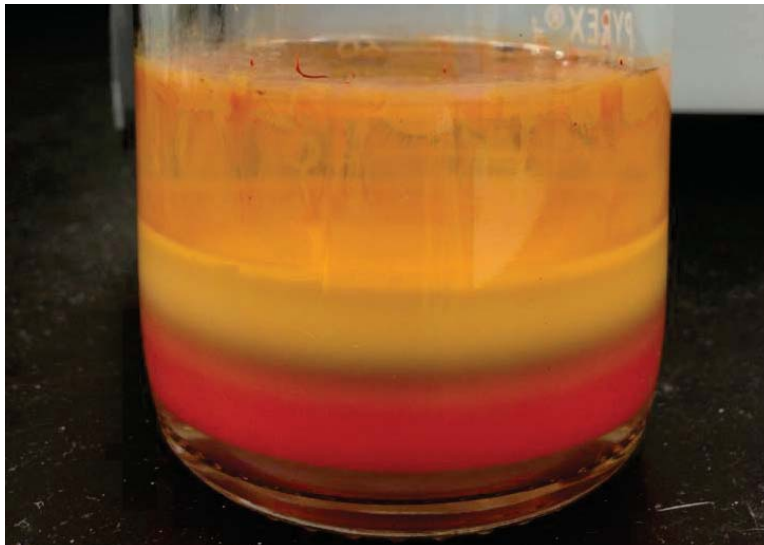


Figure 5.3 Post-crystallization (4 wk) of sphere-forming solution protocol ( $[\text{FeCl}_3]=0.018 \text{ M}$ ) mapped into the silica hydrogel showing that it did not completely transform to hematite. Yellow band is akaganeite and red band is hematite.

Looking at the hematite products formed in the silica hydrogel (Figure 5.4a-c), anisotropic structures are present in all cases; nanoscale discs are formed at the lowest concentration and gradually expand to quasi-spherical forms with two parallel flat faces at the highest concentration. All hydrogel-grown hematite crystals are observed to have the hematite crystallographic  $c$ -axis positioned collinear to the shortest diameter (TEM and corresponding SAED pattern inset), consistent with previously reported characterization of the quasi-spheres.<sup>1</sup> Under both crystallization conditions, the increased  $[\text{FeCl}_3]$  appears to be associated with increased crystal sizes. That the hydrogel-grown hematite crystals all have the  $c$ -axis positioned normal to their shortest direction is notable and consistent with the association between incorporated silicon atoms suppressing growth along  $[001]$ .<sup>1</sup>

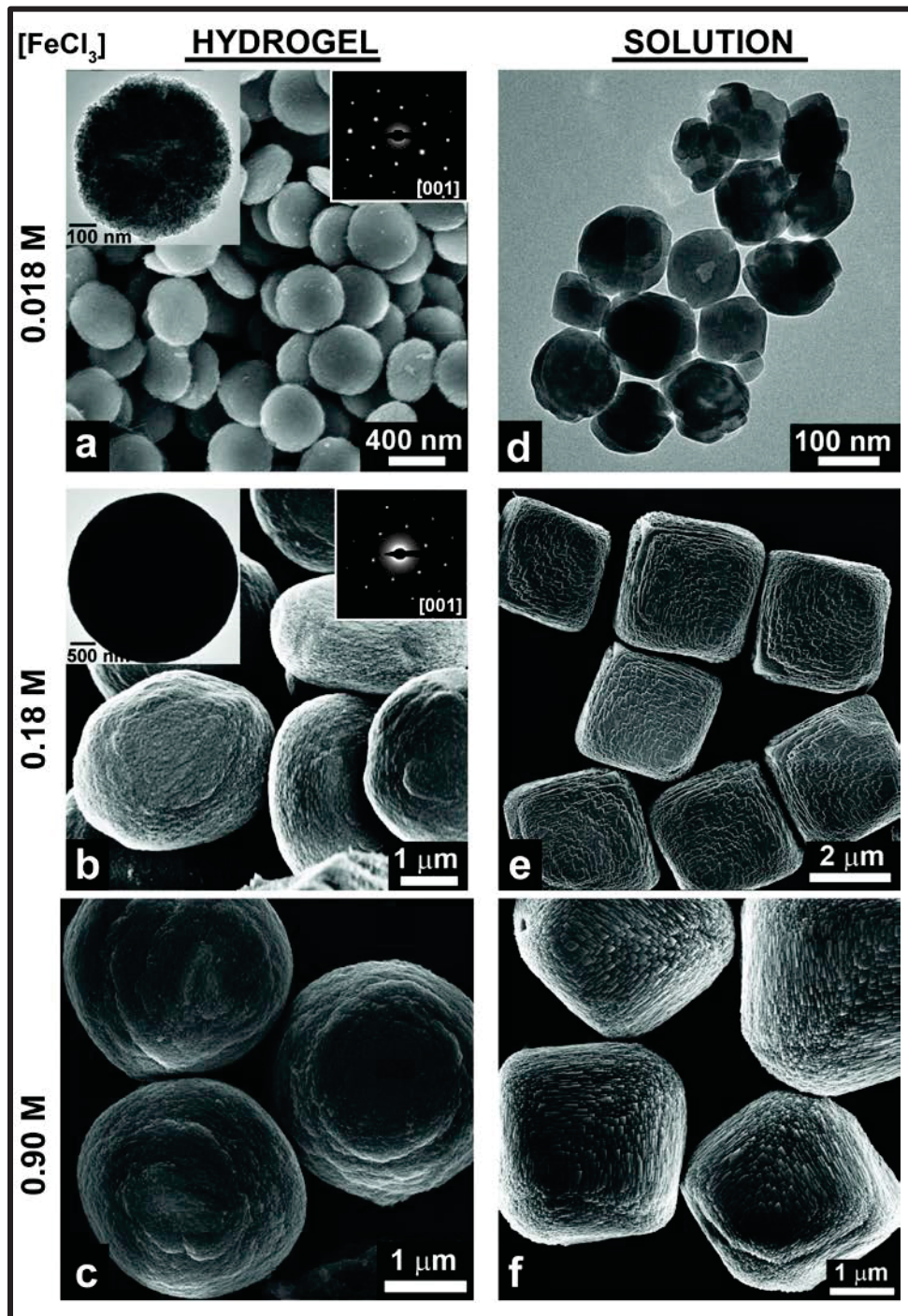
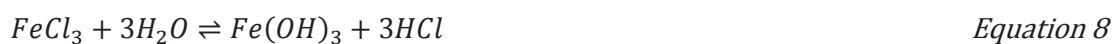


Figure 5.4 Hematite crystals grown within silica hydrogels (a-c) and from aqueous solutions (d-f) over a range of iron (III) chloride hexahydrate concentrations (0.018 – 0.90 M, see also Table 1). TEM and corresponding SAED pattern, inset in (a) and (b), show the hematite crystallographic c-axis perpendicular to the plane of the hydrogel-grown discs.

### 36.1.1 Aqueous Equilibria of Metal Salts

With the knowledge that the hematite pseudo-cubes show a morphological relationship to the akaganeite assemblages that template their growth,<sup>8</sup> we designed this investigation around the akaganeite phase. Important to the crystallization of inorganic compounds from aqueous media is the solution equilibria of the metal salts themselves. The following equilibrium clearly illustrates the interdependences of iron and chloride concentrations with pH in iron chloride solutions ( $\text{FeCl}_3 + 3\text{H}_2\text{O} \rightleftharpoons \text{Fe}(\text{OH})_3 + 3\text{HCl}$  Equation 8).



This equilibrium, wherein the iron complex has been simplified to the hydroxide phase for clarity, complicates the study of the effect of each variable, in isolation, on the crystallization of akaganeite and ultimately hematite. The highly acidic nature of these solutions ( $[\text{FeCl}_3] = 0.18 \text{ M}$ ,  $\text{pH} = 1.5$ ) further challenges the measurement of pH, and the reproducible adjustment of pH in the crystallization solutions. To quantifiably study the effect of pH on the solution crystallization of akaganeite, we varied the molarity of  $[\text{HCl}]$  in a set of akaganeite crystallizations with fixed iron concentration (0.18 M) (samples SA-A – SA-D). To separate the effect of pH from  $[\text{Cl}^-]$ , we substituted NaCl for the HCl (sample SS-A). With these experiments (Table 5.2), we aimed to elucidate which experimental variables were responsible for the change in size and aspect ratio and which factors determined twinning and branching of the akaganeite crystals.

### 36.1.2 Effect of Silica Hydrogel and $[\text{FeCl}_3]$ on Akaganeite morphology

With an overview of the hematite morphological landscape of our chosen concentration range, we turn to examine the morphology of the akaganeite crystals that precede the hematite crystallization. Growth of akaganeite within silica hydrogels was accomplished by hydrothermal treatment for 24 h. All conditions yielded only the akaganeite phase (Figure 5.5). Growth of akaganeite from solution was

achieved with 2 h of hydrothermal treatment to solutions with the same  $[\text{FeCl}_3]$  and  $[\text{HCl}]$  as listed in Table 5.1. All conditions yielded only the akaganeite phase (Figure 5.6).

Table 5.2 Experimental conditions and statistics on akaganeite ( $\beta\text{-FeOOH}$ ) crystals reported in this work.

Sample Name	Figure	$[\text{FeCl}_3]$ (mol/L)	$[\text{H}^+]$ (mol/L)	$[\text{Cl}^-]^a$ (mol/L)	Length <sup>b</sup> ( $\mu\text{m}$ )	Width <sup>b</sup> (nm)	Aspect ratio <sup>c</sup>	# arms <sup>d</sup>
HC-A	3a	0.018	n/a	0.55	$0.349 \pm 0.080$	$75 \pm 15$	4.5	n/a
HC-B	3b	0.18	n/a	1.04	$0.415 \pm 0.107$	$50 \pm 17$	8.4	n/a
HC-C	3c	0.90	n/a	3.20	$2.64 \pm 0.65$	$191 \pm 53$	13.8	n/a
SC-A	3d	0.018	0.001	0.06	$0.214 \pm 0.039$	$55 \pm 18$	3.9	n/a
SC-B	3e	0.18	0.004	0.54	$1.11 \pm 0.24$	$154 \pm 37$	7.2	n/a
SC-C	3f	0.90	0.020	2.72	$3.72 \pm 0.71$	$279 \pm 50$	13.3	n/a
SA-A	4a	0.18	0	0.540	$1.17 \pm 0.15$	$230 \pm 30$	5.2	3.3
SA-B	4b	0.18	0.004	0.544	$1.11 \pm 0.24$	$154 \pm 37$	7.2	3.9
SA-C	4c	0.18	0.017	0.560	$0.557 \pm 0.124$	$98 \pm 26$	5.7	5.5
SA-D	4d	0.18	0.067	0.610	$2.20 \pm 0.270$	$230 \pm 50$	9.7	7.4
SS-A	6a,b	0.18	0	0.610	$1.43 \pm 0.21$	$240 \pm 40$	6.0	3.7

<sup>a</sup>The listed  $[\text{Cl}^-]$  is a sum of chlorine ions supplied by the iron (III) chloride reagent and the hydrochloric acid (added to solution or contained within the hydrogel, as applicable).

<sup>b</sup>At least 50 measurements were used in the average and standard deviation of crystal length and width.

<sup>c</sup>Aspect ratio was found by dividing the averaged length by width for each sample.

<sup>d</sup>The #arms is an average of at least 30 twinned and/or branched crystals.

Both the solution and hydrogel-grown akaganeite crystals were seen to increase in aspect ratio with increasing  $[\text{FeCl}_3]$  (Table 5.2 and Figure 5.7), from 3.9 & 4.5 to 13.3 & 13.8, respectively. At the highest concentration, the ends of the solution-grown rods appear to split, forming sheaves, characteristic of growth at high driving force (related to concentration of iron reagent).<sup>25</sup> In the solution-grown crystals, the occurrence of twinned forms showed an inverse dependence on iron reagent concentration. While all solution-grown akaganeite crystals existed as discrete rods, or crystallographically-twinned structures, the

hydrogel conditions facilitated the occurrence of highly-branched forms, composed of aggregates of rods, which extend from a central point (Figure 5.7a-c).

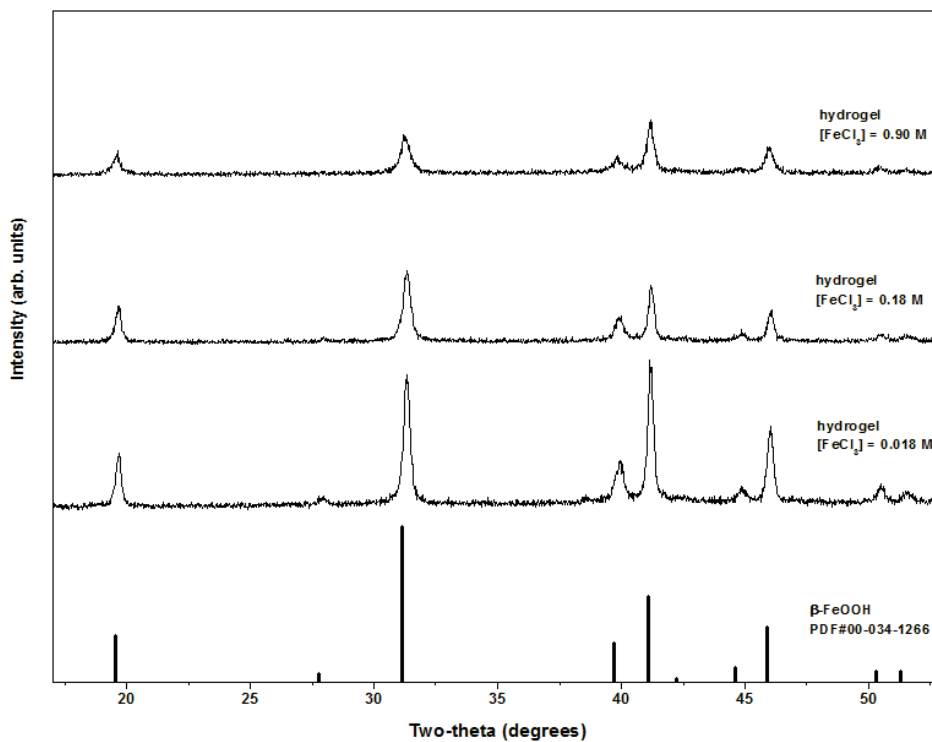


Figure 5.5 Phase analysis by pXRD of the hydrogel-based akaganeite crystallizations conducted for 24 h at 100 °C showing the complete formation of akaganeite for all iron (III) chloride concentrations. pXRD pattern acquired using  $\text{CoK}\alpha$  radiation.

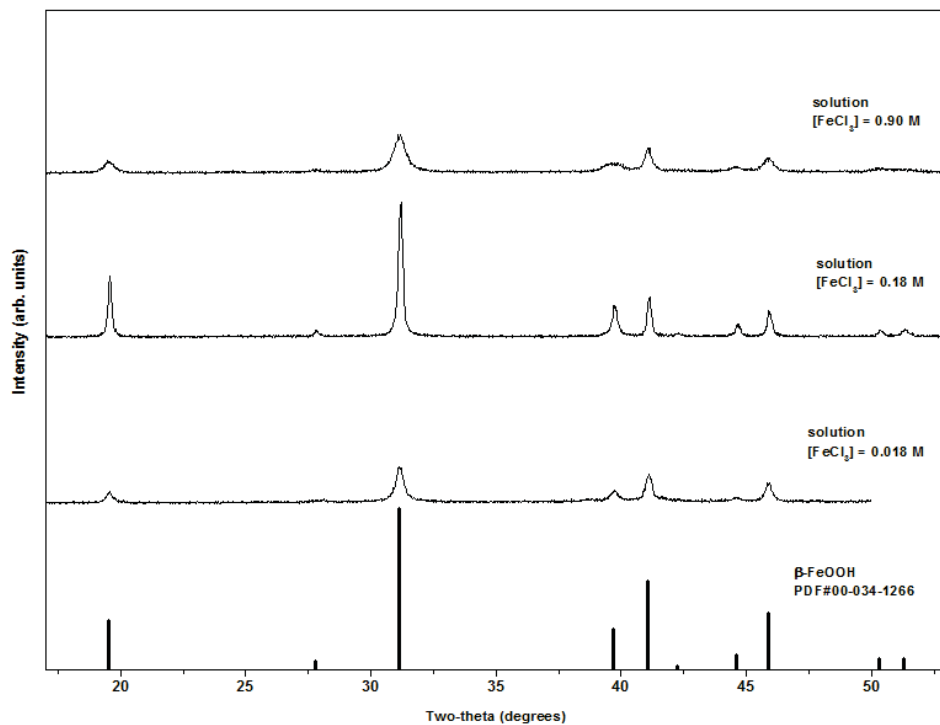


Figure 5.6 Phase analysis by pXRD of the solution-based akaganeite crystallizations conducted for 2 h at 100 °C showing the complete formation of akaganeite for all iron (III) chloride concentrations. pXRD pattern acquired using CoK $\alpha$  radiation.

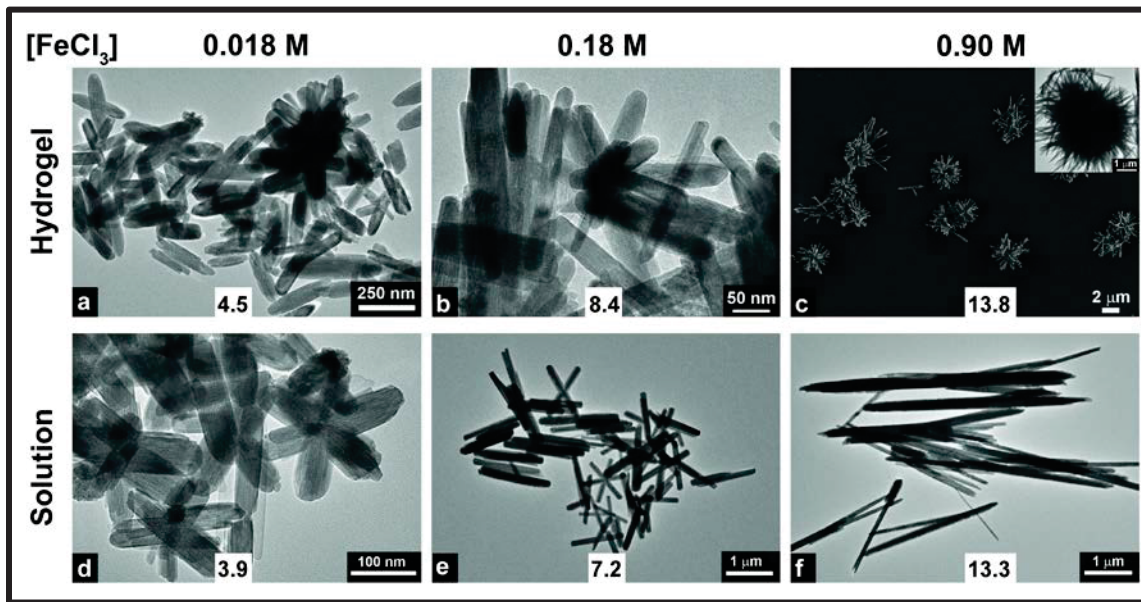


Figure 5.7 A series of akaganeite ( $\beta$ -FeOOH) crystallizations conducted with variable iron chloride concentrations (concentration labeled at top). (a) – (c) Crystallization conducted within silica hydrogel (samples HC-A, HC-B, HC-C respectively) and (d) – (f) from aqueous solution (samples SC-A, SC-B, SC-C, respectively). Aspect ratio of the crystals is inset in each panel. Additional data compiled in Table 2. Crystallographic features tracked in this study included twinning (seen as ‘x’ shaped crystals, representative form seen in upper left corner of panel a), branching (highly-branched assemblies of rods, as in panel c).

#### 151.1.1 Effect of [HCl] on Akaganeite Crystallization from Solution

The morphological results of akaganeite crystallizations, performed under both solution and hydrogel conditions, indicate that the aspect ratio of the rods are directly linked to  $[\text{FeCl}_3]$ . An important consideration is that pH and  $[\text{Cl}^-]$  are both coupled to  $[\text{FeCl}_3]$  ( $\text{FeCl}_3 + 3\text{H}_2\text{O} \rightleftharpoons \text{Fe}(\text{OH})_3 + 3\text{HCl}$

Equation 8) and known to affect the stability of iron (oxy-, hydr-)oxide phases.<sup>12,13,15</sup> In order to isolate the effect of pH, the 0.18 M  $\text{FeCl}_3$  composition was chosen for further solution-based studies with  $[\text{HCl}]$  that varied from 0 M to 0.067 M (samples SA-A – SA-D, Table 5.2).

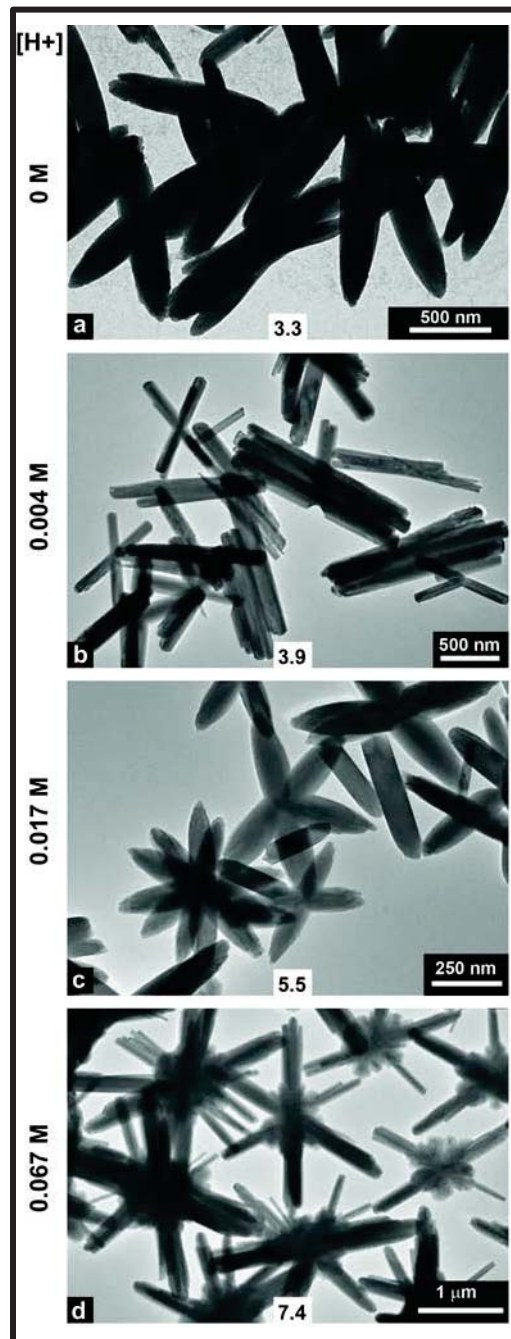


Figure 5.8 A series of akaganeite ( $\beta$ -FeOOH) crystallizations performed in solution at a fixed  $[\text{FeCl}_3]=0.18 \text{ M}$ , with variable acid (HCl) concentrations (0 – 0.067, shown on left; samples SA-A, SA-B, SA-C, SA-D, respectively), illustrating the effect of pH on the crystal morphology and twinning and branching (mean # arms inset in each panel). Crystallographic twinning is seen as the ‘x’ shaped crystals, clearly seen in panel b. In this report we define branching as assemblies of rods, which extend from a common point, and is seen in the crystals shown in panel d.

The morphologies of the akaganeite crystals formed from solution with variable [HCl] (Figure 5.8) show multiple dependences on [HCl]. First, the overall length of the rods is approximately doubled (from  $1.17 \pm 0.17 \mu\text{m}$  to  $2.20 \pm 0.27 \mu\text{m}$ ) as [HCl] increases from 0 – 0.067 M. Secondly, the emergence of branched forms changes drastically with increasing [HCl]. In the absence of additional acid, the akaganeite crystals exhibit the characteristic 4 arm twinned ‘x’ with low frequency (sample SA-A). As [HCl] is increased to 0.017 M (sample SA-C), the occurrence of twinned forms increases, as does the number of arms found on these twins (mean=5.5). In the highest acid condition (sample SA-D), almost all crystals exhibit planar (**Error! Reference source not found.**), branched forms with 6-fold symmetry (Figure 5.8d) and a mean #arms=7.4. Remarkably, these branched forms appear to be bound at their center by a crystalline product with a very different morphology. Phase analysis by pXRD on the products from this series (Figure 5.10) indicate the phase pure formation of akaganeite in all samples except SA-D where goethite was detected. Analysis by electron diffraction confirmed that the goethite phase composes the crystalline product that is located at the center of the highly branched forms, and is characteristically twinned across (210) planes (Figure 5.11).<sup>26</sup> The existence of goethite in the highest acid and lowest pH conditions is unexpected given its known stability at high pH.<sup>13</sup> Interestingly, 4 week crystallization of sample SA-D, yields crystals that are dominantly six-fold planar forms of goethite, with hematite pseudocubes in minority (Figure 5.12Figure 5.13).

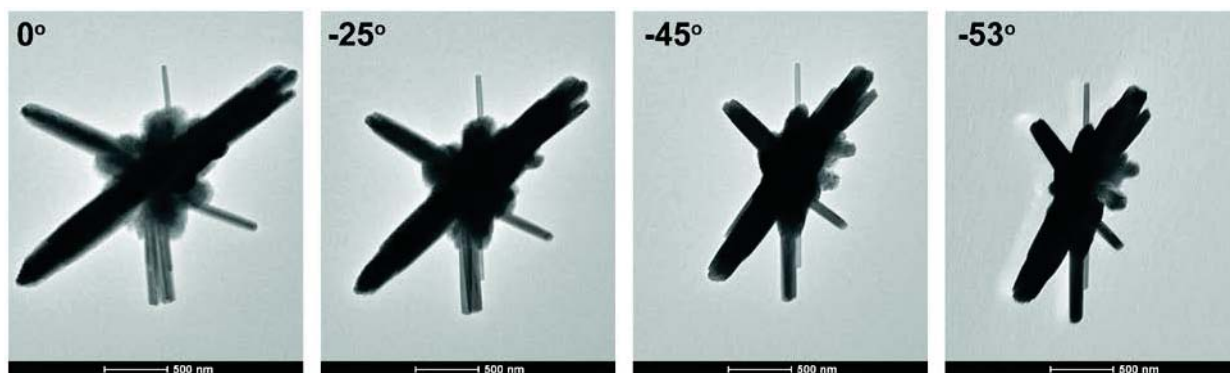


Figure 5.9 TEM tilt series confirming the planarity of sample SA-D after 4 h crystallization at 100 °C.

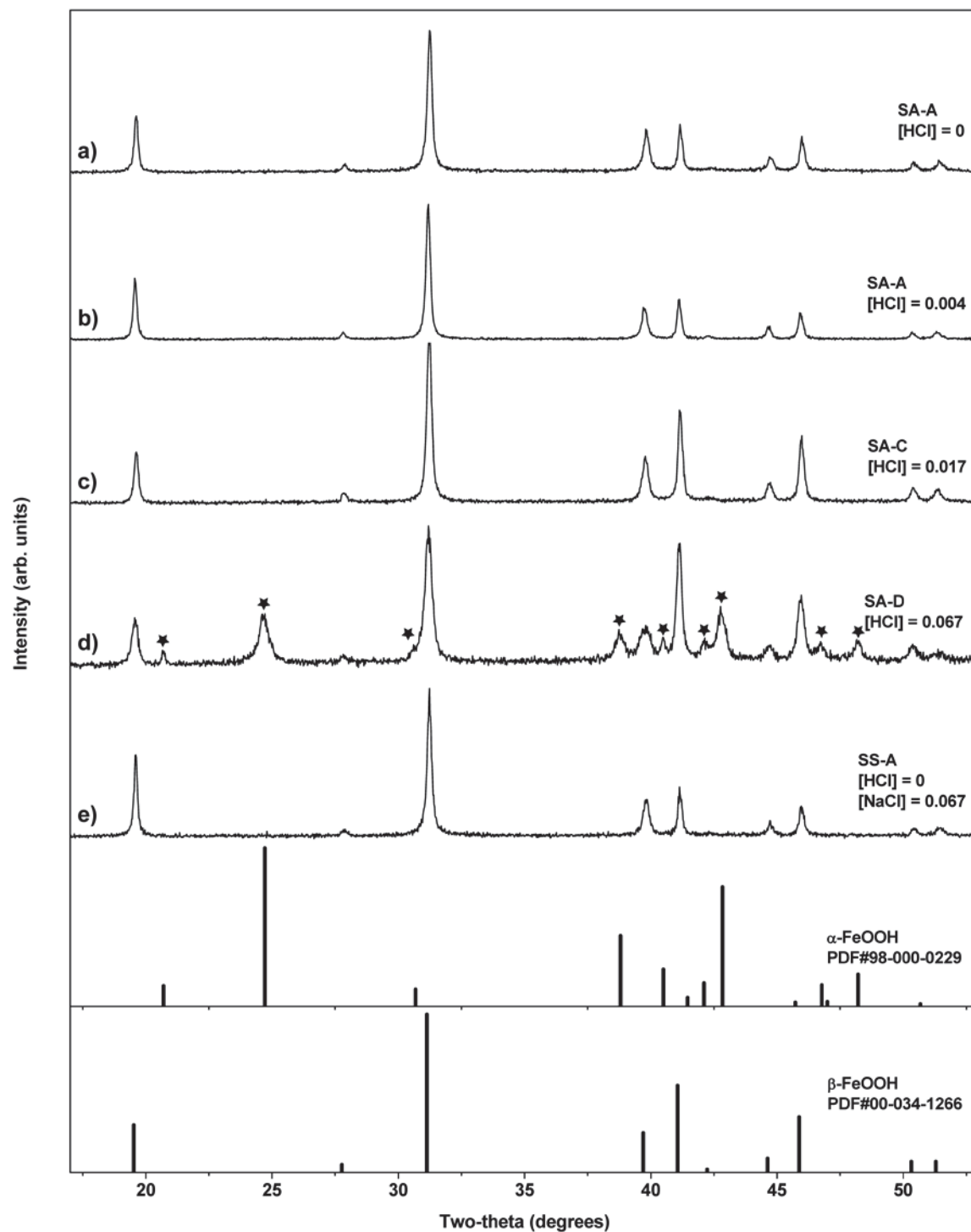


Figure 5.10 Phase analysis by pXRD on the iron oxyhydroxide crystals grown from solution with variable acid (a) – (e). Images are shown in Figure 5.8a-d & Figure 5.14a,b. The PDF reference patterns for the two polymorphs are shown in the lower panels. The peaks corresponding to goethite polymorph are labeled with a star. pXRD patterns acquired using  $\text{CoK}\alpha$  radiation.

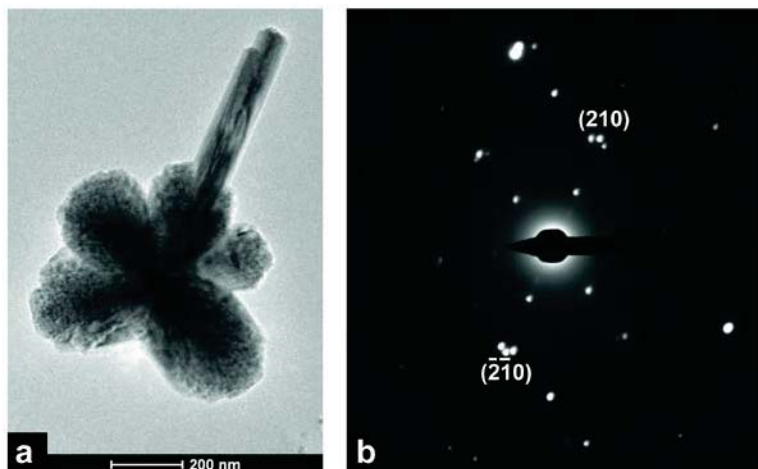


Figure 5.11 Analysis by selected-area electron diffraction of sample SA-D, after 4 h crystallization, demonstrating that the goethite phase is predominantly located at the core of the highly-branched forms, and twinned across (210) planes. The selected area aperture was positioned to include the entire crystal in panel (a).

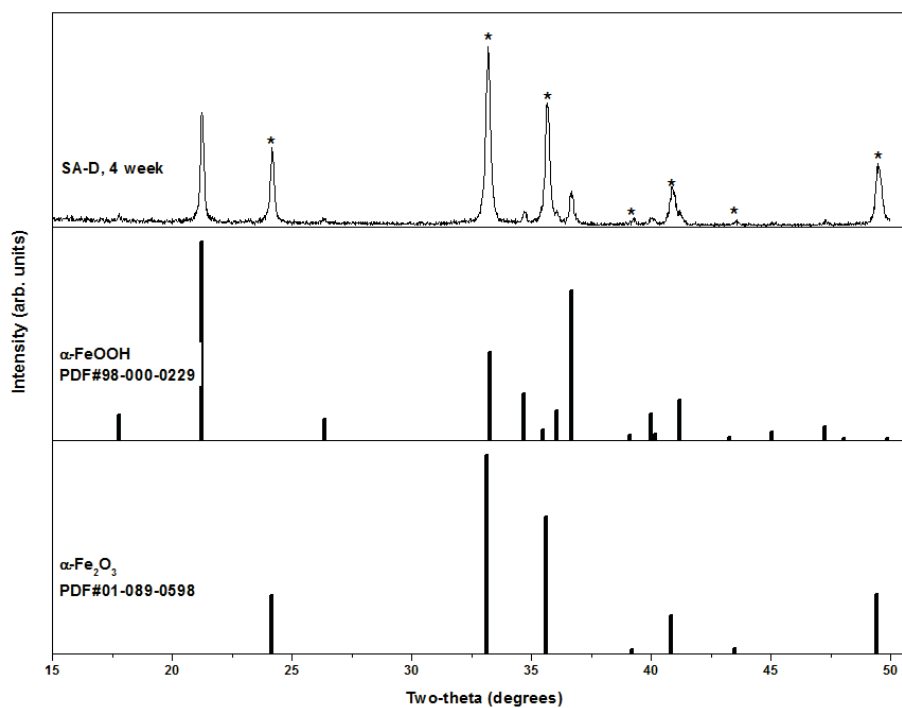


Figure 5.12 Phase analysis by pXRD of a 4 week solution-based crystallization of sample SA-D ( $[\text{FeCl}_3]=0.18 \text{ M}$ ,  $[\text{HCl}]=0.067 \text{ M}$ ), confirming that the sample contains a mixture of goethite ( $\alpha\text{-FeOOH}$ )

and hematite ( $\alpha\text{-Fe}_2\text{O}_3$ ). Hematite peaks are denoted by a star, all other peaks index to goethite. pXRD pattern acquired using  $\text{CuK}\alpha$  radiation.

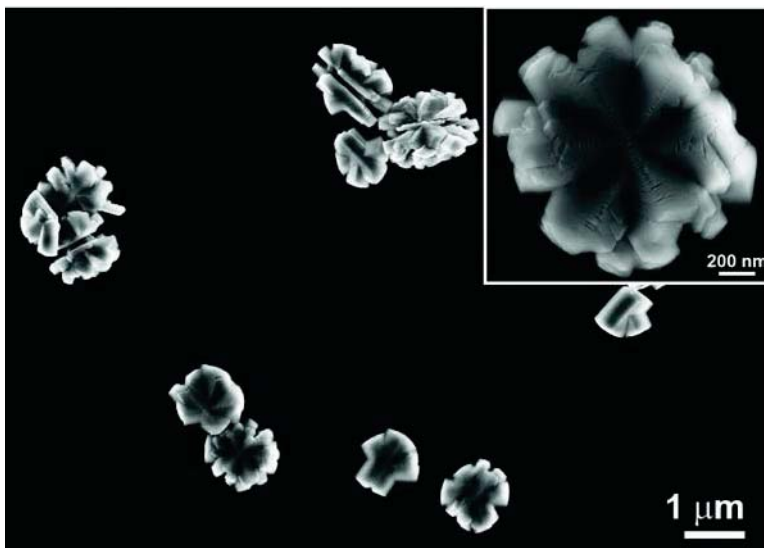


Figure 5.13 SEM images of the goethite products formed from 4 week crystallization of sample SA-D.

#### 151.1.2 Distinguishing the Effect of $[\text{Cl}^-]$ from $[\text{H}^+]$ on Akaganeite Crystallization from Solution

By probing the effect of pH on the crystallization of akaganeite by varying  $[\text{HCl}]$ , the concentration of chloride ions was also changing. Given the known association of akaganeite with low pH and high  $[\text{Cl}^-]$ , we sought to isolate these two effects with the goal of understanding which variable, pH or  $[\text{Cl}^-]$ , was responsible for the highly-branched forms and the presence of goethite in sample SA-D (Figure 5.8d). By replacing the appropriate  $[\text{HCl}]$  with  $\text{NaCl}$  (0.067 M in this case), we designed an experiment where the  $[\text{Cl}^-]$  remained fixed at 0.610 M (Figure 5.8d and Table 5.2), but the  $[\text{H}^+]$  was 0 (sample SS-A, Table 2). With this approach, we were able to investigate the effect of pH (and  $[\text{Cl}^-]$ ) on the phase and morphology of akaganeite

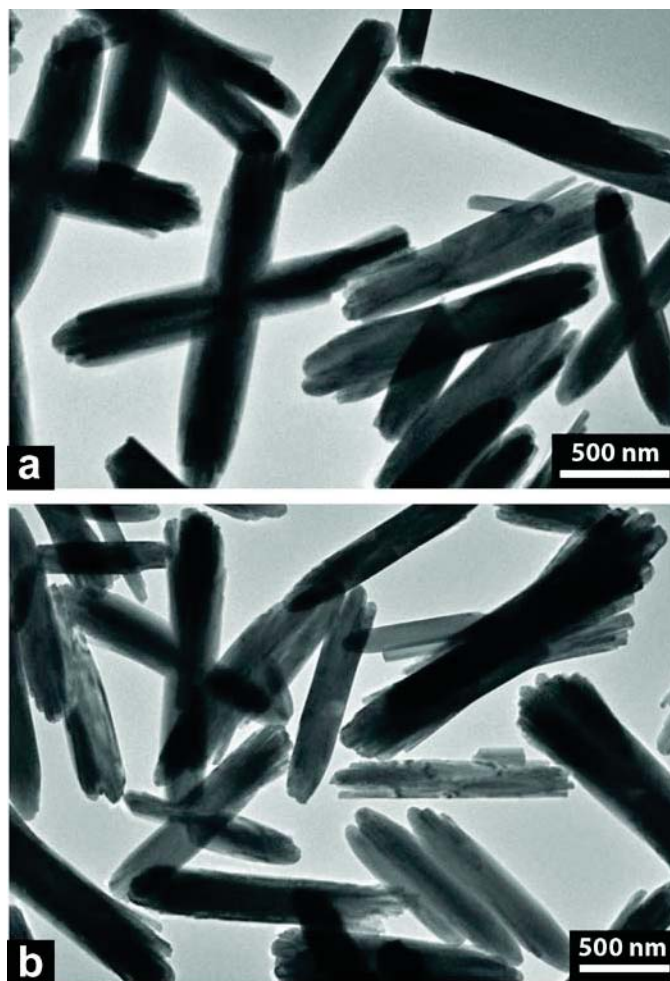


Figure 5.14 (a) and (b) TEM micrographs of akaganeite crystals (sample SS-A) grown from solution with  $[\text{FeCl}_3] = 0.18 \text{ M}$  and  $[\text{Cl}^-] = 0.610 \text{ M}$ . These conditions are identical to that shown in Figure 4d, however, in this experiment the chloride concentration was achieved by addition of  $0.067 \text{ M}$  NaCl. The mean aspect ratio is 6.0 and the mean # arms are 3.7. Other data are reported in Table 2. Panel (b) is included to illustrate the presence of crystal splitting (sheaves) at the ends of the akaganeite rods (as seen at the ends of the crystals at upper right corner of panel b).

From purely a morphological standpoint, the single spindle and twinned akaganeite crystals grown with  $[\text{Cl}^-] = 0.610$  and  $[\text{H}^+] = 0$  (Figure 5.14) come in stark contrast to the highly-branched forms that resulted from solutions with  $[\text{Cl}^-] = 0.610$  and  $[\text{H}^+] = 0.067$  (sample SA-D, Figure 5.8d). Phase analysis by pXRD indicates that the former conditions produce pure phase akaganeite (Figure 5.10e), while the latter

was found to contain goethite ( $\alpha$ -FeOOH) as reported above (Figure 5.10d). Largely, the akaganeite morphologies precipitated from solutions with  $[H^+]=0$  are visually similar, regardless of the  $[Cl^-]$  (samples SA-A, SS-A, Figures 5.8 & 5.14). Statistical analysis of the lengths and widths of these crystals formed under the highest pH conditions (no additional acid) have the lowest aspect ratio (5.2, 6.0) and number of arms (mean=3.3 & 3.7) on their twinned forms. These results implicate  $[H^+]$ , and not  $[Cl^-]$ , as the variable that drives the formation of the highly-branched structures and the emergence of goethite in sample SA-D.

### 151.1.3 Physical role of hydrogel

The results presented on the role of  $[FeCl_3]$ ,  $[H^+]$ , and  $[Cl^-]$  on akaganeite crystallization all probe the chemical effects of the crystallization microenvironment. As a growth matrix, the silica hydrogel plays an additional physical role in the crystallization microenvironment that is related to the confined nature of its porous cellular network. In order to gain some insight about the physical interaction between the akaganeite crystals and the silica hydrogel, we sought to image the crystals and the hydrogel network before extraction of the crystals. The akaganeite crystals were imaged within the hydrogel network by freeze-drying thin sections of hydrogel specimens after 24 h crystallization. We find numerous occurrences of the aggregates of radially-assembled akaganeite rods embedded within the silica hydrogel walls (Figure 5.15), consistent with the silica hydrogel as a heterogeneous nucleation substrate, and a support which prevents sedimentation during the crystallization of akaganeite (and subsequently hematite).

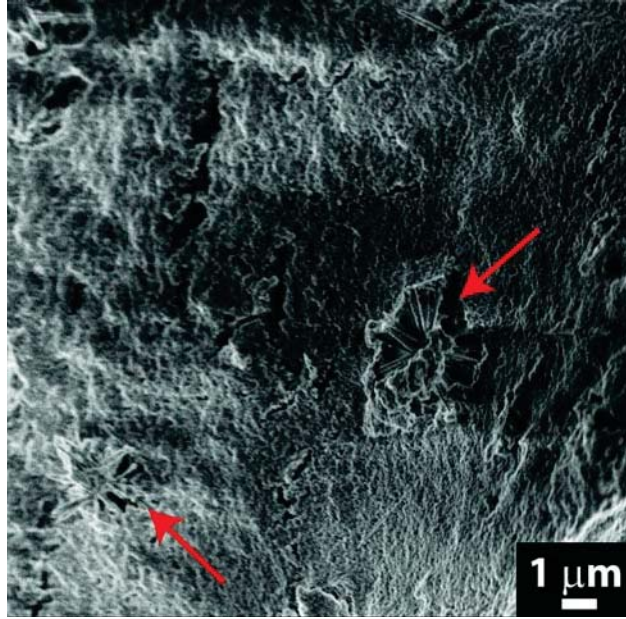


Figure 5.15 An SEM micrograph of freeze-dried silica hydrogel after 24 h crystallization (with  $[\text{FeCl}_3] = 0.90$ ), showing the highly-branched assemblies of akaganeite rods (highlighted with arrows) embedded within the cellular walls of the hydrogel network.

## 151.2 Discussion

### 151.2.1 Hematite Morphology

The morphology of hematite crystals produced from the range of iron chloride concentrations in aqueous solutions as compared to silica hydrogels show different trends: the solution-grown hematite crystals maintain isometric shapes over this concentration range (Figure 5.4d-f), while the hydrogel-grown hematite crystals remain anisotropic (Figure 5.4a-c). Qualitatively, the hydrogel-grown hematite crystals could even be said to decrease in anisotropy with increasing  $[\text{FeCl}_3]$  –the very thin discs expand out to thicker discs and finally quasi-spherical forms with six-fold symmetric internal structure (Figure 5.1). Interestingly, the hydrogel-grown hematite crystals exhibit an inverse relationship to the anisotropy in the habit of the initial akaganeite phase (Table 5.1). This inconsistency between the anisotropy of the hematite and akaganeite crystals implies that the actual growth mechanism of hematite also varies with  $[\text{FeCl}_3]$ . This suggestion is consistent with the work of Bailey et al., who observed a complete

dissolution-reprecipitation in the akaganeite-hematite pathway at low  $[\text{FeCl}_3]$  concentration, while akaganeite assemblies were found to template hematite nucleation and growth at higher concentration.<sup>8</sup>

### 151.2.2 Size and Aspect Ratio of Akaganeite Crystals

In both the solution and hydrogel akaganeite series, the crystals increased in size and aspect ratio with increasing  $[\text{FeCl}_3]$  (Figure 5.6), similar to the findings of Yue et al.<sup>23</sup> With the interdependences of  $[\text{Cl}^-]$ ,  $[\text{Fe}^{3+}]$ , and  $[\text{H}^+]$  all tied to  $[\text{FeCl}_3]$ , as discussed above, it is necessary to distinguish which variable is actually responsible for modulating size and aspect ratio of the akaganeite crystals. Further examination of the results shows that the size of the akaganeite crystals is dependent on  $[\text{Fe}^{3+}]$ , while the aspect ratio of these crystals specifically shows a dependence on  $[\text{H}^+]$ . The dependence on size is seen in the concentration series (Figure 5.6), and confirmed by experiments conducted at equal  $[\text{FeCl}_3]$  and  $[\text{H}^+]$  with different  $[\text{Cl}^-]$  (samples SA-A, SS-A, Figure 5.8a & Figure 5.14, respectively). That the size of the crystals remains relatively constant at  $\sim 1.2$   $\mu\text{m}$  length and  $\sim 230$  nm width (Table 5.2) indicates that it is truly the  $[\text{Fe}^{3+}]$  that dictates the size. The dependence of the aspect ratio on  $[\text{H}^+]$  is demonstrated by making two comparisons within our results. First, the aspect ratio of the akaganeite crystals is seen to decrease along the  $[\text{FeCl}_3] = 0.18$  series from 0.067 to 0 M HCl (Figure 5.8 & Table 5.2). Secondly, the aspect ratio decreases as  $[\text{H}^+]$  decreases with fixed  $[\text{Cl}^-]$  and  $[\text{FeCl}_3]$  (samples SA-A, SS-A, Figure 5.8d & Figure 5.14). These findings implicate pH as the main determining factor of aspect ratio: higher pH, as achieved by low  $[\text{FeCl}_3]$  and/or low  $[\text{H}^+]$  favors a low aspect ratio in the akaganeite crystal shape. These findings are consistent with previous reports that assigned low  $[\text{FeCl}_3]$  with low aspect ratio,<sup>8,10</sup> because these solutions have the highest pH ( $\text{FeCl}_3 + 3\text{H}_2\text{O} \rightleftharpoons \text{Fe}(\text{OH})_3 + 3\text{HCl}$  Equation 8).

### 151.2.3 Crystallographic Twinning, Branching and Splitting of Akaganeite Crystals

Crystallographic twinning of akaganeite crystals is seen as the 4- and 6-pointed stars resulting from the (332) twin system (Figure 5.6e), with an angle of  $62^\circ$ . In addition to crystallographic twinning, the akaganeite crystals formed in this work show branching and splitting. We define branching as the

assemblies of rods which extend from a common point (Figure 5.6c). In the term ‘splitting’ we refer to the splintering of the ends of individual rods (Figure 5.6Figure 5.14b), which may occur on rods that are isolated, crystallographically-twinned, or in larger branched assemblies. While crystallographically-twinned forms were found in solution-based crystallization of akaganeite, with increased occurrence at low  $[\text{FeCl}_3]$  (Figure 5.6d-f), akaganeite crystals formed in the silica hydrogel exhibited branched assemblies over the range of  $[\text{FeCl}_3]$  studied. It has been proposed that the crystallographic twinning of akaganeite crystals is associated with conditions of low  $[\text{Cl}^-]$ ,<sup>8</sup> which can be achieved by reducing  $[\text{HCl}]$  or  $[\text{FeCl}_3]$ . In the context of the discussions presented above, it is important to demonstrate that the twinning truly is related to low  $[\text{FeCl}_3]$ , and not a crossed association to  $[\text{H}^+]$  or  $[\text{Cl}^-]$ .

In our results, we observe crystallographic twinning of akaganeite crystals grown from solutions with  $0.018 \text{ M} \leq [\text{FeCl}_3] \leq 0.18 \text{ M}$ , and  $0 \text{ M} \leq [\text{H}^+] \leq 0.017 \text{ M}$  (Figure 5.6d,e &Figure 5.8a-c). Being that we observe twinning over iron and acid concentrations that span an order of magnitude, it is not immediately obvious which factor is responsible for the twinning. Looking at both the similar aspect ratio and mean #arms in the twinned forms of the two  $[\text{H}^+] = 0$ ,  $[\text{FeCl}_3] = 0.18$  experiments (Figure 5.8a &Figure 5.14), we find that twinning is not strongly correlated to  $[\text{Cl}^-]$ . Comparing these results to crystallization with different  $[\text{H}^+]$ , but equal  $[\text{Cl}^-]$  and  $[\text{FeCl}_3]$  (samples SA-A, SS-A, Figure 5.8a &Figure 5.14), we find that twinning is not clearly correlated to  $[\text{H}^+]$ , either: while the highest acid conditions result in the exclusive formation of six-fold symmetric forms (sample SA-D, Figure 5.8d), they are not strictly crystallographically-twinned forms of akaganeite.

In seeking to unravel the branched, radial assemblies, which we observe in hydrogel-grown akaganeite, we compare our findings to existing literature on the growth of akaganeite with additives, and find conflicting reports. Some researchers find that Si in  $\beta\text{-FeOOH}$  increases twinning,<sup>20</sup> however, other reports do not list increased twinning in akaganeite crystals that contain  $\sim 3 \text{ mol\% Si}$ .<sup>24</sup> In Ge-doped akaganeite, increased twinning is observed.<sup>21</sup> In all cases, the crystallization conditions are solution-based and the only twinned forms that are reported comply with the (332) crystallographic forms; highly

branched assemblies are not observed. In addition the additives are supplied by both organic and inorganic reagents, with limited consistency in the  $[\text{Cl}^-]$  and  $[\text{H}^+]$ .

While the dependence of crystallographic twinning still remains somewhat elusive, we are able to identify the conditions that favor branching (radial assemblies) and splitting of the akaganeite rods, both features that we observe in the hydrogel-grown akaganeite (Figure 5.6a-c). The crystallization experiments that were designed to probe the effect of pH (samples SA-D, SS-A) on akaganeite crystallization from solution (Figure 5.8d & Figure 5.14), indicate that branching and the formation of radial assemblies of akaganeite rods is favored at high  $[\text{HCl}]$ , or lower pH. Here we refer to the different growth habit of the highest acid conditions (Figure 5.8d), as ‘branching’ and not a strict demonstration of crystallographic twinning due to its association with the formation of goethite. Crystal splitting at the ends of the akaganeite rods is seen to increase with increasing  $[\text{FeCl}_3]$  in both solution and hydrogel-based crystallizations. In akaganeite specifically, the emergence of crystal splitting has also been reported to be a function of crystallization temperature.<sup>27</sup> Largely, such sheaf morphologies are characteristic of high growth rate, owing to the high supersaturation established by increased  $[\text{FeCl}_3]$ .<sup>25</sup> Consistent with our results and discussion presented above, this dependence may also imply that splitting is related to  $[\text{H}^+]$  or  $[\text{Cl}^-]$  ( $\text{FeCl}_3 + 3\text{H}_2\text{O} \rightleftharpoons \text{Fe}(\text{OH})_3 + 3\text{HCl}$  Equation 8). Comparing the occurrence of sheaf morphologies in the acid-free crystallization experiments with different  $[\text{Cl}^-]$  (samples SA-A, SS-A, Figure 5.8a & Figure 5.14b), we see that the emergence of crystal splitting at the ends of akaganeite rods may be associated specifically with a high activity of chloride ions in the crystallization environment.

#### 151.2.4 Akaganeite-Goethite-Hematite Pathway

The formation of goethite (Figure 5.8d & Figure 5.10d) under conditions that favor akaganeite (low pH and the presence of chlorine ions) is a unique feature of this report. The akaganeite polymorph is stabilized at low pH; typically goethite is stabilized at high pH, even with akaganeite as a precursor.<sup>28,29</sup> Structurally, akaganeite and goethite are both distinguished by double chains of edge-shared octahedra, however, monoclinic akaganeite has a *bcc* anion lattice, while orthorhombic goethite has a *hcp* anion

lattice.<sup>13</sup> The akaganeite polymorph is stabilized by chloride substitutions into the tunnels defined by the octahedral chains, and the transformation to goethite is facilitated by replacement of chloride with hydroxide anions.<sup>13</sup>

Structurally, the relationship of hematite to goethite is topotactic. Both have an *hcp* anion sublattice, which remains intact during dehydroxylation of goethite to hematite.<sup>13</sup> Three unit cells of goethite form one unit cell of hematite, where the *c*-axes remain collinear.<sup>13</sup> Goethite forms twins across (210) planes over a range of pH and temperature conditions.<sup>13,26</sup> This twinning is responsible for planar structures with 6-fold symmetry, owing to the mutual rotation of three crystals about [001].<sup>30</sup> This propensity for twinning is preserved during dehydroxylation to hematite, resulting in hematite twins over (100).<sup>31</sup> Hematites transformed from goethite have mosaic structures with highly-oriented crystallites separated by micropores.<sup>13,31,32</sup> Importantly, the crystallographic domains within such hematites contain twin structures as a signature of their transformation from goethite, resulting in broadened x-ray peak intensities in specific reflections.<sup>31</sup>

Under the highest [H<sup>+</sup>] conditions (sample SA-D, Figure 5.8d), we find planar stars with 6-fold symmetry and the co-existence of akaganeite and goethite polymorphs. The structural motifs within these crystals are consistent with the crystallography of goethite twinning discussed above, and consistent with the symmetry of our overgrowth experiments (Figure 5.1). With the reports that akaganeite and goethite crystal structures can be indistinguishable at the nanoscale,<sup>33,34</sup> combined with the topotactic lattice relationships between goethite and hematite, we hypothesize that the akaganeite-goethite-hematite pathway<sup>35</sup> is a viable route to modulate the structure of hematite crystals, wherein the initial structural motif of the akaganeite phase can be preserved in the final hematite crystal.

#### **151.2.5 Role of Silica in the Formation Mechanism of Hematite in Silica Hydrogel**

In the earliest stages of hematite growth in silica hydrogel we observe elongated, star-like, radial assemblies of akaganeite rods (Figure 5.6c & Figure 5.15). These aggregates are distinct in appearance from the discrete akaganeite rods that formed in our solution experiments (Figure 5.6d-f). The results

presented and discussed above have demonstrated that  $[\text{Fe}^{3+}]$  affects the size of akaganeite crystals while  $[\text{H}^+]$  determines the aspect ratio. We have elucidated that crystal splitting, also known as sheaf formation, is correlated to high  $[\text{Cl}^-]$ . In addition, we have demonstrated that branched aggregates of akaganeite rods are favored at high  $[\text{H}^+]$  and associated with a pathway to hematite that proceeds through the goethite polymorph.

Chemically, the crystallization microenvironment within the silica hydrogel appears to contain a high activity of chloride ions and low pH, thereby favoring the formation of radial assemblies of akaganeite rods, with a high degree of branching and possibly a route through goethite as an intermediate phase. In addition, the crystallization microenvironment contains dissolved silica species, which are incorporated as atomic dopants in the final hematite crystals.<sup>1</sup> With this information, and reports of the precipitation of goethite as a minor product in low pH solutions<sup>28</sup> and its stabilization at low pH in presence of dissolved silicate<sup>36</sup> we find further support for a akaganeite-goethite-hematite pathway in the crystallization of hematite in silica hydrogel.

Physically, we propose two roles for the hydrogel in the crystallization microenvironment: (i) as a heterogeneous nucleation support for the akaganeite crystallization (Figure 5.15); and (ii) as a modulator of the assembly pathway of the akaganeite rods. In the latter role, recall that at low concentration the transformation from akaganeite to hematite is reported to be purely a dissolution/reprecipitation pathway, while at higher concentration the akaganeite rods assemble into rafts, which template the hematite nucleation.<sup>8,37</sup> In close association with the confined volumes of the hydrogel's cellular pore structure, the akaganeite templates will experience limited mobility, which may further promote the formation and stabilization of radially-branched structures, leading to quasi-spherical, highly-oriented, mosaic crystals of hematite.

As a whole, we find that our results distinguish the physical and chemical aspects of the hydrogel crystallization microenvironment, leading to insight into the features that are responsible for modulating the structure of hematite (Figure 5.16). In contrast to the discrete akaganeite rods that form in solution

growth (Figure 5.16a), a distinct physical consequence of the hydrogel microenvironment is the stabilization of akaganeite as 3-D assemblies (Figure 5.16d). Under solution-based conditions, the akaganeite rods assemble into square, planar structures, which template the nucleation and growth of hematite pseudo-cubes (Figure 5.16b,c).<sup>8</sup> When grown within the confines of a silica hydrogel, akaganeite assembly pathways are modulated such that quasi-spheres of hematite are formed and carry with them a signature of the 3-D akaganeite structures that preceded their growth (Figure 5.16e,f).

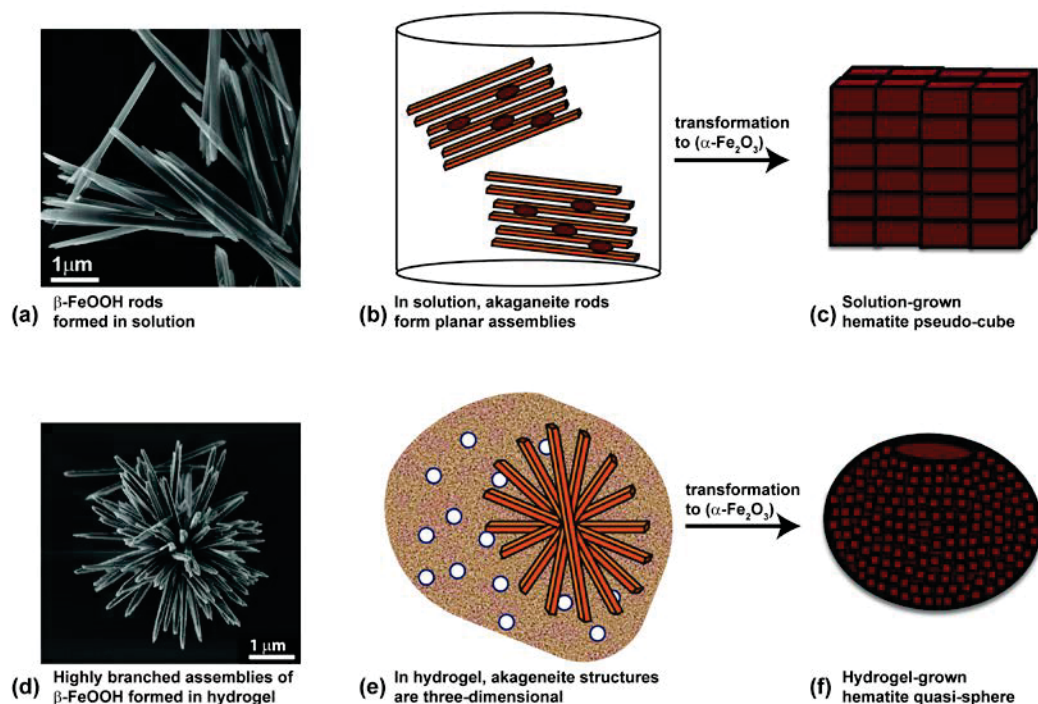


Figure 5.16 Representation of the proposed crystallization microenvironment associated with hematite quasi-sphere formation in silica hydrogel (d-e), shown in relation to hematite pseudo-cube growth from solution (a-c). At an equivalent  $[\text{FeCl}_3]$ , akaganeite ( $\beta$ -FeOOH) forms as discrete rods in solution (a), but occurs in highly branched structures when grown in silica hydrogel (d). In the solution-based crystallization microenvironment, (b) planar assemblies of akaganeite rods template the nucleation of hematite (red ovals), (c) leading to the formation of hematite pseudo-cubes. Changing the crystallization microenvironment to include (e) the physical effect of a confining hydrogel (speckled template) and the chemical effect of dissolved silicate species (white circles), the akaganeite assembly pathway is interrupted, encouraging the formation of 3-dimensionally branched structures, (f) which precede the growth of hematite quasi-spheres.

### 151.3 Summary and Conclusions

As a template for the growth of hematite, akaganeite structures can be modified by choice of chemical and physical characteristics of the crystallization microenvironment. Chemically, the size and aspect ratio of the akaganeite crystals can be modified by the  $[\text{Fe}^{3+}]$  and  $[\text{H}^+]$ , respectively. Crystal splitting and branching can be induced by high  $[\text{Cl}^-]$  and high  $[\text{H}^+]$ , respectively. By translating the iron oxide crystallization into a silica hydrogel matrix, two additional physical control parameters are achieved. The hydrogel matrix serves as both a heterogeneous nucleation sites and a means to stabilize akaganeite crystal forms, as 3-D assemblages, that are unique to growth in a hydrogel. In this way, the highly-branched, 3-D assemblies of akaganeite rods, with aspect ratios that increase with  $[\text{FeCl}_3]$ , are associated with expansion of the hematite crystal shapes along c-axis from a disc to a quasi-sphere, implicating the akaganeite structures as templates for the formation of hematite within the silica hydrogel.

We find our results to be consistent with a mechanism where the silica hydrogel defines the crystallization microenvironment as a means to modify the *atomic*, *nano*- and *microscale* features of hematite by modulating the morphology of the precursor phase, akaganeite. With the additional physical controls introduced by the hydrogel microenvironment, the structure of hematite can be tuned, while maintaining control over the net crystallographic orientation of the crystals. These findings provide insight into the formation of hierarchical structures of oxides at low temperatures and in aqueous solutions by designing the chemical *and* physical aspects of the crystallization microenvironment to modulate the structure of intermediate phases.

## **ACKNOWLEDGEMENTS**

We acknowledge support from the NSF (DMR 0845212 and DMR 1210304) and EAS acknowledges the NSF Graduate Research Fellowship (GRF, DGE-0707428), and Integrative Graduate Education and Research Traineeship (IGERT, DGE-0903653) Programs. This work was also supported in part by The Cornell Center for Materials Research (CCMR) and made use of the CCMR Shared Facilities, both funded by NSF MRSEC program (DMR 1120296).

## 151.4 Experimental

### 151.4.1 Materials

All reagents were used as received without further purification.

Iron (III) chloride hexahydrate ( $\geq 99\%$ ; Sigma-Aldrich)

Hydrochloric acid (36.5-38 %, Certified ACS Plus Reagent; Fisher Scientific)

Sodium metasilicate nonahydrate ( $\geq 98\%$ ; Sigma-Aldrich)

Sodium Hydroxide ( $\geq 97\%$ ; Fisher Scientific)

Sodium Chloride ( $\geq 99\%$ , Crystalline, Certified ACS, Fisher Scientific )

### 151.4.2 Methods

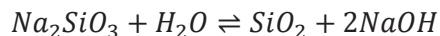
#### 151.4.2.1 Solution-based Crystallization

Solution-based crystallization experiments were performed under hydrothermal conditions (100 °C) in Teflon-lined vessels (Parr Instrument Company, USA) using a method modified from the literature.<sup>10</sup> Crystallization solutions were prepared in various concentrations (Table 1) by dilution from 1.8 M FeCl<sub>3</sub> and 1.0 M HCl solutions. After stirring for 30 min, the solutions were filtered using 0.2 μm nylon filters (Acrodisc, Pall Corporation, USA), sealed in the vessels and subject to hydrothermal treatment. To obtain akaganeite products the solutions were heated at 100 °C for 2 - 4 h. To obtain hematite products, the solutions were heated for 4 weeks.

#### 151.4.2.2 Silica Hydrogel Preparation

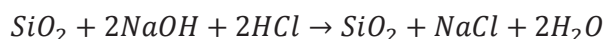
Silica hydrogels were prepared for crystallization by acidifying 15 mL of sodium metasilicate nonahydrate (0.5 M) solution with an equal volume of HCl (1.0 M), as described previously.<sup>1</sup> After stirring for 1 min, the onset of gelation was observed within minutes. The borosilicate vessels containing the hydrogel were sealed and set in a water bath at 30 °C for 24 h to reach full gelation.

Sodium metasilicate forms basic solutions when dissolved in water as described in  $\text{Na}_2\text{SiO}_3 + \text{H}_2\text{O} \rightleftharpoons \text{SiO}_2 + 2\text{NaOH}$  Equation 9.



*Equation 9*

The form of the silica(te) species that are present in solution can vary widely.<sup>38</sup> For clarity, only the general form of silica is represented here. Silica hydrogels with porous, cellular microstructure are formed by neutralizing sodium metasilicate solutions according to  $\text{SiO}_2 + 2\text{NaOH} + 2\text{HCl} \rightarrow \text{SiO}_2 + \text{NaCl} + 2\text{H}_2\text{O}$  Equation 10.



*Equation 10*

Post-crystallization, all counter salts were rinsed from the hydrogels by soaking in deionized water, leaving only the target akaganeite or hematite crystals within the porous networks.

#### 151.4.2.3 Crystallization within Silica Hydrogel

Hydrogel-based crystallization was performed using a single diffusion geometry by adding 30 mL of iron chloride hexahydrate solutions of the desired concentration to the top of the pre-formed silica hydrogels. Additional acid was not added with the iron reagent to the hydrogel-based crystallizations, as preliminary studies showed it to have little effect on the shape and morphology of the hematite crystals (results not shown). The iron chloride solutions were allowed to diffuse through the gel for 24 h in a 30 °C water bath. Crystallization was not observed prior to hydrothermal treatment. The sealed vessels were then subject to hydrothermal treatment (100 °C) for 24 h – 4 weeks depending on the crystalline phase that was desired. After reaction, the crystalline products were rinsed with deionized water (3x) and freeze-dried on a lyophilizer for 24 h. Crystalline products were isolated from the silica hydrogel matrix by soaking in NaOH (1 M) with gentle agitation for 1-3 days. Subsequently, the crystals were rinsed with deionized water (3x) and freeze-dried on a lyophilizer.

#### 151.4.2.4 Overgrowth Experiments

Hematite overgrowth experiments onto the hydrogel-grown hematite quasi-spheres was performed during isolation of the crystals from the silica hydrogel under basic conditions. Briefly, trace amounts of dissolved iron were supplied by the dissolving silica hydrogel in NaOH (1 M) with gentle agitation at room temperature for 7-10 d. After this time, the crystals were rinsed with deionized water (3x) and freeze-dried on a lyophilizer.

#### 151.4.2.5 Preparation for Characterization

Fresh hydrogel specimens were prepared for imaging the akaganeite crystals directly within the hydrogel matrices. Briefly, thin slices of freshly crystallized hydrogel samples were soaked in water to rinse out counter salts and subsequently freeze-dried on a lyophilizer for 24 h. The dried specimens were mounted on silicon wafers with conductive carbon paste (Electron Microscopy Sciences, USA), and coated with carbon while under the action of a rotating/tilting stage.

### **151.4.3 Characterization.**

Unless otherwise specified, phase analysis on the crystalline samples was performed by X-ray powder diffraction using a Scintag XDS2000 diffractometer with  $\text{CoK}\alpha$  radiation operating at 40 kV, 30 mA with a scan rate of 2 deg/min.  $\text{CuK}\alpha$  radiation on the same Scintag diffractometer was used as specified for some experiments with 40 kV and 40 mA.

Crystalline samples (uncoated) and freeze-dried hydrogel specimens (C-coated) were imaged using a Leo 1550 field-emission scanning electron microscope (Zeiss Microscopy, USA) operating at 2-5 keV. Crystalline samples were also imaged under bright-field conditions in a transmission electron microscope (TEM, Tecnai T12, FEI, USA) equipped with a  $\text{LaB}_6$  filament operating at 120 kV with a spot size of 3. High-resolution TEM was performed using a Tecnai F20 (FEI, USA) transmission electron microscope equipped with a field-emission source operating at 200 kV. Crystal size measurements for aspect ratio determination were taken on TEM images using ImageJ.

## REFERENCES

- (1) Asenath-Smith, E.; Hovden, R.; Kourkoutis, L. F.; Estroff, L. A. *in submission* **2015**.
- (2) Kokubu, T.; Oaki, Y.; Uchiyama, H.; Hosono, E.; Zhou, H. S.; Imai, H. *Chemistry-an Asian Journal* **2010**, 5.
- (3) Dang, F.; Oaki, Y.; Kokubu, T.; Hosono, E.; Zhou, H. S.; Imai, H. *Chemistry-an Asian Journal* **2013**, 8.
- (4) Asenath-Smith, E.; Li, H.; Keene, E. C.; Seh, Z. W.; Estroff, L. A. *Adv. Funct. Mater.* **2012**, 22.
- (5) Henisch, H. K. *Crystal Growth in Gels and Liesegang Rings*; Cambridge University Press: Cambridge, 1988.
- (6) Pourbaix, M. *Atlas of Electrochemical Equilibria in Aqueous Solutions*; 2 ed.; National Association of Corrosion: Houston, USA, 1974.
- (7) Gordon, L. M.; Roman, J. K.; Everly, R. M.; Cohen, M. J.; Wilker, J. J.; Joester, D. *Angewandte Chemie-International Edition* **2014**, 53.
- (8) Bailey, J. K.; Brinker, C. J.; McCartney, M. L. *J. Colloid Interface Sci.* **1993**, 157.
- (9) Asenath-Smith, E.; Estroff, L. A. *Microsc. Microanal.* **2014**, 20, 635.
- (10) Matijevic, E.; Scheiner, P. *J. Colloid Interface Sci.* **1978**, 63.
- (11) Frandsen, C.; Legg, B. A.; Comolli, L. R.; Zhang, H. Z.; Gilbert, B.; Johnson, E.; Banfield, J. F. *CrystEngComm* **2014**, 16.
- (12) Flynn, C. M. *Chem. Rev. (Washington, DC, U. S.)* **1984**, 84.
- (13) Cornell, R. M.; Schwertmann, U. *The Iron Oxides*; Wiley-VCH, 2003.
- (14) Hamada, S.; Matijevic, E. *J. Colloid Interface Sci.* **1981**, 84.
- (15) Blesa, M. A.; Matijevic, E. *Adv. Colloid Interface Sci.* **1989**, 29.
- (16) Post, J. E.; Buchwald, V. F. *Am. Mineral.* **1991**, 76.
- (17) Watson, J. H. L.; Heller, W.; Cardell, R. R. *J. Phys. Chem.* **1962**, 66.
- (18) Gallagher, K. J. *Nature* **1970**, 226.
- (19) MacKay, A. L. *Mineral. Mag.* **1960**, 32.
- (20) Cornell, R. M. *Zeitschrift Fur Pflanzenernahrung Und Bodenkunde* **1992**, 155.

- (21) Song, Y.; Bac, B. H.; Lee, Y. B.; Kim, M. H.; Kang, I. M. *CrystEngComm* **2011**, *13*.
- (22) Inouye, K.; Imamura, H.; Kaneko, K.; Ishikawa, T. *Bull. Chem. Soc. Jpn.* **1974**, *47*.
- (23) Yue, J.; Jiang, X. C.; Yu, A. B. *Journal of Nanoparticle Research* **2011**, *13*.
- (24) MacKay, A. L. *Mineralogical Magazine* **1962**, *33*.
- (25) Sunagawa, I. *Crystals: Growth, Morphology & Perfection*; Cambridge University Press: New York, 2005.
- (26) Maeda, Y.; Hirono, S. *Japanese Journal of Applied Physics* **1981**, *20*.
- (27) Hu, Y. H.; Chen, K. Z. *J. Cryst. Growth* **2007**, *308*.
- (28) Atkinson, R. J.; Posner, A. M.; Quirk, J. P. *Clays Clay Miner.* **1977**, *25*.
- (29) Cai, J.; Liu, J.; Gao, Z.; Navrotsky, A.; Suib, S. L. *Chem. Mater.* **2001**, *13*.
- (30) Cornell, R. M.; Mann, S.; Skarnulis, A. J. *Journal of the Chemical Society-Faraday Transactions I* **1983**, *79*.
- (31) Watari, F.; Vanlanduyt, J.; Delavignette, P.; Amelinckx, S. *J. Solid State Chem.* **1979**, *29*.
- (32) Loffler, L.; Mader, W. *J. Eur. Ceram. Soc.* **2006**, *26*.
- (33) Ahn, T.; Kim, J. H.; Yang, H. M.; Lee, J. W.; Kim, J. D. *J. Phys. Chem. C* **2012**, *116*.
- (34) Navrotsky, A.; Mazeina, L.; Majzlan, J. *Science* **2008**, *319*.
- (35) Lin, M.; Tng, L.; Lim, T. Y.; Choo, M.; Zhang, J.; Tan, H. R.; Bai, S. Q. *J. Phys. Chem. C* **2014**, *118*.
- (36) Glasauer, S.; Friedl, J.; Schwertmann, U. *J. Colloid Interface Sci.* **1999**, *216*.
- (37) Maeda, Y.; Hachisu, S. *Colloids Surf.* **1983**, *7*.
- (38) Iler, R. K. *The Chemistry of Silica: Solubility, Polymerization, Colloid and Surface Properties, and Biochemistry*; John Wiley & Sons: New York, 1979.

## 152 CONCLUSIONS

### 152.1 Summary

The broad goal of this dissertation was to achieve structural control over transition metal oxide architectures using a bio-inspired approach. Aiming to achieve the ability to direct the hierarchical assembly and crystal planes expressed in transition metal oxide compounds by growth in a hydrogel, this dissertation sought to investigate the hypothesis that architectural control of oxides (and their formation as nanocomposites) is a route to improved properties for sustainable energy technologies. By first establishing a set of rules (Ch. 2), which describe the biological crystallization microenvironment, synthetic approaches were designed to meet the crystallization conditions required to form transition metal oxides. Largely, this involved translating the biological model of (extracellular) matrix-mediated mineralization to hydrothermal conditions and extremes of pH. Moving to an inorganic matrix based on silica, as opposed to the low-melting-point, pH-neutral, biopolymer hydrogels used by biological organisms, afforded the chemical and thermal versatility needed to form transition metal oxides using a bio-inspired approach.

The hematite polymorph of iron (III) oxide was used as a first model system in this dissertation. Hematite was chosen as a model system due to the range of pH conditions under which it can be formed, using low (100 °C) hydrothermal temperatures. By choosing the hematite phase, the complexities of redox could be eliminated. When crystallized from aqueous solution, hematite forms in pseudo-cubic, hierarchically-structured forms, which are composed of highly-orientated, nanoscale domains (Ch. 3). The structural and crystallographic relationships within these architectures preserve a net orientation of the hematite lattice to the microscale. When crystallized within the physical confines of a silica hydrogel, hematite forms in quasi-spherical forms, which also carry a hierarchically-structured motif.

The structural control afforded by growth in a hydrogel stems from both chemical (Ch. 4) and physical (Ch. 5) aspects of the hydrogel crystallization microenvironment. Chemically, silica species are

liberated from the hydrogel matrix during crystallization and incorporated as dopants into the hematite lattice. The incorporated silicon modulates the architecture of the hematite crystals across multiple length scales: atomically, the hematite lattice is expanded along [001]; nanoscale domains grow preferentially along [110]; the mesoscale assembly has a planar radial structure, which propagates in the hematite a-b plane; crystallographic registry is maintained at the microscale, with the [001] positioned along the shortest diameter of the quasi-spheres. The conclusions of such a structural analysis are that the quasi-spherical hematite crystals grown within a silica hydrogel are defined by microscale surfaces that are composed of nanoscale high catalytic activity (110) planes. When compared to discrete, nano-sized hematite crystals we find that the structural complexities of the microscale hematite architectures is responsible for their increased photocatalytic performance. These results come in stark contrast to previous reports on the photocatalysis of hematite, wherein nano-sized crystals have been the target for improved performance. In the hydrogel-based crystallization microenvironment, the presence of the silica hydrogel can have two physical implications: as a heterogeneous nucleation template; and as a modulator of the assembly pathway of the akaganeite ( $\beta$ -FeOOH) intermediate phase, which templates the subsequent crystallization of hematite.

## **152.2 Future Directions**

The ability to characterize the complex structural relationships present within hierarchical architectures has broad-reaching implications in and of itself. With the ability to quantitatively correlate property improvements to structural modifications afforded by hydrogel growth, a whole new approach to the design of transition metal oxides for sustainable energy technologies has been achieved. These results open the possibility to grow other functional oxide materials in hydrogels and exhibit predictive control over their structures and properties by judicious choice of the chemical and physical aspects of the hydrogel and the exploitation of intermediate oxyhydroxide phases as structure directing templates for the corresponding oxide phases.

A logical progression from the iron oxides to other transition metal oxide compounds is easily conceived. The inter-conversion of iron oxide phases provides many pathways to access functional materials for a range of applications. As an example, consider the introduction of a reducing agent into the silica-hydrogel-based growth of hematite, leading to the formation of the magnetite phase. Hierarchically-structuring these crystals on specific length scales could lead to materials that are optimized for medical imaging. With a reducing agent in the hydrogel system, new transition metal oxide compounds can be pursued for hydrogel-growth. As an example, consider the formation of cuprous oxide ( $\text{Cu}_2\text{O}$ ) using a crystallization approach derived from Fehling's test for reducing sugars. The formation of hierarchically-structured architectures based on cuprous oxide may yield materials which are optimized for solar applications; with increased absorption and decreased recombination achieved by architectural control afforded by the hydrogel crystallization microenvironment.

### **152.3 Outlook**

Broadly speaking, I have interpreted the crystallization by a bio-inspired approach as, "the growth of a target compound under diffusion-limited conditions in the presence of a matrix." The target compound can be a carbonate, phosphate or an oxide. The matrix can be biopolymer hydrogel, an inorganic hydrogel, a template or an array of colloids or nanoparticles. The diffusion-limited conditions mean that at least one reagent is supplied via diffusion, which may take place in either the liquid phase or the vapor phase. With such an expansive synthetic interpretation of biological mineralization one can hypothetically combine any materials they like and form them into hierarchically-structured nanocomposite architectures for almost any application. The ability to combine materials with different chemical, structural and atomic characteristics is a powerful strategy to modulate materials properties, some of which may even drive the development of new technologies.

## 152.4 Related works

My broad, expansive interpretation of bio-inspired crystallization presented above (Section 6.3) has come with no shortage of research ideas to pursue during my graduate studies. The biggest challenge was that I simply didn't have enough hours in the day to pursue them all. The solution to one set of ideas that I developed became the basis for international research collaboration and the senior theses of two undergraduate students.

Some of fundamental questions that linger in the biomineralization community stem from the unusual characteristics of biominerals as nanocomposites: How can an otherwise single crystal occlude second phase guests within its structure with no loss to the long-range crystallographic order? Such questions have motivated many biomimetic studies, which have focused on calcium carbonate's amenability to form single crystal composites by growth in hydrogels, within templates and in colloidal arrays. While the bulk of my thesis developed the use of a hydrogel as a feature of the crystallization microenvironment for transition metal oxides, I had ideas to explore crystallization within confinement and in the presence of particles as a means to access other materials combinations. Moving to particles as the growth matrix would allow me to study of the effect of surface chemistry on incorporation. Moving to crystallization within confining templates would allow me to study the physical aspects of incorporation under diffusion limited conditions. Using metals as the particles and transition metal oxides as the crystals would form a robust system that could be fully interrogated to unravel the fundamental implications of structure and composition on the interface between the two intimately associated materials.

The 'biomimetic crystallization in confinement' approach, using calcium carbonate as a model system, has been pioneered by Prof. Fiona Meldrum at University of Leeds, UK. Through discussions with her, I learned of ways to use the confinement of a template to facilitate the incorporation of particles. When paired with my extensive knowledge about the formation of transition metal oxides from aqueous solutions, our collaboration was off and running. I chose cuprous oxide as the target oxide and gold as

the target colloid. I chose these materials for two reasons: potential applications to sustainable energy applications; and amenability to fundamental studies using electron microscopies. First, this combination of materials would build on the application of cuprous oxide ( $\text{Cu}_2\text{O}$ ) in solar energy technologies.<sup>1-6</sup> Second, the atomic number differences between copper and gold would make for very good contrast in the transmission electron microscope and the thermal stability of  $\text{Cu}_2\text{O}$  would ensure that beam damage was negligible. It is important to note that all biomimetic single crystals composites up to this point were based on calcium carbonate, which decomposes under electron beams, and polymer colloids, which have poor contrast with calcium minerals. Due to this reality, the kind of information that has been gleaned from these studies, concerning structural and compositional relationships at the interface between two dissimilar materials, has been very limited. The combination of  $\text{Cu}_2\text{O}$  and Au nanoparticles (np) would eliminate these historical challenges and possibly open the door to a hybrid metal-semiconductor material with new properties.

This project quickly bifurcated into two: the crystallization of cuprite within the pores of track-etched membranes; and the crystallization of cuprite within the confinement of a wedge. To introduce the Au np into these systems, the Au np could be loaded into the membrane pores and the wedge space, allowing the formation of the metal-semiconductor nanocomposites that we desired. The appeal of the track-etched membranes was that they would allow us to crystallize the cuprite mineral in high aspect ratio rods (non-equilibrium morphologies) of different diameters, thereby forming electron transparent specimens without any sample preparation. The elegance of the wedge derived from our ability to form equilibrium polyhedral crystals of cuprite and study the effect of particles on crystallization.

The first hurdle in getting these projects going was to expand the cuprite synthesis so that crystallization could be induced by the vapor phase diffusion of a reducing agent at elevated temperatures ( $\sim 60^\circ\text{C}$ ). Using a double-walled, heated reaction chamber, and the vapor diffusion of hydrazine hydrate, a robust approach to the crystallization of cuprite was achieved. As these projects evolved, it became clear that the membrane system was best for studying the physical aspects of incorporation in

confinement, while the wedge system was an elegant approach to studying the chemical effects associated with the interaction between growing crystals and guest particles. Clearly, each project had evolved into an entire thesis of its own. In order to ensure the successful progression of these projects, I initiated a mentorship with two undergraduate students: one a rising junior from Chemistry; the other a rising senior from Materials Science and Engineering. I paired these students using a modified dyad model wherein the students with different strengths and skills are matched to facilitate their growth as each other's mentors. The membrane and wedge projects would serve as separate, but complimentary projects for each of these students. I deliberately sought to connect their projects by a common scientific approach, to encourage their collaboration and knowledge exchange as they solved problems specific to their own projects.

Upon seeing these two undergraduate students develop independence both as individuals and as a team, I approached my advisor, advocating for these two students as good candidates to travel abroad and conduct research in an international setting in support of our collaboration with Prof. Meldrum's Group in Leeds, UK. These students completed an 8-week session of research in England, and demonstrated huge growth as researchers in synthesis and characterization of inorganic crystals. They each took ownership for their roles in each of the projects, writing senior theses, which formed the basis for publications of these works that are currently in progress. Through this platform, I have grown as a researcher and as a mentor, while learning how to tackle new problems from a basis of fundamental knowledge about science and how people learn.

### **152.5 Career Development**

At the heart of it all, I have a true passion to use materials chemistry and characterization to develop solutions to the challenges facing sustainable energy technologies. In planning my career, I am specifically searching for opportunities that will leverage my expertise in materials chemistry and characterization, and my zeal for collaboration in research and mentoring. I enjoy working collaboratively

with my colleagues and mentees toward a common goal. I am committed to the power of teams to combine a diversity of individual strengths to form a unit that is stronger than the sum of its parts. With my research skills and expertise stemming from my broad understanding of the interactions of matter from the atomic level to the macro-scale, I am confident in my ability to make valuable contributions to the development of materials for sustainable energy technologies.

## REFERENCES

- 1 Britzman, S. *et al.* Epitaxially aligned cuprous oxide nanowires for all-oxide, single-wire solar cells. *Nano Letters* **14**, 4665-4670, (2014).
- 2 Cushing, S. K. *et al.* Photocatalytic activity enhanced by plasmonic resonant energy transfer from metal to semiconductor. *Journal of the American Chemical Society* **134**, 15033-15041, (2012).
- 3 Atwater, H. A. & Polman, A. Plasmonics for improved photovoltaic devices. *Nature Materials* **9**, 205-213, (2010).
- 4 Pan, Y. L. *et al.* Plasmon-enhanced photocatalytic properties of cu<sub>2</sub>o nanowire-au nanoparticle assemblies. *Langmuir* **28**, 12304-12310, (2012).
- 5 Wang, X. *et al.* Silicon/hematite core/shell nanowire array decorated with gold nanoparticles for unbiased solar water oxidation. *Nano Letters* **14**, 18-23, (2014).
- 6 Zhang, L., Blom, D. A. & Wang, H. Au-cu<sub>2</sub>o core-shell nanoparticles: A hybrid metal-semiconductor heteronanostructure with geometrically tunable optical properties. *Chemistry of Materials* **23**, 4587-4598, (2011).